Numerical Investigation of the Formation and Translation of a Field Reversed Configuration with Neutrals and External Circuits Effects

Akihisa Shimazu

A dissertation
submitted in partial fulfillment of the
requirements for the degree of

Doctor of Philosophy

University of Washington

2020

Reading Committee:

Richard Milroy, Chair

Uri Shumlak

Brian Nelson

Program Authorized to Offer Degree:
Aeronautics & Astronautics

University of Washington

Abstract

Numerical Investigation of the Formation and Translation of a
Field Reversed Configuration with Neutrals and External Circuits Effects

Akihisa Shimazu

Chair of the Supervisory Committee:
Research Professor Emeritus Richard Milroy
William E. Boeing Department of Aeronautics & Astronautics

A Field Reversed Configuration (FRC) is a high-β closed field line magnetic confinement topology, categorized as a compact toroid. Effects of plasma-neutral interactions in FRC formation and translation processes are studied using numerical simulations performed using the Cygnus code in axisymmetric two-dimensional geometries. A plasma-neutral interaction model is implemented in the Hall magnetohydrodynamics (MHD) code, Cygnus, that supports full coupling of external circuits driven magnetic fields to plasma fluid dynamics. Electron impact ionization, radiative recombination, and resonant charge exchange reactions are included in the plasma-neutral interactions. Results from simulations are compared to experimental measurements from the Venti Formation experiment at Helion Energy. After tuning anomalous transport coefficients to match experimental results, reasonable agreements to the experimental data are obtained. However, the level of agreements obtained by the code suggests that there are additional physics that are important in the FRC formation processes such as molecular neutral effects.

In order to understand the importance of molecular neutral effects in FRC formations, an extension to the plasma-neutral fluid model that includes effects of diatomic deuterium species is developed. The model retains the simplicity of the original single species plasma-neutral model but allows for species generation and destruction for the following species:

D, D_2, D^+, D_2^+, D_3^+, and e. Electron impact reactions including ionization, dissociative ionization, dissociation, dissociative excitation, dissociative recombination, and radiative recombination are implemented in the model. Heavy particle impact reactions including both resonant and non-resonant charge exchange and plasma-chemical reactions are implemented. A derivation of the molecular model including the required reaction collision terms is given.

The molecular model is used to perform simulations of experimental conditions from the Venti Formation experiment using the same anomalous transport settings as the single species plasma-neutral model. Results from the molecular model is compared to both experimental and single species plasma-neutral simulation results to determine the importance of molecular neutral effects. Results from the molecular model show similar level of agreements to the experiment as the single species plasma-neutral model. However, it shows improved agreements to the experimentally measured single chord averaged plasma density in the early preionization phase. The simulation results show non-negligible diatomic deuterium population at the end of the preionization process, suggesting the importance of the diatomic deuterium species during the field reversal in the FRC formation processes.

TABLE OF CONTENTS

LIST OF FIGURES

LIST OF TABLES

Chapter 1

INTRODUCTION

This chapter introduces the Field Reversed Configuration (FRC) and the numerical model used for this research. Section 1.1 gives motivation and a brief description of this study. The background of FRCs is given in Section 1.2. Section 1.3 gives a brief description of the experiment to which the results from the numerical simulation are compared. Section 1.4 gives a brief survey of past works that investigated neutral effects in FRCs and gives an overall placement of this research compared with past works. Finally, in Section 1.5, a brief discussion of the computational tool used for this research, Cygnus, is presented.

In Chapter 2, details of the Cygnus code after modifications are made to include neutral effects as part of this study are presented. In Chapter 3, simple problems involving FRC formation and translation are simulated using the modified Cygnus code, and resulting behaviors for various initial conditions are discussed. In Chapter 4, the modified Cygnus code is used to simulate conditions from the actual experiment and best efforts are made to match experimental measurements. In the subsequent Chapter 5, possible sources of error in matching the experiment are discussed.

In Chapter 6, the numerical model presented in Chapter 2 is extended to include effects of molecular deuterium species. In the subsequent Chapter 7, the simulations in Chapter 4 are repeated using the new extended model to determine the importance of the additional molecular physics added to the model. Finally, in Chapter 8, results from this research are summarized.

1.1 Motivation

A Field Reversed Configuration (FRC) is a closed field line magnetic confinement topology that is categorized as a compact toroid. Recently, there has been large interest in the FRCs for applications in both space propulsion and as an alternative path towards fusion.

In the space propulsion community, there are strong interests in FRC based thrusters as it enables true electrodeless operation of an electric propulsion (EP) system. An example of an FRC based thruster is the Electrodeless Lorentz Force (ELF) thruster that was developed by MSNW [1]. Electrodes in traditional EP devices such as Ion thrusters are a serious thruster lifetime limiting component; removal of such component promises a longer operating life for FRC based thrusters. Furthermore, because the electrode erosion is no longer an issue in the design of the thruster, a wide range of propellants can be used as long as the propellant is ionizable. This opens potentials for using non-traditional EP propellants such as water in the thruster, allowing for in-situ resource utilization (ISRU) [2].

The community interest in an FRC based thruster concept is apparent, as the ELF thruster research at MSNW was selected as one of the three advanced propulsion system for NASA's Next Space Technologies for Exploration Partnerships (NextSTEP) projects [3]. Through the NextSTEP project, it is expected that an ELF thruster capable of 100 to 300 kW power operation is developed and tested, which lays the path for future lifetime testing and technology demonstration missions. There also exists separate FRC thruster research program at the Air Force Research Laboratory to develop FRC based thruster concepts for high power EP applications [4].

For fusion energy applications, various unique attributes of the FRCs are drawing interest in its use for commercial fusion energy reactors. Traditionally, magnetic confinement and inertial confinement fusion have been explored for fusion energy applications. However, while significant progresses have been made to both concepts, no commercially viable fusion reactor has been developed to this date from these two concepts. There is a third path to fusion that utilizes the intermediate conditions of magnetic and inertial confinement fusion called

magneto-inertial fusion, for which the FRC is well suited. Since the magneto-inertial fusion is expected to significantly reduce the reactor cost compared to the traditional magnetic and inertial fusion concepts [5], this makes investigating fusion reactor systems using the FRCs attractive for commercial electricity generations.

Due to promising fusion applications of the FRCs, private companies are now studying FRCs for economical fusion reactor applications. TAE Technologies [6] is studying the use of FRCs for aneutronic fusion applications. They have made significant progresses in obtaining high performance FRC configurations with the FRC total energy and particle confinement lifetime far better than any experiments in the past. Using the High Performance Field-reversed configuration (HPF) state [7], in 2014, they obtained total energy and particle confinement times of roughly 0.8 and 2 ms, respectively [8]. Another company, Helion Energy [9], is investigating a staged magnetic compression of FRCs to fusion conditions. The Venti experiment was awarded funding from the ARPA-E ALPHA program, and the experiment made significant advances in furthering the understanding of the staged compression physics of FRCs [10].

For both space propulsion and fusion energy applications, numerical modeling plays an important role in understanding experimental observations and extrapolating results to future designs. Thus, the ability to model FRCs in experimental conditions is of great interest to both space propulsion and fusion energy communities. In both communities, plasma-neutral interactions and inductive couplings of FRCs to external conductors are some of common effects that are often encountered. This is an area that has not been fully explored in the past, and it may be important for FRC dynamics.

In this study, effects of neutrals on FRC formation and translation processes are studied using numerical simulations. In order to study neutral effects on an FRC that has strong coupling to external dynamic circuits, the plasma-neutral model developed by Meier and Shumlak [11] is implemented in the existing resistive and Hall magnetohydrodynamics (MHD) code, Cygnus, that supports coupling between plasma dynamics and external circuits. This allows development of a numerical model that captures plasma-neutral inter-

actions in an FRC that is driven by external circuits. The developed model is tested against experimental results from the Venti Formation experiment provided by Helion Energy [9] to determine the effectiveness of the present model at capturing experimentally observed behaviors of the FRC.

1.2 Background of Field Reversed Configurations

An FRC is a high-β, cylindrical magnetic confinement system with a little to no azimuthal magnetic field. The basic schematic of an FRC in a rz-plane is shown in Fig. 1.1, and key features such as separatrix, X-point, and O-point can be observed. The separatrix defines a region of closed magnetic field lines, which is isolated from the external magnetic field lines. The X-point is a magnetic null point caused by the field line termination. The O-point is a circular magnetic field axis for the internal magnetic field. Due to the linear nature of an FRC, it is neutrally stable to axial translation and is an axially movable object.

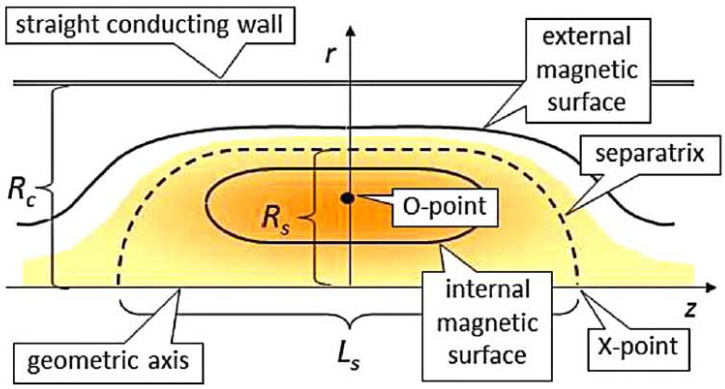

Figure 1.1: A schematic of a Field Reversed Configuration [12].

The size of the FRC is generally defined by the separatrix length (L_s) and separatrix radius (R_s) as shown in Fig. 1.1. Typically, normalized FRC geometric quantities are used. The relative radius (X_s) is defined as

$$X_s \equiv R_s/R_c \tag{1.1}$$

where R_c is the radius of the coil. The separatrix elongation (E) is defined as

$$E \equiv L_s / (2R_s) \tag{1.2}$$

Additional details of the FRCs can be found in the review papers by Tuszewski [13] and Steinhauer [12]. Here, only selected details of the FRCs that are pertinent to this study are discussed.

1.2.1 Formation

The formation (or the start-up) of an FRC can be achieved through various means. A survey of common techniques for the FRC formation can be found in Steinhauer [12]. Here, the details of the field-reversed theta-pinch (FRTP) formation method is briefly introduced. This is the FRC formation method modeled in this project. The complete process of the traditional FRTP method is covered in detail by Tuszewski [13]; more modern improvements to the FRTP method are summarized by Steinhauer [12].

In the FRTP formation, a preionized gas is initially placed inside a theta-pinch, a device with cylindrical and linear magnetic coils surrounding the insulating plasma chamber. To start the formation process, a bias capacitor bank is discharged into the magnetic coils to imbed the bias magnetic field into the preionized gas. The bias field is directed in an opposite direction to the field that is to be produced by the main bank. The main bank is then discharged into the magnetic coils to rapidly reverse the magnetic field in the theta-pinch. A current sheet forms in the outer radius of the plasma column to buck the rising forward field. This results in a radial implosion of the plasma into a field reversed condition due to the Lorentz force. A rapid ionization of the preionized gas occurs in the radial implosion. Finally, the magnetically isolated FRC contracts axially due to magnetic tension force, resulting in a creation of a quiescent FRC [12, 13]. The formation processes of the FRTP method are illustrated in Fig. 1.2.

To improve the FRTP formation, various techniques have been developed and are often

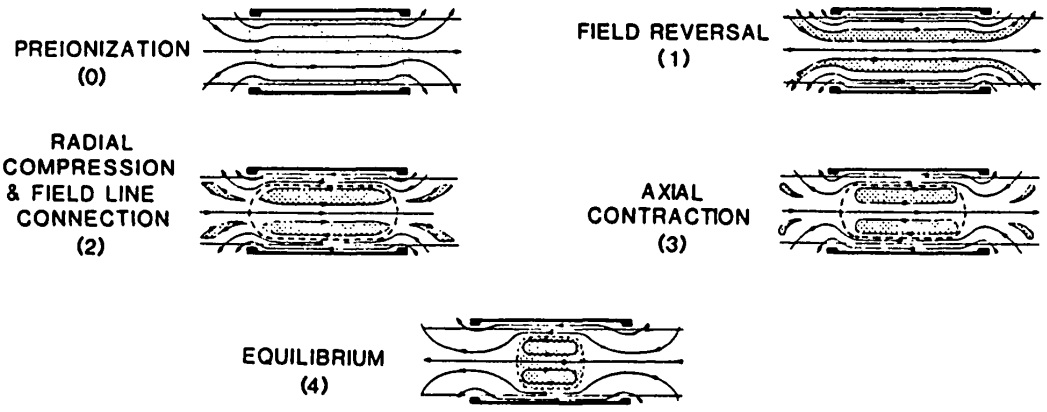

Figure 1.2: Steps of the field-reversed theta-pinch (FRTP) formation method [13].

used. For example, a crowbar circuit is a common technique to extend the pulse from the main bank. In a crowbar circuit, the typical circuit system containing a capacitor bank and coil (which is approximately an RLC circuit) is modified by adding a crowbar leg parallel to the coil. This is illustrated in a simple crowbar circuit shown in Fig. 1.3. In the crowbar leg, either switch or diode is used to keep the crowbar leg open during the first quarter-cycle of the capacitor bank firing. At the end of the first quarter-cycle, the circuit is crowbarred by closing the crowbar leg to produce a bypass that isolates the capacitor bank from the system. This allows a resistive decay of the coil current through the crowbar resistor instead of the LC oscillation [12].

Another technique often used in the FRTP formation process is a programmed formation technique that was originally developed in the works of Kurmullaev et al. [14] and further improved in the TRX program [15]. In the programmed formation, trigger (or plug) coils are added to the two ends of the main formation coil. Trigger coils produce an initial cusp magnetic field by providing a forward bias when the main formation coil is providing a reverse bias field. This cusp field defines the location of X-points during the formation process and allows the system to be in an isolated field reversed condition immediately after the plasma lift-off from the formation chamber wall. As a result, one can control initial FRC conditions

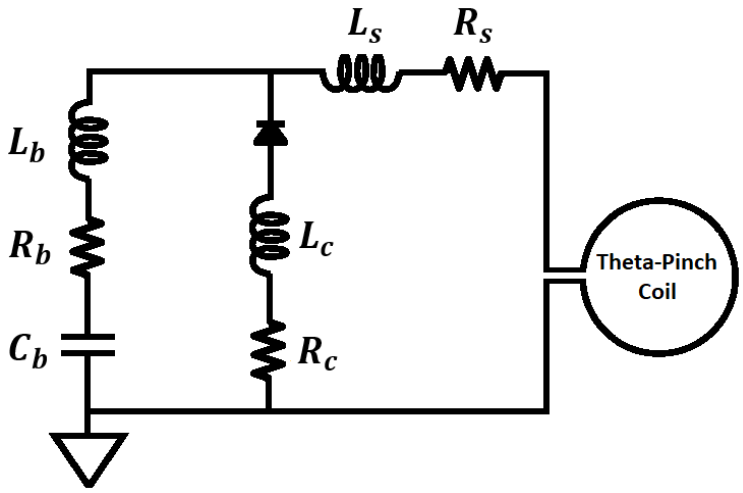

Figure 1.3: A circuit diagram of an RLC circuit with an additional crowbar diode leg connected to a theta pinch coil.

better than the case without the trigger coils where a tearing magnetic reconnection is required to establish an isolated field reversed condition [13]. A formation of an FRC using the programmed formation method is illustrated in Fig. 1.4.

To improve the flux retention in the FRC during the formation process, a multipole barrier coil may be added to the formation chamber [15]. The barrier coil produces a local transverse magnetic field (barrier field) at the inner wall of the formation chamber [12]. In the process of forming an FRC, the plasma and frozen magnetic fields are moved towards the wall as the applied magnetic field goes through zero. This can result in plasma wall contacts, leading to impurity injection and trapped flux losses [14]. The barrier field serves to hinder the movement of the cylindrical plasma column during the field reversal to limit these negative effects [12].

Lastly, the translation of the FRC formed by the FRTP method is significantly improved when a dynamic formation technique is used [16]. In the dynamic formation, a single formation coil is replaced by a series of short magnetic coils that are operated independently. These coils serve as both formation and accelerator coils; the coils are sequentially fired such

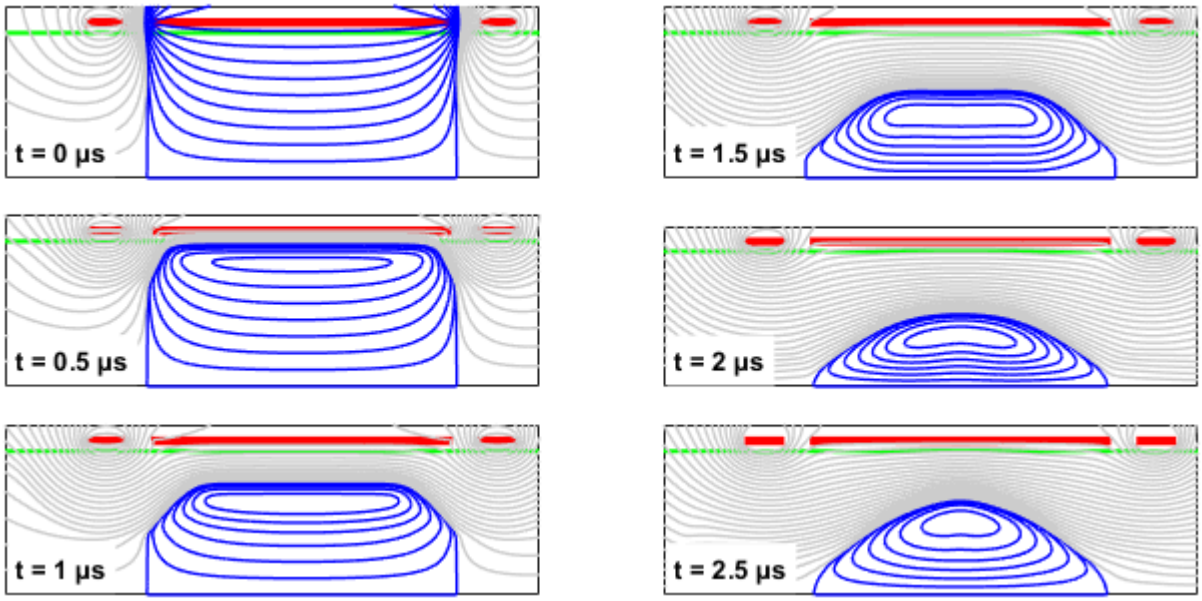

Figure 1.4: Flux contours from a 2-D MHD simulation using a programmed formation of an FRC.

that each coil continuously reverses the magnetic field to compress and accelerate the FRC. Thus, the FRC formation and translation are achieved together. This technique is especially useful in a collisional merging formation method, where two FRCs are formed, accelerated, and collided against each other in order to form a single FRC. With the sequential execution of the field reversal, the FRC flux is sustained throughout the entire collisional merging formation process, and the condition of the FRC before the merge is improved [17].

1.2.2 Staged Compression of FRCs

A staged compression of an FRC is a relatively new concept that is an extension of the dynamic formation process. In the staged compression process, an FRC is compressed to a high temperature and density and then translated using a pulsed and sequential firing of magnetic coils [17]. This process is similar to the dynamic formation process, except that each coil sequentially compresses the FRC to a smaller radius. In a typical system, staged compression is followed by a collisional merging process. The compressed FRC is injected

into a final compression chamber where it collides and merges with the second FRC that was injected into the chamber in the same manner but from the opposite direction. The merged FRC is further compressed to a high magnetic field, achieving fusion conditions. A conceptual schematic of the FRC fusion reactor using the staged compression concept by Slough et al. is shown in Fig. 1.5 [17].

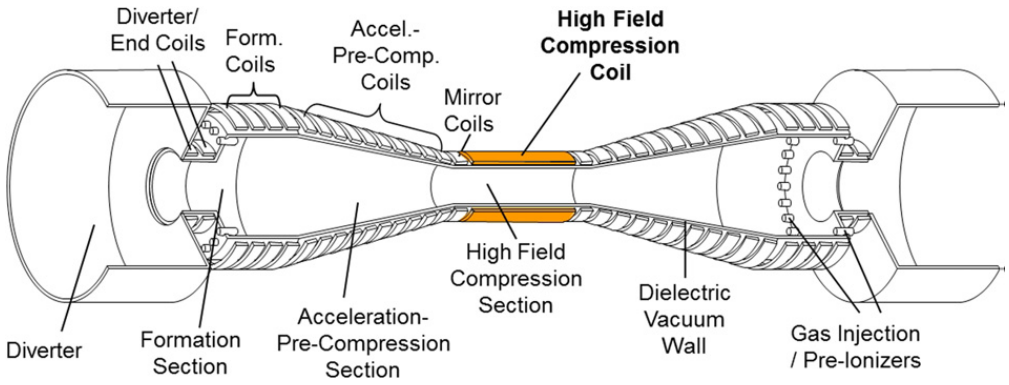

Figure 1.5: Conceptual schematic of an FRC fusion reactor using staged compression [17].

In a staged compression device, there are three distinct regions: formation, acceleration, and compression. Typically, staged compression occurs in the accelerator section, and the formation section uses the dynamic formation technique. One key feature of the staged compression device is the use of pulsed gas-puffs that inject the neutral gas to the formation section. As such, the initial gas fill process is dynamic. The preionization and formation processes are performed in the dynamically filled formation chamber, and each formation coil is fired in a sequential manner to form, push, and compress the FRC into the acceleration section [18].

1.2.3 Preionization

In order to form an FRC using FRTP based methods, one must start with a preionized gas in the formation chamber with a sufficient reverse bias field imbedded before the main theta-pinch coil is fired. There exists many techniques for preionization in the formation chamber

and no single preionization method is superior or standard for FRC formations [13]. Here, two preionization techniques relevant to the systems being simulated in this study are discussed. They are the ringing theta-pinch and ringing barrier ionization techniques.

The ringing theta-pinch ionization uses an additional capacitor bank that has a higher oscillation frequency compared to the bias bank, which is connected to the formation coil. The ringing field is applied on top of the bias field to induce an electric field in the chamber for ionization. The resulting axial magnetic field profile as a function of time is shown in Fig. 1.6. Free seed electrons can be provided to assist the breakdown process, while the ringing field results in a complete gas breakdown when it is fired at the bias field maximum [19]. An important feature in the ringing theta-pinch ionization is the existence of the magnetic zero-crossing, where the ringing field nullifies the applied bias field [20].

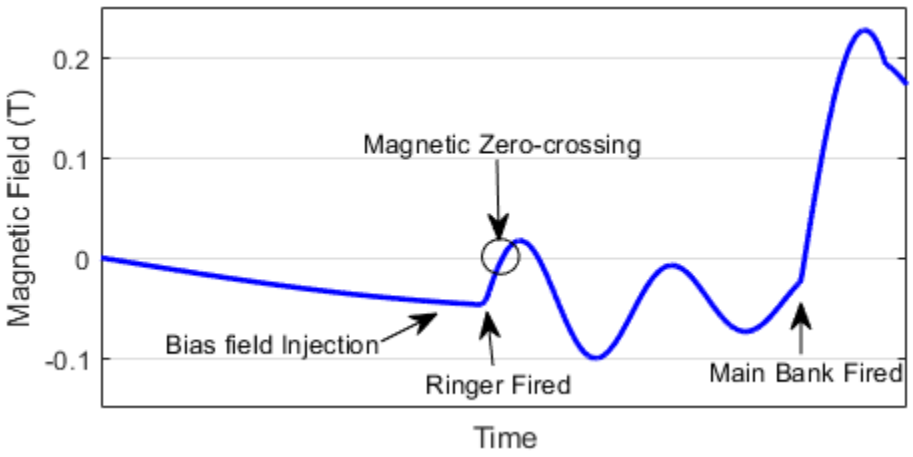

Figure 1.6: A sample axial magnetic field profile from the ringing theta-pinch ionization process for FRC formation.

Based on the experimental observations, the gas breakdown due to the ringing theta-pinch occurs at the magnetic zero-crossing. The subsequent ringing cycles implode and oscillate the zero-crossing generated plasma, leading to further breakdown [20]. For example, in the FRX-C experiment, the breakdown was first observed at the time of the second zero-crossing for a lower bias field; for a higher bias field, it was first observed at the time of the maximum

reversed field. The transition point was found to be at 0.11 T for the FRX-C device [21]. Typical experiments have a few ringing cycles prior to the main bank firing with a sufficient number of magnetic zero-crossings to ensure complete ionization.

One of the biggest disadvantages of the ringing theta-pinch ionization is the flux loss associated with the magnetic zero-crossing. Both experimental and numerical studies on the FRX-B device indicated that the use of ionization techniques involving magnetic zero-crossing reduced the final trapped flux to 50% of the original flux injected by the bias field [19, 20]. This loss is caused by the final plasma produced from the ringing theta-pinch method trapping only 50% of the flux applied by the bias field. When the main discharge occurs, the plasma column from the preionization process is too conductive to allow any additional magnetic flux to diffuse into the column, resulting in all magnetic flux outside of the plasma column to be lost during the reversal process [20]. This loss is inherent to the preionization method, and it does not account for any additional flux loss during the field reversal process [22].

The ringing barrier ionization is an ionization method developed to overcome the inherent flux loss issue associated with the magnetic zero-crossing [20]. In this method, multipole barrier coils are rung with a higher oscillation frequency compared to the bias field to generate a local oscillating transverse field near the formation chamber wall. The ringing field induces a local axial electric field for breakdown and ionization. In an unassisted ringing barrier ionization method, the magnetic zero-crossing is removed by removing the ringing theta-pinch all together. In a multistage method, the ringing barrier field is used with the ringing theta-pinch to reduce the influence of the magnetic zero-crossing during the preionization process.

The unassisted ringing barrier ionization method for FRC formation was first attempted in the FRX-A device by using a ringing quadrupole as an ionization source. A high degree of ionization was observed in the experiment when the quadrupole field magnitude was comparable to the applied bias field, but the breakdown was less effective when the quadrupole field magnitude was less than the bias field magnitude [20]. Commisso et al. notes that an

improved ionization can be obtained for the high initial bias case if the quadrupole field magnitude is increased to compensate it; however, it results in an excessive heating and imbedding of an unwanted quadrupole structure in the formed FRC. Due to these issues, the unassisted method has not been commonly used, and the multistage method is used instead.

The multistage ringing barrier ionization method has been used more frequently in the past experiments compared to the unassisted method. For example, in FRX-A, a multistage method using an initial RF pre-preionization followed by a half-cycle ring of the quadrupole followed by the main formation coil firing was found to be a reproducible optimal operating condition for maximum ionization [20]. In other experiments, a ringing octupoles system was used in the work of the Kurtmullaev [14] and in the CF-I facility [23]. A duododecapole system was used in TRX-2 [24]. In all devices, the magnetic zero-crossing is still present, but the ringing barrier field is found to improve the symmetry of the formed FRC and enhance the initial preionization.

1.2.4 FRC Diagnostics

Experimental measurements of internal FRC conditions are typically difficult because the FRTP formed FRCs have high temperature and density. Because FRCs have closed and isolated magnetic field structure, internal magnetic profiles cannot be measured directly using external magnetic probes. Furthermore, the use of the internal magnetic probes are not practical for most FRCs of interest because of material constraints for invasive diagnostics. Nevertheless, few important experimental diagnostics exist for FRCs that are crucial in understanding the formation process. They are the excluded flux, line integrated plasma density $\int n \, \mathrm{d}l$ (NDL), and light emission measurements.

The excluded flux measurement is the most fundamental diagnostic in FRC experiments. The diagnostic uses a set of magnetic flux loop and field probe located in the vicinity of each other. Sets of a magnetic flux loop and a field probe are placed at various axial positions of the device to form an excluded flux array that measures the axial variation of the excluded

flux in the device [25]. The excluded flux is defined as

$$\Delta\bar{\phi} = B_p \pi R_p^2 - \phi_p \tag{1.3}$$

where $\Delta\bar{\phi}$ is the excluded flux, B_p is the local axial magnetic field measured by the field probe, R_p is the radial position of the field probe that is approximately equal to the radius of the flux loop, and ϕ_p is the magnetic flux measured by the flux loop [12].

For excluded flux measurements, a vacuum reference shot is usually used to remove geometric effects from magnetic field measurements [26]. A vacuum reference shot is an experimental shot performed with the exact same conditions as the full plasma shot except with the gas injection removed (hence, the device operates in vacuum). The vacuum referenced excluded flux is then defined as

$$\Delta\phi = \Delta\bar{\phi}_p - \Delta\bar{\phi}_v \tag{1.4}$$

where $\Delta\phi$ is the vacuum referenced excluded flux, $\Delta\bar{\phi}_p$ is the excluded flux measured in the plasma shot, and $\Delta\bar{\phi}_v$ is the excluded flux measured in the associated vacuum reference shot. Since the vacuum referenced excluded flux is used almost exclusively in the diagnostic, here after, the excluded flux will simply refer to the vacuum referenced excluded flux.

A related quantity to the excluded flux is the excluded flux radius, defined as

$$R_{\Delta\phi} = R_p \sqrt{1 - \frac{\Delta\phi}{B_p \pi R_p^2}} \tag{1.5}$$

where $R_{\Delta\phi}$ is the excluded flux radius [12]. For a highly elongated FRC in equilibrium, one can show that the excluded flux radius measured in the straight section of the FRC is approximately equal to the separatrix radius [25]. Thus, the approximate location and separatrix shape of the FRC can be inferred from the excluded flux array by computing the excluded flux radius at each axial diagnostic location.

Second diagnostic that is fundamental in understanding FRCs are the line integrated plasma density $\int n \, \mathrm{d}l$ (NDL). For the NDL measurement, a single-chord interferometry is

used to measure the chord integrated electron density across the diameter. For a highly elongated FRC in equilibrium, the NDL measurement gives a direct measurement of the average density inside the FRC, as

$$\langle n \rangle \approx \frac{1}{2R_{\Delta\phi}} \int n \, \mathrm{d}l \tag{1.6}$$

where $\langle n \rangle$ is the volume averaged plasma density inside the FRC and $\int n \, \mathrm{d}l$ is experimentally obtained from the interferometer [12].

One issue with the NDL measurement in dynamic FRCs is the inverse radius weighting of the line integrated density for cylindrical devices. While the NDL measurement gives an accurate volume averaged density when the density profile within the FRC is largely flat, when there is a significant radial profile in the FRC density, the accuracy of the averaged density computed from the NDL becomes poor. This is due to the fact that the actual number of particles in a cylindrical shell at a given radius scales as $dN \sim n(r)r$ where r is the local radius. Thus, to obtain the true averaged density, one needs $\int n \, r \, \mathrm{d}r$. Due to the missing dependence of r in the NDL measured data, the local density near the axis is more pronounced.

In the formation process of FRCs, visual light emissions can be measured to obtain a reasonable time dependent understanding of reaction processes. Typically, during the preionization process, increased visual light emissions correspond to a higher ionization activity. However, this is only a qualitative measurement, as the resulting signal is due to a combination of ionization, dissociation, excitation, and recombination processes occurring in the chamber. The measured visual light emissions can also be filtered to obtain a bremsstrahlung emission measurement that approximately gives a chord integrated density squared $\int n^2 \, \mathrm{d}l$ [12]. However, bremsstrahlung emissions are only dominant during and after the formation of the FRC; thus, it does not offer reasonable density measurement during the preionization process.

1.3 Venti Program at Helion Energy

Since experimental results from the Venti Formation experiment that are provided by Helion Energy are used in this study, the Venti program at Helion Energy is briefly discussed in this section. The Venti device at Helion Energy is a staged compression FRC fusion experiment funded partially by the Department of Energy's ARPA-E ALPHA project [10]. The ALPHA program is designed to fund projects that create and demonstrate tools for developing a lower-cost path towards fusion energy [27]. The Venti program attempts to achieve these goals using the magnetic staged compression of an FRC target to a high magnetic field.

The Venti Formation experiment is a subset of the Venti program aimed at obtaining good understandings of the FRC formation and translation into the accelerator section. In the Venti Formation device, FRCs are formed using the FRTP method with both static and dynamic formation methods. For FRC preionization, ringing-theta pinch, multistage ringing barrier, and unassisted ringing barrier ionizations were tested. Diagnostics such as excluded flux probe array, single-chord interferometer, and visual light detectors were available in the formation section to obtain experimental data during the FRC formation process.

In addition to the experimental program, a two-dimensional resistive magnetohydrodynamics (MHD) code called Cygnus was improved to model the experiment. The Cygnus code was originally developed by D. C. Barnes at Coronado Consulting for general FRC modeling applications. As a part of the Venti program, Barnes improved the code considerably. The final version of the code by Barnes included supports for arbitrary axisymmetric geometries using a finite difference cut-cell formulation and static and dynamic external circuits coupled to the MHD equations. An experimental support for Hall and neutral effects were implemented, but it was not completed [28].

The Cygnus code has been an integral tool for the Venti program to design and understand the experiment. Coil firing times obtained by the simulation are used to guide the coil firing time used in the actual experiment [26]. The Cygnus circuits have been instrumental in the design of capacitor banks and switches in the experiment, as Cygnus captures modifications

in external circuit responses caused by the FRC. Remarkably good agreements between the experimental and Cygnus results were obtained by Milroy for the FRC excluded flux when the Cygnus code was run in a two-dimensional resistive MHD mode [18, 26].

1.4 Brief Survey of Past Works on Neutral Effects for FRCs

A brief survey of past works that explored neutral effects on FRC formation, translation, and sustainment is given in this section. Due to the wide range of formation techniques that exist, the discussion here is limited to works that used the FRTP based formation technique. As such, while a significant amount of literatures exists on neutral effects in a rotating magnetic field (RMF) generated FRCs, they are outside the scope here. Furthermore, works related to the study of neutral effects during FRC translation are limited to those that consider interactions with background neutrals. As such, the works related to neutral-beam injection sustainment and current drive schemes for FRCs are also outside the scope of this short survey.

For the FRC formation, preionization techniques were explored significantly in the FRX program [21, 29] as discussed previously in Section 1.2.3. Effects of the magnetic zero-crossing and the preionization of the initial neutral fill were explored in the FRX experiments [19, 20]. Much of the early work on the preionization process of the ringing theta-pinch was experimental and the numerical work came much later; first such study was by Meeks and Rovey. Meeks and Rovey explored effects of the magnetic zero-crossing in the ringing theta-pinch preionization technique and compared with the data from the FRCHX experiment [30]. Using Particle-In-Cell (PIC) simulations, Meeks and Rovey found that electrons only gain sufficient kinetic energy to ionize the deuterium after the magnetic zero-crossing is passed, which agrees with experimental observations.

The ionization due to a radial implosion of the FRCs was explored in the TRX-1 device by Armstrong et al. [15]. In the TRX-1 experiment, preionized plasma was incompletely ionized before the main coil firing; the ionization level only increased to a significant level during the radial implosion of the FRC formation. Even with a low level of the initial ioniza-

tion, most of the gas was found to be swept up by the implosion. Milroy et al. modeled flux retention processes during the FRC formation in the TRX-1 device using a one-dimensional MHD model with an independent neutral fluid included [31]. Contrary to the experimental measurement by Armstrong et al. [15], the model by Milroy et al. predicted that the preionization level had negligible effect on the flux retention and azimuthal asymmetries in the experiment were blamed for the disagreement in the flux retention results from the initial preionization level.

While not technically an FRC experiment, Sgro has performed one-dimensional hybrid simulations of the ionization in a theta-pinch during the radial implosion process [32]. Effects of the incomplete ionization in the chamber were accounted in the model using a kinetic treatment of ions and neutrals and a massless fluid treatment of electrons. Only electron impact ionization processes were considered for plasma-neutral interactions. In the simulation, Sgro found that partial ionization caused broadening of the radial plasma density profile during the radial implosion process of a theta-pinch.

For the FRC translation, effects of neutral and plasma backgrounds on a translating FRC were studied experimentally in the NUCTE-III device at Nihon University in Japan [33–35]. Improvements in confinement properties of the FRC were seen due to the reduction of the particle inventory and poloidal field decay; a delay of $n = 2$ rotational instability was also observed. The NUCTE-III group claimed that the heat and particles injected into the FRC by the neutral background are equivalent to the neutral-beam injection sustainment of the FRC. Based on this argument, NUCTE-III group modeled interactions between the translating FRC and the stationary background neutrals as a stationary FRC with neutral beams injected. A particle-based Monte-Carlo model developed by Takahashi et al. [36] was used by the NUCTE-III group to numerically analyze experimental results [34, 35, 37].

Similar particle-based kinetic approaches have been used in the space propulsion community to model plasma-neutral interactions in FRC thrusters. In the work of Brackbill et al. [38], the neutral entrainment FRC thruster concept was modeled by including effects of neutral atoms, meta-stable atoms, and ions with various binary collision and reaction pro-

cesses between three species. Both zero-dimensional direct simulation Monte-Carlo model and two-dimensional planar PIC model with Monte-Carlo collisions were used by Brackbill. A new kinetic model is being developed by Koo et al. for FRC thruster applications [39]. Koo et al. are using coupled physics model for the FRC modeling, where a kinetic or fluid model is used depending on applications. A collisional-radiative model to capture reaction processes is also being developed to couple with a PIC based kinetic model.

Fluid models have also been used to simulate translating FRCs with background neutrals. Meier successfully demonstrated the ability to use a fluid model to resolve neutral entrainment effects in FRC thrusters [11]. Experimental results obtained by MSNW showed favorable agreement with the results obtained by Meier [40]. TAE Technologies has also developed a two-dimensional resistive MHD code for FRC applications called LamyRidge that includes circuit and neutral models with ionization and charge exchange processes [41]. However, while LamyRidge is reported to have neutral modeling functionality, no simulation results utilizing this feature have been found in the literature. Thus, it is still unclear how well the neutral model in LamyRidge captured experimental observations.

Since FRC dynamics and external pulse circuits are inductively coupled, plasma-neutral interactions in the FRC can cause a non-negligible feedback in the external pulse circuits. As such, the optimal circuit configuration and timings for FRC formation and translation can be altered by plasma-neutral interactions. In order to capture this feedback, both neutral and circuit effects must be accounted consistently. This is an area that can be explored using Cygnus if the neutral model is improved.

1.5 Primary Computational Tool: Cygnus

The original Cygnus code is an axisymmetric two-dimensional Hall-MHD code that was developed by D. C. Barnes at Coronado Consulting for studying FRC formation, translation, merging, and compression [28].

The basic Cygnus code structure including the global time stepping strategy has remained largely unchanged when the neutral model was added from the original implementation by

Barnes. As such, the majority of detailed code algorithms discussed in this section is based on the original work of Barnes [28]. However, in order to add new physics such as plasma-neutral interactions, significant modifications were made to the Cygnus code base since the last update by Barnes in December of 2016. As such, details of the Cygnus code given here are based on the current developmental version.

This section only gives a brief introduction to the Cygnus code. Implementation details of the plasma-neutral model in the code are discussed in Chapter 2.

1.5.1 General Overview of the Cygnus Code

Key features of the Cygnus code are the following:

- Supports arbitrary axisymmetric geometries using a Cut-Cell formulation with a finite difference discretization.
- Supports both static and dynamic external circuits coupled to the plasma region.
- Correctly captures boundary eddy and far field effects for the magnetic flux.
- Uses mixed semi-implicit and implicit formulations to reduce Courant-Friedrichs-Lewy (CFL) time-step limitations.
- Supports both electron and ion temperatures.

1.5.2 Geometry Implementation in Cygnus

In Cygnus, the problem domain is split into the fluid and exterior vacuum regions. Plasma and neutral species are assumed to be contained in the fluid region; only external conductors are allowed in the vacuum region. Circuits are only allowed to be connected to the external conductors. Boundary conditions for fluid equations are applied at the boundary of the fluid and vacuum regions; no fluid is allowed to penetrate into the vacuum region. Only the magnetic flux is coupled in both regions.

To discretize the problem domain, a finite difference method is used inside the fluid region. A regular grid in the radial and axial directions is produced; a simple Cut-Cell formulation is used to remove finite difference grid nodes that are outside of the fluid region. Since the vacuum region only contains external conductors that couple to the plasma region through the magnetic flux, conductors are represented by line segments in the rz-plane, which carries uniform azimuthal current density. With the simple Cut-Cell formulation, Cygnus applies all fluid boundary conditions (excluding the magnetic flux) at the grid nodes adjacent to the boundary (called skin nodes). As such, the Cut-Cell algorithm is only applied to the magnetic flux.

In order to couple the magnetic flux in the finite differenced fluid region and the segment based vacuum region, the boundary of the two regions is discretized with both boundary segments and cut-edge nodes. The fluid region interfaces with the cut-edge nodes through the finite difference, and the vacuum region interfaces with the boundary segments. The coupling of two regions is obtained by interpolating the magnetic flux on the cut-edge nodes using the magnetic flux on the boundary segments. An illustration of a problem geometry tracked internally inside Cygnus is shown in Fig. 1.7.

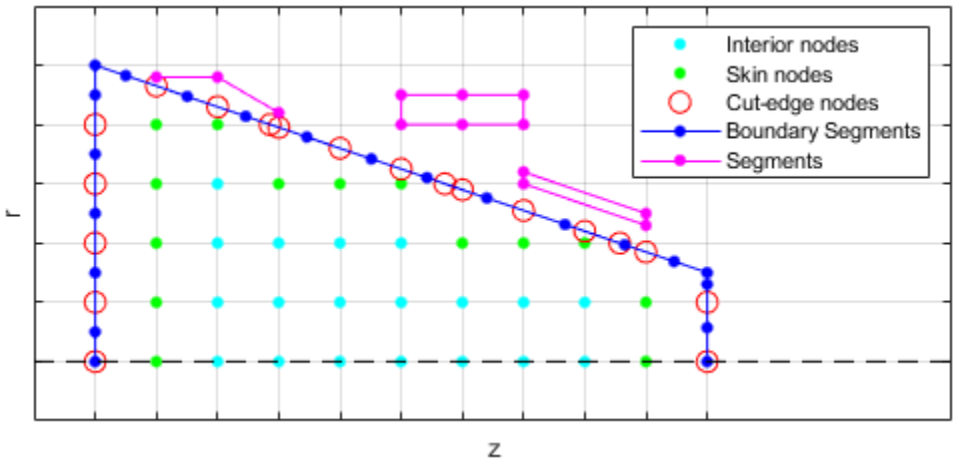

Figure 1.7: Illustration of the internal representation of the grid and geometry in Cygnus.

While a finite difference approach is used in Cygnus for spatial discretization of the fluid

equations, a hybrid formulation that mixes the finite difference and finite element formulation is used for anisotropic transports. For example, an anisotropic thermal conduction in plasma is solved using a time-step splitting approach similar to that described in Jardin [42]. As such, the anisotropic thermal conduction is solved with a finite element method while the remaining energy equation is solved with a finite difference approach. Details of the hybrid finite difference/finite element approach for anisotropic transports are discussed later in Section 2.5. Here, it is sufficient to state that the fluid domain must be meshed with finite elements that are compatible with the underlying finite difference grid nodes.

Using the grid generated by the finite difference discretization, a rectangular mesh of finite elements (cells) are generated. Because the boundary conditions are applied at the skin nodes, cut-edge nodes are neglected in the formation of the cells. Illustration of cells generated in Cygnus is shown in Fig. 1.8.

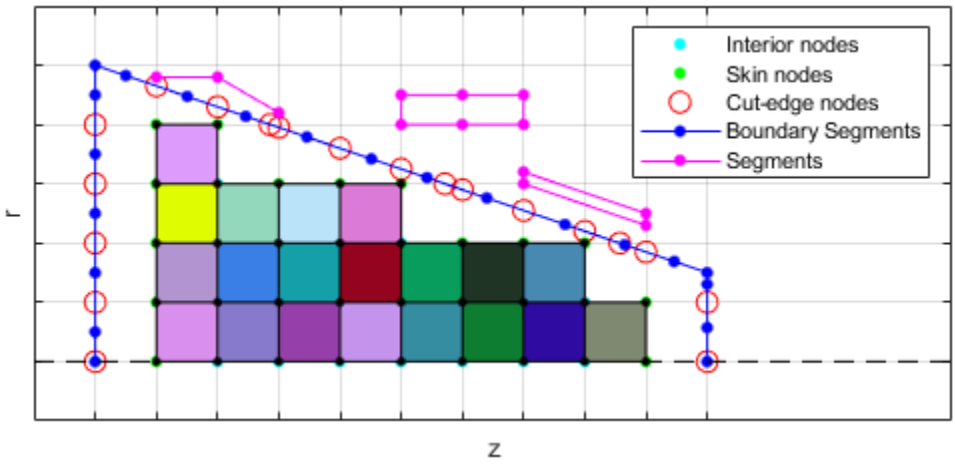

Figure 1.8: Illustration of Cygnus cells imposed onto a geometry given in Fig. 1.7.

As it can be seen from the internal representation of the geometry in Cygnus shown in Fig. 1.7 and Fig. 1.8, there are some limitations in the fluid boundary conditions that are applied at skin nodes. Dirichlet boundary conditions are assumed for velocity, temperature, and azimuthal magnetic field. The density boundary condition is a zero-mass flux condition. To imitate slip boundary conditions, the viscosity is reduced to a small value near skin

nodes in order to minimize the velocity drag by the wall. For a plasma with negligible wall interactions (such as typical FRCs), this approach is sufficient to resolve slip boundary conditions.

1.5.3 Overview of the Cygnus Algorithm

Cygnus advances the fluid equations in a time-split fashion, where various components of the equations are advanced separately in time using appropriate numerical methods for each split equation. A leapfrog algorithm is used to obtain a natural time centering of the coupled fluid equations. When there is no natural time splitting from the leapfrog time staggering, a predictor-corrector approach is used to properly time center terms in the equations. All equations are advanced linearly in time, and non-linear terms are handled with a predictor-corrector loop rather than Newton iterations.

The velocity and energy are advanced at the integer time level while the magnetic flux, azimuthal magnetic field, density, and temperature are advanced at the half-integer time level. External circuits are advanced with the magnetic flux advance. Only the non-thermal components of the energy equation is advanced in the integer time level; non-thermal components of the energy equation are terms that are not associated with the thermal conduction and equilibration.

As a result of the leapfrog staggered time advance, Cygnus time advance can be understood as a two-step process. In the first step, the velocity and non-thermal component of the energy equations are pushed together (VP step); in the second step, the density, thermal component of the energy, and magnetic field (including external circuits) equations are pushed together (NTB step). In each step, equations are further split to obtain a simpler set of equations with a well-defined stability and are coupled using predictor-corrector loops.

Because Cygnus implements time-split approaches to solve the coupled fluid equations, appropriate numerical methods are applied to each split advance to ensure numerical stability. For equations that exhibit a wave-like instability, a semi-implicit operator is introduced to stabilize the time advance. Conservative advection terms are handled explicitly using the

SMART advection algorithm [43] combined with a predictor-corrector loop. A time-step sub-cycling approach is used to maintain a CFL limit of no more than 0.5 for each sub step. Equations that include elliptic operators are handled implicitly. Remaining terms are either naturally time-centered with a leapfrog staggering or time centered using a predictor-corrector step.

A semi-implicit operator is used in the velocity and Hall magnetic field advance. A Hermitian symmetric semi-implicit operator is used exclusively for Cygnus applications. For the velocity advance, the semi-implicit implementation in Cygnus is derived from past works of Harned and Schnack [44] and Schnack et al. [45]. The semi-implicit advance for the Hall advance uses a split-step approach similar to that of Harned and Mikic [46], and a symmetric second-order semi-implicit operator is used. While it is known from the work of Sovinec [47] that the symmetric second-order semi-implicit operator for the Hall advance does not fully stabilize the total magnetic field advance, a Hermitian symmetric operator is still implemented in Cygnus for simpler numerical convergences. While this approach requires introduction of numerical dissipations to remove weak instabilities (implemented as a hyper-resistivity), it avoids using Sovinec's 4th-order asymmetric semi-implicit operator that may have poor numerical convergence in practice due to its lack of Hermitian symmetric property [28].

1.5.4 Energy Advance Algorithm

Due to the split advance of the energy equation over the two distinct time levels (integer and half-integer) in Cygnus, it is possible that for some problems, errors introduced by the splitting are too severe to ignore for a sensible choice of time-step. Due to this concern, Cygnus implements three forms of the energy equation formulation to allow the user to select an appropriate formulation to use for a given simulation. Three forms of the supported energy formulations are the (1) total energy, (2) pressure, and (3) temperature.

For the total energy formulation, a conservative form of the energy equation is used in the VP step. For the pressure formulation, a non-conservative internal energy (pressure) equation

is used in the VP step. For both formulations, the thermal contributions are pushed in the NTB step using the temperature equation. For temperature dependent transport terms, the temperature is assumed to be constant in time during the VP step; in the NTB step, it is handled using a predictor-corrector loop. In both cases, the electron temperature is pushed in the same split equation fashion using either the temperature or pressure formulation.

The two energy schemes can also be combined together to obtain a final energy solution from the VP step that is obtained by taking a weighted average of two schemes using local Mach number [28]. The combined scheme allows a reasonable energy advance for challenging simulations where there may be wide range of Mach numbers in the simulation domain.

Unlike the total energy and pressure formulations, for the temperature formulation, the energy is not advanced in the VP step, and the full temperature equation is advanced in the NTB step. This formulation introduces the least error from the time splitting of the energy equation (since it is not split), but it generally does not conserve energy as well as the total energy and pressure formulations. In addition, since the non-linear terms are handled using a predictor-corrector loop, the solution from the temperature formulation can become noisy from the update process. From numerical experiments, the first two schemes and the mixed scheme are more robust for most FRC problems and lead to stable results.

Chapter 2

IMPLEMENTATION OF MEIER-SHUMLAK PLASMA-NEUTRAL MODEL IN CYGNUS

2.1 System of Equations

For modeling FRCs in this project, a system of equations based on the two-fluid plasma-neutral model of Meier and Shumlak in the two-dimensional axisymmetric limit is used. As opposed to the original two-fluid model presented by Meier and Shumlak [11], the time evolution of the electron temperature is retained in the model. This is due to the fact that a significant variation in the electron and ion temperatures can develop in the FRC, and its ratio is highly dependent on FRC dynamics. Since, ionization and recombination rates are strongly dependent on the electron temperature, the evolution of the electron temperature must be tracked reasonably.

Hall contributions to the MHD equations are neglected in all of the simulations performed for this study. However, implementation details of Cygnus including the Hall terms are given here for completeness. The evolution equations for the macroscopic fluid state variables implemented in Cygnus are given to be as follows:

Continuity Equations:

$$\frac{\partial n}{\partial t} + \boldsymbol{\nabla} \cdot (n\mathbf{u}) = \Gamma_{iz} - \Gamma_{rc} \tag{2.1}$$

$$\frac{\partial n_n}{\partial t} + \boldsymbol{\nabla} \cdot (n_n\mathbf{u}_n) = \Gamma_{rc} - \Gamma_{iz} \tag{2.2}$$

Velocity Equations:

$$mn\frac{\partial \mathbf{u}}{\partial t} = -mn\mathbf{u}\cdot\boldsymbol{\nabla}\mathbf{u} + \mathbf{J}\times\mathbf{B} - \boldsymbol{\nabla}p - \boldsymbol{\nabla}\cdot\overleftrightarrow{\Pi} + m\left(\Gamma_{iz}+\Gamma_{cx}\right)\left(\mathbf{u}_n - \mathbf{u}\right) + \mathbf{R}_{in}^{cx} - \mathbf{R}_{ni}^{cx} \tag{2.3}$$

$$mn_n\frac{\partial \mathbf{u}_n}{\partial t} = -mn_n\mathbf{u}_n\cdot\boldsymbol{\nabla}\mathbf{u}_n - \boldsymbol{\nabla}p_n - \boldsymbol{\nabla}\cdot\overleftrightarrow{\Pi}_n - m\left(\Gamma_{rc}+\Gamma_{cx}\right)\left(\mathbf{u}_n-\mathbf{u}\right) - \mathbf{R}_{in}^{cx} + \mathbf{R}_{ni}^{cx} \quad (2.4)$$

Generalized Ohm's Laws:

$$\frac{\partial \Psi}{\partial t} = -\left(\mathbf{u} - \frac{\boldsymbol{\nabla}\times\mathbf{B}_\phi}{\mu_0 en}\right)\cdot\boldsymbol{\nabla}\Psi + \frac{\eta}{\mu_0}\Delta^*\Psi \quad (2.5)$$

$$\frac{\partial B_\phi}{\partial t} = \boldsymbol{\nabla}_{2D}\cdot\left\{\left[\mathbf{u}\times\mathbf{B} - \eta\mathbf{J} - \frac{1}{en}\left(\mathbf{J}\times\mathbf{B} - \boldsymbol{\nabla}p_e\right)\right]\times\hat{\boldsymbol{\phi}}\right\} \quad (2.6)$$

Energy Equations:

$$\begin{aligned}\frac{\partial \varepsilon}{\partial t} = &-\boldsymbol{\nabla}\cdot\left[\left(\frac{\gamma p}{\gamma-1}+\frac{1}{2}mnu^2\right)\mathbf{u} + \mathbf{u}\cdot\overleftrightarrow{\Pi} - \frac{\gamma p_e}{ne\left(\gamma-1\right)}\mathbf{J}\right] + \mathbf{u}\cdot\mathbf{J}\times\mathbf{B} + \eta J^2 \\ &- \frac{1}{en}\mathbf{J}\cdot\boldsymbol{\nabla}p_e + Q_\Delta^{in} + Q_\Delta^{en} + \Gamma_{iz}\left(\frac{1}{2}mu_n^2 + \frac{3}{2}kT_n - \varphi_{iz}\right) - \Gamma_{rc}\left(\frac{1}{2}mu^2+\frac{3}{2}kT_i\right) \\ &+ \Gamma_{cx}\frac{1}{2}m\left(u_n^2-u^2\right) + \mathbf{u}_n\cdot\mathbf{R}_{in}^{cx} - \mathbf{u}\cdot\mathbf{R}_{ni}^{cx} + Q_{in}^{cx} - Q_{ni}^{cx} - \boldsymbol{\nabla}\cdot\left(\mathbf{q}_i+\mathbf{q}_e\right)\end{aligned} \quad (2.7)$$

$$\begin{aligned}\frac{\partial \varepsilon_n}{\partial t} = &-\boldsymbol{\nabla}\cdot\left[\left(\frac{\gamma p_n}{\gamma-1}+\frac{1}{2}mn_nu_n^2\right)\mathbf{u}_n + \mathbf{u}_n\cdot\overleftrightarrow{\Pi}_n\right] - Q_\Delta^{in} - Q_\Delta^{en} \\ &- \Gamma_{iz}\left(\frac{1}{2}mu_n^2+\frac{3}{2}kT_n\right) + \Gamma_{rc}\left(\frac{1}{2}mu^2+\frac{3}{2}kT_i\right) - \Gamma_{cx}\frac{1}{2}m\left(u_n^2-u^2\right) \\ &- \mathbf{u}_n\cdot\mathbf{R}_{in}^{cx} + \mathbf{u}\cdot\mathbf{R}_{ni}^{cx} - Q_{in}^{cx} + Q_{ni}^{cx} - \boldsymbol{\nabla}\cdot\mathbf{q}_n\end{aligned} \quad (2.8)$$

$$\begin{aligned}\frac{\partial T_e}{\partial t} = &-\left(\gamma-1\right)T_e^{(\gamma-2)/(\gamma-1)}\boldsymbol{\nabla}\cdot\left[T_e^{1/(\gamma-1)}\left(\mathbf{u}-\frac{\mathbf{J}}{en}\right)\right] - \left(\Gamma_{iz}-\Gamma_{rc}\right)\frac{T_e}{n} \\ &+ \frac{\gamma-1}{kn}\left[\eta J^2 - Q_\Delta^{ie} + Q_\Delta^{en} - \Gamma_{iz}\varphi_{iz} - \boldsymbol{\nabla}\cdot\mathbf{q}_e\right]\end{aligned} \quad (2.9)$$

In addition to the evolution equations for the macroscopic fluid variables, equations of state and Maxwell's equations are required. These equations are defined as follows:

Equation of States:

$$p_e = nkT_e \tag{2.10}$$

$$p = nk\left(T_i + T_e\right) \tag{2.11}$$

$$p_n = n_n k T_n \tag{2.12}$$

$$\varepsilon = \frac{p}{\gamma - 1} + \frac{1}{2}mnu^2 \tag{2.13}$$

$$\varepsilon_n = \frac{p_n}{\gamma - 1} + \frac{1}{2}mn_n u_n^2 \tag{2.14}$$

Maxwell's Equations:

$$\mathbf{B} = \boldsymbol{\nabla} \times \left(\frac{\Psi}{r}\hat{\boldsymbol{\phi}}\right) + B_\phi \hat{\boldsymbol{\phi}} \tag{2.15}$$

$$\mathbf{J} = \frac{1}{\mu_0}\left[\boldsymbol{\nabla} \times \left(B_\phi \hat{\boldsymbol{\phi}}\right) - \left(\frac{1}{r}\Delta^* \Psi\right)\hat{\boldsymbol{\phi}}\right] \tag{2.16}$$

In the above equations, n is the plasma number density, n_n is the neutral number density, $\mathbf{u}$ is the plasma center-of-mass flow velocity, $\mathbf{u}_n$ is the neutral center-of-mass flow velocity, ε is the plasma energy density, ε_n is the neutral energy density, Ψ is the magnetic flux function, B_ϕ is the toroidal component of the magnetic field, $\mathbf{B}$ is the magnetic field, $\mathbf{J}$ is the current density, p is the plasma pressure, p_e is the electron pressure, p_n is the neural pressure, T_i is the ion temperature, T_e is the electron temperature, T_n is the neutral temperature, m is the species mass, e is the unit charge, γ is the adiabatic index, and k is the Boltzmann's constant. The operator Δ^* is the elliptic axisymmetric Grad-Shafranov operator defined to be

$$\Delta^* \psi \equiv r^2 \boldsymbol{\nabla} \cdot \left(\frac{1}{r^2}\boldsymbol{\nabla}\psi\right) = r\frac{\partial}{\partial r}\left(\frac{1}{r}\frac{\partial \psi}{\partial r}\right) + \frac{\partial^2 \psi}{\partial z^2}$$

and the operator $\boldsymbol{\nabla}_{2D}$ is the Cartesian divergence operator defined to be

$$\boldsymbol{\nabla}_{2D} \cdot \mathbf{A} \equiv \left(\boldsymbol{\nabla} - \frac{\hat{\mathbf{r}}}{r}\right) \cdot \mathbf{A} = \frac{\partial A_r}{\partial r} + \frac{\partial A_z}{\partial z}$$

where r is the radius from the cylindrical axis and $\hat{\mathbf{r}}$ is the unit vector in the cylindrical radial direction. $\hat{\boldsymbol{\phi}}$ is the unit vector in the azimuthal direction.

As discussed in Section 1.5.4, Cygnus may use non-conservative internal energy (pressure) equations or temperature equations for the energy advance. The pressure and temperature equations are given to be as follows:

Pressure Equations:

$$\begin{aligned}\frac{\partial}{\partial t}\left(\frac{p}{\gamma-1}\right) = &-\boldsymbol{\nabla}\cdot\left(\frac{\gamma p}{\gamma-1}\mathbf{u}\right) + \mathbf{u}\cdot\boldsymbol{\nabla}p - \overleftrightarrow{\Pi} : \boldsymbol{\nabla}\mathbf{u} + \eta J^2 + Q_{\Delta}^{in} + Q_{\Delta}^{en} \\ &+ \Gamma_{iz}\left(\frac{1}{2}m\left|\mathbf{u}-\mathbf{u}_n\right|^2 + \frac{3}{2}kT_n - \varphi_{iz}\right) - \Gamma_{rc}\frac{3}{2}kT_i + \frac{1}{2}m\Gamma_{cx}\left|\mathbf{u}-\mathbf{u}_n\right|^2 \\ &+ \mathbf{R}_{in}^{cx}\cdot(\mathbf{u}_n-\mathbf{u}) + Q_{in}^{cx} - Q_{ni}^{cx} - \boldsymbol{\nabla}\cdot(\mathbf{q}_i+\mathbf{q}_e) \quad (2.17)\end{aligned}$$

$$\begin{aligned}\frac{\partial}{\partial t}\left(\frac{p_n}{\gamma-1}\right) = &-\boldsymbol{\nabla}\cdot\left(\frac{\gamma p_n}{\gamma-1}\mathbf{u}_n\right) + \mathbf{u}_n\cdot\boldsymbol{\nabla}p_n - \overleftrightarrow{\Pi}_n : \boldsymbol{\nabla}\mathbf{u}_n - Q_{\Delta}^{in} - Q_{\Delta}^{en} \\ &- \Gamma_{iz}\frac{3}{2}kT_n + \Gamma_{rc}\left(\frac{1}{2}m\left|\mathbf{u}-\mathbf{u}_n\right|^2 + \frac{3}{2}kT_i\right) + \frac{1}{2}m\Gamma_{cx}\left|\mathbf{u}-\mathbf{u}_n\right|^2 \\ &+ \mathbf{R}_{ni}^{cx}\cdot(\mathbf{u}-\mathbf{u}_n) - Q_{in}^{cx} + Q_{ni}^{cx} - \boldsymbol{\nabla}\cdot\mathbf{q}_n \quad (2.18)\end{aligned}$$

$$\begin{aligned}\frac{\partial}{\partial t}\left(\frac{p_e}{\gamma-1}\right) = &-\boldsymbol{\nabla}\cdot\left[\frac{\gamma p_e}{\gamma-1}\left(\mathbf{u}-\frac{\mathbf{J}}{en}\right)\right] + \left(\mathbf{u}-\frac{\mathbf{J}}{en}\right)\cdot\boldsymbol{\nabla}p_e + \eta J^2 \\ &- Q_{\Delta}^{ie} + Q_{\Delta}^{en} - \Gamma_{iz}\varphi_{iz} - \boldsymbol{\nabla}\cdot\mathbf{q}_e \quad (2.19)\end{aligned}$$

Temperature Equations:

$$\frac{\partial T_i}{\partial t} = -(\gamma-1)\,T_i^{(\gamma-2)/(\gamma-1)}\boldsymbol{\nabla}\cdot\left[T_i^{1/(\gamma-1)}\mathbf{u}\right] - (\Gamma_{iz}-\Gamma_{rc})\,\frac{T_i}{n} + \frac{\gamma-1}{kn}\Bigg[Q_\Delta^{ie} + Q_\Delta^{in} + (\Gamma_{iz}+\Gamma_{cx})\,\frac{1}{2}m\,|\mathbf{u}_n-\mathbf{u}|^2 + \Gamma_{iz}\frac{3}{2}kT_n - \Gamma_{rc}\frac{3}{2}kT_i + \mathbf{R}_{in}^{cx}\cdot(\mathbf{u}_n-\mathbf{u}) + Q_{in}^{cx} - Q_{ni}^{cx} - \overleftrightarrow{\Pi}:\boldsymbol{\nabla}\mathbf{u} - \boldsymbol{\nabla}\cdot\mathbf{q}_i\Bigg] \quad (2.20)$$

$$\frac{\partial T_n}{\partial t} = -(\gamma-1)\,T_n^{(\gamma-2)/(\gamma-1)}\boldsymbol{\nabla}\cdot\left[T_n^{1/(\gamma-1)}\mathbf{u}_n\right] + (\Gamma_{iz}-\Gamma_{rc})\,\frac{T_n}{n_n} + \frac{\gamma-1}{kn_n}\Bigg[-Q_\Delta^{in} - Q_\Delta^{en} + (\Gamma_{rc}+\Gamma_{cx})\,\frac{1}{2}m\,|\mathbf{u}_n-\mathbf{u}|^2 - \Gamma_{iz}\frac{3}{2}kT_n + \Gamma_{rc}\frac{3}{2}kT_i - \mathbf{R}_{ni}^{cx}\cdot(\mathbf{u}_n-\mathbf{u}) - Q_{in}^{cx} + Q_{ni}^{cx} - \overleftrightarrow{\Pi}_n:\boldsymbol{\nabla}\mathbf{u}_n - \boldsymbol{\nabla}\cdot\mathbf{q}_n\Bigg] \quad (2.21)$$

Remaining terms are transport and collision terms. The reaction and binary collision terms involving neutrals are defined by Meier and Shumlak [11]. For the binary collision terms for ions and electrons, Meier and Shumlak refer to the results from Braginskii [48]. The form of the transport related terms implemented in Cygnus is discussed in Section 2.2.

2.2 Closure and Transport Relations for the FRC

In this section, required transport and closure relations for fluid equations that are suitable for the Cygnus code are discussed.

2.2.1 Reaction and Collision Contributions

For reaction terms, the form of closures discussed by Meier and Shumlak [11] is used for Cygnus. For reaction source rates for ionization, recombination, and charge exchange, a Maxwellian form of the distribution function is assumed in the collision operator to produce

the following results [11]:

$$\Gamma_{iz} = nn_n \langle \sigma_{iz} v_e \rangle \tag{2.22a}$$

$$\Gamma_{rc} = n^2 \langle \sigma_{rc} v_e \rangle \tag{2.22b}$$

$$\Gamma_{cx} = nn_n u_{cx} \sigma_{cx} \tag{2.22c}$$

where $\langle \sigma_{iz} v_e \rangle$ and $\langle \sigma_{rc} v_e \rangle$ are the ionization and recombination reaction rates, respectively, which are parametrized as a function of the electron temperature T_e, and σ_{cx} is the charge exchange cross section that is parametrized by the effective charge exchange velocity u_{cx} that is defined as [11]:

$$u_{cx} = \sqrt{\frac{8k}{\pi m}(T_i + T_n) + |\mathbf{u} - \mathbf{u}_n|^2} \tag{2.23}$$

As given by Meier and Shumlak, the frictional transfer of momentum due to charge exchange is defined as the followings [11]:

$$\mathbf{R}_{in}^{cx} \approx -nn_n u_{in}^{cx} \sigma_{cx} m (\mathbf{u} - \mathbf{u}_n) \tag{2.24a}$$

$$\mathbf{R}_{ni}^{cx} \approx nn_n u_{ni}^{cx} \sigma_{cx} m (\mathbf{u} - \mathbf{u}_n) \tag{2.24b}$$

where

$$u_{in}^{cx} = \frac{kT_n}{m}\left[u_{cx}^2 + \frac{9\pi^2 - 64}{8\pi m} kT_n\right]^{-1/2} \tag{2.25a}$$

$$u_{ni}^{cx} = \frac{kT_i}{m}\left[u_{cx}^2 + \frac{9\pi^2 - 64}{8\pi m} kT_i\right]^{-1/2} \tag{2.25b}$$

Note that the charge exchange cross section σ_{cx} is still parametrized by the effective charge exchange velocity u_{cx} in the above equations.

As given by Meier and Shumlak, the frictional transfer of thermal energy due to charge

exchange is defined as the followings [11]:

$$Q_{in}^{cx} \approx n n_n \tilde{u}_{in}^{cx} \sigma_{cx} \frac{3}{2} k T_n \tag{2.26a}$$

$$Q_{ni}^{cx} \approx n n_n \tilde{u}_{ni}^{cx} \sigma_{cx} \frac{3}{2} k T_i \tag{2.26b}$$

where

$$\tilde{u}_{in}^{cx} = \sqrt{u_{cx}^2 + \frac{56k}{9\pi m} T_n} \tag{2.27a}$$

$$\tilde{u}_{ni}^{cx} = \sqrt{u_{cx}^2 + \frac{56k}{9\pi m} T_i} \tag{2.27b}$$

Again, the charge exchange cross section σ_{cx} is still parametrized by the effective charge exchange velocity u_{cx} in the above equations.

The thermal equilibration terms due to elastic scattering are defined as the follows:

$$Q_{\Delta}^{ie} = n^2 K_{ie}^T \left(k T_e - k T_i\right) \tag{2.28a}$$

$$Q_{\Delta}^{in} = n n_n K_{in}^T \left(k T_n - k T_i\right) \tag{2.28b}$$

$$Q_{\Delta}^{en} = n n_n K_{en}^T \left(k T_n - k T_e\right) \tag{2.28c}$$

where $K_{\alpha\beta}^T$ is the thermal equilibration rate coefficient for thermal equilibration of species α and species β.

2.2.2 Resistivity

The generalized Ohm's law in the limit of negligible electron inertia is given to be

$$\mathbf{E} + \mathbf{u} \times \mathbf{B} - \frac{1}{ne} \left(\mathbf{J} \times \mathbf{B} - \boldsymbol{\nabla} p_e\right) = \frac{1}{ne} \left[\frac{\delta \mathbf{M}_e}{\delta t} - \boldsymbol{\nabla} \cdot \overleftrightarrow{\Pi}_e\right]$$

where the right-hand-side corresponds to the collision and transport terms: $\delta \mathbf{M}_e / \delta t$ represents the momentum transfer to the electrons due to collision and reaction processes and $\overleftrightarrow{\Pi}_e$

is the higher order moment term (electron viscous stress tensor) that is defined as a function of the lower order moment terms through the closure process. As such, the right-hand-side terms represent the resistive and dissipative contribution.

In order to obtain an expression for plasma resistivity, consider only the right-hand-side. For simplicity, neglect the electron viscous stress tensor contribution for resistivity. In the two-fluid model of Meier and Shumlak, momentum transfer processes for electrons are due to ion-electron scattering, electron-neutral scattering, ionization, and recombination processes [11]. In order to account for both elastic collision and reaction terms, consider a closure based on the Grad's 13-moment model [49]. To obtain the right-hand-side dissipation term in the generalized Ohm's law, apply Burger's semi-linear collision model for elastic scattering terms and the reaction model used by Meier and Shumlak for ionization and recombination processes.

The Burger's semi-linear collision model for the momentum of species α is given to be the following [50, 51]:

$$\left.\frac{\delta \mathbf{M}_\alpha}{\delta t}\right|_{coll.} = -\sum_\beta n_\alpha m_\alpha \nu_{\alpha\beta} \left(\mathbf{u}_\alpha - \mathbf{u}_\beta\right) + \sum_\beta \nu_{\alpha\beta} \frac{z_{\alpha\beta}\mu_{\alpha\beta}}{kT_{\alpha\beta}} \left(\mathbf{q}_\alpha - \frac{m_\alpha n_\alpha}{m_\beta n_\beta}\mathbf{q}_\beta\right)$$

In the above equation, $\nu_{\alpha\beta} = (16/3) n_\beta m_\beta \Omega_{\alpha\beta}^{(1,1)} / (m_\alpha + m_\beta)$ is the momentum transfer collision frequency, $\mu_{\alpha\beta} = m_\alpha m_\beta / \left(m_\alpha + m_\beta\right)$ is the reduced mass, $T_{\alpha\beta} = \left(m_\alpha T_\beta + m_\beta T_\alpha\right) / \left(m_\alpha + m_\beta\right)$ is the reduced temperature, $z_{\alpha\beta} = 1 - (2/5)\Omega_{\alpha\beta}^{(1,2)} / \Omega_{\alpha\beta}^{(1,1)}$, and $\Omega_{\alpha\beta}^{(l,j)}$ is the Chapman-Cowling collision integral [52].

From Meier and Shumlak's model, the electron momentum transfer associated with reactions is given to be the following:

$$\left.\frac{\delta \mathbf{M}_e}{\delta t}\right|_{reac.} = -\Gamma_{iz} m_e \mathbf{u}_n - \Gamma_{rc} m_e \mathbf{u}_e$$

Combining the two collision terms for electrons, simplifying, and keeping only the first

order terms in electron inertia, the electron collision term becomes the following:

$$\frac{1}{ne}\frac{\delta \mathbf{M}_e}{\delta t} = \frac{m_e}{ne^2}\left(\nu_{ei}+\nu_{en}+\nu_{rc}\right)\mathbf{J} + \frac{m_e}{e}\left[\nu_{en}\left(\mathbf{u}_n-\mathbf{u}\right)+\nu_{iz}\mathbf{u}_n-\nu_{rc}\mathbf{u}\right] + \frac{m_e}{e}\left(\nu_{ei}z_{ei}+\nu_{ei}z_{en}\right)\frac{\mathbf{q}_e}{p_e} \quad (2.29)$$

where ν_{ei} is the electron-ion collision frequency that is dominated by the Coulomb collision process, ν_{en} is the electron-neutral collision frequency, $\nu_{iz} = \Gamma_{iz}/n$ is the ionization frequency, and $\nu_{rc} = \Gamma_{rc}/n$ is the recombination frequency. To obtain a simple expression for the resistivity in terms of the current alone, assume that the effect of current density $\mathbf{J}$ dominates over that of velocity and heat flow vector. Furthermore, note that in general, the recombination frequency is small compared with other collision frequency terms. With these assumptions, a simple isotropic form of the plasma resistivity is obtained to be the following:

$$\eta = \frac{m_e}{ne^2}\left(\nu_{ei}+\nu_{en}\right)$$

In addition, there may be anomalous collision time scales that are not captured by the simple derivation performed up until now. In order to account for anomalous resistivities, the plasma resistivity can be written as

$$\eta = \frac{m_e}{ne^2}\left(\nu_{ei}+\nu_{en}+\nu_{an}\right) \quad (2.30)$$

where ν_{an} is the anomalous collision frequency. Note that for ν_{ei}, a standard Spitzer-like form of the plasma resistivity can be used, given to be the following [48]:

$$\nu_{sp} = \frac{4\sqrt{2\pi}}{3}\frac{e^{5/2}n\ln(\Lambda)}{\left(4\pi\epsilon_0\right)^2 m_e^{1/2}}\left(\frac{kT_e}{e}\right)^{-3/2} \quad (2.31)$$

For the anomalous collision frequency, for FRC problems, the empirically tunable Chodura

resistivity is often used. The Chodura collision frequency is defined to be

$$\nu_{ch} = C_c \omega_{pi} \left[1 - \exp\left(-\frac{v_d}{f_c \bar{v}_T} \right) \right] \tag{2.32}$$

where $\omega_{pi} = \sqrt{ne^2/(m\epsilon_0)}$ is the plasma frequency, $v_d = |\mathbf{J}|/(ne)$ is the electron drift velocity, $\bar{v}_T = \sqrt{k(T_i + T_e)/m}$ is the effective thermal velocity defined in terms of the total temperature, and C_c and f_c are the Chodura C and F parameter, respectively [53, 54].

In addition to Chodura, the anomalous Bohm transport can be assumed. The Bohm collision frequency is defined to be the following:

$$\nu_{bh} = \frac{e|\mathbf{B}|}{16 m_e} \tag{2.33}$$

Similar to Bohm, an anomalous transport based on a gyro-Bohm frequency can be used alternatively. The gyro-Bohm frequency is simply the Bohm frequency multiplied by the ion gyro-radius normalized by a density scale length. As discussed by Steinhauer, anomalous transports based on Chodura, Bohm, and gyro-Bohm are closely related for a fully ionized plasma when the ion temperature is equal to the electron temperature [12]. When neutrals are present or when there are significant temperature difference between ions and electrons, behaviors of three anomalous transports are distinctly different. Implementation of three forms of anomalous transport mechanisms allows flexibility in matching experimental results.

For the electron-neutral collision frequency, the theoretical work of Bydder that uses Born-type differential cross-section is applied here to obtain a form of electron-neutral collision frequency that is valid over all temperature range [55]. From Bydder, the Chapman-Cowling collision integral for the elastic collision between an electron and hydrogen atom can be expressed as

$$\Omega_{en}^{(1,1)} = \frac{\pi^{1/2}(0.45)\bar{e}^4\gamma^3}{2\mu_{en}} \left[-\exp(1/b) E_i(-1/b) \right]$$

where $E_i(-1/b) = -E_1(1/b)$ is the exponential integral function, $b = a_0^2 \mu_{en}^2/(\gamma\hbar)^2$, $\bar{e}^2 = e^2/(4\pi\epsilon_0)$, $\gamma^{-2} = 2kT_{en}$, μ_{en} is the reduced mass for the electron and hydrogen atom, and

a_0 is the Bohr radius [55]. After applying the small electron inertia approximation, the electron-neutral elastic collision frequency becomes the following:

$$\nu_{en} \approx \frac{3\sqrt{2\pi}}{5} \frac{e^{5/2} n \exp(\beta) E_1(\beta)}{(4\pi\epsilon_0)^2 m_e^{1/2}} \left(\frac{1-f_i}{f_i}\right) \left(\frac{kT_e}{e}\right)^{-3/2} \tag{2.34}$$

where f_i is the ionization fraction and $\beta = \hbar/(2a_0^2 m_e kT_e) \approx 13.606/(kT_e/e)$. As it can be seen from the obtained form of the electron-neutral collision frequency, it has the similar $T_e^{-3/2}$ dependence as the Spitzer resistivity but with additional electron temperature correction due to the β term. Thus, in essence, the effect of the electron-neutral collision process is to alter the effective charge state in the Spitzer resistivity.

In Cygnus, multipliers are applied on each resistivity formulation based on different transport processes. In essence, resistivities associated with each transport mechanism are tunable by the user to best match experimental results. This is due to the fact that anomalous modifications to the resistivity are expected for FRCs; e.g., contributions from micro-turbulent electron dynamics [53]. Since the diffusion of the magnetic field is governed by the magnetic diffusivity, $\kappa_m = \eta/\mu_0$ [56], the plasma resistivity is a crucial term in the dynamics of the FRC formation process that must be matched to experimental observations.

2.2.3 Heat Flow

For the heat flow vector, Cygnus uses anisotropic formulation of the plasma thermal conductivity by Braginskii, given to be the followings [48]:

$$\mathbf{q}_i = -\left[\left(\chi_\parallel^i - \chi_\perp^i\right)\frac{\mathbf{BB}}{B^2} + \chi_\perp^i \overleftrightarrow{\mathrm{I}}\right] \cdot \boldsymbol{\nabla} T_i \tag{2.35a}$$

$$\mathbf{q}_e = -\left[\left(\chi_\parallel^e - \chi_\perp^e\right)\frac{\mathbf{BB}}{B^2} + \chi_\perp^e \overleftrightarrow{\mathrm{I}}\right] \cdot \boldsymbol{\nabla} T_e \tag{2.35b}$$

where $\chi_\parallel^i$ and $\chi_\perp^i$ are the ion thermal conductivity in the parallel and perpendicular directions with respect to the local magnetic field, respectively, and $\chi_\parallel^e$ and $\chi_\perp^e$ are the electron thermal conductivity in the parallel and perpendicular directions with respect to the local magnetic

field, respectively. The form of the parallel and perpendicular thermal conductivities for both ions and electrons are given in Braginskii [48].

For the neutral heat flow vector, a typical isotropic formulation of the heat flow vector based on the hard-sphere model is used. The neutral heat flux vector can be defined as the following:

$$\mathbf{q}_n = -\chi_n \boldsymbol{\nabla} T_n \tag{2.36}$$

where χ_n is the neutral thermal conductivity.

Note that the closure of the heat flow vectors employed here does not include the coupling between the plasma and neutral species. The closure for both plasma and neutral heat flow vectors assumes that the plasma-neutral collision frequency is small compared with the plasma-plasma and neutral-neutral collision frequencies. Furthermore, the modification of the collision frequency due to reactions are neglected.

To obtain a closure of the heat flow vector that includes effects of the coupling and reactions, one can consider using a closure based on Grad's moment method to simultaneously solve for the species heat flow vectors using the coupled species heat flow vector advance equations. In principle, one can carry out this procedure and obtain either non-linear or linear closure with plasma-neutral coupling and reactions included; however, in practice, the mathematics involved are too complex to carry out analytically. In addition, as it is shown by Zhdanov, the usual 13-moment collision model has insufficient accuracy to resolve Coulomb collisions in a fully ionized plasma case. As such, even higher order moment model (21-moment) is required to accurately resolve the transport of the fully ionized plasma case [57].

Due to difficulties in obtaining a closure for heat flow vectors with effects of plasma-neutral collisions and reactions, they are neglected. Instead, in order to obtain a reasonable value of the thermal conductivities that result in FRC simulations that match experimental observations, the thermal diffusivity is limited in Cygnus using user defined maximum and minimum values.

2.2.4 Viscosity

Similar to the closure for the heat flow vector, the closure for the viscous stress tensor assumes that plasma-neutral collisions and reactions are negligible compared with self-collision processes for species.

For both plasma and neutral species, Cygnus supports an isotropic viscosity that has similar form as the usual isotropic viscous stress tensor defined as

$$\Pi = -\nu \left[\boldsymbol{\nabla}\mathbf{u} + (\boldsymbol{\nabla}\mathbf{u})^T - \frac{2}{3} (\boldsymbol{\nabla} \cdot \mathbf{u}) \overleftrightarrow{\mathrm{I}} \right]$$

but with the cross coupling of the velocity in different coordinate directions (due to fluid shear) neglected. This allows the viscous contribution for each coordinate direction in the velocity equation to be decoupled. To ensure Hermitian symmetry of the isotropic viscosity operator, the form of the isotropic viscosity operator used in Cygnus is defined to be

$$N_{r,\phi} = \left[\frac{\partial}{\partial r} \left(\frac{\nu}{r} \frac{\partial}{\partial r} \right) + \frac{\partial}{\partial z} \left(\frac{\nu}{r} \frac{\partial}{\partial z} \right) \right] r$$

for the radial and the azimuthal component, and

$$N_z = \frac{1}{r} \left[\frac{\partial}{\partial r} \left(r\nu \frac{\partial}{\partial r} \right) + \frac{\partial}{\partial z} \left(r\nu \frac{\partial}{\partial z} \right) \right]$$

for the axial component, where $N[\mathbf{u}] = -\boldsymbol{\nabla} \cdot \overleftrightarrow{\mathrm{N}}$ is the isotropic viscosity operator, $\overleftrightarrow{\mathrm{N}}$ is the isotropic viscosity tensor, and ν is the isotropic viscosity that is defined based on a user defined constant kinematic viscosity [28].

In addition to the isotropic viscosity, anisotropic plasma viscosity is implemented in Cygnus. Using the Braginskii closure, the viscous stress tensor for plasma can be defined to be the following:

$$\overleftrightarrow{\Pi} = \overleftrightarrow{\Pi}_c + \overleftrightarrow{\Pi}_g$$

where $\overleftrightarrow{\Pi}_c$ and $\overleftrightarrow{\Pi}_g$ are the viscous and gyroviscous component of the viscous stress tensor,

respectively, and are defined to be the followings [48]:

$$\overleftrightarrow{\Pi}_c = -\eta_0 \overleftrightarrow{\mathrm{W}}_0 - \eta_1 \overleftrightarrow{\mathrm{W}}_1 - \eta_2 \overleftrightarrow{\mathrm{W}}_2$$

$$\overleftrightarrow{\Pi}_g = \eta_3 \overleftrightarrow{\mathrm{W}}_3 + \eta_4 \overleftrightarrow{\mathrm{W}}_4$$

where

$$\overleftrightarrow{\mathrm{W}}_0 = \frac{3}{2}\left(\hat{\mathbf{b}}\hat{\mathbf{b}} - \frac{1}{3}\overleftrightarrow{\mathrm{I}}\right)\left(\hat{\mathbf{b}}\hat{\mathbf{b}} - \frac{1}{3}\overleftrightarrow{\mathrm{I}}\right) : \overleftrightarrow{\mathrm{W}}$$

$$\overleftrightarrow{\mathrm{W}}_1 = \overleftrightarrow{\mathrm{I}}_\perp \cdot \overleftrightarrow{\mathrm{W}} \cdot \overleftrightarrow{\mathrm{I}}_\perp + \frac{1}{2}\overleftrightarrow{\mathrm{I}}_\perp \left(\hat{\mathbf{b}} \cdot \overleftrightarrow{\mathrm{W}} \cdot \hat{\mathbf{b}}\right)$$

$$\overleftrightarrow{\mathrm{W}}_2 = \overleftrightarrow{\mathrm{I}}_\perp \cdot \overleftrightarrow{\mathrm{W}} \cdot \hat{\mathbf{b}}\hat{\mathbf{b}} + \hat{\mathbf{b}}\hat{\mathbf{b}} \cdot \overleftrightarrow{\mathrm{W}} \cdot \overleftrightarrow{\mathrm{I}}_\perp$$

$$\overleftrightarrow{\mathrm{W}}_3 = \frac{1}{2}\left[\left(\hat{\mathbf{b}} \times \overleftrightarrow{\mathrm{W}}\right) \cdot \overleftrightarrow{\mathrm{I}}_\perp - \overleftrightarrow{\mathrm{I}}_\perp \cdot \left(\overleftrightarrow{\mathrm{W}} \times \hat{\mathbf{b}}\right)\right]$$

$$\overleftrightarrow{\mathrm{W}}_4 = \left(\hat{\mathbf{b}} \times \overleftrightarrow{\mathrm{W}}\right) \cdot \hat{\mathbf{b}}\hat{\mathbf{b}} - \hat{\mathbf{b}}\hat{\mathbf{b}} \cdot \left(\overleftrightarrow{\mathrm{W}} \times \hat{\mathbf{b}}\right)$$

$$\overleftrightarrow{\mathrm{W}} = \boldsymbol{\nabla}\mathbf{u} + (\boldsymbol{\nabla}\mathbf{u})^T - \frac{2}{3}(\boldsymbol{\nabla} \cdot \mathbf{u})\overleftrightarrow{\mathrm{I}}$$

$$\overleftrightarrow{\mathrm{I}}_\perp = \overleftrightarrow{\mathrm{I}} - \hat{\mathbf{b}}\hat{\mathbf{b}}$$

$$\left[\overleftrightarrow{\mathrm{W}} \times \hat{\mathbf{b}}\right]_{rs} = -\left[\hat{\mathbf{b}} \times \overleftrightarrow{\mathrm{W}}\right]_{rs} = \mathrm{W}_{lr}\varepsilon_{slm}\hat{b}_m$$

In the above equations, $\hat{\mathbf{b}} = \mathbf{B}/|\mathbf{B}|$, ε_{slm} is the Levi-Civita permutation operator, and η_i for $i \in [0, 5]$ is the viscosity for each tensor contribution as given by Braginskii [48]. Note that the zeroth component corresponds to the parallel viscosity, while the first and second components correspond to the perpendicular viscosity.

2.2.5 Effective Ionization Potential

In order to account for additional energy loss mechanisms during the ionization process due to electron impact excitation and scattering, an effective ionization potential is used in Cygnus as a loss term for each ionization reaction. The effective ionization potential is an

energy loss per electron-ion pair created by the ionization reaction. The ionization reaction implemented in Cygnus for ions (i), electrons (e), and neutrals (n) are given to be

$$e + n \rightarrow i + 2e - \varphi_{iz}$$

where φ_{iz} is the effective ionization potential.

The effective ionization potential is an energy loss term for electrons in the fluid model, and it only shows up in the fluid equations associated with the electron temperature. This is due to the fact that the physical origin of this loss term is the electron impact collision reactions with neutrals that produce excited state neutrals. In this simple picture, one can consider this process as a two-step process given to be

$$e^* + n \rightarrow n^* + e$$
$$n^* \rightarrow n + h\nu$$

where superscript $*$ denotes the excited or energetic state (for the electron, it is associated with its kinetic energy). It is assumed that the plasma is optically thin to allow the radiated energy from the excited neutrals to be lost from the system. Thus, the net result of this two-step process is the electron energy loss from the system. Since there are finite probability of ionization, excitation, or elastic scattering for every electron impact collision with a neutral atom, the effective ionization potential is used to represent electron energy losses from non-ionization processes.

In order to account for the change in the electron impact cross section for ionization, excitation, and elastic scattering as a function of the electron impact energy, the electron temperature dependent effective ionization potential is implemented in Cygnus. Accounting for the energy loss associated with the electron impact excitation and scattering, the effective

ionization potential can be defined to be [58, 59]

$$\varphi_{iz} = \mathcal{E}_{iz} + \sum_i \frac{K_{ex,i}}{K_{iz}} \mathcal{E}_{ex,i} + \frac{K_{el}}{K_{iz}} \frac{3m_e}{m} T_e \tag{2.39}$$

where $\mathcal{E}_{iz}$ and $\mathcal{E}_{ex}$ are the ionization and excitation threshold energy, respectively, K_{iz}, K_{ex}, and K_{el} are the ionization, excitation, and elastic scattering reaction rates, respectively, m_e is the electron mass, m is the neutral species mass, and T_e is the electron temperature.

Based on the results compiled by Lieberman and Lichtenberg [58], for argon, one can use $E_{iz} = 15.76$ eV, and $E_{ex} = 12.14$ eV for the ionization and excitation energy, and for reaction rates, one can use following fits (T_e is in units of eV):

$$K_{iz} = \left(2.34 \times 10^{-14}\right) T_e^{0.59} \exp\left(-17.44/T_e\right) \ (\mathrm{m}^3/\mathrm{s})$$

$$K_{ex} = \left(2.48 \times 10^{-14}\right) T_e^{0.33} \exp\left(-12.78/T_e\right) \ (\mathrm{m}^3/\mathrm{s})$$

$$K_{el} = \left(2.336 \times 10^{-14}\right) T_e^{1.609} \exp\left[0.0618 \ln\left(T_e\right)^2 - 0.1171 \ln\left(T_e\right)^3\right] \ (\mathrm{m}^3/\mathrm{s})$$

In the above form of the fits for the reaction rates, the fit is made to be accurate for lower temperatures (1–7 eV as reported in Liberman and Lichtenberg) and is made to ensure that φ_{iz} asymptotically reduces to E_{iz} for elevated electron temperatures by using an Arrhenius form of the reaction rates [58].

Similar procedure can be applied for hydrogen to obtain a reasonable form of the effective ionization potential. Based on the Bohr model for hydrogen, the ionization energy is $E_{iz} = 13.6$ eV. Using the reaction rate coefficient for the hydrogen ionization compiled by Janev et al. [60] and making a fit with a similar Arrhenius form as Gudmundsson [59], the following fit can be used for the ionization reaction rate (T_e is in units of eV):

$$K_{iz} = \left(5.413 \times 10^{-15}\right) T_e^{0.5574} \exp\left(-13.84/T_e\right) \ (\mathrm{m}^3/\mathrm{s}) \tag{2.40}$$

For the electron impact excitation, the reaction rate coefficient for hydrogen-electron

impact excitation produced by Park [61] is used. Based on Park, the reaction rate for excitation of the hydrogen atom from n_0 to n_1 energy level is given to be

$$K_{ex}\left(n_0, n_1\right) = \frac{C\left(1.1604\, T_e\right)^r g_{n_1}}{n_0^5 n_1^5 \left(1/n_0^2 - 1/n_1^2\right)^4} \exp\left(-\frac{E_{n_1} - E_{n_0}}{T_e}\right)$$

where C and r are the fit parameters, g is the statistical weight, and E is the average energy of the level [61]. To compute the contribution to the effective ionization potential, one can consider the transition from the $n_0 = 1$ to the higher energy level. Considering first 16 transitions, the fit to the hydrogen-electron impact excitation reaction rate can be represented as

$$K_{ex,i} = \frac{C_i\left(1.1604\, T_e\right)^{r_i} g_i}{(1+i)^5\left[1 - 1/(1+i)^2\right]^4} \exp\left(-\mathcal{E}_{ex,i}/T_e\right) \tag{2.41}$$

where $i \in [1, 16]$ and T_e is in units of eV. The values of C_i, r_i, g_i, and $\mathcal{E}_{ex,i}$ has been tabulated by Park, and selected data suitable for hydrogen excitation reaction rates for the effective ionization potential calculations are shown in Table 1. Note that the fit to the reaction rate by Park is reported to be valid for electron temperature in the range of 0.38–6.9 eV [61].

For the electron elastic scattering reaction coefficient for hydrogen, results from the theoretical work of Bydder [55] is used. Based on the collision frequency given in Eq. 2.34, the reaction rate coefficient for electron elastic scattering reaction can be expressed as

$$K_{el} = \left(1.3079 \times 10^{-12}\right) \exp\left(13.606/T_e\right) E_1\left(13.606/T_e\right) T_e^{-3/2}\, (\mathrm{m}^3/\mathrm{s}) \tag{2.42}$$

where T_e is in units of eV.

The resulting effective ionization potential for both argon and deuterium is shown in Fig. 2.1. As it can be seen, the effective ionization potential is significantly larger for temperatures approaching 1 eV, as effects from the electron-neutral scattering are important. For temperature above 2–3 eV, the elastic scattering contribution becomes negligible, and it is the electron impact excitation that enhances the ionization potential. At 3 eV, the effective ionization potential for deuterium is approximately 100 eV, while for argon, it is 61 eV.

Table 2.1: Fit coefficients for hydrogen electron impact excitation reaction rate [61]

i	$\mathcal{E}_{ex}$ (eV)	g	C (10^{-14}m^3/s)	r
1	10.198	8	2.2	0.12
2	12.087	18	3.0	0.09
3	12.748	32	3.5	0.09
4	13.054	50	4.2	0.08
5	13.220	72	4.5	0.08
6	13.320	98	5.0	0.08
7	13.385	128	5.5	0.08
8	13.430	162	5.9	0.07
9	13.462	200	6.4	0.07
10	13.485	242	6.8	0.07
11	13.504	288	7.2	0.07
12	13.517	338	7.6	0.07
13	13.528	392	8.0	0.07
14	13.537	450	8.3	0.07
15	13.545	512	8.7	0.07
16	13.551	578	9.0	0.07

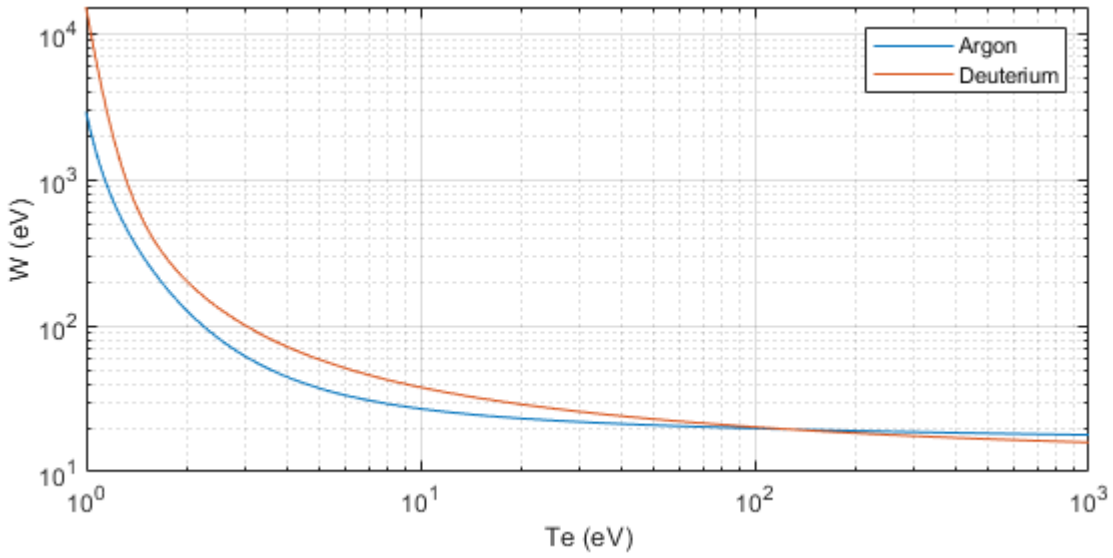

Figure 2.1: Electron temperature dependent effective ionization potential for argon and deuterium.

2.3 Implementation of the Meier-Shumlak Model in Cygnus

Details of the Cygnus algorithm and the implementation of the Meier-Shumlak model in it is discussed here. As discussed in Section 1.5.3, Cygnus time step algorithm can be split into two main steps: the velocity and pressure (VP) advance and density, temperature, and magnetic field (NTB) advance. The neutral fluid advance is implemented in the same manner as the plasma fluid, and predictor-corrector loops are used to couple two fluids.

2.3.1 VP Advance

The pressure and velocity equations are solved using a predictor-corrector loop in which the updated pressure is computed first. The electron pressure is advanced after updated pressure and the velocity are obtained. As discussed previously, Cygnus supports various forms of the energy equation to compute updated pressure.

For the total energy advance, since none of the terms exhibit a wave-like instability, the equation can be advanced explicitly in time as long as the advective contribution is handled using a time-step sub-cycling approach to satisfy the local advective CFL limit [28]. The form of the temporally discretized equations are given as the followings:

$$\begin{aligned}\frac{\varepsilon^{**}-\varepsilon^{n}}{\Delta t} = -\nabla\cdot\left[\left(\gamma\varepsilon^{*}-\frac{\gamma-1}{2}mn^{n+1/2}\left|\mathbf{u}^{*}\right|^{2}\right)\mathbf{u}^{*}+\mathbf{u}^{*}\cdot\overleftrightarrow{\mathrm{N}}^{*}+\mathbf{u}^{*}\cdot\overleftrightarrow{\Pi}^{*}\right] \\ +\mathbf{u}^{*}\cdot\mathbf{J}^{n+1/2}\times\mathbf{B}^{n+1/2}+\eta\left|\mathbf{J}^{n+1/2}\right|^{2}+\frac{\delta\tilde{E}^{*}}{\delta t}\end{aligned} \tag{2.43a}$$

$$\frac{\varepsilon_{n}^{**}-\varepsilon_{n}^{n}}{\Delta t} = -\nabla\cdot\left[\left(\gamma\varepsilon_{n}^{*}-\frac{\gamma-1}{2}mn_{n}^{n+1/2}\left|\mathbf{u}_{n}^{*}\right|^{2}\right)\mathbf{u}_{n}^{*}+\mathbf{u}_{n}^{*}\cdot\overleftrightarrow{\mathrm{N}}_{n}^{*}\right]-\frac{\delta\tilde{E}_{n}^{*}}{\delta t} \tag{2.43b}$$

where

$$\begin{aligned}\frac{\delta\tilde{E}_{n}^{*}}{\delta t} = \Gamma_{iz}^{n+1/2}\left(\frac{1}{2}m\left|\mathbf{u}_{n}^{*}\right|^{2}+\frac{3}{2}kT_{n}^{n+1/2}\right)-\Gamma_{rc}^{n+1/2}\left(\frac{1}{2}m\left|\mathbf{u}^{*}\right|^{2}+\frac{3}{2}kT_{i}^{n+1/2}\right) \\ +\Gamma_{cx}^{*}\frac{1}{2}m\left(\left|\mathbf{u}_{n}^{*}\right|^{2}-\left|\mathbf{u}^{*}\right|^{2}\right)+\left(Q_{in}^{cx}\right)^{*}-\left(Q_{ni}^{cx}\right)^{*}+\mathbf{u}_{n}^{*}\cdot\left(\mathbf{R}_{in}^{cx}\right)^{*}-\mathbf{u}^{*}\cdot\left(\mathbf{R}_{ni}^{cx}\right)^{*}\end{aligned}$$

and

$$\frac{\delta\tilde{E}^*}{\delta t} = \frac{\delta\tilde{E}^*_n}{\delta t} - \Gamma^{n+1/2}_{iz}\varphi_{iz}$$

are the contributions due to reactions. In the above equations, the superscripts denote the value of the quantities at the specified time level (n, $n+1/2$, $n+1$, $*$, and $**$) where the $*$ time level defined to be an estimate of the $n+\alpha$ time level using the predictor-corrector loop; α is usually equal to 1/2 (time centered) or 1 (pseudo-implicit) [28]. The $**$ time level is at the updated time after the energy advance.

For the case of the internal energy (pressure) advance, the equation can be advanced explicitly in time similar to the total energy advance [28]. The form of the temporally discretized equations are given as the followings:

$$\begin{aligned}\frac{1}{\gamma-1}\frac{p^{**}-p^n}{\Delta t} = &-\boldsymbol{\nabla}\cdot\left(\frac{\gamma p^*}{\gamma-1}\mathbf{u}^*\right) + \mathbf{u}^*\cdot\boldsymbol{\nabla}p^* - \overleftrightarrow{\mathrm{N}}^* : \boldsymbol{\nabla}\mathbf{u}^* - \overleftrightarrow{\Pi}^* : \boldsymbol{\nabla}\mathbf{u}^* \\ &+ \eta\left|\mathbf{J}^{n+1/2}\right|^2 + \frac{\delta E^*}{\delta t}\end{aligned} \tag{2.44a}$$

$$\frac{1}{\gamma-1}\frac{p^{**}_n-p^n_n}{\Delta t} = -\boldsymbol{\nabla}\cdot\left(\frac{\gamma p^*_n}{\gamma-1}\mathbf{u}^*_n\right) + \mathbf{u}^*_n\cdot\boldsymbol{\nabla}p^*_n - \overleftrightarrow{\mathrm{N}}^*_n : \boldsymbol{\nabla}\mathbf{u}^*_n - \frac{\delta E^*_n}{\delta t} \tag{2.44b}$$

where

$$\begin{aligned}\frac{\delta E^*}{\delta t} = \Gamma^{n+1/2}_{iz}\left(\frac{1}{2}m\left|\mathbf{u}^*-\mathbf{u}^*_n\right|^2 + \frac{3}{2}kT^{n+1/2}_n - \varphi^{n+1/2}_{iz}\right) - \Gamma^{n+1/2}_{rc}\frac{3}{2}kT^{n+1/2}_i \\ + \frac{1}{2}m\Gamma^*_{cx}\left|\mathbf{u}^*-\mathbf{u}^*_n\right|^2 + (\mathbf{R}^{cx}_{in})^*\cdot(\mathbf{u}^*_n-\mathbf{u}^*) + (Q^{cx}_{in})^* - (Q^{cx}_{ni})^*\end{aligned}$$

and

$$\begin{aligned}\frac{\delta E^*_n}{\delta t} = \Gamma^{n+1/2}_{iz}\frac{3}{2}kT^{n+1/2}_n - \Gamma^{n+1/2}_{rc}\left(\frac{1}{2}m\left|\mathbf{u}^*-\mathbf{u}^*_n\right|^2 + \frac{3}{2}kT^{n+1/2}_n\right) - \frac{1}{2}m\Gamma^*_{cx}\left|\mathbf{u}^*-\mathbf{u}^*_n\right|^2 \\ - (\mathbf{R}^{cx}_{ni})^*\cdot(\mathbf{u}^*-\mathbf{u}^*_n) + (Q^{cx}_{in})^* - (Q^{cx}_{ni})^*\end{aligned}$$

are the contributions due to reactions.

From the total energy advance, the internal energy advance, or both, the updated fluid pressure can be obtained. The updated fluid pressures are calculated as

$$p^{***} = f_k \left(\gamma - 1\right) \left(\varepsilon^{**} - \frac{1}{2} m n^{n+1/2} \left|\mathbf{u}^*\right|^2\right) + \left(1 - f_k\right) p^{**} \tag{2.45a}$$

$$p_n^{***} = f_{kn} \left(\gamma - 1\right) \left(\varepsilon_n^{**} - \frac{1}{2} m n_n^{n+1/2} \left|\mathbf{u}_n^*\right|^2\right) + \left(1 - f_{kn}\right) p_n^{**} \tag{2.45b}$$

where $f_k \in [0,1]$ and $f_{kn} \in [0,1]$ are the mixing ratios to compute the updated pressure in the case when both energy formulations are used. For the case of the total energy advance, $f_k = f_{kn} = 1$; for the case of the internal energy advance, $f_k = f_{kn} = 0$ [28]. For the temperature equation formulation, since both temperature and density are solved on the half integer time level, $p^{***} = n^{n+1/2} k T^{n+1/2}$ and $p_n^{***} = n_n^{n+1/2} k T_n^{n+1/2}$.

After the updated fluid pressures are known, velocities can be advanced. The plasma velocity equation is discretized temporally to be

$$\begin{aligned} m n^{n+1/2} \frac{\Delta \mathbf{u}}{\Delta t} - L\left[\Delta \mathbf{u}\right] = -m n^{n+1/2} \mathbf{u}^* \cdot \boldsymbol{\nabla} \mathbf{u}^* - \boldsymbol{\nabla} p^{***} + N\left[\mathbf{u}^{n+1}\right] \\ + \mathbf{J}^{n+1/2} \times \mathbf{B}^{n+1/2} + \frac{\delta \mathbf{M}^*}{\delta t} - \boldsymbol{\nabla} \cdot \overleftrightarrow{\Pi}^{n+1} \end{aligned} \tag{2.46}$$

where

$$\frac{\delta \mathbf{M}^*}{\delta t} = m \left(\Gamma_{iz}^{n+1/2} + \Gamma_{cx}^*\right) \left(\mathbf{u}_n^* - \mathbf{u}^*\right) + \left(\mathbf{R}_{in}^{cx}\right)^* - \left(\mathbf{R}_{ni}^{cx}\right)^*$$

is the contribution from reactions and $\Delta \mathbf{u} = \mathbf{u}^{n+1} - \mathbf{u}^n$. In the above equation, a semi-implicit operator term (L) is added to both updated and current time level in order to stabilize the wave-like instability in the velocity advance, and the viscous transport terms are handled implicitly [28].

The semi-implicit operator used in Cygnus is a decoupled Hermitian symmetric operator similar to what was defined previously for the isotropic viscosity operator in Section 2.2.4. The form of the semi-implicit operator is similar to the diagonal semi-implicit operator from the earlier work of Schnack et al. [45]. The semi-implicit operator used here is a modified

Laplacian operator [28]. For the radial and azimuthal components, the semi-implicit operator is defined to be

$$L_{r,\phi} = \left[\frac{\partial}{\partial t}\left(\frac{\tilde{p}_{r,\phi}}{r}\frac{\partial}{\partial r}\right) + \frac{\partial}{\partial z}\left(\frac{\tilde{p}_{r,\phi}}{r}\frac{\partial}{\partial z}\right)\right] r$$

while for the axial component, it is defined to be

$$L_z = \frac{1}{r}\left[\frac{\partial}{\partial r}\left(r\tilde{p}_z\frac{\partial}{\partial r}\right) + \frac{\partial}{\partial z}\left(r\tilde{p}_z\frac{\partial}{\partial z}\right)\right]$$

The terms $\tilde{p}_k$ for $k = r, \phi, z$ are the semi-implicit stiffness factors that are defined to be

$$\tilde{p}_k = \frac{f_{si}\Delta t}{4}\left[\gamma p\left(1 - \delta_{k\phi}\right) + \frac{1}{\mu_0}\left(B^2 - B_k^2\right)\right]$$

where f_{si} is the semi-implicit stabilization factor and δ_{kl} is the Kronecker delta. Both the semi-implicit and isotropic viscosity operators are symmetric and positive definite when finite differences are taken.

When the anisotropic viscous stress tensor is neglected and a Dirichlet zero boundary condition is assumed for the velocity, the discretized vector velocity equation decouples for each coordinate direction. Thus, the velocity equation for each component can be advanced independent of each other as the implicit contributions are decoupled. Implementation details of the anisotropic viscous stress tensor in the velocity advance is addressed in Section 2.5.

Similar to the plasma velocity advance, the temporally discretized neutral velocity advance is defined to be

$$mn_n^{n+1/2}\frac{\Delta \mathbf{u}_n}{\Delta t} - L_n\left[\Delta \mathbf{u}_n\right] = -mn_n^{n+1/2}\mathbf{u}_n^* \cdot \boldsymbol{\nabla}\mathbf{u}_n^* - \boldsymbol{\nabla}p_n^{***} + N_n\left[\mathbf{u}_n^{n+1}\right] - \frac{\delta \mathbf{M}_n^*}{\delta t} \tag{2.47}$$

where

$$\frac{\delta \mathbf{M}_n^*}{\delta t} = m\left(\Gamma_{rc}^{n+1/2} + \Gamma_{cx}^*\right)\left(\mathbf{u}_n^* - \mathbf{u}^*\right) + \left(\mathbf{R}_{in}^{cx}\right)^* - \left(\mathbf{R}_{ni}^{cx}\right)^*$$

is the contribution from reactions and $\Delta \mathbf{u}_n = \mathbf{u}_n^{n+1} - \mathbf{u}_n^n$. The semi-implicit operator L_n with the same form as the plasma velocity advance is introduced in the neutral velocity equation

for numerical stabilization. Only difference from the plasma advance is the removal of the magnetic pressure term in the semi-implicit stiffness factor $\tilde{p}_k$.

For the case when the total or internal energy formulation is used, after the plasma and neutral pressures and velocities are advanced to the $n+1$ time level, the electron pressure (or temperature) is advanced using a predictor-corrector loop to determine the partition of the total plasma temperature between ions and electrons at the updated time level. The temporally discretized electron temperature equation is given as

$$\frac{\Delta T_e}{\Delta t} = -\left(\gamma-1\right)\left(T_e^*\right)^{(\gamma-2)/(\gamma-1)} \boldsymbol{\nabla}\cdot\left[\left(T_e^*\right)^{1/(\gamma-1)}\mathbf{u}_e^{n+1/2}\right] + \frac{\eta\left(\gamma-1\right)}{kn^{n+1/2}}\left|\mathbf{J}^{n+1/2}\right|^2 + \frac{\delta T_e^*}{\delta t} \quad (2.48)$$

where

$$\frac{\delta T_e^*}{\delta t} = \left(\Gamma_{rc}^{n+1/2} - \Gamma_{iz}^{n+1/2}\right)\frac{T_e^{n+1/2}}{n^{n+1/2}} - \frac{\gamma-1}{kn^{n+1/2}}\Gamma_{iz}^{n+1/2}\varphi_{iz}$$

and $\mathbf{u}_e = \mathbf{u} - \mathbf{J}/(en)$ is the electron velocity. For the electron pressure formulation, the temporally discretized electron pressure equation is given as

$$\frac{1}{\gamma-1}\frac{p_e^{**}-p_e^n}{\Delta t} = -\boldsymbol{\nabla}\cdot\left[\frac{\gamma p_e^*}{\gamma-1}\mathbf{u}_e^{n+1/2}\right] + \mathbf{u}_e^{n+1/2}\cdot\boldsymbol{\nabla}p_e^* + \eta\left|\mathbf{J}^{n+1/2}\right|^2 + \frac{\delta E_e^*}{\delta t} \quad (2.49)$$

where

$$\frac{\delta E_e^*}{\delta t} = -\Gamma_{iz}^{n+1/2}\varphi_{iz}$$

Note that for the case when the temperature equation formulation of the plasma and neutral energy equations is used, the electron energy is not advanced here, and it handled in the NTB advance at the $n+1/2$ time level.

2.3.2 NTB Advance

In the NTB advance, density, magnetic field and external circuit, and temperature are advanced in time. As discussed in Section 1.5.3, this step corresponds to the half-integer time step advance. Unlike the VP advance, the NTB advance is not fully time centered using

a global predictor-corrector loop over the entire coupled advance. This is due to the fact that the magnetic field advance with coupled external circuits and conductors is numerically demanding and requires most computational time. In order to speed up the time advance algorithm, errors due to time misalignment are accepted in the NTB advance in order to only advance the magnetic field equation once outside of a predictor-corrector loop [28].

Due to this compromise, the NTB advance is performed in a sequential manner in the following order: density advance; magnetic field and circuit advance; and temperature advance. Implementation details of each sub-steps are discussed in their respective subsections.

2.3.3 Density Advance

Species densities are advanced using a split equation formulation with the first step being the ideal conservative advance and the second step being the reaction advance. This splitting allows the ideal advance to be handled explicitly with a predictor-corrector loop; the reaction advance is handled implicitly to avoid instabilities. The temporally discretized ideal advance of the density is given to be

$$\frac{n_\alpha^{**} - n_\alpha^{n+1/2}}{\Delta t} = -\boldsymbol{\nabla} \cdot \left(n_\alpha^{*} \mathbf{u}_\alpha^{n+1} \right) \tag{2.50}$$

for species α. The above equation can be advanced explicitly with a predictor-corrector loop to determine the updated density at the $**$ time step.

For the implicit reaction advance, note that the equation that is advanced is given as the following:

$$\frac{\mathrm{d}n}{\mathrm{d}t} = -\frac{\mathrm{d}n_n}{\mathrm{d}t} = n n_n \left\langle \sigma_{iz} v_e \right\rangle - n^2 \left\langle \sigma_{rc} v_e \right\rangle \tag{2.51}$$

Since no advective term exists in the above equation, the total number density at each computational node is conserved. Thus, the density at each computational node can be updated independently. When the implicit time differencing is applied to the above equation,

it forms a quadratic equation as a function of the density change given to be the following:

$$\alpha \left(\Delta n\right)^2 + \beta \left(\Delta n\right) + \gamma = 0$$

where

$$\begin{aligned}
\alpha &= \Delta t \left[\langle \sigma_{iz} v_e \rangle + \langle \sigma_{rc} v_e \rangle\right] \\
\beta &= 1 + \Delta t \left(n^{**} - n_n^{**}\right) \langle \sigma_{iz} v_e \rangle + 2\Delta t \, n^{**} \langle \sigma_{iz} v_e \rangle \\
\gamma &= \Delta t \left(n^{**}\right)^2 \langle \sigma_{rc} v_e \rangle - n^{**} n_n^{**} \Delta t \langle \sigma_{iz} v_e \rangle
\end{aligned}$$

The above equation for Δn can be solved exactly with the quadratic equation, and the plasma and neutral number density at the updated time can be computed trivially as the followings:

$$n^{n+3/2} = n^{**} + \Delta n \tag{2.53a}$$

$$n_n^{n+3/2} = n_n^{**} - \Delta n \tag{2.53b}$$

2.3.4 Magnetic Field Advance

For the magnetic field advance, in order to solve the coupled system of equations for the magnetic flux and the azimuthal magnetic field, a modified implementation of the time-step splitting method of Harned and Mikic is used [46]. In Cygnus, instead of splitting the magnetic field advance into two steps (Hall and everything else), a three step time-step splitting is used with the splitting organized into following three steps: (1) ideal advance, (2) Hall advance, and (3) resistive advance [28]. The current implementation in Cygnus carries out the coupled magnetic field advance in the following order: (1) ideal advance of the azimuthal magnetic field (explicit advection); (2) Hall advance of the azimuthal magnetic field (semi-implicit); (3) Hall advance of the magnetic flux (semi-implicit); (4) resistive advance of the azimuthal magnetic field (implicit); (5) ideal advance of the magnetic flux (semi-Lagrangian);

and (6) resistive advance of the magnetic flux (implicit). Contributions from external circuits are only included in step 6, where the resistive advance of the magnetic flux is taken.

(1) Ideal Advance of the Azimuthal Magnetic Field

In the ideal advance of the azimuthal magnetic field, the form of the equation that is advanced in time is

$$\frac{\partial B_\phi}{\partial t} = \boldsymbol{\nabla}_{2D} \cdot \left[(\mathbf{u} \times \mathbf{B}) \times \hat{\boldsymbol{\phi}} \right]$$

which after the time discretization and simplification becomes the following:

$$B_\phi^{**} = B_\phi^{n+1/2} + \Delta t \, \boldsymbol{\nabla}_{2D} \cdot \left(u_\phi^{n+1} \mathbf{B}^{n+1/2} - B_\phi^* \mathbf{u}^{n+1} \right) \tag{2.54}$$

Note that because the magnetic flux advance is not coupled into the predictor-corrector loop for the azimuthal magnetic field, the magnetic field vector $\mathbf{B}$ from the previous time step is used.

(2) Hall Advance of the Azimuthal Magnetic Field

In the Hall advance of the azimuthal magnetic field, the form of the equation that is advanced in time is

$$\frac{\partial B_\phi}{\partial t} = \boldsymbol{\nabla}_{2D} \cdot \left[\frac{1}{en} \left(\boldsymbol{\nabla} p_e - \mathbf{J} \times \mathbf{B} \right) \times \hat{\boldsymbol{\phi}} \right]$$

which after the time discretization and simplification becomes the following:

$$\frac{\Delta B_\phi}{\Delta t} - L_h \left[\Delta \mathbf{B} \right] = b^* \tag{2.55}$$

where

$$b^* = \frac{n^{n+1}}{e} \left[\frac{1}{n^{n+1}}, T_e^{**} \right] + \left[\Psi^{n+1/2}, \frac{J_\phi^{n+1/2}}{e r n^{n+1}} \right] - \frac{B_\phi^*}{\mu_0 e r} \left(\left[r B_\phi^*, \frac{1}{n^{n+1}} \right] + \frac{1}{n^{n+1}} \left[r^2, \frac{B_\phi^*}{r} \right] \right)$$

and the Poisson's bracket $[f, g]$ is defined to be the following [28]:

$$[f, g] = \frac{\partial f}{\partial z}\frac{\partial g}{\partial r} - \frac{\partial f}{\partial r}\frac{\partial g}{\partial z}$$

Note that the semi-implicit operator L_h is introduced in the above equation for stabilization. The $*$ time step corresponds to the current guess for the intermediate state based on the predictor-corrector loop coupled to the ideal advance. The $**$ time level corresponds to the current guess for the updated state.

Assuming a second-order semi-implicit operator for the Hall term, it takes the following form:

$$L_h = -\boldsymbol{\nabla} \times c_h \boldsymbol{\nabla} \times \tag{2.56}$$

where c_h is the semi-implicit stiffness factor defined to be

$$c_h = f_{si}\Delta t \frac{|\mathbf{B}|}{\mu_0 e n}$$

Solving for the azimuthal component of the semi-implicit operator, the semi-implicit Hall advance takes the following form [28]:

$$\left\{\frac{1}{r} - \left[\frac{\partial}{\partial r}\left(\frac{c_h}{r}\frac{\partial}{\partial r}\right) + \frac{\partial z}{\partial z}\left(\frac{c_h}{r}\frac{\partial}{\partial z}\right)\right]\right\}\frac{r\Delta B_\phi}{\Delta t} = b^* \tag{2.57}$$

(3) Hall Advance of the Magnetic Flux

In the Hall advance of the magnetic flux, the form of the equation that is advanced in time is the following:

$$\frac{\partial \Psi}{\partial t} = \frac{1}{\mu_0 e n}\left(\boldsymbol{\nabla} \times \mathbf{B}_\phi\right) \cdot \boldsymbol{\nabla}\Psi$$

In order to solve the Hall term in the magnetic flux equation consistently using the same semi-implicit operator used for the azimuthal magnetic field advance, multiply both side of the equation by $\hat{\boldsymbol{\phi}}/r$ and take the curl of both side to represent the above equation in

terms of the magnetic field. The same semi-implicit operator can now be introduced to the evolution equation for the non-azimuthal component of the magnetic field as the following:

$$(1 + \boldsymbol{\nabla} \times c_h \boldsymbol{\nabla} \times) \frac{\partial \tilde{\mathbf{B}}}{\partial t} = \boldsymbol{\nabla} \times \left[\frac{1}{r} \left(\frac{\boldsymbol{\nabla} \times \mathbf{B}_\phi}{\mu_0 e n} \cdot \boldsymbol{\nabla} \Psi \right) \hat{\boldsymbol{\phi}} \right]$$

where $\tilde{\mathbf{B}} = \boldsymbol{\nabla} \times (\Psi \hat{\boldsymbol{\phi}}/r)$ is the non-azimuthal component of the magnetic field.

Re-introducing the magnetic flux in the above equation instead of $\tilde{\mathbf{B}}$, the above equation simplifies to the following form:

$$\boldsymbol{\nabla} \times \left[(1 + c_h \boldsymbol{\nabla} \times \boldsymbol{\nabla} \times) \left(\frac{1}{r} \frac{\partial \Psi}{\partial t} \hat{\boldsymbol{\phi}} \right) \right] = \boldsymbol{\nabla} \times \left[\frac{1}{r} \left(\frac{\boldsymbol{\nabla} \times \mathbf{B}_\phi}{\mu_0 e n} \cdot \boldsymbol{\nabla} \Psi \right) \hat{\boldsymbol{\phi}} \right]$$

The curl on both side can now be removed to give the following:

$$\left[(1 + c_h \boldsymbol{\nabla} \times \boldsymbol{\nabla} \times) \left(\frac{1}{r} \frac{\partial \Psi}{\partial t} \hat{\boldsymbol{\phi}} \right) \right] \cdot \hat{\boldsymbol{\phi}} = \frac{1}{r} \left(\frac{\boldsymbol{\nabla} \times \mathbf{B}_\phi}{\mu_0 e n} \cdot \boldsymbol{\nabla} \Psi \right) \tag{2.58}$$

After the time discretization, the above equation simplifies to the following:

$$\left\{ 1 - r c_h \left[\frac{\partial}{\partial r} \left(\frac{1}{r} \frac{\partial}{\partial r} \right) + \frac{\partial}{\partial z} \left(\frac{1}{r} \frac{\partial}{\partial z} \right) \right] \right\} \frac{\Delta \Psi}{\Delta t} = \frac{r}{e n^{n+1}} \left(J_r^{**} B_z^{n+1/2} - J_z^{**} B_r^{n+1/2} \right) \tag{2.59}$$

where the $**$ time level corresponds to a guess based on the current state of B_ϕ.

(4) Resistive Advance of the Azimuthal Magnetic Field

In the resistive advance of the azimuthal magnetic field, the form of the equation that is advanced in time is

$$\frac{\partial B_\phi}{\partial t} = -\boldsymbol{\nabla}_{2D} \cdot \left(\eta \mathbf{J} \times \hat{\boldsymbol{\phi}} \right)$$

which after the implicit time discretization and simplification becomes the following:

$$\left\{ \frac{1}{r \Delta t} - \left[\frac{\partial}{\partial r} \left(\frac{\eta}{\mu_0 r} \frac{\partial}{\partial r} \right) + \frac{\partial}{\partial z} \left(\frac{\eta}{\mu_0 r} \frac{\partial}{\partial z} \right) \right] \right\} \left(r B_\phi^{n+3/2} \right) = \frac{B_\phi^{**}}{\Delta t} \tag{2.60}$$

(5) Ideal Advance of the Magnetic Flux

The ideal advance of the magnetic flux is given as the following:

$$\frac{D\Psi}{Dt} = \frac{\partial \Psi}{\partial t} + \mathbf{u} \cdot \boldsymbol{\nabla} \Psi = 0 \tag{2.61}$$

where D/Dt is the total (Lagrangian) derivative. Since the Lagrangian derivative of the magnetic flux is zero, the above equation can be advanced trivially with a semi-Lagrangian method.

(6) Resistive Advance of the Magnetic Flux

In the resistive advance of the magnetic flux, the form of the equation that is advanced in time is given as

$$\frac{\partial \Psi}{\partial t} = \frac{\eta}{\mu_0} \Delta^* \Psi$$

which after the time discretization and simplification becomes the following:

$$\left[\frac{\Delta r \Delta z}{r \eta \Delta t} - \frac{\Delta r \Delta z}{\mu_0 r} \Delta^* \right] \Delta \Psi = \left[\frac{\Delta r \Delta z}{\mu_0 r} \Delta^* \right] \Psi^* \tag{2.62}$$

where $\Delta \Psi = \Psi^{n+3/2} - \Psi^*$ is the change in the magnetic flux and Ψ^* is the most up-to-date magnetic flux calculated thus far. To simplify couplings to external conductors, additional spatial discretization factors of Δr, Δz, and r are introduced in the above equation based on the observation such that

$$I_\alpha = - \left. \frac{\Delta r \Delta z \Delta^* \Psi}{\mu_0 r} \right|_\alpha$$

for the finite difference node α. I_α is the nodal current for node α. Note that when the spatial discretization of the elliptic operator is taken, the boundary cut-edge nodes are included, since the the boundary magnetic flux is coupled with the external conductors.

In addition to the fluid region magnetic flux evolution, the magnetic flux advance in the vacuum regions due to external conductors must also be considered. On external conductors,

the magnetic flux advance can be expressed as the following from the Faraday's law:

$$\frac{\mathrm{d}\Psi_s}{\mathrm{d}t} = \frac{1}{2\pi}\frac{V_s}{N_s} \tag{2.63}$$

where Ψ_s is the magnetic flux on the external conductors, V_s is the local azimuthal voltage drop for the external conductors, and N_s is the local turn number for the external conductors. Since external conductors are discretized with current carrying segments, the above equation for the magnetic flux on the vacuum regions are discretized with the magnetic flux, voltage, and current on the individual segments including the boundary.

Details of the magnetic flux advance coupling between the vacuum and fluid regions are discussed in Section 2.4. For now, it is sufficient to say that in the vacuum region, one obtain a discretized linear system of equations for changes in the segment magnetic flux when an implicit time difference is taken. Since both the fluid and vacuum domain magnetic flux advances contain the flux unknowns associated with the boundary, the two equations are coupled by relating their respective boundary flux representations to each other.

In the fluid region, boundary unknowns are the flux on the cut-edge nodes, while in the vacuum region, boundary unknowns are the flux on the boundary segments. Since the cut-edge nodes are located on the boundary segments, they can be related to each other. In Cygnus, a quadratic interpolation of the boundary segment flux to the cut-edge nodal flux is used to couple the two regions together [28]. With this coupling, the implicit and linear matrix system of equations for the resistive magnetic flux advance is completed, and it can be advanced in time.

2.3.5 Temperature Advance

In this step, the plasma and neutral total energies are converted into the ion, electron, and neutral temperatures, and thermal conduction and equilibration steps are applied directly to the temperatures. For the case when the total or internal energy formulation is used, the

current temperatures can be computed to be the followings:

$$T^{**} = \frac{1}{n^{n+1}k}\left[f_k\left(\gamma-1\right)\left(\varepsilon^{**} - \frac{1}{2}mn^{n+1}\left|\mathbf{u}^{n+1}\right|^2\right) + \left(1-f_k\right)p^{**}\right] \tag{2.64a}$$

$$T_n^{**} = \frac{1}{n_n^{n+1}k}\left[f_{kn}\left(\gamma-1\right)\left(\varepsilon_n^{**} - \frac{1}{2}mn_n^{n+1}\left|\mathbf{u}_n^{n+1}\right|^2\right) + \left(1-f_{kn}\right)p_n^{**}\right] \tag{2.64b}$$

where the $**$ time level for the energy and pressure advances is associated with the final results from the VP step. For the case when the temperature formulation is used, $T^{**} = T^{n+1/2}$ which is simply the previous value of the temperature from this routine at the previous time step.

The temperature advance is further split into the thermal conduction and thermal equilibration step with a predictor-corrector loop used to couple two advances for all fluid species. For both thermal conduction and thermal equilibration, an implicit time advance is used for stability. For the thermal conduction, the time discretized equation is given as

$$\frac{kn_\alpha^{n+1}}{\gamma-1}\frac{T_\alpha^{***} - T_\alpha^{**}}{\Delta t} = \boldsymbol{\nabla}\cdot\overleftrightarrow{\chi}_\alpha^*\cdot\boldsymbol{\nabla}T_\alpha^{***} + b_\alpha^* \tag{2.65}$$

and for the thermal equilibration, it is given as

$$\frac{T_\alpha^{n+3/2} - T_\alpha^{***}}{\Delta t} = \sum_\beta \nu_{\beta\alpha}^*\left(T_\beta^{n+3/2} - T_\alpha^{n+3/2}\right) \tag{2.66}$$

where $\nu_{\alpha\beta}$ is the thermal equilibration frequency and $\overleftrightarrow{\chi}$ is the anisotropic thermal conductivity for ions and electrons and isotropic thermal conductivity for neutrals. The values associated with the $*$ time level indicates the predicted value based on the predictor-corrector loop. For the case when the total or internal energy formulation is used, $b^* = 0$, and for the case when the temperature equation is used, it corresponds to the right-hand-side contribution of the temperature equation neglecting the thermal equilibration contribution.

For the anisotropic thermal conduction, spatial difference requires additional care to ensure that there are no numerical errors introduced from the misalignment of the finite

difference grid to the local magnetic field. Details of the spatial difference implementation for the anisotropic thermal conduction are discussed in Section 2.5. For the neutral thermal conductivity, the spatial difference can be taken trivially with the finite difference.

For the thermal equilibration, since there are no spatial differences, the thermal equilibration can be performed on each node without any coupling to its neighbors. For each node, the implicit thermal equilibration advance can be expressed as a linear equation of the following form:

$$\begin{pmatrix} 1+(\nu_{ei}^*+\nu_{ni}^*)\,\Delta t & -\nu_{ei}^*\Delta t & -\nu_{ni}^*\Delta t \\ -\nu_{ie}^*\Delta t & 1+(\nu_{ie}^*+\nu_{ne}^*)\,\Delta t & -\nu_{ne}^*\Delta t \\ -\nu_{in}^*\Delta t & -\nu_{en}^*\Delta t & 1+(\nu_{in}^*+\nu_{en}^*)\,\Delta t \end{pmatrix} \begin{pmatrix} T_i^{n+3/2} \\ T_e^{n+3/2} \\ T_n^{n+3/2} \end{pmatrix} = \begin{pmatrix} T_i^{***} \\ T_e^{***} \\ T_n^{***} \end{pmatrix} \tag{2.67}$$

The above 3×3 matrix equation can be inverted trivially for each node.

With the predictor-corrector advance for the species temperatures complete, total and internal energies can be updated to include contributions from the thermal conduction and equilibration. The final total energies are obtained as the followings:

$$\varepsilon^{n+1} = \varepsilon^{**} + \frac{kn^{n+1}}{\gamma-1}\left(T^{n+3/2} - T^{**}\right) \tag{2.68a}$$

$$\varepsilon_n^{n+1} = \varepsilon_n^{**} + \frac{kn_n^{n+1}}{\gamma-1}\left(T_n^{n+3/2} - T_n^{**}\right) \tag{2.68b}$$

While for the internal energy advance, the final pressures are obtained as the followings:

$$p^{n+1} = p^{**} + kn^{n+1}\left(T^{n+3/2} - T^{**}\right) \tag{2.69a}$$

$$p_n^{n+1} = p_n^{**} + kn_n^{n+1}\left(T_n^{n+3/2} - T_n^{**}\right) \tag{2.69b}$$

With this final step, the Cygnus time advance is completed, and steps are repeated until the simulation end time is reached.

2.4 Coupling of the External Circuit with the Plasma Dynamics

2.4.1 External Circuit Advance

The ability to couple external circuits to the plasma advance is by far the most important feature of Cygnus for FRC modelings. For typical problems, there are two possible general types of external circuits that can exist: one is the case when the output current is fixed as a function of time (the fixed case); the other is the case when the output voltage determines the output current (the active case). Since the fixed current case only introduces a background magnetic flux, Cygnus splits the problem into fixed and active problems using the superposition principle [28]. For the fixed case, the output current is set to a pre-determined value in the circuit advance to remove any noise introduced from other advances. For the active case, full coupling of the external circuits must be considered.

While the exact form of the external circuit advance for the active case cannot be specified without first specifying the external circuit, a general algorithm can be derived assuming that the circuit equation for the given external circuit is discretized implicitly in time using a backwards Euler algorithm and linearized. The linearized implicit circuit equation can be expressed generally in the matrix form as

$$\overleftrightarrow{\mathrm{M}}\mathbf{x}^{n+3/2} = \mathbf{b}^{n+1/2} - \overleftrightarrow{\mathrm{P}}\mathbf{I}_t^{n+3/2} \tag{2.70}$$

where $\overleftrightarrow{\mathrm{M}}$ is a matrix of the circuit coefficients, $\mathbf{x}$ is a vector of circuit unknowns (voltages and currents), $\mathbf{b}$ is a vector of known circuit quantities at the current time step, $\overleftrightarrow{\mathrm{P}}$ is a matrix of the circuit coefficients related with the circuit terminals to which the external segments connect, and $\mathbf{I}_t$ is a vector of the total currents flowing through the circuit terminals to which the external segments connect. The above system of equations is underdetermined, since the total current flowing through the terminals at the future time level is unknown at the time level where the circuit equation must be evaluated.

To remove the underdetermined nature of the system of circuit equations, a modified

equation of the form

$$\overleftrightarrow{\mathrm{M}}\mathbf{x}^{*} = \mathbf{b}^{n+1/2} - \overleftrightarrow{\mathrm{P}}\mathbf{I}_t^{n+1/2}$$

is considered. A modification to the original system of equations is made such that the unknown terminal currents are replaced with the known values at the current time level. The solution to the modified circuit equation is defined as $\mathbf{x}^{*}$. After some algebra, it can be shown that the solution at the time $n + 3/2$ can be defined as

$$\mathbf{x}^{n+3/2} = \mathbf{x}^{*} - \overleftrightarrow{\mathrm{Z}}\left(\mathbf{I}_t^{n+3/2} - \mathbf{I}_t^{n+1/2}\right) \tag{2.71}$$

where $\overleftrightarrow{\mathrm{Z}}$ is the impedance matrix defined to be

$$\overleftrightarrow{\mathrm{Z}} = \overleftrightarrow{\mathrm{M}}^{-1}\overleftrightarrow{\mathrm{P}} = -\frac{\left(\mathbf{x}^{n+3/2} - \mathbf{x}^{*}\right)\left(\mathbf{I}_t^{n+3/2} - \mathbf{I}_t^{n+1/2}\right)^{T}}{\left|\mathbf{I}_t^{n+3/2} - \mathbf{I}_t^{n+1/2}\right|^{2}}$$

Thus, given the total current flowing through the circuit terminals at the updated time, the circuit states at the updated time can also be determined.

In the subset of the circuit unknowns $\mathbf{x}$, one term that must be included is the voltage drop across all of the terminals ($\mathbf{V}_t$ for vector of all terminal voltages). Similar to other circuit unknowns, the voltage drop across the terminals at the updated time can be defined to be

$$\mathbf{V}_t^{n+3/2} = \mathbf{V}_t^{*} - \overleftrightarrow{\mathrm{Z}}_t\left(\mathbf{I}_t^{n+3/2} - \mathbf{I}_t^{n+1/2}\right) \tag{2.72}$$

where $\overleftrightarrow{\mathrm{Z}}_t$ is the square matrix subset of the impedance matrix $\overleftrightarrow{\mathrm{Z}}$ that corresponds to the voltage drop across the terminals. Since the voltage drop over the segment is associated with the magnetic flux on the segment with the Faraday's law, the above equation can be coupled with the resistive advance of the magnetic flux for the segments in order to solve the circuit equations implicitly with the coupled plasma dynamics.

To illustrate the circuit formulation discussed thus far with a simple example, consider

a case for an RLC circuit connected to the external segments. This simple system can be represented by a system of two differential equations given as

$$V_c - V_0 = RI_0 + L\frac{\mathrm{d}I_0}{\mathrm{d}t}$$
$$C\frac{\mathrm{d}V_c}{\mathrm{d}t} = -I_0$$

where V_c is the voltage drop over the capacitor, V_0 is the voltage drop over the terminal, I_0 is the total current through the terminal, and R, L, and C are the resistance, inductance, and capacitance, respectively. Discretizing the above equation implicitly in time, a matrix system of equations can be obtained to be the following:

$$\begin{bmatrix} -\Delta t & \Delta t \\ 0 & C \end{bmatrix} \begin{bmatrix} V_0^{n+3/2} \\ V_c^{n+3/2} \end{bmatrix} = \begin{bmatrix} -LI_0^{n+1/2} \\ CV_c^{n+1/2} \end{bmatrix} - \begin{bmatrix} -\left(R\Delta t + L\right) \\ \Delta t \end{bmatrix} I_0^{n+3/2}$$

It can be seen that the above equation has the same form as Eq. 2.70.

For the simple case of the RLC circuit, the analytical solution for $\mathbf{x}^*$ and $\overleftrightarrow{\mathrm{Z}}$ can be obtained exactly. Directly solving, one obtains that

$$\mathbf{x}^* = \begin{bmatrix} V_0^* \\ V_c^* \end{bmatrix} = \begin{bmatrix} V_c^{n+1/2} - \left(R + \Delta t/C\right) I_0^{n+1/2} \\ V_c^{n+1/2} - \left(\Delta t/C\right) I_0^{n+1/2} \end{bmatrix}$$

and

$$\overleftrightarrow{\mathrm{Z}} = \begin{bmatrix} R + L/\Delta t + \Delta t/C \\ \Delta t \end{bmatrix}$$

A subset of the above solution is a solution for the terminal voltage, which is given to be

$$V_0^{n+3/2} = V_0^* - Z_0\left(I_0^{n+3/2} - I_0^{n+1/2}\right)$$

where $Z_0 = R + L/\Delta t + \Delta t/C$. Note that for the simple example considered, only one terminal is present in the circuit. Thus, a scalar equation for the terminal voltage with a

scalar terminal impedance is obtained. This simple example shows how the general form of the circuit advance algorithm can be used to advance any user supplied external circuits.

2.4.2 Coupling of the External Circuits with the Segment Magnetic Flux

Recall that the external conductors are discretized into current carrying segments. From Faraday's law, the time change of magnetic flux over the external segments are given to be

$$\frac{\mathrm{d}\boldsymbol{\Psi}_s}{\mathrm{d}t} = \frac{1}{2\pi}\mathbf{V}_s \oslash \mathbf{N}_s \tag{2.74}$$

where $\boldsymbol{\Psi}_s$ is a vector of the external segment magnetic flux, $\mathbf{V}_s$ is a vector of the voltage drop across the segments, and $\mathbf{N}_s$ is a vector of the turn number for the segments. Note that $\overleftrightarrow{\mathrm{A}} \oslash \overleftrightarrow{\mathrm{B}}$ is a Hadamard (elementwise) division.

In order to couple the segment magnetic flux to the external circuits, the relationship for the voltage and circuit between the circuit terminals and segments must be made. Since the segments are connected in parallel to the circuit terminal, one can express the relationship between the circuit terminal and the external segment voltage as

$$\mathbf{V}_s = \overleftrightarrow{\mathrm{F}}_p \mathbf{V}_g - \mathbf{R}_s \circ \mathbf{I}_s \tag{2.75}$$

where $\overleftrightarrow{\mathrm{F}}_p$ is a parallel segment coupling matrix that maps the circuit terminal voltage associated with the segment to the segment voltage, $\mathbf{V}_g$ is a vector assembly of all of terminal voltages ($\mathbf{V}_t$) in all active circuits, $\mathbf{R}_s$ is a vector of segment resistivities, and $\mathbf{I}_s$ is a vector of segment currents. Note that $\overleftrightarrow{\mathrm{A}} \circ \overleftrightarrow{\mathrm{B}}$ is a Hadamard (elementwise) product.

Since the total current flowing in a circuit terminal is a sum of currents flowing in all parallel segments associated with the terminal normalized by the segment turn number, one can express the relationship between the circuit terminal and the external segment current as

$$\mathbf{I}_g = \overleftrightarrow{\mathrm{F}}_p^T \left(\mathbf{I}_s \oslash \mathbf{N}_s\right) \tag{2.76}$$

where $\overset{\leftrightarrow}{\mathrm{F}}_p^T$ is a transpose of the parallel segment coupling matrix defined previously and $\mathbf{I}_g$ is a vector assembly of all terminal currents ($\mathbf{I}_t$) in all active circuits.

Discretizing the Faraday's law for the segments implicitly in time and using the relationship between the segment and terminal voltages, one obtains

$$\frac{2\pi}{\Delta t}\Delta\mathbf{\Psi}_s \circ \mathbf{N}_s + \mathbf{R}_s \circ \mathbf{I}_s^{n+3/2} = \overset{\leftrightarrow}{\mathrm{F}}_p \mathbf{V}_g^{n+3/2} \tag{2.77}$$

where $\Delta\mathbf{\Psi}_s = \mathbf{\Psi}_s^{n+3/2} - \mathbf{\Psi}_s^{n+1/2}$ is a change in the segment flux. Using the result for the terminal voltage obtained by the circuit advance equation, one can define the following relationship from the global assembled active circuit quantities:

$$\mathbf{V}_g^{n+3/2} = \mathbf{V}_g^* - \overset{\leftrightarrow}{\mathrm{Z}}_g^* \left(\mathbf{I}_g^{n+3/2} - \mathbf{I}_g^{n+1/2}\right) \tag{2.78}$$

where $\overset{\leftrightarrow}{\mathrm{Z}}_g$ is the global impedance matrix, which is an assembly of all of the $\overset{\leftrightarrow}{\mathrm{Z}}_t$ from all of the external circuits in the system. Using this results for the active circuits, following advance equation for the segment magnetic flux can be obtained after some simplification:

$$\begin{aligned}\frac{2\pi}{\Delta t}\Delta\mathbf{\Psi}_s + \left[\mathrm{diag}\left(\mathbf{R}_s \oslash \mathbf{N}_s\right) + \left(\overset{\leftrightarrow}{\mathrm{F}}_p \overset{\leftrightarrow}{\mathrm{Z}}_g \overset{\leftrightarrow}{\mathrm{F}}_p^T\right) \oslash \left(\mathbf{N}_s \otimes \mathbf{N}_s\right)\right] \mathbf{I}_s^{n+3/2} \\ = \left[\overset{\leftrightarrow}{\mathrm{F}}_p \left(\mathbf{V}_g^* + \overset{\leftrightarrow}{\mathrm{Z}}_g \mathbf{I}_g^{n+1/2}\right)\right] \oslash \mathbf{N}_s\end{aligned} \tag{2.79}$$

where $\mathrm{diag}\left(\mathbf{d}\right)$ denotes a diagonal matrix with the diagonal entries defined by vector $\mathbf{d}$ and $\mathbf{A} \otimes \mathbf{B}$ denotes dyadic product.

The final task is to relate the currents to the magnetic flux to reduce the unknowns on the left-hand-side. Since there exists a linear relationship between the magnetic flux and current in the discretized system, one can assume that there exists a segment coupling matrix which relates the segment current to the segment magnetic flux with a following relationship:

$$\mathbf{I}_s = \overset{\leftrightarrow}{\mathrm{S}} \mathbf{\Psi}_s$$

where $\overleftrightarrow{\mathrm{S}}$ is the segment coupling matrix [28]. With this relationship, the implicit advance of the external magnetic flux with coupled active circuits can be expressed as the following:

$$\left\{\frac{2\pi}{\Delta t}\overleftrightarrow{\mathrm{I}}+\left[\mathrm{diag}\left(\mathbf{R}_s\oslash\mathbf{N}_s\right)+\left(\overleftrightarrow{\mathrm{F}}_p\overleftrightarrow{\mathrm{Z}}_g\overleftrightarrow{\mathrm{F}}_p^T\right)\oslash\left(\mathbf{N}_s\otimes\mathbf{N}_s\right)\right]\overleftrightarrow{\mathrm{S}}\right\}\boldsymbol{\Psi}_s^{n+3/2} = \left[\overleftrightarrow{\mathrm{F}}_p\left(\mathbf{V}_g^*+\overleftrightarrow{\mathrm{Z}}_g\mathbf{I}_g^{n+1/2}\right)\right]\oslash\mathbf{N}_s+\frac{2\pi}{\Delta t}\boldsymbol{\Psi}_s^{n+1/2} \quad (2.80)$$

Thus, given the definition of the segment coupling matrix, a complete coupled equation of the segment flux and the external circuit advance is obtained, and it can be coupled with the magnetic flux advance in the fluid domain.

Note that the above equation is rather complex to solve numerically, especially when it is coupled with the fluid domain. The above equation can be simplified significantly when few assumptions are made to the circuit. First, assume that all circuits in the system only contain a single terminal to which the segments can connect. This reduces the global impedance matrix to a diagonal matrix. Next, assume that the turn ratio for all segments connected in parallel are equal to each other. Under this assumption, there is only a single turn ratio associated with the terminal, and $\mathbf{N}_s=\overleftrightarrow{\mathrm{F}}_p\mathbf{N}_g$, where $\mathbf{N}_g$ is the vector assembly of the turn ratios associated with terminals.

With these two assumptions, the implicit advance of the external magnetic flux reduces to the following:

$$\left\{\frac{2\pi}{\Delta t}\overleftrightarrow{\mathrm{I}}+\left[\mathrm{diag}\left(\mathbf{R}_s\oslash\mathbf{N}_s\right)+\overleftrightarrow{\mathrm{F}}_p\,\mathrm{diag}\left(\mathbf{Z}_g\oslash\mathbf{N}_g\oslash\mathbf{N}_g\right)\overleftrightarrow{\mathrm{F}}_p^T\right]\overleftrightarrow{\mathrm{S}}\right\}\boldsymbol{\Psi}_s^{n+3/2} = \left[\overleftrightarrow{\mathrm{F}}_p\left(\mathbf{V}_g^*+\mathbf{Z}_g\circ\mathbf{I}_g^{n+1/2}\right)\right]\oslash\mathbf{N}_s+\frac{2\pi}{\Delta t}\boldsymbol{\Psi}_s^{n+1/2} \quad (2.81)$$

To further simplify the above equation, consider splitting the above equation to explicit and implicit advances. Assume that only the implicit contribution couple with the implicit resistive magnetic flux advance for the fluid domain. Since the segment resistance is typically small compared with the impedance associated with circuits, consider advancing the segment

resistance with an explicit advance rather than the implicit one, which reduces the coupling of the parallel segments in the implicit advance. Then, one obtains

$$\boldsymbol{\Psi}_s^* = \boldsymbol{\Psi}_s^{n+1/2} + \frac{\Delta t}{2\pi}\left[\overleftrightarrow{\mathrm{F}}_p\left(\mathbf{V}_g^* + \mathbf{Z}_g \circ \mathbf{I}_g^{n+1/2}\right) - \mathbf{R}_s \circ \mathbf{I}_s^{n+1/2}\right] \oslash \mathbf{N}_s \tag{2.82}$$

for the explicit advance and

$$\frac{2\pi}{\Delta t}\left(\boldsymbol{\Psi}_s^{n+3/2} - \boldsymbol{\Psi}_s^*\right) + \overleftrightarrow{\mathrm{F}}_p \operatorname{diag}\left(\mathbf{Z}_g \oslash \mathbf{N}_g \oslash \mathbf{N}_g\right)\overleftrightarrow{\mathrm{F}}_p^T \overleftrightarrow{\mathrm{S}}\, \boldsymbol{\Psi}_s^{n+3/2} = 0 \tag{2.83}$$

for the implicit advance.

The implicit advance can be further reduced by noting that after the splitting of the equation into the explicit and implicit advance, the unknown magnetic flux for parallel segments are redundant. This is due to the fact that under the simplifying assumptions, the change of flux in the parallel segments are all equal to each other, so $\Psi_s = \overleftrightarrow{F}_p \Psi_g$. Thus, the reduced implicit advance is given to be the following:

$$\left[\frac{2\pi}{\Delta t}\operatorname{diag}\left(\mathbf{N}_g \circ \mathbf{N}_g \oslash \mathbf{Z}_g\right) + \overleftrightarrow{\mathrm{F}}_p^T \overleftrightarrow{\mathrm{S}} \overleftrightarrow{\mathrm{F}}_p\right]\Delta\boldsymbol{\Psi}_g = -\overleftrightarrow{\mathrm{F}}_p^T \overleftrightarrow{\mathrm{S}} \overleftrightarrow{\mathrm{F}}_p \boldsymbol{\Psi}_g^* \tag{2.84}$$

where $\boldsymbol{\Psi}_s^{n+3/2} = \boldsymbol{\Psi}_s^* + \overleftrightarrow{\mathrm{F}}_p \Delta\boldsymbol{\Psi}_g$. The above equation is Hermitian symmetric, and it is generally far simpler to solve than the original equation [28].

2.4.3 Derivation of Segment Coupling Matrix

To derive the segment coupling matrix, consider a variational formulation of the azimuthal current density, given to be

$$J_\phi(r,z) = -\frac{1}{\mu_0}\frac{1}{r}\Delta^*\Psi = \frac{\delta W}{\delta \Psi} \tag{2.85}$$

where

$$W = \frac{1}{2}\int J_\phi \Psi \, \mathrm{d}A = \frac{1}{\mu_0}\left[\int_{\Omega_{int}} \frac{1}{r}\left|\boldsymbol{\nabla}\Psi\right|^2 \, \mathrm{d}A + \int_{\Omega_{ext}} \frac{1}{r}\left|\boldsymbol{\nabla}\Psi\right|^2 \, \mathrm{d}A\right]$$

where W is the total magnetic energy, Ω_{int} is the fluid domain, and Ω_{ext} is the external vacuum domain in the rz-plane [62]. It can be seen from the construction of the variational formulation that a form of equation $\mathbf{I}_s = \overleftrightarrow{\mathrm{S}}\boldsymbol{\Psi}_s$ with a Hermitian symmetric operator $\overleftrightarrow{\mathrm{S}}$ can be obtained with a suitable spatial discretization of the variational formulation [28].

In the external region, a general solution for Ψ is given to be

$$\Psi\left(r,z\right) = \frac{\mu_0}{4\pi}\int_{\Omega_{ext}} J_\phi\left(r',z'\right) G_D\left(r,z;r',z'\right) \, \mathrm{d}A' - \frac{1}{4\pi}\oint_{\partial\Omega_{ext}} \frac{1}{r'}\Psi_D\left(r',z'\right)\frac{\partial G_D}{\partial n'}\mathrm{d}l'$$

where G_D is a Green's function for the given domain Ω_{ext} with a boundary condition satisfied in the boundary of the Ω_{ext} domain ($\partial\Omega_{ext}$), and Ψ_B is the value of the magnetic flux on the boundary Unfortunately, the form of G_D is not known in general for an arbitrary fluid domain boundary.

Instead, Green's reciprocity theorem can be considered to obtain a general solution for the magnetic energy for any arbitrary axisymmetric geometry. The Green's reciprocity theorem is given to be

$$\int_\Omega \left(\Psi J'_\phi - \Psi' J_\phi\right) \, \mathrm{d}A = -\frac{1}{\mu_0}\oint_{\partial\Omega}\left(\Psi B'_t - \Psi' B_t\right) \, \mathrm{d}l$$

where B_t is the tangent magnetic field on the boundary $\partial\Omega$. Let the unprimed system be the original system with the fluid domain and external domain, and the primed system to be the transformed system with the same domain geometry as the original system, but with the currents in the plasma domain equal to zero ($J'_\phi = 0 \in \Omega_{int}$). The primed system is assumed to have the same magnetic structure in the external domain as the original unprimed system ($\Psi' = \Psi \in \Omega_{ext}$ and $B'_t|_{\partial\Omega_{ext}} = B_t|_{\partial\Omega_{ext}}$).

Using the Green's theorem, the contribution to the total magnetic energy due to the

external domain can be expressed as

$$\begin{aligned} W_{ext} &= \frac{1}{2\mu_0}\int_{\Omega_{ext}} \frac{1}{r}\left|\boldsymbol{\nabla}\Psi_{ext}\right|^2 \,\mathrm{d}A \\ &= \frac{1}{2}\int_{\substack{all\\space}} \Psi_{ext}J^* \,\mathrm{d}A - \frac{1}{2}\oint_{\partial\Omega_{ext}} \Psi_{ext}\left(K'_\phi + \frac{1}{\mu_0}B_t\right)\,\mathrm{d}l \end{aligned} \tag{2.86}$$

where K'_ϕ is a surface current density on the boundary $\partial\Omega_{ext}$ and J^* is the current density in all space in the primed system, including the surface current density K'_ϕ. Note that the first integral on the right-hand-side has been extended to all space using the fact that $J^* = 0$ in the fluid region. Mathematically, J^* can be expressed as

$$J^*\left(r,z\right) = J'_\phi\left(r,z\right) + K'_\phi\left(r,z\right)S_K\left(r,z\right) \tag{2.87}$$

where

$$S_K\left(r,z\right) = \begin{cases} 1 & \in \partial\Omega_{ext} \\ 0 & \text{otherwise} \end{cases}$$

In the primed system, the currents everywhere in space is defined by J^*. Thus, the solution to the magnetic flux in the external region (Ψ_{ext}) can be defined in terms of the well-known vacuum magnetostatics Green's function in the axisymmetric geometry as

$$\Psi_{ext}\left(r,z\right) = \frac{\mu_0}{4\pi}\int J^*\left(r',z'\right)\tilde{G}\left(r,z;r',z'\right)\,\mathrm{d}A' \tag{2.88}$$

where $\tilde{G}$ is a Green's function for the vacuum magnetostatics in the axisymmetric geometry defined to be

$$\tilde{G}\left(r,z;r',z'\right) = \sqrt{\left(r+r'\right)^2 + \left(z-z'\right)^2}\left[\left(2-k^2\right)K\left(k\right) - 2E\left(k\right)\right] \tag{2.89}$$

where

$$k^2 = \frac{4rr'}{\left(r+r'\right)^2 + \left(z-z'\right)^2}$$

and $K(k)$ and $E(k)$ are the complete elliptic integral of the first and the second kind, respectively.

In the primed system, an additional care is required in defining B_t because of the boundary surface current K'_ϕ. Using the interface condition, the surface magnetic field can be defined in terms of the vacuum magnetics Green's function and the surface current as

$$B_t = \frac{\mu_0}{4\pi} \int J^*(r', z') \frac{\partial \tilde{G}}{\partial n'} \, \mathrm{d}A' - \frac{1}{2}\mu_0 K'_\phi \tag{2.90}$$

where the direction of the normal vector is defined from the fluid domain to the external domain. With the solution of Ψ_{ext} and B_t obtained in terms of the Green's function and the variables in the primed system, the solution for the magnetic energy in the exterior region can be obtained to be

$$W_{ext} = \frac{\mu_0}{8\pi} \Bigg\{ \iint \left[J^*(r,z) J^*(r',z') - \frac{1}{2} K'_\phi(r,z) J^*(r',z') S_K(r,z) \right] \tilde{G}(r,z;r',z') \, \mathrm{d}A' \, \mathrm{d}A \\ - \oint_{\partial\Omega_{ext}} \frac{\Psi}{\mu_0} \int J^*(r',z') \frac{1}{r} \frac{\partial \tilde{G}}{\partial n} \, \mathrm{d}A' \, \mathrm{d}l \Bigg\} \tag{2.91}$$

The final task is to discretize the current and flux on the segments to obtain a discretized system of equations for magnetic energy. The current density J^* is discretized assuming a constant current density on each segment such that

$$J^*(r,z) = \sum_\alpha I^*_\alpha S_\alpha(r,z) \tag{2.92}$$

where

$$S_\alpha(r,z) = \begin{cases} 1 & \text{on } \alpha\text{-th segment} \\ 0 & \text{otherwise} \end{cases}$$

and I^*_α is the current flowing in the segment α in the primed system.

The expression for the discretized magnetic flux in the segments can be obtained using

the mutual inductance matrix as

$$\Psi_\alpha = \sum_\beta M_{\alpha\beta} I^*_\beta \tag{2.93}$$

where $M_{\alpha\beta}$ is a mutual inductance of segment α and β defined to be

$$M_{\alpha\beta} = \frac{\mu_0}{4\pi} \frac{1}{l_\alpha l_\beta} \iint \tilde{G}\left(r, z; r', z'\right) \, \mathrm{d}l \, \mathrm{d}l' \tag{2.94}$$

where l_α and l_β are the length of the segment α and β, respectively [28].

Finally, the spatially discretized expression for the external magnetic energy is obtained to be

$$W_{ext} = \frac{1}{2} \Psi_\alpha M^{-1}_{\beta\gamma} \left[\delta_{\alpha\gamma} - \eta_{\alpha\sigma} \left(K_{\sigma\gamma} + \frac{1}{2} \delta_{\sigma\gamma} \right) \right] \Psi_\beta \tag{2.95}$$

where $\delta_{\alpha\beta}$ is the the Kronecker delta and Einstein summation convention is assumed in the above equation. The two matrices $K_{\alpha\beta}$ and $\eta_{\alpha\beta}$ are defined to be

$$K_{\alpha\beta} = \frac{\mu_0}{4\pi} \frac{1}{l_\alpha l_\beta} \iint \frac{\partial \tilde{G}}{\partial n} \, \mathrm{d}l \, \mathrm{d}l' \tag{2.96}$$

and

$$\eta_{\alpha\beta} = \begin{cases} \delta_{\alpha\beta} & \alpha \text{ is boundary segment} \\ 0 & \text{otherwise} \end{cases}$$

Taking the variation of W_{ext} with respect to Ψ, the explicit form of the segment coupling matrix $\overleftrightarrow{\mathrm{S}}$ can be obtained to be

$$S_{\alpha\beta} = \frac{1}{2} \left\{ M^{-1}_{\beta\gamma} \left[\delta_{\alpha\gamma} - \eta_{\alpha\sigma} \left(K_{\sigma\gamma} + \frac{1}{2} \delta_{\sigma\gamma} \right) \right] + \left[\delta_{\gamma\alpha} - \left(K_{\gamma\sigma} + \frac{1}{2} \delta_{\gamma_\sigma} \right) \eta_{\sigma\alpha} \right] M^{-1}_{\gamma\beta} \right\} \tag{2.97}$$

where the Einstein summation convention is assumed in the above equation. It can be seen from the structure of the segment coupling matrix that it is indeed Hermitian symmetric.

2.5 Anisotropic Thermal Conduction and Viscous Velocity Transport

The anisotropic thermal conductions for ions and electrons require additional numerical cares to deal with the strong anisotropy that exists. For both ions and electrons, the thermal conduction problem is given as

$$\frac{n_\alpha k}{\gamma - 1}\frac{\partial T_\alpha}{\partial t} = -\boldsymbol{\nabla}\cdot\mathbf{q}_\alpha + b_\alpha \tag{2.98}$$

where

$$\mathbf{q}_\alpha = -\left[\left(\chi_\parallel^\alpha - \chi_\perp^\alpha\right)\frac{\mathbf{BB}}{|\mathbf{B}|^2} + \chi_\perp^\alpha \overleftrightarrow{\mathrm{I}}\right]\cdot\boldsymbol{\nabla}T_\alpha$$

and $\chi_\parallel$ and $\chi_\perp$ are the parallel and perpendicular thermal conductivity, respectively. The term b_α represents the additional terms in the temperature equation of species α.

As discussed by Gunter et al. [63], when a naive finite difference implementation of the anisotropic thermal conduction operator is taken (asymmetric scheme), one obtains significant pollution in the perpendicular direction from the numerical errors caused by the parallel direction. To fix this issue, Gunter proposes a symmetric finite difference approach which minimizes the errors introduced by the parallel to the perpendicular direction. With the symmetric scheme, a finite difference of $\boldsymbol{\nabla}\cdot\mathbf{q}$ at node (i, j) is defined based on the heat flux vector $\mathbf{q}$ defined at a staggered node $(i \pm 1/2, j \pm 1/2)$, which is located at the center of the four cells surrounding the node (i, j). The heat flux at the staggered node is computed using the four nodes associated with the cell on which the staggered node is located. Gunter reports positive results for anisotropic thermal conduction with this approach, and accuracies equivalent or better than that of the higher-order finite element method of the NIMROD code is reported.

While the application of the Gunter's symmetric finite difference approach is possible, numerical testings suggested issues associated with the numerical instability for typical FRC formation and translation problems. This is caused by the existence of a region with a large and rapid magnetic change. The location of the staggered node on which the cell-

based quantities are computed becomes highly important, as the normalized magnetic field vector direction may vary significantly over a cell in a single time step. This introduces high frequency noise of significant local magnitude, and in the explicit portion of the energy advance, such rapid local variation in temperature can lead to highly prohibitive CFL time-step conditions.

While the rapid local variation of the magnetic direction vector can be reduced by using cell averaged quantities or through the judicious choice of flux limiting, when the final finite difference divergence of the heat flux vector is taken, one cannot ensure that the local finite difference approximation remains stable. This is due to the fact that such stabilizing method is typically applied over a cell where the heat flow vectors are computed for the symmetric differencing approach. Even when a reasonable approximation of the heat flow vector is made over the cell, one cannot ensure that collection of four cells for every node in the domain results in well behaving finite difference of the divergence operator. This is especially problematic near the axis where the axis symmetry conditions are enforced for the cylindrical coordinate. As such, near challenging magnetic field regions, numerical instability may develop and cause the code to become unreliable.

2.5.1 Hybrid Finite Difference/Finite Element Implementation of the Thermal Conduction

As an alternative to the finite difference approach, Barnes developed a hybrid Finite Difference/Finite Element implementation of the anisotropic thermal conduction for Cygnus [28]. A finite element formulation allows continuous functions to represent magnetic field and temperature, which largely avoids the issue of the finite difference case where the selection of the approximation location causes significant change in the obtained solution. On the other hand, converting the entire code already written with a finite difference scheme is no trivial task. Thus, by using a hybrid scheme, the anisotropic terms can be handled with finite elements to take advantage of the improved spatial representation, while the remaining terms can be handled using the existing finite difference method.

To obtain a finite element representation of the heat equation given in Eq. 2.98, first,

a variational form of the heat equation is constructed. To obtain the variational form of the problem, multiply both side of Eq. 2.98 by a test function T^* and perform a volume integration to obtain

$$\int_V T^* \left[\frac{nk}{\gamma - 1} \frac{\partial T}{\partial t} - b \right] \mathrm{d}V = \int_V \mathbf{q} \cdot \boldsymbol{\nabla} T^* \, \mathrm{d}V \tag{2.99}$$

where

$$\int_V \mathbf{q} \cdot \boldsymbol{\nabla} T^* \, \mathrm{d}V = - \int_V \left[\frac{\chi_{\parallel} - \chi_{\perp}}{B^2} \left(\mathbf{B} \cdot \boldsymbol{\nabla} T^* \right) \left(\mathbf{B} \cdot \boldsymbol{\nabla} T \right) + \chi_{\perp} \left(\boldsymbol{\nabla} T^* \right) \cdot \left(\boldsymbol{\nabla} T \right) \right] \mathrm{d}V$$

Note that the subscript α has been dropped from the above equation. In the above equation, a Dirichlet boundary condition has been assumed for the temperature.

In order to remove the left-hand-side of Eq. 2.99 from the finite element discretization, one can consider applying a "mass lumping" procedure to the left-hand-side to essentially diagonalize the left-hand-side terms to nodal quantities with no cross-couplings to other nodes in the finite element context. Note that the left-hand-side term can be expressed as the following:

$$\frac{1}{2\pi} \int_V T^* \left[\frac{nk}{\gamma - 1} \frac{\partial T}{\partial t} - b \right] \mathrm{d}V = \iint T^* \left[\frac{nk}{\gamma - 1} \frac{\partial T}{\partial t} - b \right] r \, \mathrm{d}r \, \mathrm{d}z \tag{2.100}$$

One can see from the structure of Eq. 2.100 that after the basis function is defined and the variation with respect to the nodal T^* is taken, when all of the local contributions from the finite elemental matrices are assembled into the global matrix, the sum of the local matrices for each nodes essentially represents a numerically approximated nodal volume integrated contribution to the nodal temperature advance. As such, it is not unreasonable to approximate the above equation with a diagonal "mass lumping" such that when a variation with respect to the nodal T^* is taken, one obtains

$$\frac{\delta}{\delta T^*_\alpha} \left\{ \frac{1}{2\pi} \int_V T^* \left[\frac{nk}{\gamma - 1} \frac{\partial T}{\partial t} - b \right] \mathrm{d}V \right\} \approx V_\alpha F_\alpha \tag{2.101}$$

for the α-th node, where V_α is the effective nodal volume for the α-th node and F_α represents the finite difference approximation to the left-hand-side contribution for the α-th node.

Now consider the right-hand-side term of Eq. 2.99. In order to make further progress, a finite element discretization must be introduced. Since a rectangular grid from the finite difference method already exists, a 4-node rectangular element can be introduced to define the problem domain. Defining an areal coordinate, $a = r^2/2$, following four basis functions can be defined [28]:

$$\varphi_0(a,z) = N_0(a)N_1(z) \tag{2.102a}$$

$$\varphi_1(a,z) = N_3(a)N_1(z) \tag{2.102b}$$

$$\varphi_2(a,z) = N_0(a)N_2(z) \tag{2.102c}$$

$$\varphi_3(a,z) = N_3(a)N_2(z) \tag{2.102d}$$

where

$$N_0(a) = \frac{a_1 - a}{\Delta a} \tag{2.102e}$$

$$N_1(z) = \frac{z_1 - z}{\Delta z} \tag{2.102f}$$

$$N_2(z) = \frac{z - z_0}{\Delta z} \tag{2.102g}$$

$$N_3(a) = \frac{a - a_0}{\Delta a} \tag{2.102h}$$

where $\Delta a = a_1 - a_0$ and $\Delta z = z_1 - z_0$. With these basis functions, the temperature over the element can be expressed as the following:

$$T = \sum_{i=0}^{3} T_i \varphi_i \tag{2.103}$$

Since the azimuthal gradient is zero for an axisymmetric problem, there are no contribution from the azimuthal magnetic field in the vector terms. Thus, it is convenient to replace $\mathbf{B}$

in terms of the magnetic flux Ψ to obtain:

$$(\mathbf{B}\cdot\boldsymbol{\nabla}T^*)(\mathbf{B}\cdot\boldsymbol{\nabla}T) = \left(\frac{\partial\Psi}{\partial a}\frac{\partial T^*}{\partial z} - \frac{\partial\Psi}{\partial z}\frac{\partial T^*}{\partial a}\right)\left(\frac{\partial\Psi}{\partial a}\frac{\partial T}{\partial z} - \frac{\partial\Psi}{\partial z}\frac{\partial T}{\partial a}\right) \tag{2.104}$$

Note that the same basis function as the temperature is used for the magnetic flux [28].

With the finite element discretization defined, the right-hand-side terms of Eq. 2.99 can be integrated locally over a cell, and the variation can be taken to generate a linear system of equations for the local nodes. Then the local matrices are assembled into a global matrix to solve with the finite differenced left-hand-side terms. The obtained integrals are simple to evaluate with the exception of the denominator term B^2. To simplify the problem of performing the exact integral, note that the heat conduction contributions are obtained by a linear first order differential operator on the temperature. As found by Barnes, one can replace the accurate description of $\left(\chi_\parallel - \chi_\perp\right)/B^2$ (and similarly $\chi_\perp$ term) by a constant value over the cell of interest without introducing additional errors that may change the spatial error order of the numerical approach [28]. As such, terms dependent on the thermal conductivities can be pulled out of the integral and the remaining terms can be integrated exactly.

One difficulty with this approach, as discovered by Barnes, is that when an "incorrect" value of B^2 is used in the denominator, it becomes possible that the magnitude of the local finite element representation of $\mathbf{BB}/B^2$ becomes greater than unity in certain region of the cell when there are large gradient in the magnetic field over the cell. As such, a negative diffusive behavior may be introduced due to the presence of the negative eigenvalues associated with the perpendicular conductivity operator [28].

The solution by Barnes for this problem is to use the maximum value of B^2 over the cell of interest. By using the maximum magnitude over the cell element, this ensures that the locally varying magnetic field direction vector and its average over the cell are always less than or equal to unity [28]. In practice, this can be achieved by maximizing the following

function:

$$B^2 = \left|\frac{\partial \Psi}{\partial a}\right|^2 + \frac{1}{2a}\left|\frac{\partial \Psi}{\partial z}\right|^2 + B_\phi^2 \tag{2.105}$$

In Eq. 2.105, the first term on the right-hand-side is independent of a and second term is independent of z, when the finite element defined in Eq. 2.102 is used. As such, if the azimuthal component can be neglected, the maximum magnetic field magnitude over the cell can be obtained exactly by maximizing the first two terms independently and summing the maximum of the two terms [28]. However, the presence of the azimuthal component makes the maximization difficult, as it contains terms with products of a and z.

In order to circumvent this complexity in computing the maximum magnetic field magnitude, one can note that the purpose of maximizing the magnetic field magnitude over the cell is simplify for numerical stability. This goal can be achieved if the approximated magnetic field magnitude is greater than or equal to the exact maximum value over the cell. Since the sum of the maximum of the magnetic field components are always greater than or equal to the exact maximum of the magnetic field magnitude, one can replace the maximum value of the magnetic field with the maximum of each components such that

$$\max\left(B^2\right) \leq \max\left(\left|\frac{\partial \Psi}{\partial a}\right|^2\right) + \max\left(\frac{1}{2a}\left|\frac{\partial \Psi}{\partial z}\right|^2\right) + \max\left(B_\phi^2\right) \tag{2.106}$$

The above equation is numerically simpler to evaluate and, in the case, when $B_\phi = 0$ in the cell, the above expression is exactly equal to the maximum magnetic field magnitude over the cell.

With this modification, the finite element representation of the left-hand-side contribution of Eq. 2.99 can be defined fully. By combining the left-hand-side contribution defined using the finite element method with the right-hand-side contribution defined using the finite difference method, the combined hybrid finite element/finite difference formulation of the anisotropic heat equation can be obtained. Numerical testings by Barnes showed good results using the hybrid approach even in regions with large magnetic field gradients [28].

2.5.2 Hybrid Finite Difference/Finite Element Implementation of the Anisotropic Viscosity

In the process of implementing the plasma-neutral model of Meier and Shumlak, an anisotropic plasma viscosity was also implemented to improve the transport physics. To implement the anisotropic plasma viscosity, Barnes' hybrid finite difference/finite element implementation of the anisotropic thermal conduction is extended for anisotropic viscous stress tensor. Again, one starts with a variational formulation to derive a finite element representation. To obtain a variational formulation of the velocity equation, one can consider the virtual power principle for the fluid mechanics [64]. Using the virtual power principle, the variational form of the velocity equation is given to be

$$\int_V \mathbf{u}^* \left(mn \frac{\partial \mathbf{u}}{\partial t} - \mathbf{b} \right) \mathrm{d}V = \int_V (\boldsymbol{\nabla} \mathbf{u}^*) : \overleftrightarrow{\Pi} \, \mathrm{d}V \tag{2.107}$$

where $\mathbf{u}^*$ is the virtual velocity and $\mathbf{b}$ is the generalized body force. In the above equation, a Dirichlet boundary condition is assumed for the velocity, and the hydrostatic pressure contribution to the full pressure stress tensor has been included in the generalized body force $\mathbf{b}$. It can be seen that when the variation of the above equation with respect to the virtual velocity is taken, the original fluid velocity equation is obtained.

As it has been written, the right-hand-side of Eq. 2.107 contains a "stiffness matrix" associated with the anisotropic viscosity. The left-hand-side contains all terms from the velocity advance equation that are implemented in Cygnus with a finite difference discretization. While it is possible to obtain a full finite element formulation of the velocity advance from the variational formulation, since the finite difference implementation of the velocity equation without the anisotropic viscosity already exists, it is desirable to take advantage of the existing code. Implementing a full finite element implementation of the velocity advance requires complete rewriting of the velocity advance algorithms, and it may also introduce additional issues that are not present with the current finite difference implementation (e.g. ensuring upstream differencing in fluid advection, etc.).

In order to remove the left-hand-side of Eq. 2.107 from the finite element discretization,

one can consider applying a "mass lumping" procedure to the left-hand-side to remove nodal cross-couplings in the finite element approximation. Note that this does not mean that the left-hand-side is made fully diagonal, as the finite difference implementation may introduce an additional nodal coupling (e.g. isotropic viscosity, semi-implicit operators, etc.). Since the finite difference left-hand-side has a block diagonal structure with respect to the coordinate direction, in order to make the finite element formulation compatible with the existing implementation, the radial, azimuthal, and axial components must be treated separately in the finite element.

For the radial and azimuthal components, the left-hand-side is expressed as the following:

$$\frac{1}{2\pi}\int_V u^*_{r,\phi}\left(mn\frac{\partial u_{r,\phi}}{\partial t}-b_{r,\phi}\right)\,\mathrm{d}V=\iint\left(ru^*_{r,\phi}\right)\left[\frac{mn}{r}\frac{\partial}{\partial t}\left(ru_{r,\phi}\right)-b_{r,\phi}\right]\,\mathrm{d}r\,\mathrm{d}z \tag{2.108}$$

For the radial and azimuthal components, velocity unknowns in the finite difference implementation use flux quantities (radius times velocity). It can be seen from Eq. 2.108 that when the finite element implementation is carried out and the system of equations is converted into a numerical system, the above contribution for a node essentially represents a numerically approximated nodal area integrated contribution to the nodal velocity advance. As such, it is not unreasonable to approximate the above equation with a diagonal "mass lumping" such that when a variation with respect to the nodal virtual velocity is taken, one obtains

$$\frac{\delta}{\delta\left(ru^*_{r,\phi}\right)_\alpha}\left[\frac{1}{2\pi}\int_V u^*_{r,\phi}\left(mn\frac{\partial u_{r,\phi}}{\partial t}-b_{r,phi}\right)\,\mathrm{d}V\right]\approx A_\alpha F^{r,\phi}_\alpha \tag{2.109}$$

for the α-th node, where A_α is the effective nodal area for the α-th node and $F^{r,\phi}_\alpha$ represents the finite difference approximation of the left-hand-side contribution for the α-th node.

Similarly, for the axial component, the left-hand-side is expressed as the following:

$$\frac{1}{2\pi}\int_V u^*_z\left(mn\frac{\partial u_z}{\partial t}-b_z\right)\,\mathrm{d}V=\iint u^*_z\left(mn\frac{\partial u_z}{\partial t}-b_z\right)r\,\mathrm{d}r\,\mathrm{d}z \tag{2.110}$$

Similar to the radial and azimuthal case, when the finite element implementation of Eq. 2.110

is carried out and the system of equations is converted into a numerical system, the above contribution for a node essentially represents a numerically approximated nodal volume integrated contribution to the nodal velocity advance. As such, it is not unreasonable to approximate the above equation with a diagonal "mass lumping" such that when a variation with respect to the nodal virtual velocity is taken, one obtains

$$\frac{\delta}{\delta\left(u_z^*\right)_\alpha}\left[\frac{1}{2\pi}\int_V u_z^*\left(mn\frac{\partial u_z}{\partial t}-b_z\right)\,\mathrm{d}V\right]\approx V_\alpha F_\alpha^z \tag{2.111}$$

for the α-th node, where F_α^z represents the finite difference approximation to the left-hand-side contribution for the α-th node.

Now consider the right-hand-side stiffness term of Eq. 2.107. First, the non-gyroviscous contribution can be expanded into the following form:

$$(\boldsymbol{\nabla}\mathbf{u}^*):\overleftrightarrow{\Pi}_c=-\sum_{i=1}^{5}\tilde{\eta}_i F_i \tag{2.112}$$

where

$$\begin{aligned}
\tilde{\eta}_1&=\eta_1\\
\tilde{\eta}_2&=(\eta_0-\eta_1)\left|\hat{\mathbf{b}}\right|^2+\eta_1\\
\tilde{\eta}_3&=\frac{\eta_1-\eta_0}{B^2}\\
\tilde{\eta}_4&=\frac{\eta_2-\eta_1}{B^2}\\
\tilde{\eta}_5&=\frac{3\eta_0+\eta_1-4\eta_2}{B^4}
\end{aligned}$$

$$\begin{aligned}
F_1&=(\boldsymbol{\nabla}\mathbf{u}^*):(\boldsymbol{\nabla}\mathbf{u})+(\boldsymbol{\nabla}\mathbf{u}^*):(\boldsymbol{\nabla}\mathbf{u})^T-(\boldsymbol{\nabla}\cdot\mathbf{u}^*)(\boldsymbol{\nabla}\cdot\mathbf{u})\\
F_2&=\frac{1}{3}(\boldsymbol{\nabla}\cdot\mathbf{u}^*)(\boldsymbol{\nabla}\cdot\mathbf{u})\\
F_3&=(\boldsymbol{\nabla}\cdot\mathbf{u}^*)[(\mathbf{BB}):(\boldsymbol{\nabla}\mathbf{u})]+(\boldsymbol{\nabla}\cdot\mathbf{u})[(\mathbf{BB}):(\boldsymbol{\nabla}\mathbf{u}^*)]\\
F_4&=[(\boldsymbol{\nabla}\mathbf{u}^*)\cdot\mathbf{B}]\cdot[(\boldsymbol{\nabla}\mathbf{u})\cdot\mathbf{B}]+[\mathbf{B}\cdot(\boldsymbol{\nabla}\mathbf{u}^*)]\cdot[\mathbf{B}\cdot(\boldsymbol{\nabla}\mathbf{u})]+[(\boldsymbol{\nabla}\mathbf{u}^*)\cdot\mathbf{B}]\cdot[\mathbf{B}\cdot(\boldsymbol{\nabla}\mathbf{u})]\\
&\quad+[\mathbf{B}\cdot(\boldsymbol{\nabla}\mathbf{u}^*)]\cdot[(\boldsymbol{\nabla}\mathbf{u})\cdot\mathbf{B}]
\end{aligned}$$

$$F_5 = [(\mathbf{BB}) : (\boldsymbol{\nabla}\mathbf{u}^*)]\,[(\mathbf{BB}) : (\boldsymbol{\nabla}\mathbf{u})]$$

Next, the gyroviscous contribution can be expanded into the following form:

$$(\boldsymbol{\nabla}\mathbf{u}^*) : \overleftrightarrow{\Pi}_g = -\sum_{i=6}^{7} \tilde{\eta}_i F_i \tag{2.114}$$

where

$$\tilde{\eta}_6 = \frac{1}{2}\frac{\eta_3}{B}$$
$$\tilde{\eta}_7 = \frac{1}{2}\frac{2\eta_4 - \eta_3}{B^3}$$
$$F_6 = \left(\overleftrightarrow{\mathrm{G}}_1 \times \mathbf{B}\right) : \overleftrightarrow{\mathrm{I}}$$
$$F_7 = \left(\overleftrightarrow{\mathrm{G}}_2 \times \mathbf{B}\right) : \overleftrightarrow{\mathrm{I}}$$

$$\overleftrightarrow{\mathrm{G}}_1 = (\boldsymbol{\nabla}\mathbf{u}) \cdot (\boldsymbol{\nabla}\mathbf{u}^*) + (\boldsymbol{\nabla}\mathbf{u})^T \cdot (\boldsymbol{\nabla}\mathbf{u}^*) + (\boldsymbol{\nabla}\mathbf{u}) \cdot (\boldsymbol{\nabla}\mathbf{u}^*)^T + (\boldsymbol{\nabla}\mathbf{u})^T \cdot (\boldsymbol{\nabla}\mathbf{u}^*)^T$$

$$\overleftrightarrow{\mathrm{G}}_2 = [\mathbf{B} \cdot (\boldsymbol{\nabla}\mathbf{u})]\,[\mathbf{B} \cdot (\boldsymbol{\nabla}\mathbf{u}^*)] + [(\boldsymbol{\nabla}\mathbf{u}) \cdot \mathbf{B}]\,[(\boldsymbol{\nabla}\mathbf{u}^*) \cdot \mathbf{B}] + [\mathbf{B} \cdot (\boldsymbol{\nabla}\mathbf{u})]\,[(\boldsymbol{\nabla}\mathbf{u}^*) \cdot \mathbf{B}]$$
$$+ [(\boldsymbol{\nabla}\mathbf{u}) \cdot \mathbf{B}]\,[\mathbf{B} \cdot (\boldsymbol{\nabla}\mathbf{u}^*)]$$

In order to make further progress, a finite element discretization must be introduced. Using the basis functions introduced in Eq. 2.102, the velocities and the magnetic fields over the element can be expressed as the following:

$$u_r = \frac{1}{\sqrt{2a}} \sum_{i=0}^{3} (r u_r)_i \, \varphi_i(a, z)$$
$$u_\phi = \frac{1}{\sqrt{2a}} \sum_{i=0}^{3} (r u_\phi)_i \, \varphi_i(a, z)$$
$$u_z = \sum_{i=0}^{3} (u_z)_i \, \varphi_i(a, z)$$
$$B_r = \frac{1}{\sqrt{2a}} \left[N_0(a) \left(\frac{d_0}{\Delta z} \right) + N_3(a) \left(\frac{d_3}{\Delta z} \right) \right]$$
$$B_\phi = \frac{1}{\sqrt{2a}} \sum_{i=0}^{3} (r B_\phi)_i \, \varphi_i(a, z)$$

$$B_z = N_1(z)\left(\frac{d_1}{\Delta a}\right) + N_2(z)\left(\frac{d_2}{\Delta a}\right)$$

where

$$d_0 = \Psi_0 - \Psi_2$$
$$d_1 = \Psi_1 - \Psi_0$$
$$d_2 = \Psi_3 - \Psi_2$$

and

$$d_3 = \Psi_1 - \Psi_3$$

Note that the flux variable has been used for the radial and azimuthal direction in order to retain compatibility with the finite difference formulation.

As it is written, at the axis where $a_0 = 0$, the finite element representation looks as if it is divergent. However, one can use the axial symmetry condition to remove the divergence on the axis. Thus, when $a_0 = 0$, $(ru_r)_0 = (ru_r)_2 = (ru_\phi)_0 = (ru_\phi)_2 = (rB_\phi)_0 = (rB_\phi)_2 = d_0 = 0$. It can be shown relatively easily that when the axial symmetry condition is applied to the above finite element representation, the divergence at the axis is removed from the finite element representation.

With the finite element discretization defined, the right-hand-side terms of Eq. 2.107 can be integrated locally over a cell, and then the variation can be taken to generate a linear system of equations. Then the local matrix can be assembled into a global matrix to solve with the finite differenced left-hand-side terms. Taking the integral of the right-hand-side, one obtains

$$\int_V (\boldsymbol{\nabla}\mathbf{u}^*) : \overleftrightarrow{\Pi}\, \mathrm{d}V = -\sum_{i=1}^{7} \int_V \eta_i F_i \, \mathrm{d}V \tag{2.118}$$

where the volume integral is now over a single finite element cell.

The above integral in Eq. 2.118 is rather difficult to solve exactly due to the nonlinearities in the terms in front of the F_i terms (viscosities and terms with inverse magnetic field magnitudes). In order to simplify the above equation, the procedure of Barnes for the anisotropic thermal conduction is applied [28]. Following Barnes, one can replace the accurate descriptions of the terms in from of the F_i terms with a constant value over a cell of interest. As such, the terms in front of F_i can be pulled out of the integral, and the remaining integral can be solved exactly once the finite element descriptions of the velocities and magnetic fields are introduced. Once the variation with respect to the nodal virtual velocities is taken, the local finite element matrix is obtained to be

$$\overleftrightarrow{\mathrm{M}} = -\sum_{i=1}^{7} \bar{\eta}_i \overleftrightarrow{\mathrm{M}}^i \tag{2.119}$$

where $\bar{\eta}_i$ are the averaged constant values of the $\tilde{\eta}_i$ over the cell and the sub matrices are defined as the following:

$$\mathrm{M}^i_{jk} = \frac{\mathrm{d}^2}{\mathrm{d}x^*_j \, \mathrm{d}x_k} \int_V F_i \left(\mathbf{x}^*, \mathbf{x}\right) \, \mathrm{d}V \tag{2.120}$$

where x_i is an array of the nodal velocities (e.g. $(ru_r)_i$, $(ru_\phi)_i$, and $(u_z)_i$). It is worthwhile to note that the local matrices generated from the non-gyroviscous terms are fully symmetric, while the matrices generated from the gyroviscous terms are fully skew-symmetric.

The integration of F_i can be performed exactly and an analytical solution can be readily obtained. The final task is to obtain the constant cell averaged values of the modified viscosity coefficients for each sub-matrix ($\bar{\eta}_i$). Again, following Barnes' approach, a modified maximum magnitude of the magnetic field over the cell is used in the evaluation of the constant viscosity coefficients (used in the denominator as a normalization magnitude) as discussed earlier.

With the both side of Eq. 2.107 defined, the combined system of equations can be solved numerically. In Cygnus, since the viscosities are treated implicitly, this results in inversion of the global coupled stiffness matrix generated from the finite element approach. Since the

boundary condition is Dirichlet zero, this is implemented by simply removing the terms in the global matrix corresponding to the skin nodes.

Unlike the original finite difference case, the anisotropic viscosity introduces a cross coupling of the velocities in different coordinate directions. The implicit finite difference contributions are introduced as a block diagonal contribution to the global matrix equation system. The explicit finite difference contributions are introduced on the right-hand-side vector. Thus, the finite element implementation of the anisotropic viscosity can be introduced into the plasma velocity equation with minimal modification to the original finite difference implementation.

With the finite element based anisotropic viscosity implemented in the velocity equation, the viscous heating contribution in the energy equation must be accounted to obtain a consistent set of equations. In principle, it is possible to carry out the finite element approach similar to what has been carried out in the velocity equation for the energy equation, but this is rather cumbersome calculation in a cylindrical coordinate. Rather, it would be more ideal to re-use the global finite element matrix generated for the velocity equation to obtain an approximation for the viscous heating for the energy equation.

Since the viscous heating is given as $(\boldsymbol{\nabla}\mathbf{u}) : \overleftrightarrow{\Pi}$ it can be seen that the generated finite element matrix already contains information for the viscous heating. For node α, the anisotropic viscosity in the finite element representation is given to be

$$\frac{\delta}{\delta\left(\tilde{\mathbf{u}}^*\right)_\alpha}\frac{1}{2\pi}\int\left(\boldsymbol{\nabla}\mathbf{u}^*\right) : \overleftrightarrow{\Pi}\,\mathrm{d}V = -(\overleftrightarrow{\mathrm{M}}\cdot\tilde{\mathbf{u}})_\alpha$$

where $\tilde{\mathbf{u}}$ is an array of the global nodal velocity unknowns (given earlier as $\mathbf{x}$ over the local element). Thus,

$$\frac{1}{2\pi}\int\left(\boldsymbol{\nabla}\mathbf{u}\right) : \overleftrightarrow{\Pi}\,\mathrm{d}V = -\tilde{\mathbf{u}}\cdot\overleftrightarrow{\mathrm{M}}\cdot\tilde{\mathbf{u}}$$

which states that the global sum of the viscous heating is given by the dot products of the global nodal velocity unknowns to the finite element matrix from both side. Since the gyroviscous contribution does not contribute to the viscous heating because it is skew-

symmetric, one can consider a nodal contribution of the viscous heating by performing a symmetric distribution of the global viscous heating sum, ensuring that the skew-symmetric terms vanish naturally in the formulation.

The simplest yet effective symmetric approximation for the nodal viscous heating contribution is given to be

$$\left[(\boldsymbol{\nabla}\mathbf{u}) : \overleftrightarrow{\Pi}\right]_\alpha \approx -\frac{1}{2V_\alpha}\tilde{\mathbf{u}}_\alpha \cdot \left[\left(\overleftrightarrow{\mathrm{M}} \cdot \tilde{\mathbf{u}}\right)_\alpha + \left(\tilde{\mathbf{u}} \cdot \overleftrightarrow{\mathrm{M}}\right)_\alpha\right] \tag{2.121}$$

It can be seen that when the nodal viscous heating contribution is multiplied by the nodal volume and a sum is taken over the entire domain, it exactly reproduces the total global viscous heating energy sum from the finite element representation.

The above form for the viscous heating can be used for any non-energy conservative implementation of the energy equation (such as temperature equation, pressure equation, etc.). However, for the energy conservative implementation, the viscosity contribution to the kinetic energy must also be accounted. The kinetic energy contribution from the viscosity is $\mathbf{u} \cdot (\boldsymbol{\nabla} \cdot \overleftrightarrow{\Pi})$. From the finite element representation, the nodal contribution of $(\boldsymbol{\nabla} \cdot \overleftrightarrow{\Pi})$ is represented as

$$\left[(\boldsymbol{\nabla} \cdot \overleftrightarrow{\Pi})_{r,\phi}\right]_\alpha \approx \frac{1}{A_\alpha}\frac{\delta}{\delta\left(ru^*_{r,\phi}\right)_\alpha}\frac{1}{2\pi}\int (\boldsymbol{\nabla}\mathbf{u}^*) : \overleftrightarrow{\Pi}\,\mathrm{d}V$$

for the radial and the azimuthal component, and

$$\left[(\boldsymbol{\nabla} \cdot \overleftrightarrow{\Pi})_z\right]_\alpha \approx \frac{1}{V_\alpha}\frac{\delta}{\delta\left(u^*_z\right)_\alpha}\frac{1}{2\pi}\int (\boldsymbol{\nabla}\mathbf{u}^*) : \overleftrightarrow{\Pi}\,\mathrm{d}V$$

for the axial component. Thus, the nodal kinetic energy contribution of the viscosity can be approximated to be

$$\left[\mathbf{u} \cdot (\boldsymbol{\nabla} \cdot \overleftrightarrow{\Pi})\right]_\alpha \approx \frac{1}{V_\alpha}\left[\tilde{\mathbf{u}}_\alpha \cdot (\overleftrightarrow{\mathrm{M}} \cdot \tilde{\mathbf{u}})_\alpha\right] \tag{2.122}$$

Combining the internal and the kinetic energy contribution from the viscosity, the nodal

viscous energy contribution for the energy conservative implementation is given to be

$$\left[\boldsymbol{\nabla}\cdot\left(\overleftrightarrow{\Pi}\cdot\mathbf{u}\right)\right]_{\alpha}\approx\frac{1}{2V_{\alpha}}\tilde{\mathbf{u}}_{\alpha}\cdot\left[\left(\tilde{\mathbf{u}}\cdot\overleftrightarrow{\mathrm{M}}\right)_{\alpha}-\left(\overleftrightarrow{\mathrm{M}}\cdot\tilde{\mathbf{u}}\right)_{\alpha}\right] \tag{2.123}$$

Thus, the contribution from the finite element representation of the anisotropic viscosity to the plasma velocity and energy equation can be formulated to be compatible with the existing finite difference formulation in Cygnus.

Chapter 3

SAMPLE PROBLEMS FOR FRC FORMATION AND TRANSLATION

In this chapter, sample problems for FRC formation and translation using simplified geometries are used to explore effects of neutrals on the FRC formation and translation processes. Results from the plasma-neutral model are compared with calculations made with the original fully ionized MHD implementation of the Cygnus code. Simplified problems are used to run parametric sweeps of various simulation conditions to determine the overall response of the FRC formation and translation processes predicted by the model. In particular, simulation results are used to generate data similar to that from common experimental diagnostics to understand the response of the collected experimental data on the simulation conditions.

Results from these simplified problems are useful in guiding the selection of simulation initial conditions and transport coefficients when trying to match experimental behaviors. The knowledge of the FRC response due to the change in the simulation setup can speed up the tuning process of simulation parameters in order to agree with the experiment. It also helps shed some new light on the local behavior of the FRCs when, as in the experiment, only limited sets of diagnostics are available.

In Section 3.1, the effect of the initial ionization level on the static formation of an FRC is explored. In Section 3.2, the effect of the various Cygnus transport coefficients on the static formation of an FRC is explored. In Section 3.3, the effect of various neutral distributions on the dynamic formation and translation processes is explored.

3.1 Effect of the Initial Ionization Level for Static FRC Formation

In order to understand the response of the FRC formation process due to the initial ionization level, a static FRC formation problem is constructed using a simple three-coil formation system using the programmed formation technique. The initial plasma density in the formation chamber is initialized after the bias flux is imbedded in the preionized plasma; thus, the dynamics of the partially ionized gas due to the magnetic force from the bias field injection are neglected.

The idealized problem is set up to be simple but reasonable for typical FRC formation experiments. The geometry of the formation chamber used for this problem is shown in Fig. 3.1. The initial magnetic flux topology at the start of the simulation is also shown on the same figure. The formation coil is initialized with a reversed bias flux of 11 mWb, while the two trigger coils on the ends are initialized with a forward bias flux of 14 mWb. The external circuit is constructed to allow the magnetic flux on the coils to be specified as a function of time; a sinusoidal quarter-cycle increase to the peak forward flux followed by a linear decay is used. A quarter-cycle time of 3 μs with a decay time of 30 μs is used, which is a reasonable approximation of the typical crowbar circuit used for FRC formations. A flux swing of 55 mWb and 60 mWb are used for the formation and trigger coils, respectively.

To simulate the experimental diagnostics, magnetic flux and axial magnetic field probes are positioned under the coils. This allows the computation of the excluded flux similar to the experimental outputs. Total of seven diagnostic probes with equal spacing are used with the first (on the right) and the last (on the left) probes located directly under the mid-plane of the two trigger coils. In addition, NDL at the midplane of the formation coil and at the gap between the formation and the trigger coils are computed. Using the excluded flux and NDL results from the simulation, one obtains clues on how to discern the initial ionization level from the experimental measurements.

As a reference simulation, a fully ionized static gas fill case is used. An initial atomic deuterium fill density of $3.5 \times 10^{20}\,\mathrm{m}^{-3}$ with the initial ion and electron temperatures of

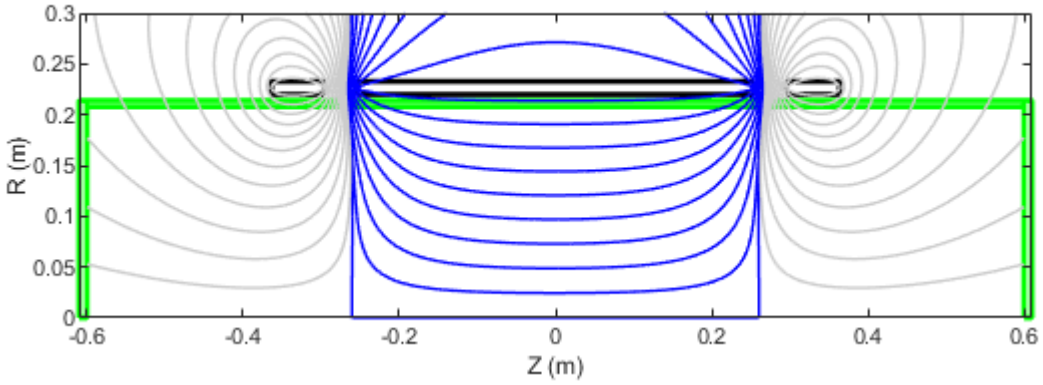

Figure 3.1: Simplified formation chamber geometry used for the simulation. The initial magnetic flux topology due to the bias fields are shown with the negative flux shown in blue.

0.5 eV is used. For all subsequent simulations in this section, a kinematic isotropic viscosity of 1000 m^2/s and 10 m^2/s are used for the plasma in the closed and open field line region, respectively; that of 100 m^2/s is used for the neutrals. Both the Spitzer and electron-neutral collision resistivities are included, with the anomalous Chodura resistivity set to $C_c = 0.5$ and $f_c = 3$. For both electrons and ions, the Braginskii thermal conductivities are used with the parallel diffusivity capped from 10^2 to 10^6 m^2/s and the perpendicular diffusivity capped from 1 to 10^2 m^2/s. The neutral thermal conduction is based on the hard-sphere collision model, and it is capped to the same value as the parallel diffusivity limit for the plasma. The plasma transport settings are based on the past MHD simulations, while the neutral transports are selected for numerical stability.

3.1.1 Uniform Initial Preionization

For this set of simulations, the initial ionization level of the uniform gas fill in the chamber is adjusted. A sweep of the initial ionization level with 90%, 70%, 50%, 30%, and 10% ionization is performed. The neutral species is initialized with an initial temperature of 0.025 eV that roughly corresponds to the room temperature. An effective ionization potential of 100 eV is

used for all simulations.

The resulting FRC separatrix shape at the time of the first minimum excluded flux radius is shown in Fig. 3.2. Effectively, it corresponds to the state of the maximum radial implosion before the axial contraction starts. The time evolution of the FRC relative radius and separatrix elongation is shown in Fig. 3.3. The effect of the radial implosion and axial contraction can be seen early in time, and by 20 µs, the FRC is mostly quiescent with its dynamics governed by the resistive loss of the magnetic flux.

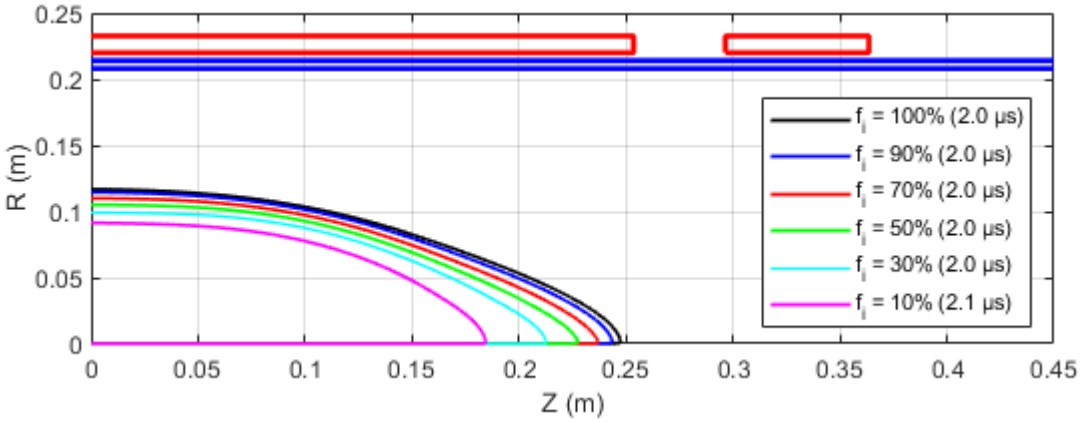

Figure 3.2: The shape of the FRC separatrix at the time of the first minimum excluded flux radius for a sweep of the initial ionization fraction. Only the right half of the separatrix shape is shown due to the symmetry of the result.

As it can be seen from Fig. 3.2 and Fig. 3.3, when the initial ionization level in the formation chamber is reduced, an FRC with a smaller separatrix radius and length is obtained. In addition, the FRC has a greater axial contraction as the initial ionization is reduced, resulting in a more prolate FRC as opposed to the elongated one. This is due to the reduced trapped flux and particles in the FRC when the initial ionization is reduced as shown in Fig. 3.4.

Since it takes a finite time for the neutrals to be ionized by the current sheath that forms during the radial implosion, some neutrals are not ionized inside the closed field line and are lost from the FRC. Thus, the final particle inventory is lower when the initial ionization

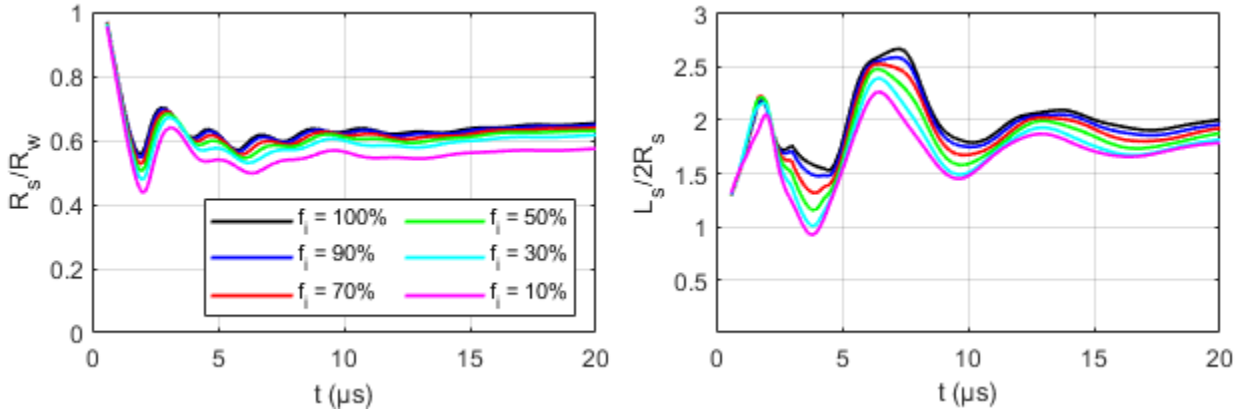

Figure 3.3: The time evolution of the FRC (left) relative radius and (right) separatrix elongation for a sweep of the initial ionization fraction.

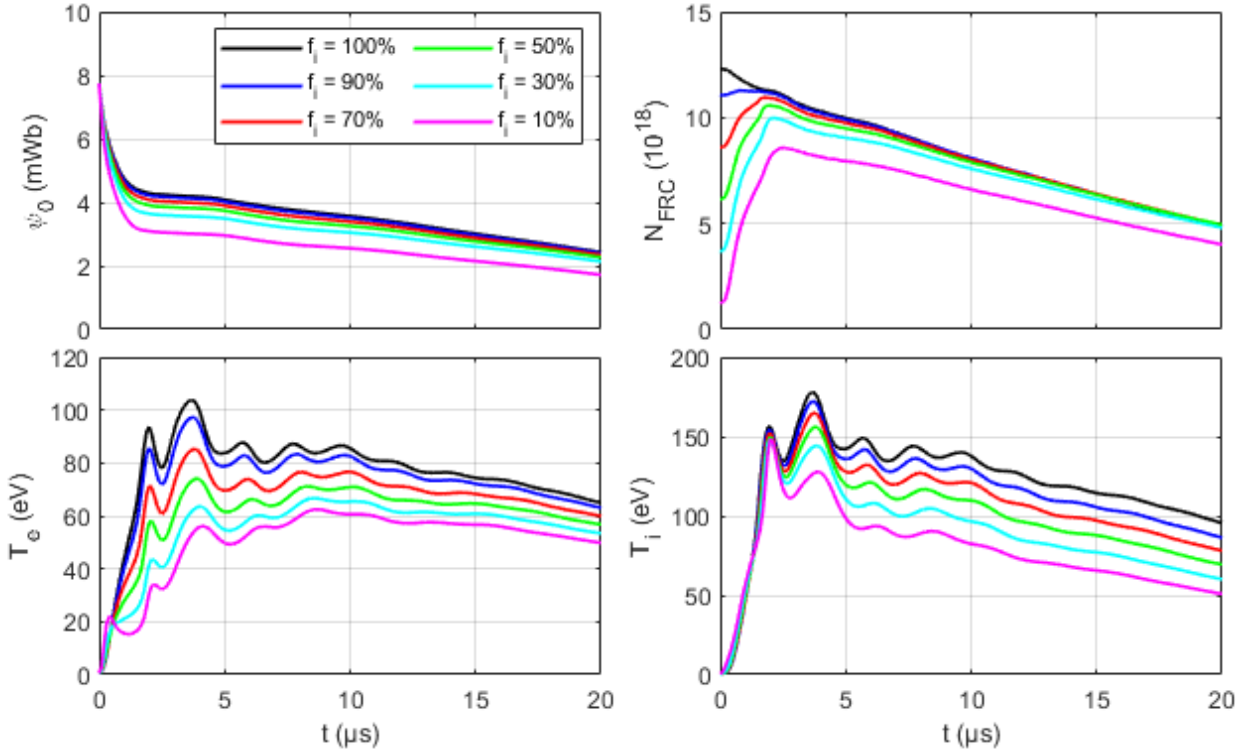

Figure 3.4: The time evolution of the (top left) trapped flux, (top right) trapped particles, (bottom left) volume averaged electron temperature, and (bottom right) volume averaged ion temperature for a sweep of the initial ionization fraction.

level is lower. In addition, since there are reduced initial plasma inventory in the FRC, the magnetic field is allowed to diffuse more readily during the implosion due to the higher resistivity. However, for the initial ionization level of 30% or higher, the trapped flux and particle inventory in the FRC is not significantly different from the fully ionized case once the FRC reaches a quiescent state. It is only the case with the initial ionization level of 10% that diverges significantly from others for the trapped flux and particles.

The greatest effect of the initial ionization level can be seen in the time evolution of the electron temperature. Since there are electron energy losses associated with each ionization event, when there is a large initial population of neutrals, a significant energy is expended by the electrons in the FRC. The ion temperature, on the other hand, is dominated by the heating due to the radial implosion and axial contraction; thus, the ion temperature at the first peak is similar for all simulated cases. The late time divergence of the ion temperature is due to the thermal equilibration process with electrons.

For the case when the initial ionization level is 10%, an early drop in the electron temperature during the implosion process can be observed. This is caused by too much ionization occurring during the radial implosion that reduces the electron temperature to a level where the ionization process is significantly hindered. As a result, the neutral particle loss during the reversal process is enhanced. For all other cases, no visible drop in the electron temperature is observed. This suggests that the loss of the ionization efficiency due to the reduced electron temperature during the radial implosion is the primary source of the reduced trapped flux and particle inventory for the 10% ionized case. Thus, there exists a minimum threshold initial ionization level to ensure that the efficiency of the ionization process is not compromised during the field reversal.

The simulation generated excluded flux and NDL measurements for the tested cases are shown in Fig. 3.5 and Fig. 3.6, respectively. In general, the excluded flux signal is reduced as the initial ionization level is reduced. The behavior of the excluded flux signal is similar to the case when the resistivity is enhanced. Thus, if only the excluded flux signal is available, one may incorrectly conclude that the reduction in the excluded flux amplitude is due to

anomalous resistivities rather than the initial ionization level.

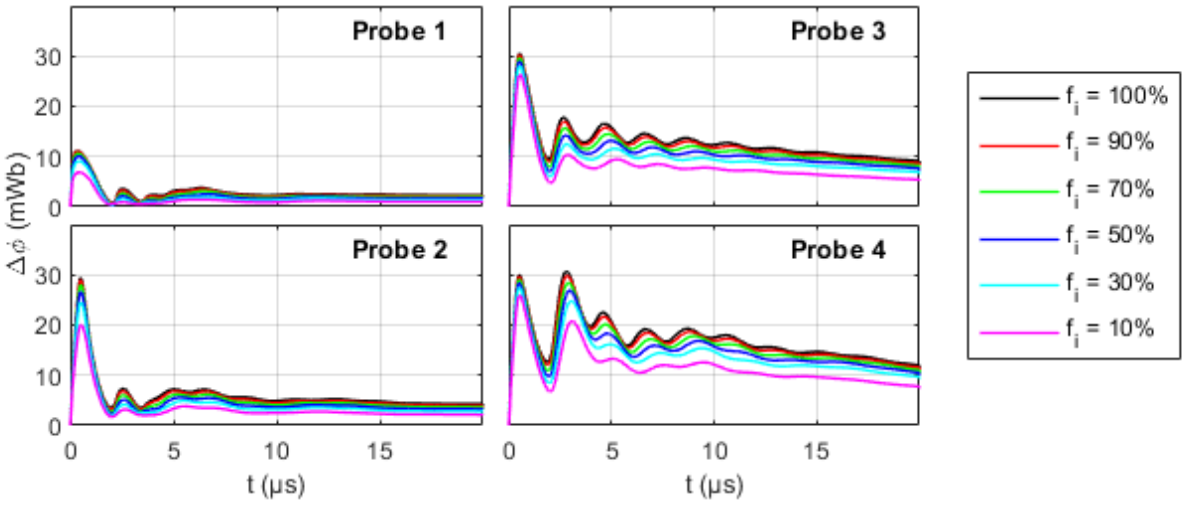

Figure 3.5: The simulation generated excluded flux measurements for a sweep of the initial ionization fraction.

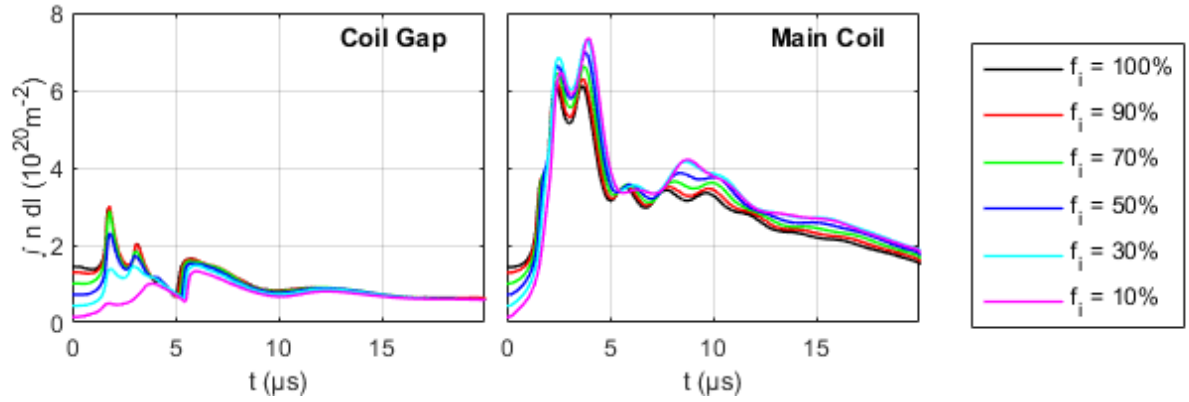

Figure 3.6: The simulation generated line integrated plasma density (NDL) for a sweep of the initial ionization fraction.

As it can be seen from Fig. 3.6, the NDL signal offers far better indication of the initial ionization level, as the initial value of the NDL corresponds to the initial ionization level. The NDL measured in the coil gap region shows very little signal in the early time for the 10% ionized case, which correctly shows that the bulk of the FRC is missing on the line chord

that the NDL is computed. This is contrary to other cases where the excluded flux signal shows reasonable strength in this region during the same time period. Unfortunately, at the peak, the NDL signal does not offer clear indication of the lower particle inventory for the 10% ionized case due to the volume averaging effect from the radial weighting as discussed in Section 1.2.4.

The volume averaged density inside the FRC is shown in Fig. 3.7. The averaged density is computed using both experimental results (using Eq. 1.6) and raw simulation data. It can be seen that while the 10% case has the least particle inventory, it has the highest volume averaged density due to its small volume. Thus, unless an accurate FRC volume can be discerned from the excluded flux signal, the FRC particle inventory may be incorrectly inferred from the NDL signal. Thus, the greatest experimental clue for the initial ionization level in the formation chamber is the early time NDL signal before the firing of the main formation coils, as the late time results from the NDL signal requires accurate understanding of the FRC geometry. Furthermore, while the experimentally computed value captures the average FRC density well in the quiescent period, it fails to accurately capture the magnitude of the average FRC density during the dynamic phase.

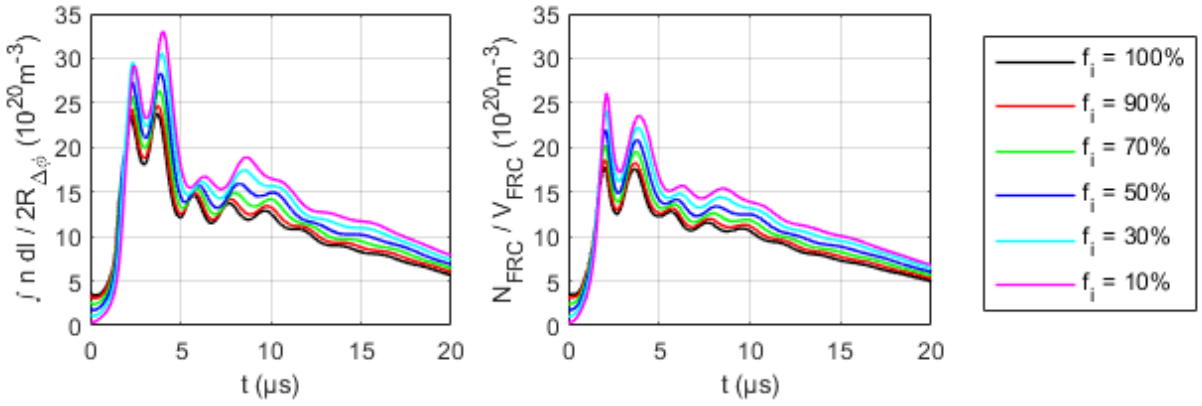

Figure 3.7: The average FRC density for a sweep of the initial ionization fraction computed using (left) NDL and excluded flux radius and (right) direct simulation results.

In summary, for FRCs formed with a static uniform fill with uniform initial ionization level, a reduction in the initial ionization level causes a reduction in the FRC trapped flux and particle inventory. Due to the lower trapped flux and particles, the resulting FRC becomes smaller in radius and length. The strongest indicator of the ionization event is in the electron temperature, as it is directly influenced by the energy loss associated with the ionization process. The excluded flux signal does not give clear indication of the influence from initial ionization level, as the resulting loss in the excluded flux signal looks similar to resistive effects. The NDL signal offers better indication of the initial ionization level. However, care must be taken in interpreting its result, as it is strongly influenced by the local plasma geometry.

3.1.2 Wall Localized Preionization

For this simulation, a sweep of the initial ionization level from Section 3.1.1 is repeated with a modification: the initial ionization is assumed to be localized near the formation chamber wall. For the initial density profile in the simulation, a fully ionized layer is initialized near the outer radius with the neutral gas populated everywhere else. The initial ionization level is now understood to be the volume averaged ionization level in the chamber. With this simple setup, the radius at which the gas transitions from a neutral gas to a fully ionized plasma can be computed as

$$r = \sqrt{1 - f_i}\, R_w$$

where r is the transition radius, f_i is the volume averaged initial ionization level, and R_w is the radius of the formation chamber.

The resulting FRC separatrix shapes at the time of the first minimum excluded flux radius is shown in Fig. 3.8. The time evolution of the FRC relative radius and the separatrix elongation is shown in Fig. 3.9. The effect of the radial implosion and axial contraction can be seen early in time, and by 20 µs, the FRC is mostly quiescent, and its dynamics are governed by the resistive loss of the magnetic flux.

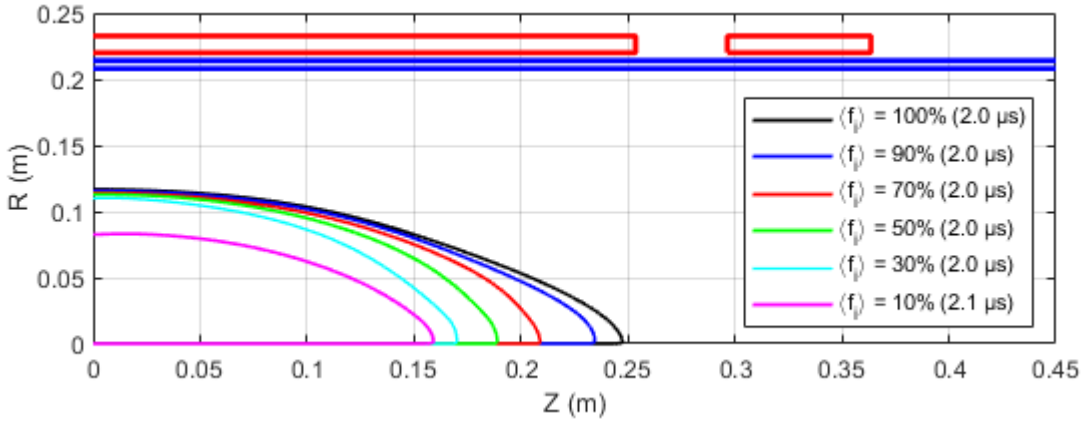

Figure 3.8: The shape of the FRC separatrix at the time of the first minimum excluded flux radius for a sweep of the wall localized ionization. Only right half of the separatrix shape is shown due to the symmetry of the result.

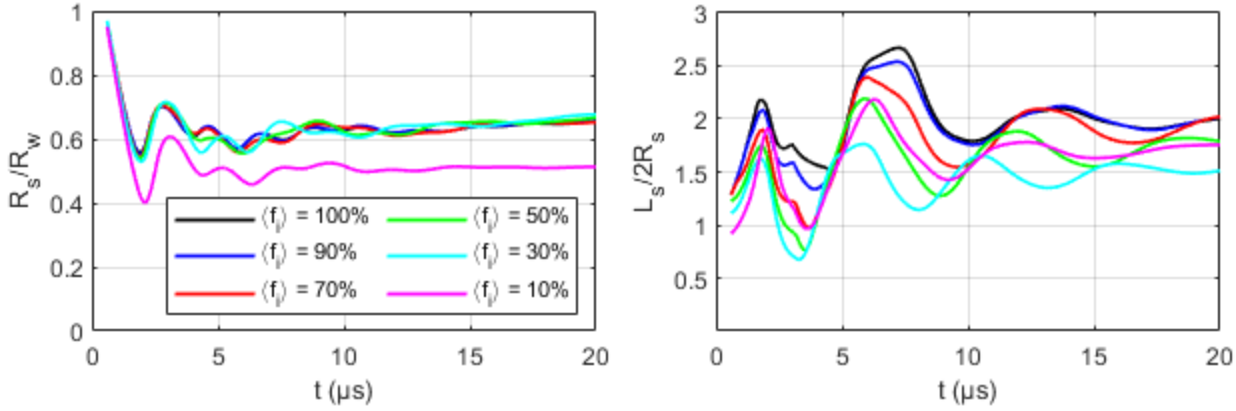

Figure 3.9: The time evolution of the FRC (left) relative radius and (right) separatrix elongation for a sweep of the wall localized ionization.

Compared to the uniform ionization case, the FRC length has a stronger dependence on the initial volume averaged ionization level for the wall localized case. The separatrix radius at the time of the maximum radial implosion is largely the same for all cases except for the 10% case. Again, the FRC geometry is governed by the trapped flux and particles, and the time evolution of key FRC parameters computed from the simulation results is shown in Fig. 3.10.

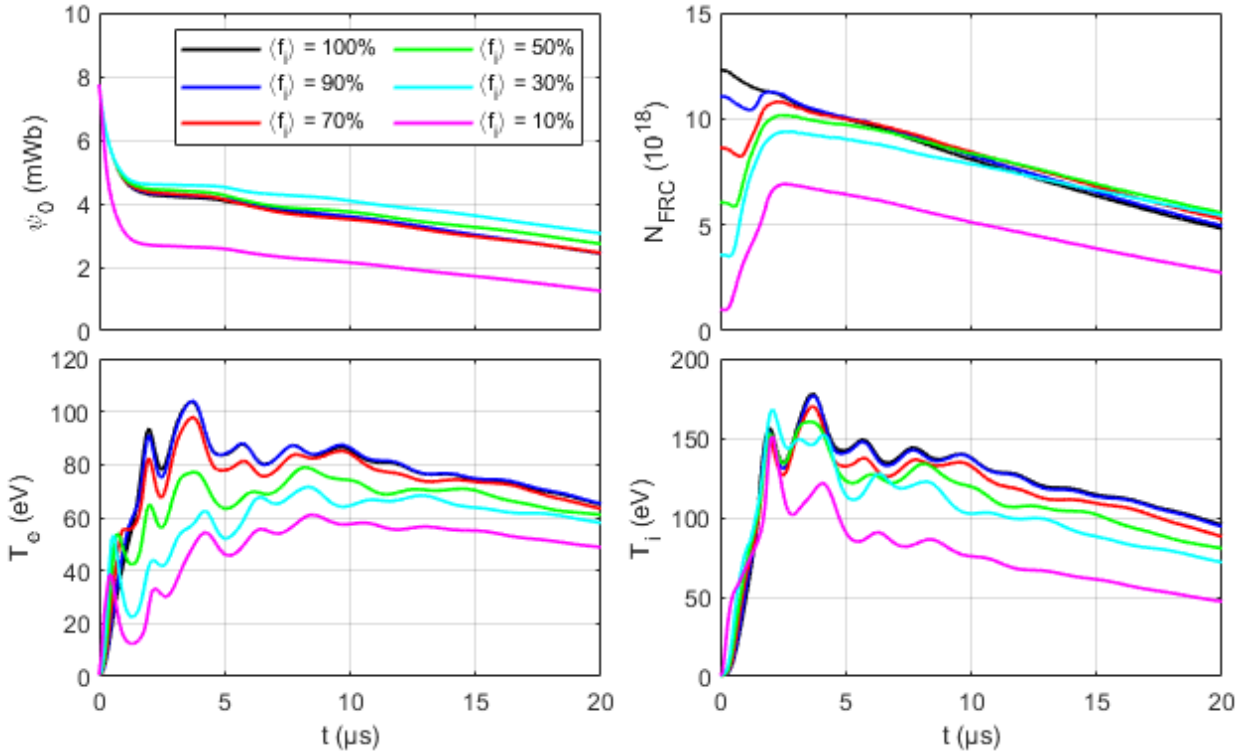

Figure 3.10: The time evolution of the FRC (top left) trapped flux, (top right) trapped particle, (bottom left) volume averaged electron temperature, and (bottom right) volume averaged ion temperature for a sweep of the wall localized ionization.

As it can be seen in Fig. 3.10, the trapped flux increases in general as the initial volume averaged ionization level is reduced. Furthermore, more flux is trapped with the wall localized ionization compared with a uniform ionization. The exception to this trend is the 10% case where the trapped flux is reduced when the initial ionization is concentrated near the wall. This behavior is caused by the fact that as long as a plasma layer of a sufficient thickness exists near the wall, the gas behaves similar to the fully ionized case when the main formation coil is fired. This is due to the skin depth effect in the plasma layer where the penetration and diffusion of the magnetic field through the plasma is governed. This effect can be observed in the time evolution of the FRC particle inventory, as early in the implosion process, the particle loss follows the same rate as the fully ionized case until the plasma production from

the ionization begins to dominate.

The FRC length reduction for the wall localized case is caused by the enhanced axial diffusion of the magnetic field near the cusp region. While the radial diffusion of the magnetic field is hindered by the fully ionized outer layer, the axial diffusion is not because the plasma initially only exists in the thin layer. In the uniform ionization case, the plasma covers the entire radius of the device, so the rate of the axial diffusion is not distinctively different from that of the radial diffusion. The enhanced axial diffusion of the magnetic field causes the formed FRC to be shorter, but the radius is largely unchanged due to the reduced radial diffusion. For the 10% ionized case, the initial ionization layer is not large enough compared to the local skin depth thickness. Thus, the radial bucking of the magnetic field is not enhanced, and only the axial magnetic diffusion is enhanced due to concentration of the initial plasma in a thin layer; this results in an FRC with a lower trapped flux and particle inventory.

The simulation generated excluded flux and NDL signals are shown in Fig. 3.11 and Fig. 3.12, respectively. As it can be seen, the excluded flux signal for all cases excluding the 10% case behaves largely the same as the fully ionized case early in time, and it is only in the late time bouncing that they begins to diverge. The 10% case diverges from the rest as expected. When there is a sufficient amount of highly ionized plasma near the wall, the information of the local ionization level is largely lost from the excluded flux signal, as it closely follows the case of the fully ionized case. The only time the experimental excluded flux signal can be used as an indicator for detecting a wall concentration of the initial ionization is when the experimental excluded flux can be matched well with a fully ionized simulation model, but the NDL signal has a poor agreement.

The NDL signal offers better indication of the initial ionization level, but it is complicated by the radial dependence. Compared to the uniform ionization case, the initial NDL signal before the main coil firing for the wall localized case is smaller for the same volume averaged ionization level. Thus, unless one knows the accurate radial dependence of the initial ionization, the volume averaged initial ionization level could be interpreted incorrectly from

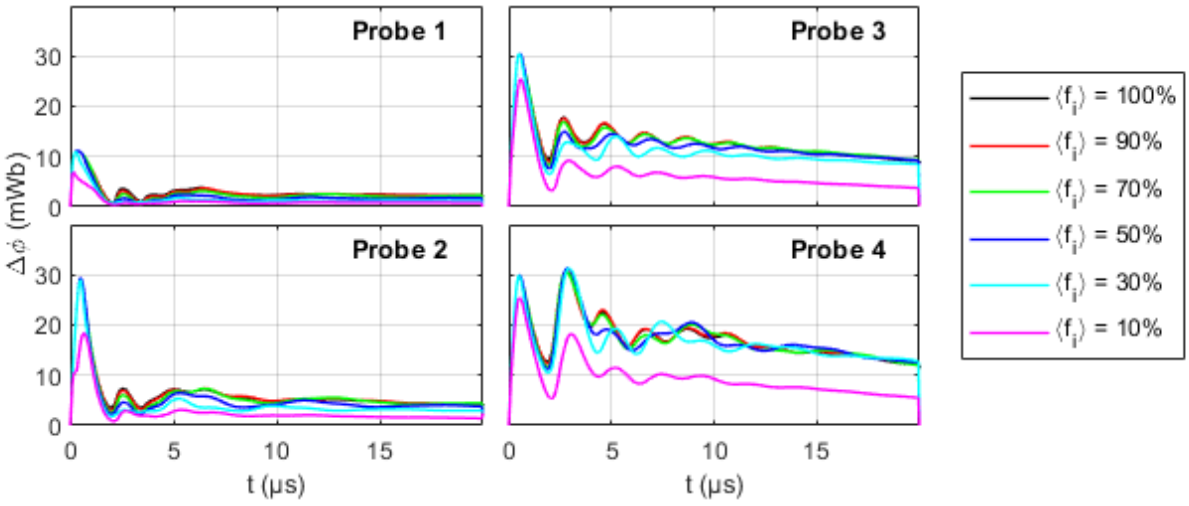

Figure 3.11: The simulation generated excluded flux measurements for a sweep of the wall localized ionization.

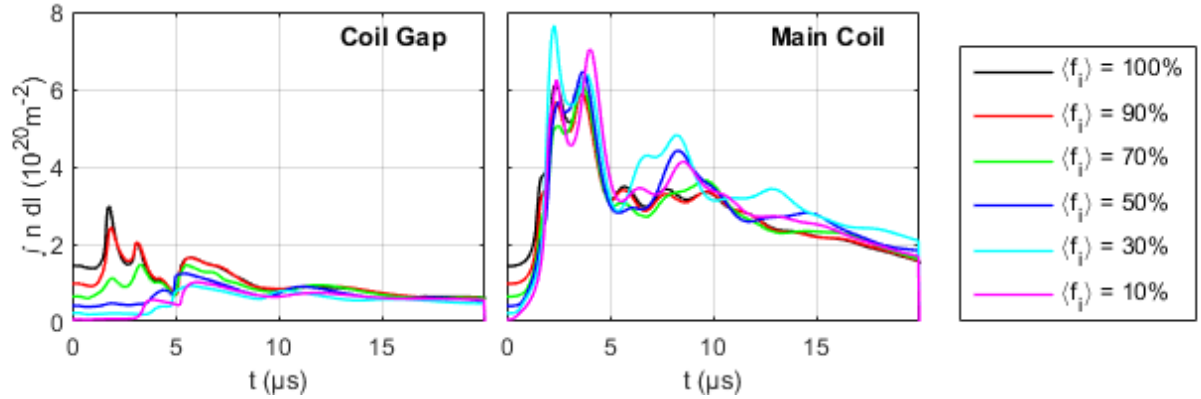

Figure 3.12: The simulation generated line integrated plasma density (NDL) for a sweep of the wall localized ionization.

the experimental data. One indication of the wall concentrated ionization can be observed in the early time behavior of the NDL signal right after the main coil firing. When there is a concentration of the ionization near the wall, the initial NDL signal begins flat with a behavior similar to the fully ionized case before it starts increasing. As such, if the initial signal from the NDL is small and the NDL signal begins flat immediately after the main bank firing, there is a good chance that the initial ionization is concentrated near the formation

chamber wall.

The volume averaged density inside the FRC is shown in Fig. 3.13. Again, the volume averaged density is computed using both the experimental and the raw simulation data. The agreement early in time during the FRC dynamics is quite poor. Since only the late time experimental results are useful in obtaining the actual volume averaged density, the effect of radial ionization dependence early in time cannot be extracted easily from the experimental results.

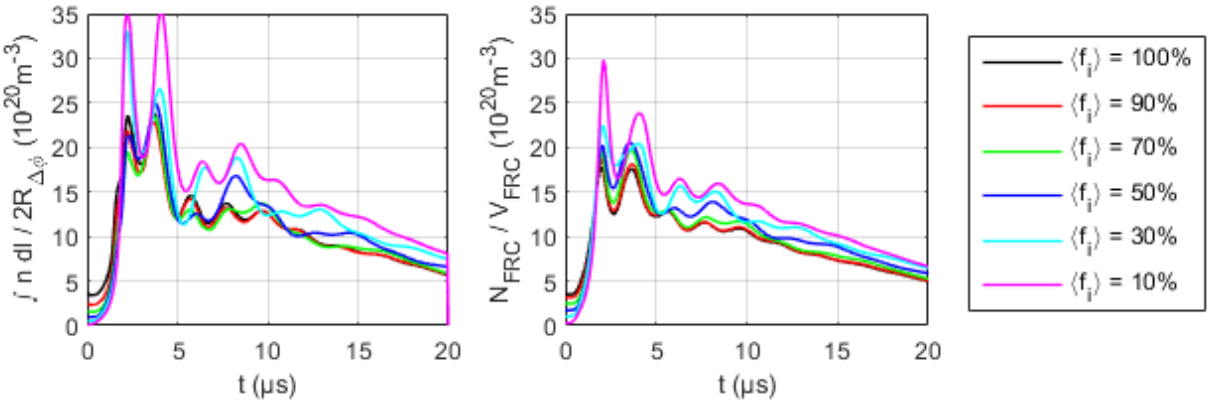

Figure 3.13: The average plasma density in the FRC for a sweep of the wall localized ionization computed using (left) NDL and excluded flux radius and (right) direct simulation results.

In summary, when the initial ionization is concentrated near the wall, the resulting FRC contains more trapped flux and particle inventory compared with the uniform ionization case with the same initial volume averaged ionization level. Furthermore, the FRC length is shorter for this case. However, the reduction in the FRC length is difficult to extract from the excluded flux signal, as the diagnostic is not sensitive enough to track a small reduction in the FRC length. This is due to the fact that the excluded flux signal cannot resolve a separatrix characteristic scale length smaller than the coil radius [25]. Unless multiple interferometers are used to measure the axial density data of the FRC as it is oscillating axially, the reduction in the FRC length due to the wall concentrated ionization cannot be

determined experimentally with ease. The only indication of the wall localization effect is in the early NDL signal right after the main bank firing, as the NDL signal will remain relatively flat similar to the fully ionized case before it begins to increase.

3.1.3 Radially Imploded Preionization

In the process of imbedding the bias flux in the preionized gas, it is possible for an azimuthal current to develop as the conducting gas tries to buck the axial magnetic field from diffusing in. As a result, it is possible for the preionized gas to be imploded radially to evacuate a region near the wall before the main formation bank is fired. In order to study the effect of the plasma implosion early in the preionization, series of tests are conducted where the initial radius of the gas fill is reduced.

To test for this effect, the 30% initial uniform ionization case from Section 3.1.1 is taken as a reference. The cases with the initial fill density reduced to 90%, 70%, and 50% wall radii are tested. It is assumed that the number of particles in the chamber is same for all cases. Thus, when the radius is reduced, the fill density is increased to compensate for the volume reduction. The initial fill density for each radius can be computed as

$$n = \left(\frac{R_w}{R_o}\right)^2 n_0$$

where R_w is the wall radius, R_o is the outer radius of the initial gas fill, and n_0 is the fill density when $R_o = R_w$.

The resulting FRC separatrix shape at the time of the first minimum excluded flux radius is shown in Fig. 3.14. The time evolution of the FRC relative radius and separatrix elongation is shown in Fig. 3.15 for all simulated cases. It can be seen from two figures that reduction in the initial gas radius has a direct influence on the final radius of the imploded FRC. The length of the FRC is not influenced as strongly as its radius. Thus, more elongated FRCs are produced.

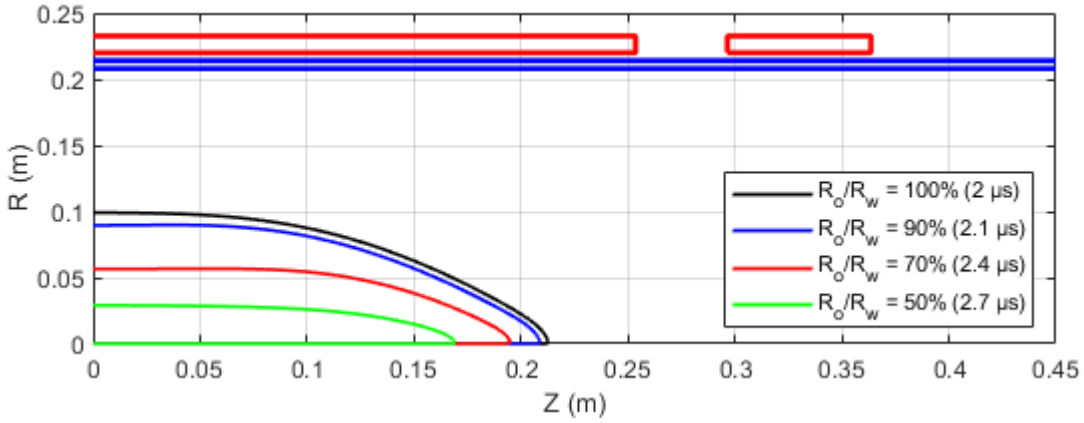

Figure 3.14: The shape of the FRC separatrix at the time of the first minimum excluded flux radius for a sweep of the initial implosion radius. Only right half of the separatrix shape is shown due to the symmetry of the result.

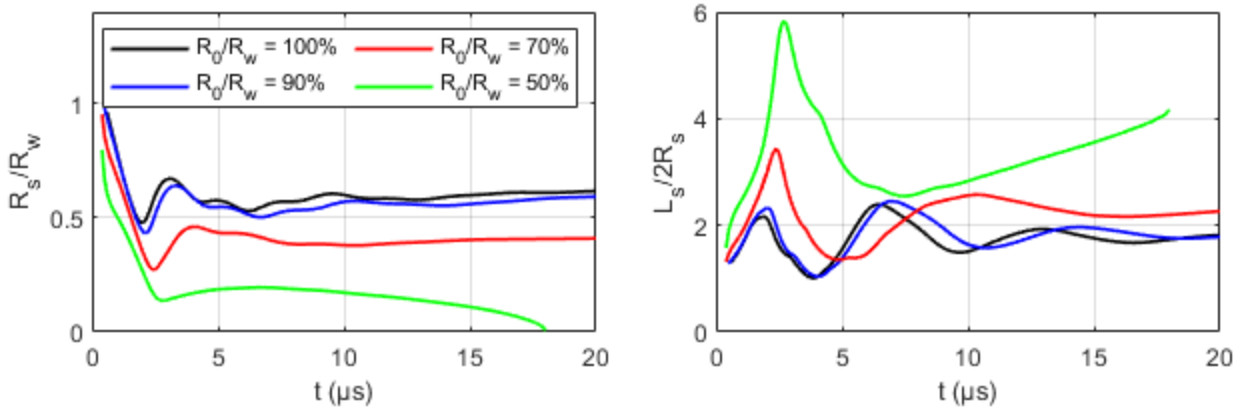

Figure 3.15: The time evolution of the FRC (left) relative radius and (right) separatrix elongation for a sweep of the initial implosion radius.

The time evolution of key FRC parameters computed from the simulation results is shown in Fig. 3.16. As it can be seen, the resulting trapped flux is severely reduced when the initial fill radius is decreased. This is caused by the loss of all of the initial magnetic field in the vacuum region between the outer radius of the initial fill and the wall. Since there is no plasma in which the bias magnetic flux is frozen, all of the flux in this vacuum region is lost during the field reversal. This behavior is same as what was discussed previously in

Section 1.2.3 for the inherent flux loss associated with the ringing theta-pinch ionization method.

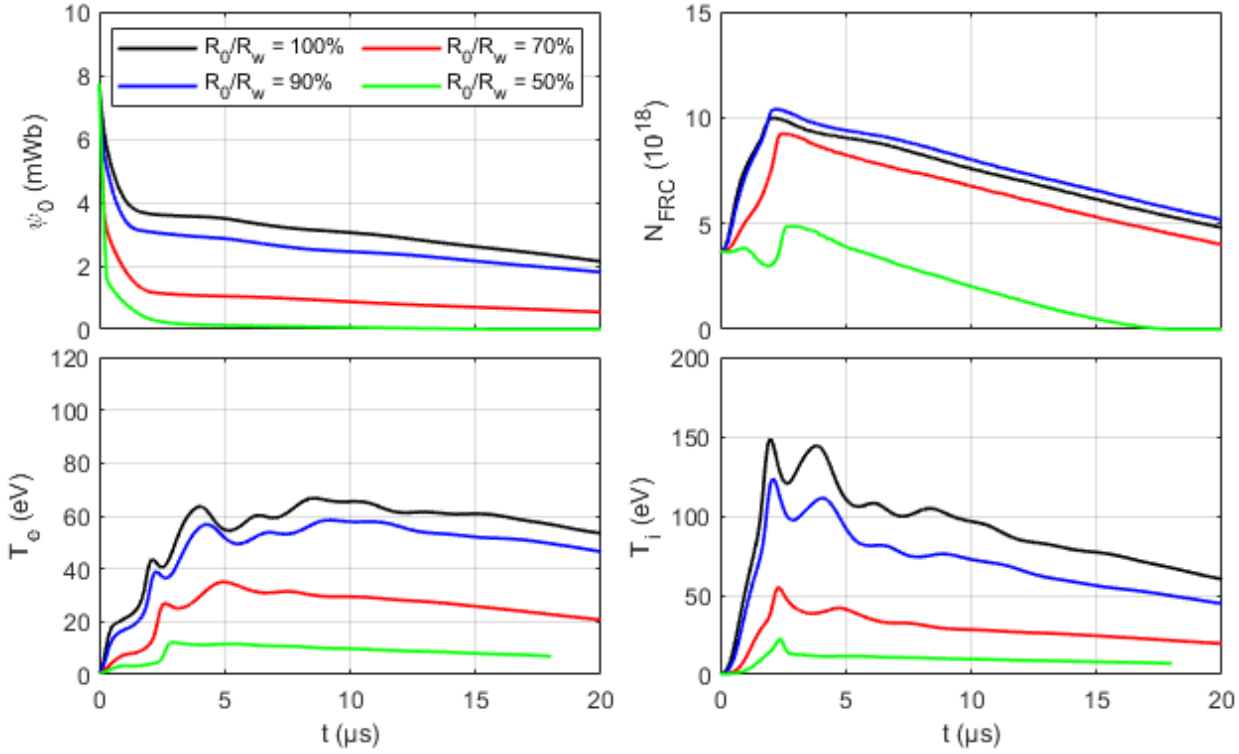

Figure 3.16: The time evolution of the FRC (top left) trapped flux, (top right) trapped particle, (bottom left) volume averaged electron temperature, and (bottom right) volume averaged ion temperature for a sweep of the initial implosion radius.

On the other hand, the particle inventory is largely unchanged compared to the drastic decrease in the trapped flux, except for the 50% radius case. As a result of the lower trapped flux compared to its particle inventory, more elongated FRCs are produced compared with FRCs formed in the same device with a same level of trapped flux but with the gas fill right up to the wall. This is due to the fact that for the case when the gas fill is right up to the wall, in order to shed the same amount of the magnetic flux to form the FRC, the particle in the outer flux surfaces will be lost together with the trapped flux. As such, the particle inventory in such case is lower, and more prolate FRCs are produced.

For the 50% radius case, the particle inventory is significantly lower than other cases due to lack of ionization occurring in the closed field region. Since most of the flux loss is associated with the vacuum region, there is not much initial flux trapped within the preionized gas. As a result, only weak azimuthal currents develop in the plasma sheath during the implosion process. Thus, the electron Joule heating is reduced, and the electron temperature cannot increase efficiently to a level where large amounts of ionization processes occur. As it can be seen in Fig. 3.16, the electron temperature in the FRC remains capped and flat for the 50% radius case. The average electron temperature is below 13.6 eV, which is the ionization threshold for deuterium; thus, the ionization efficiency is severely degraded.

While it is not as severe as the 50% radius case, the capping of the electron temperature can also be seen for the 70% radius case. However, the electron temperature is still able to slowly increase to a level sufficient for reasonable ionization. As such, while the particle inventory for the 70% case is lower than that for the fully ionized case, it is reasonably close, considering its significantly lower trapped flux.

The initial fill radius has more dominant effect on the ion temperature. While the reduction in the electron temperature was caused by the reduced Joule heating and ionization energy loss, the ion temperature loss is caused by the reduced radial stroke distance of the FRC radial implosion. Due to this reduction, the FRC develops a lower radial kinetic energy during the implosion process as the plasma coupling to the external circuit is reduced. Thus, when the radial kinetic energy is converted into the thermal energy at the end of the implosion process, resulting ion temperature is lower.

The simulation generated excluded flux signal is shown in Fig. 3.17. The effect of the reduced trapped flux can be seen clearly from the excluded flux signal as the lift-off flux is reduced for the smaller radius cases. The reduction in the lift-off flux is caused by the lack of plasma near the wall that can hinder magnetic field diffusions. Since all bias flux in the vacuum region is completely lost during the field reversal, the lift-off flux is governed by the amount of initial flux that is trapped by the reduced radius gas fill. Furthermore, as the fill radius is reduced, due to the smaller radius FRC that is produced, the excluded flux signal

is smaller at the time of the maximum radial implosion. Furthermore, the radial oscillation in the excluded flux signal is reduced due to the lower radial kinetic energy from the radial implosion.

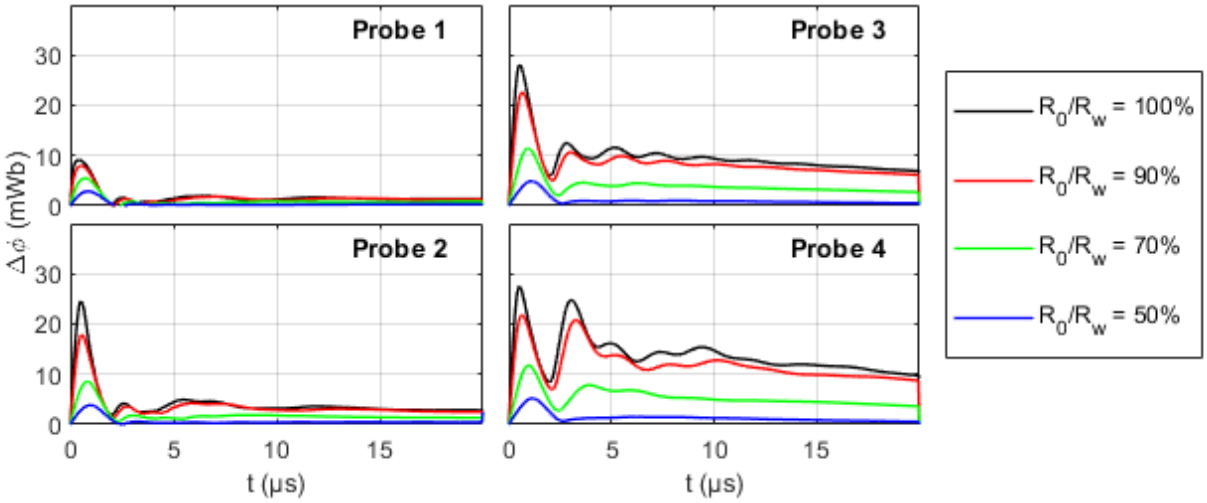

Figure 3.17: The simulation generated excluded flux measurements for a sweep of the initial implosion radius.

The simulation generated NDL signal is shown in Fig. 3.18. For the case with a smaller initial fill radius, the NDL signal is amplified both initially and after the radial implosion. As it can be seen in the average plasma density shown in Fig. 3.19, due to the larger particle inventory compared with the FRC volume, the average plasma density in the FRC is increased as the initial fill radius is reduced. Furthermore, as the initial fill radius is reduced, the width of the peak NDL signal increases. This is due to the reduction in the radial bounce of the formed FRC.

In summary, when the initial fill radius of the FRC is reduced, the resulting FRC has a reduced trapped flux, but with a larger particle inventory compared with an FRC of similar flux level. This results in more elongated FRCs to be produced. As a result, the NDL shows much larger signal compared with similar FRCs that are more prolate. In addition, both the ion and electron temperatures are reduced as the initial fill radius is reduced. The excluded

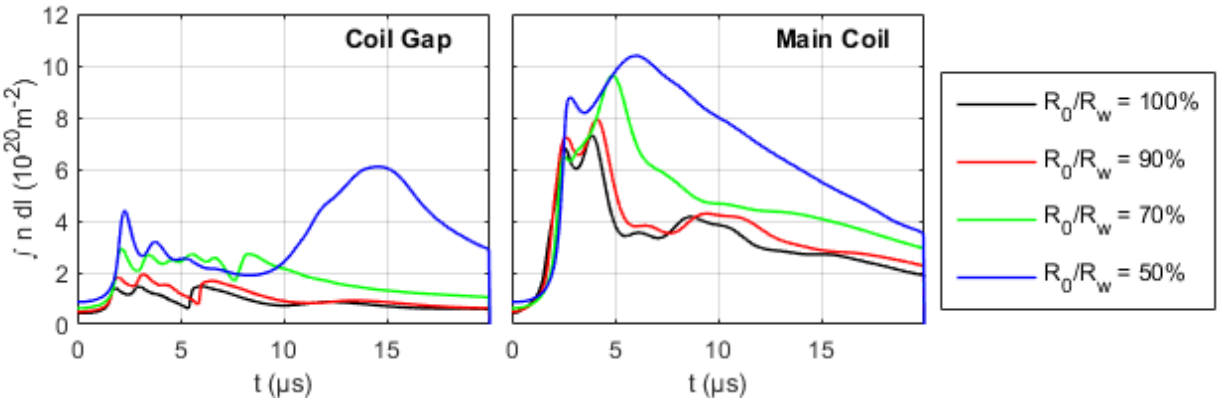

Figure 3.18: The simulation generated line integrated plasma density (NDL) for a sweep of the initial implosion radius.

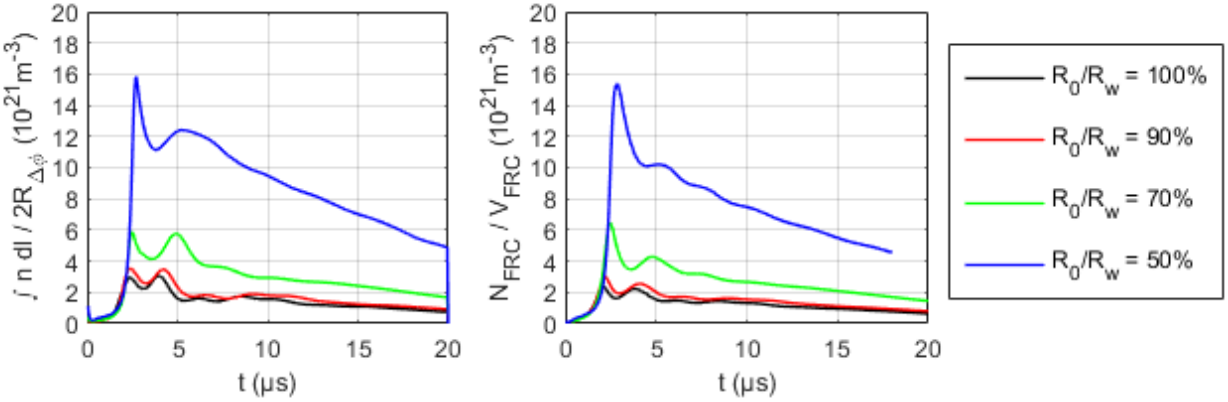

Figure 3.19: The average plasma density in the FRC for a sweep of the initial implosion radius computed using (left) NDL and excluded flux radius and (right) direct simulation results.

flux signal generally shows reasonable indication of the reduced fill radius, as the lift-off flux is significantly reduced and the FRC dynamics after the maximum radial implosion are largely dampened.

3.1.4 Outer Radius Localized Preionization with Radial Implosion

Similar to the previous simulation, consider a case where the initial gas in the formation chamber is radially imploded by the process of imbedding the bias flux. This time consider the case when the initial ionization is concentrated at the outer radius. Thus, the initial distribution of the gas is similar to the case of the wall localized ionization in Section 3.1.2, except with the initial outer radius reduced. As a reference, the wall localized ionization with an initial volume averaged density of 30% from Section 3.1.2 is used as a reference. The cases with 90%, 70%, and 50% wall radii are tested. Similar to the previous radially imploded simulations, the number of particles in the chamber is the same for all cases, and the total fill density can be computed to be

$$n_t = \left(\frac{R_w}{R_o}\right)^2 n_{t0}$$

where n_{t0} is the total fill density when $R_o = R_w$ and n_t is the total density of the reduced radius case. The radius at which the gas transitions from a neutral gas to a fully ionized gas can be computed as the following:

$$r = \sqrt{1 - f_i}\, R_o$$

The resulting FRC separatrix shape at the time of the first minimum excluded flux radius is shown in Fig. 3.20. The time evolution of the FRC relative radius and separatrix elongation is shown in Fig. 3.21. Compared with the uniform ionization cases, the FRC length is shorter while the FRC radius is larger. This is due to the enhanced radial bucking and axial diffusion of the magnetic field as discussed previously for the wall localized ionization case. Besides this change, the behavior of the FRC is similar to what is seen in Section 3.1.3

The time evolution of key FRC parameters computed from the simulation results is shown in Fig. 3.22. Similar to the previous case, the reduction of the trapped flux due to the smaller initial fill radius is observed. Compared with the uniformly ionized case, the trapped

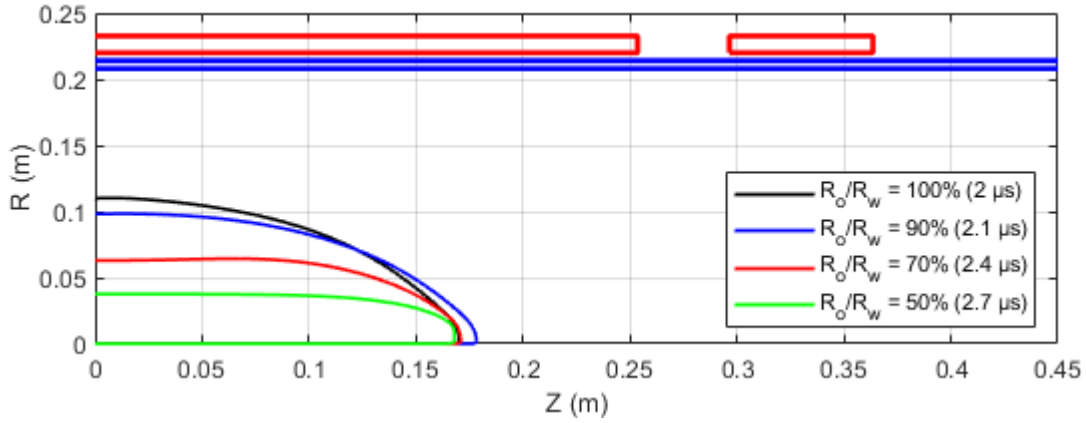

Figure 3.20: The shape of the FRC separatrix at the time of the first minimum excluded flux radius for a sweep of the initial implosion radius with a localized ionization. Only right half of the separatrix shape is shown due to the symmetry of the result.

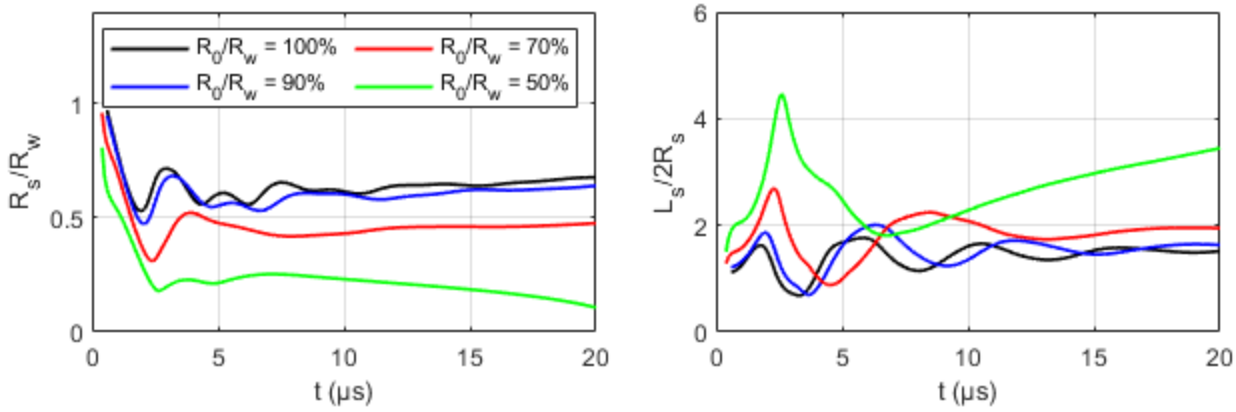

Figure 3.21: The time evolution of the FRC (left) relative radius and (right) separatrix elongation for a sweep of the initial implosion radius with a localized ionization.

flux is larger, as observed previously for the wall localized ionization case. Compared with the previous simulation, the biggest effect of the local concentration of the ionization is in the electron temperature. Since the outer radial layer of the initial fill is fully ionized, a sufficient azimuthal current can be generated in the outer layer during the radial implosion. Because of this, there is sufficient Joule heating to maintain the electron temperature from being quenched by the ionization process. As a result, a reasonable ionization efficiency is

maintained even for the 50% radius case, and the number of the particles trapped in the FRC is increased.

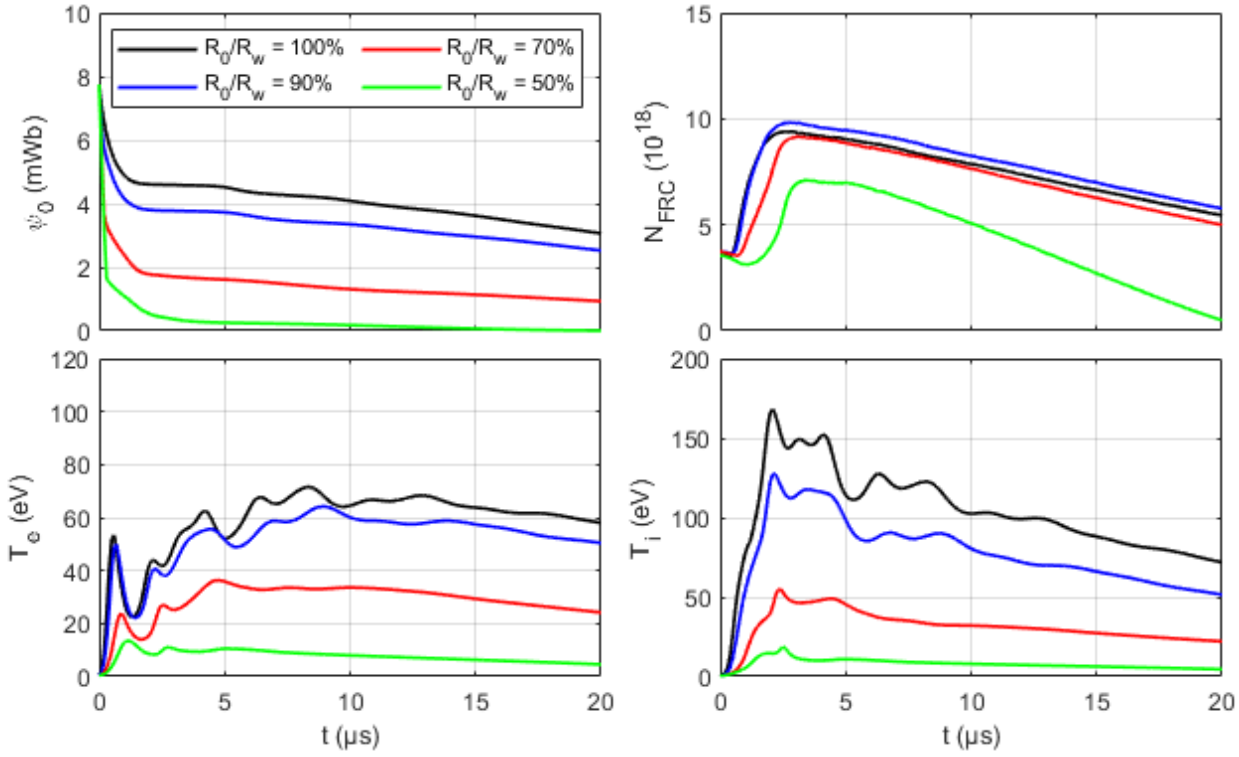

Figure 3.22: The time evolution of the FRC (top left) trapped flux, (top right) trapped particle, (bottom left) volume averaged electron temperature, and (bottom right) volume averaged ion temperature for a sweep of the initial implosion radius with a localized ionization.

The simulation generated excluded flux signal is shown in Fig. 3.23. Similar to the previous case, the excluded flux is reduced for the smaller radius. However, compared to the previous simulation, the excluded flux is larger in general due to the plasma layer that enhance the radial bucking of the magnetic field. Since the radius reduction has the most effect on the excluded flux signal, the details of the local concentration of the ionization cannot be determined from the excluded flux signal with ease.

The simulation generated NDL signal is shown in Fig. 3.24, and the averaged FRC density

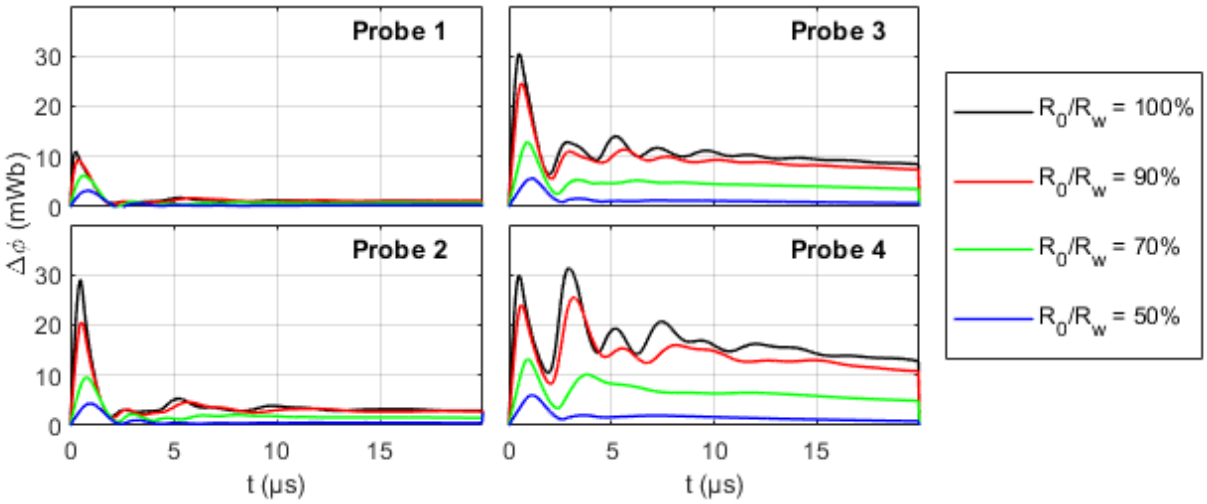

Figure 3.23: The simulation generated excluded flux measurements for a sweep of the initial implosion radius with a localized ionization.

is shown in Fig. 3.25. The NDL signals shows a flat profile immediately after the coil firing, which is a characteristic of the outer radius concentrated ionization. Similar to the previous radial implosion case, the NDL signal is significantly amplified for the case with smaller fill radius due to the small FRC radius and large particle inventory. In general, the NDL signal for the localized ionization case has a smaller amplitude than the similar condition with a uniform ionization. This is caused by the smaller FRC radius in the uniform ionization case. Thus, while the localized ionization case has a higher particle inventory, the NDL signal for the uniform ionization case has a higher magnitude.

In summary, when the initial ionization is concentrated near the outer radius, the trapped flux and particle inventory is improved over the similar condition with a uniform initial ionization. As such, more prolate FRCs are produced. In general, conclusions from Section 3.1.2 and Section 3.1.3 both apply here, as this case is a hybrid of the previous two cases. By concentrating the ionization near the outer radius, the electron heating is improved, and the issue of the electron temperature quenching seen from the uniform ionization case is removed. It is noteworthy that although the particle inventory is improved here, the resulting NDL

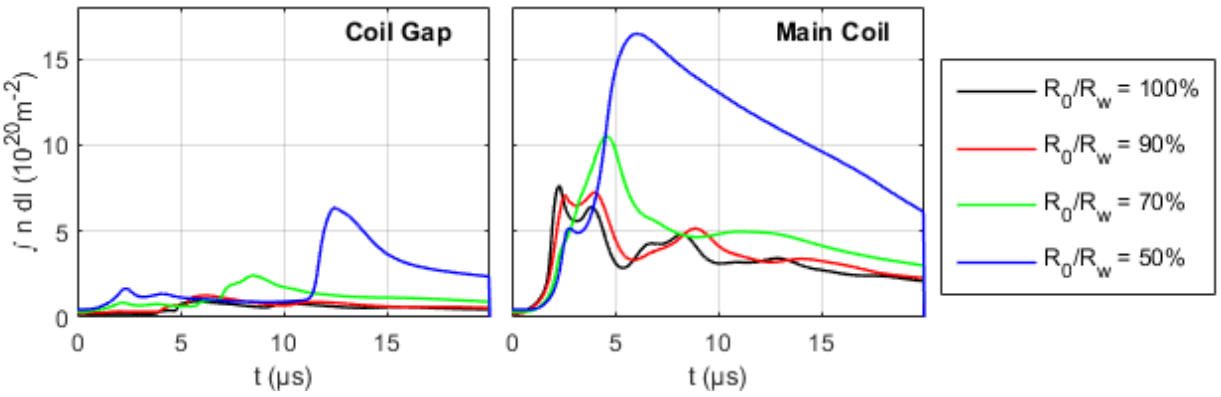

Figure 3.24: The simulation generated line integrated plasma density (NDL) for a sweep of the initial implosion radius with a localized ionization.

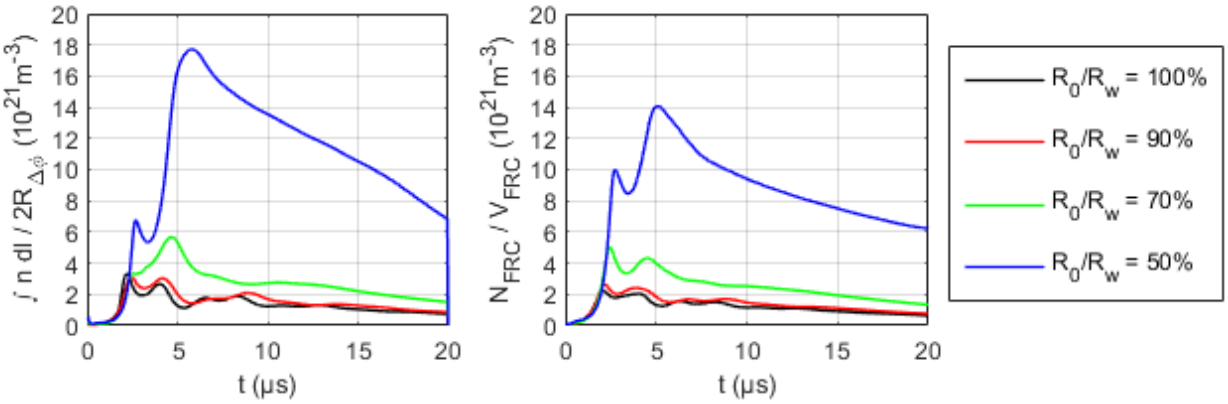

Figure 3.25: The average plasma density in the FRC for a sweep of the initial implosion radius with a localized ionization computed using (left) NDL and excluded flux radius and (right) using direct simulation results.

signal shows reduced magnitude over the similar uniform density case. Thus, the result from the NDL signal requires significant care in its interpretation, as it is strongly dependent on the FRC geometry.

3.2 Survey of the Effect of the Transport Coefficients in the FRC Formation

In order to understand the response of the FRC formation process due to various transport coefficients available in the Cygnus code, the static FRC formation problem from the previous section is used to perform a parametric sweep of the Cygnus transport coefficients. Again, the initial plasma density in the formation chamber is initialized after the bias flux is imbedded in the preionized plasma, so the dynamics of the bias field injection are neglected.

The case with a uniform 30% ionization from Section 3.1.1 is used as a reference simulation for the parametric sweep of the transport coefficients. In general, the default transport options discussed in Section 3.1 is used for coefficients not being varied in a sweep. Exceptions are noted. Sweeps of following transports are performed in this section: effective ionization potential (Section 3.2.1), Chodura resistivity (Section 3.2.2), Bohm resistivity (Section 3.2.3), isotropic viscosity (Section 3.2.4), and anisotropic viscosity (Section 3.2.5).

3.2.1 Effect of the Effective Ionization Potential on FRC Formation

As discussed in Section 2.2.5, in order to account for the energy loss associated with the electron impact excitation of neutrals during the ionization process, an effective ionization potential is used. In order to obtain the change in the FRC formation behavior caused by different levels of the effective ionization potential, a sweep of the following potential values is performed: 13.6 eV, 50 eV, 100 eV, 150 eV, 200 eV, and the electron temperature dependent dynamic effective ionization potential discussed in Section 2.2.5.

The resulting FRC separatrix shape at the time of the first minimum excluded flux radius is shown in Fig. 3.26. The time evolution of the FRC relative radius and the separatrix elongation is shown in Fig. 3.27. As the effective ionization potential is increased, smaller initial FRCs are produced due to the enhanced electron energy loss. The dynamic effective ionization case shows similar length as the higher potential cases, but with a larger radius. This is due to the fact that for the dynamic case, the effective ionization potential is large for low electron temperature, but small for high electron temperature. Thus, when the neutrals

are ionized with a radially imploded plasma layer, the effective ionization is lower due to the higher electron temperature in the imploded plasma layer.

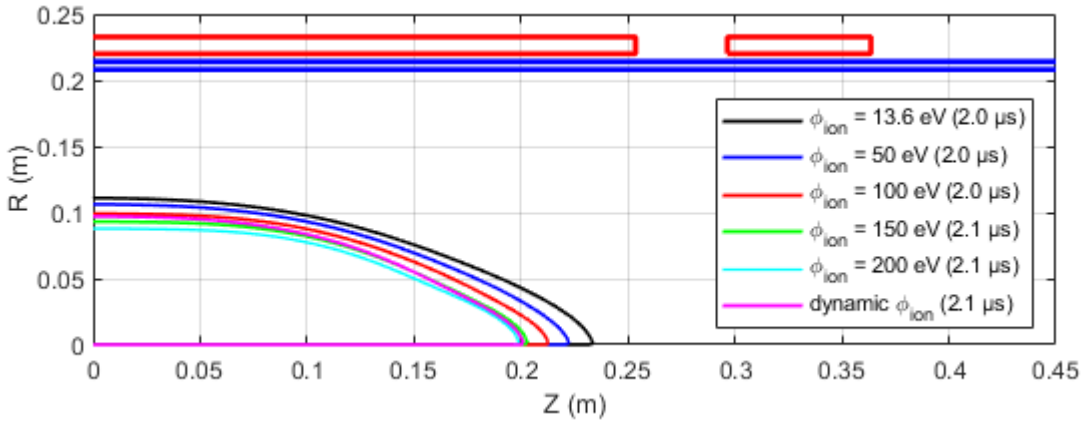

Figure 3.26: The shape of the FRC separatrix at the time of the first minimum excluded flux radius for a sweep of the effective ionization potential. Only right half of the separatrix shape is shown due to the symmetry of the result.

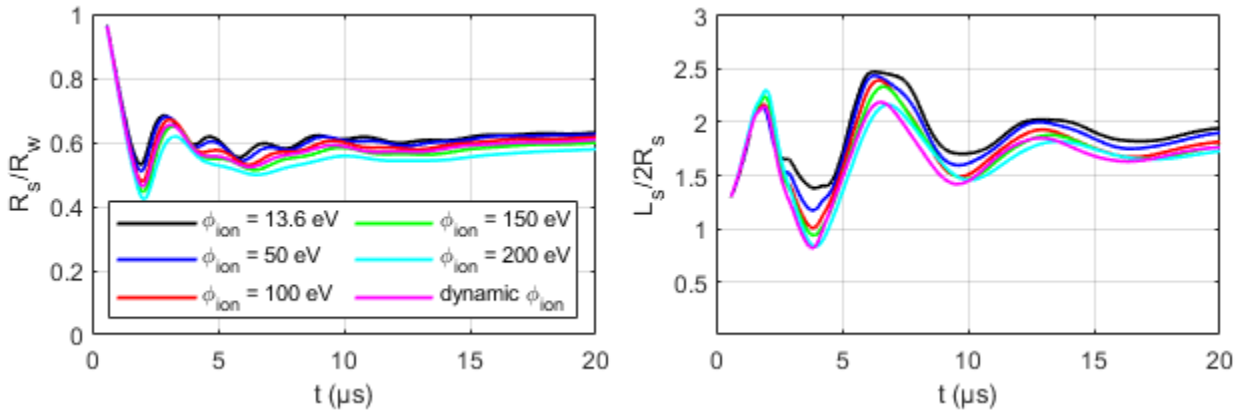

Figure 3.27: The time evolution of the FRC (left) relative radius and (right) separatrix elongation for a sweep of the effective ionization potential.

The time evolution of key FRC parameters computed from the simulation results is shown in Fig. 3.28. As it can be seen, the biggest effect of the effective ionization potential is a modification in the electron temperature. For the higher potential, the electron temperature

is capped until the ionization is completed. The particle inventory for all cases is similar, but for smaller potential, the ionization is completed earlier in time as it can be seen from the peaks of the particle inventory. The trapped flux is also larger for the lower effective ionization potential, as more plasma are generated quicker to prevent the bias flux from diffusing out.

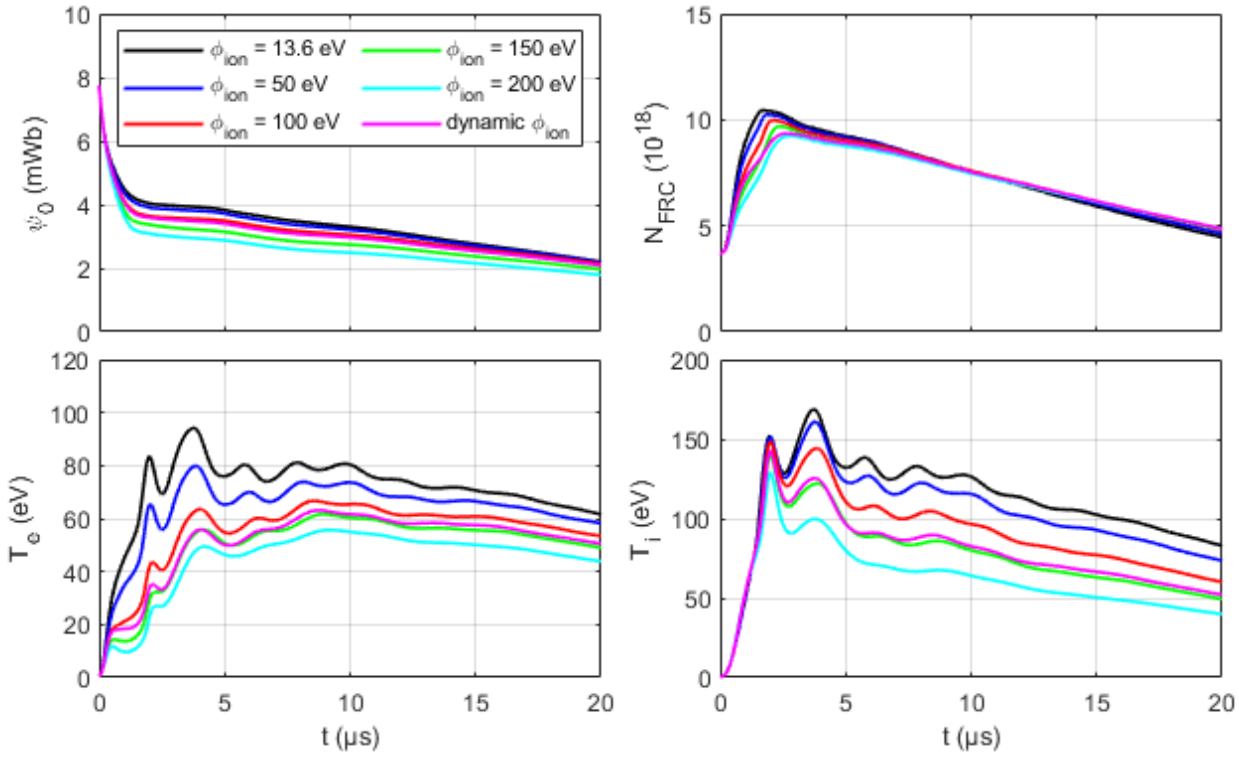

Figure 3.28: The time evolution of the FRC (top left) trapped flux, (top right) trapped particle, (bottom left) volume averaged electron temperature, and (bottom right) volume averaged ion temperature for a sweep of the effective ionization potential.

The simulation generated excluded flux signal is shown in Fig. 3.29. The lift-off flux is largely the same for all cases. This is due to the fact that no significant ionization occurs by the time the plasma lifts off from the wall; thus, differences in the effective ionization potential have negligible effects on the lift-off flux. The difference between the cases occurs at the first minimum of the excluded signal. Since significant ionizations occurred during the

radial implosion, the excluded flux signal begins to diverge at this point due to the difference in the trapped flux and particles. When the effective ionization potential is increased, the excluded flux is lower after the radial implosion, and successive oscillations are dampened.

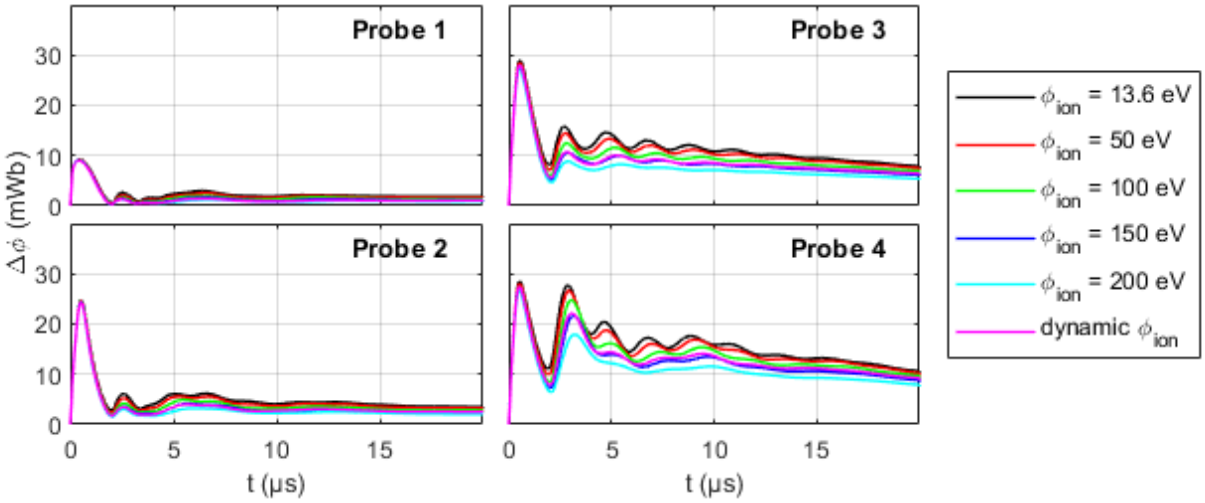

Figure 3.29: The simulation generated excluded flux measurement for a sweep of the effective ionization potential.

The simulation generated NDL signal is shown in Fig. 3.30. The general shape of the NDL signal is similar for all cases under the main coil, but larger signal is observed for the higher effective ionization potential. Since the particle inventory for all cases are similar, the difference in the NDL signal is caused by the difference in the FRC volume for each case. In general, the only change seen in the NDL signal due to the change in the effective ionization potential is the signal amplification due to smaller FRC radius.

From the simulation results, it can be seen that results from the dynamic effective ionization potential case generally fall between the 150 eV and 200 eV cases. Based on Fig. 2.1, this suggests that there are sufficient ionization processes occurring in the 2–3 eV electron temperature regime that cause this case to show behavior similar to the 150 eV and 200 eV cases. This suggests that while the electron temperature quickly increases during the radial implosion to a level where the dynamic effective ionization potential is below 20 eV, low

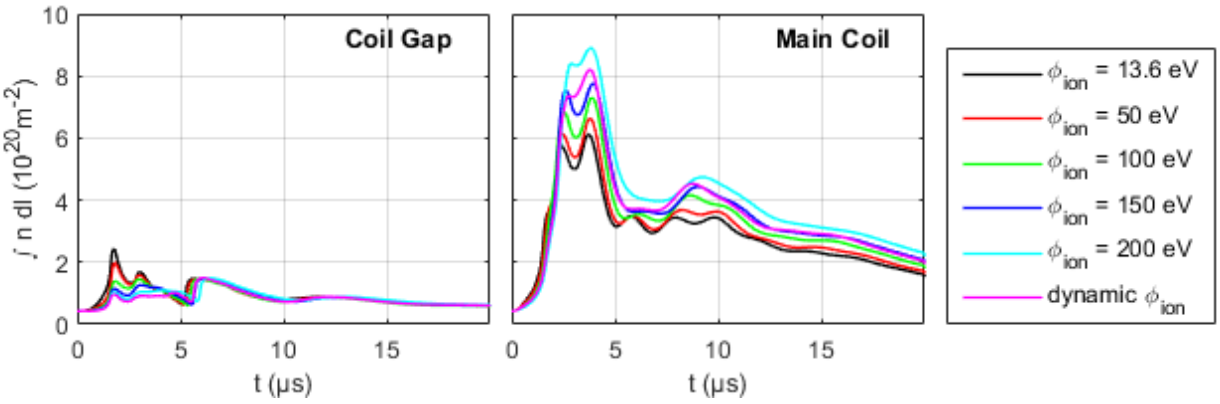

Figure 3.30: The simulation generated line integrated plasma density (NDL) for a sweep of the effective ionization potential.

temperature effects cannot be neglected in the ionization as the energy and particle losses are dominated in the low temperature regime.

In summary, increasing the effective ionization potential directly reduces the electron temperature in the FRC. As a result of the electron temperature decrease, ionization is reduced during the radial implosion, and smaller FRC is produced with lower trapped flux. The particle inventories for all cases are similar in the quiescent state after formation. In general, changes in FRC dynamics are driven by the modification in the electron temperature.

3.2.2 Effect of Chodura Resistivity on FRC Formation

Typically in the FRC modeling, the empirically adjustable Chodura resistivity is used to tune the computed FRC trapped flux to the experimentally observed value. Thus, choosing appropriate Chodura resistivity coefficients is important part of the FRC modeling process. In many cases, only the Chodura C-factor needs to be adjusted, and the Chodura F-factor of 3 is a reasonable choice. For fully ionized MHD calculations, Chodura resistivity is adjusted to obtain a reasonable trapped flux loss during the field reversal process.

To obtain the influence of the Chodura resistivity in the plasma-neutral model, a sweep of the Chodura resistivity is performed. Again, the previous uniform 30% ionization case is used

as a reference. Chodura C-factors of 0, 0.05, 0.5, 1.0, and 2.0 are used in the sweep. These values corresponds to the typical range of the Chodura C-factors used in MHD simulations of FRCs.

The resulting FRC separatrix shape at the time of the first minimum excluded flux radius is shown in Fig. 3.31. The time evolution of the FRC relative radius and separatrix elongation is shown in Fig. 3.32. In general, increased C-factor leads to a smaller FRC with reduced radius and length. While the FRC size is reduced, the profile of the formed FRC is not influenced strongly by the modification in the C-factor, as the separatrix elongation early in time is quite similar. For C-factors of 0 and 0.05, the axial contraction begins before the maximum radial implosion is obtained; thus, the profile at the time of first minimum excluded flux radius has a distinctive hump at $z = 0.15$.

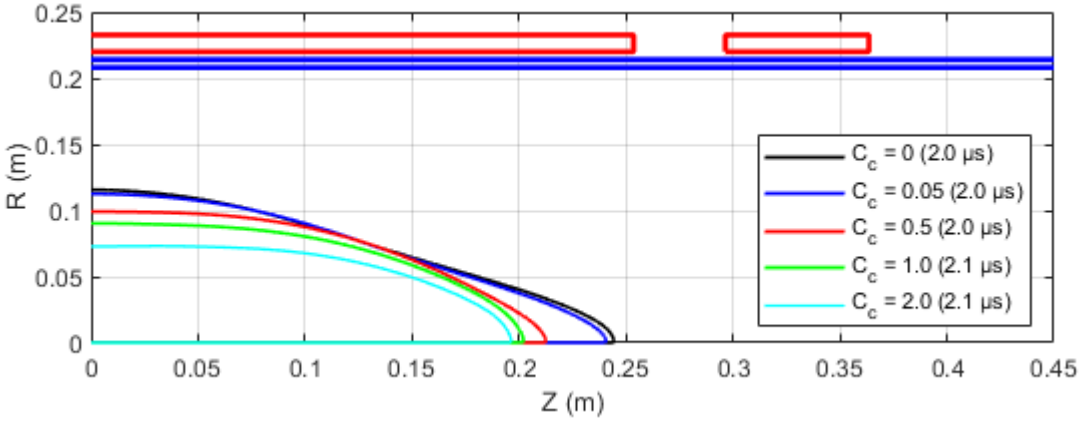

Figure 3.31: The shape of the FRC separatrix at the time of the first minimum excluded flux radius for a sweep of the Chodura C-factor. Only right half of the separatrix shape is shown due to the symmetry of the result.

The time evolution of key FRC parameters computed from the simulation results is shown in Fig. 3.33. As it can be seen, the amount of trapped flux is drastically reduced as the Chodura C-factor is increased. The particle inventory is reduced with the trapped flux because all of the frozen plasma on the outer flux line is lost when the resistivity is enhanced. The electron and ion temperatures for all cases are similar, but minor differences are created

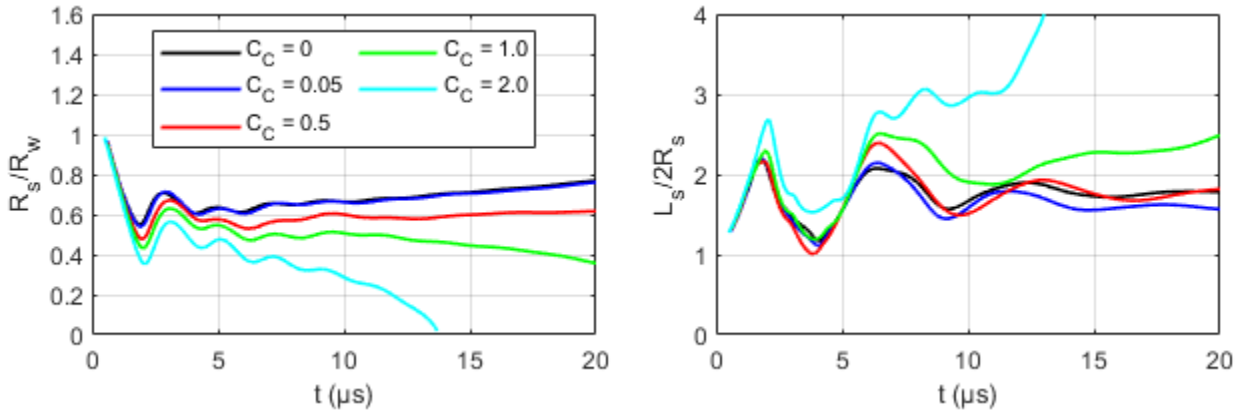

Figure 3.32: The time evolution of the FRC (left) relative radius and (right) separatrix elongation for a sweep of the Chodura C-factor.

due to different Joule heating. However, the temperatures of the quiescent FRC late in time are similar for all tested cases except for the Chodura C-Factor of 2.0, where the FRC decays resistivity by 14 μs.

The simulation generated excluded flux signal is shown in Fig. 3.34. It can be seen that the increased Chodura C-factor leads to smaller excluded flux overall, including the lift-off flux. The oscillation in excluded flux signals due to the radial and axial oscillation of the FRC is similar for all cases, and the differences are caused by the time dependent decay of the excluded flux signal for those with higher C-factor. Thus, increase in the Chodura resistivity does not lead to damping of the FRC oscillation after the radial implosion.

The simulation generated NDL signal is shown in Fig. 3.35. While the volume of the FRC is reduced as the Chodura C-factor is increased, the particle inventory is also reduced to compensate the loss in volume. Thus, despite the smaller FRC volume, the NDL signal for the higher Chodura C-factor is smaller in magnitude. The late time reduction in the NDL signal is caused by the enhanced resistive loss of the trapped flux. Similar decay can also be observed in the excluded flux signal.

In summary, the Chodura resistivity allows one to control the size of the FRC without significantly altering its profile. With Chodura resistivity, the flux and particle losses from

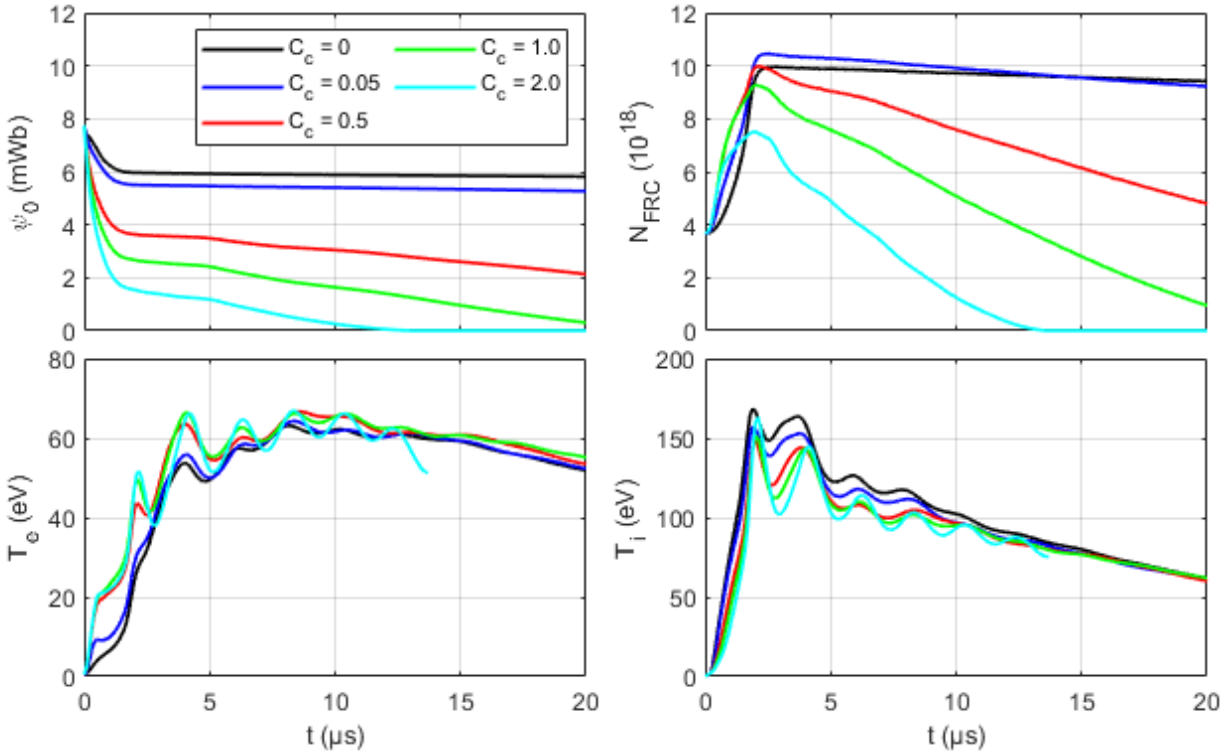

Figure 3.33: The time evolution of the FRC (top left) trapped flux, (top right) trapped particle, (bottom left) volume averaged electron temperature, and (bottom right) volume averaged ion temperature for a sweep of the Chodura C-factor.

the FRC caused by resistivity are tightly linked. As a result, the increase in the Chodura resistivity does not cause significant changes to the volume averaged density of the formed FRC. Thus, while the trapped flux and particle inventory are different for the tested values of the C-factor, the elongation of the FRC is largely unmodified, as the general profile of the FRC for all cases are similar. In general, the behavior of the Chodura resistivity is unmodified by the presence of the neutrals. Thus, the Chodura resistivity can be tuned similar to the fully ionized MHD simulations to match experimental flux and particle losses in simulations.

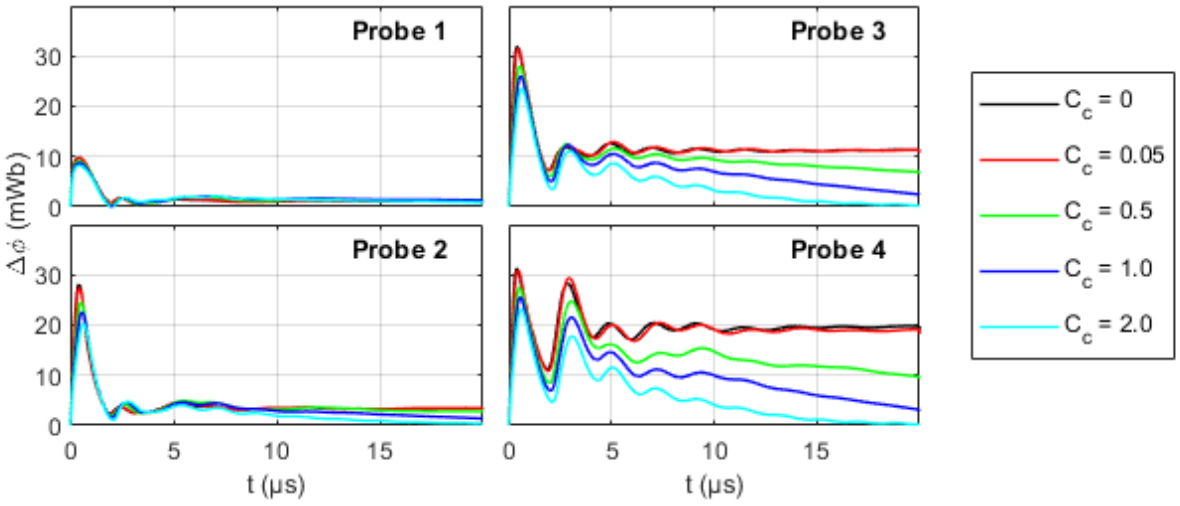

Figure 3.34: The simulation generated excluded flux measurement for a sweep of the Chodura C-factor.

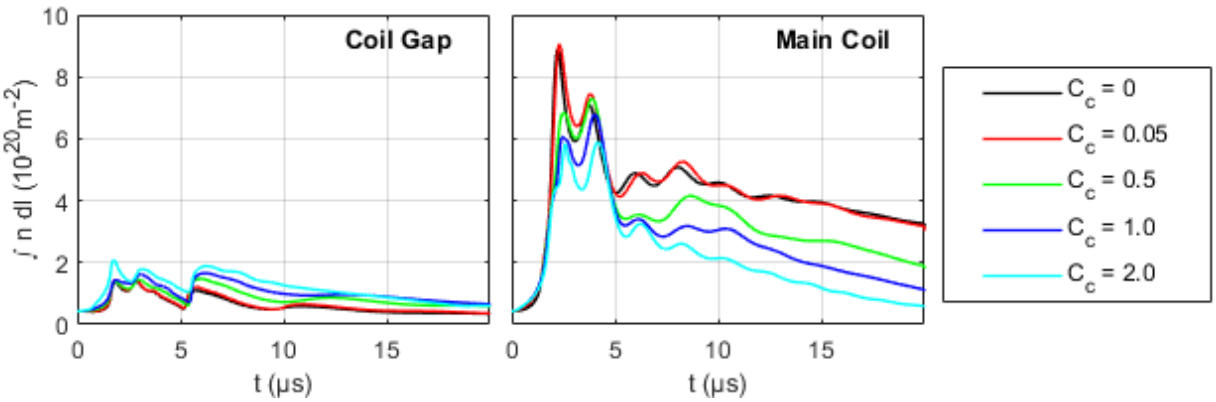

Figure 3.35: The simulation generated line integrated plasma density (NDL) for a sweep of the Chodura C-factor.

3.2.3 Effect of Bohm Resistivity on FRC Formation

Bohm diffusion is a common form of an anomalous transport used for plasma systems that have poor confinement characteristics. Such scaling may be observed when there is a high neutral content in the system and the global transport processes are neutrally dominant. For the FRC formation process, this condition is encountered in systems with low ionization.

To obtain the influence of the Bohm resistivity in the plasma-neutral model, a sweep of Bohm resistivity is performed. Again, the previous uniform 30% ionization case is used as a reference. The anomalous Chodura resistivity is disabled for this sweep so the effect from the anomalous Bohm resistivity can be isolated. A multiplier on the Bohm resistivity of 0, 1, 5, 10, and 20 are used.

The resulting FRC separatrix shape at the time of the first minimum excluded flux radius is shown in Fig. 3.36. The time evolution of the FRC relative radius and the separatrix elongation is shown in Fig. 3.37. In general, since an increase in the Bohm resistivity is enhancement of the resistive effects similar to the Chodura resistivity, the FRC size is reduced. Compared to the Chodura resistivity, increase in Bohm resistivity leads to a shorter FRC with larger radius. Thus, it leads to formation of a more elliptic FRC.

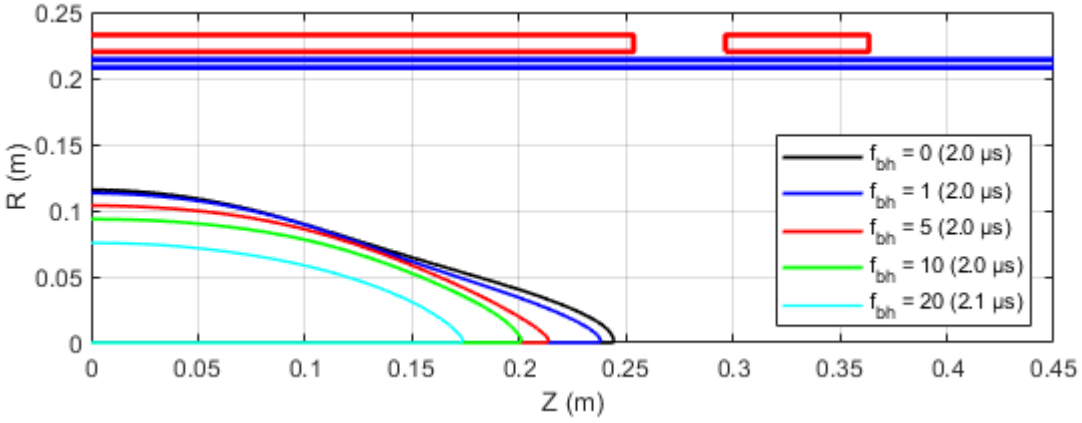

Figure 3.36: The shape of the FRC separatrix at the time of the first minimum excluded flux radius for a sweep of the Bohm multiplier. Only right half of the separatrix shape is shown due to the symmetry of the result.

The time evolution of key FRC parameters computed from the simulation results is shown in Fig. 3.38. For all high Bohm case, the FRC decays away before the completion of the simulation. Unlike the Chodura resistivity, the Bohm resistivity is not dynamically adjusted by FRC dynamics. For Chodura resistivity, as the FRC reaches quiescent state, the resistivity is naturally reduced from its peak value during the radial implosion. For Bohm

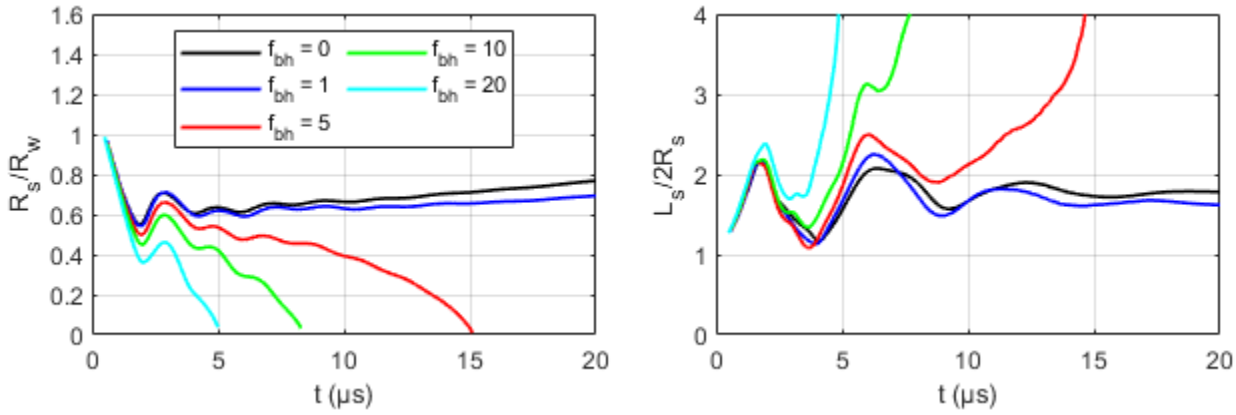

Figure 3.37: The time evolution of the FRC (left) relative radius and (right) separatrix elongation for a sweep of the Bohm multiplier.

resistivity, no such mechanism for dynamic adjustment exists. Thus, even after the FRC reaches quiescent state, the Bohm resistivity continues to shed trapped flux and particles, causing rapid resistive decay of the FRC.

Due to the enhanced resistivity, the electron temperature is higher for high Bohm cases. This behavior is distinctively different from the anomalous Chodura resistivity, where the change in the electron temperature was negligible late in time for all cases. As such, the initial ionization proceeds quicker for the high Bohm case as it can be seen in the rapid increase in the particle inventory early in time. However, due to the large flux loss due to the high resistivity, the enhanced initial ionization is offset by the particle loss on the outer flux surface.

The simulation generated excluded flux and NDL signal are shown in Fig. 3.39 and Fig. 3.40, respectively. Similar to the Chodura resistivity, the excluded flux is reduced overall when the Bohm resistivity is increased. A similar decay profile is seen in the late time behavior of the excluded flux due to the resistive decay process. Again, the increase in the anomalous resistivity does not enhance the damping of the oscillation in the excluded flux signal. One major difference compared to the Chodura resistivity is the more aggressive loss in the NDL signal as the Bohm resistivity is increased. While the increase in the Chodura

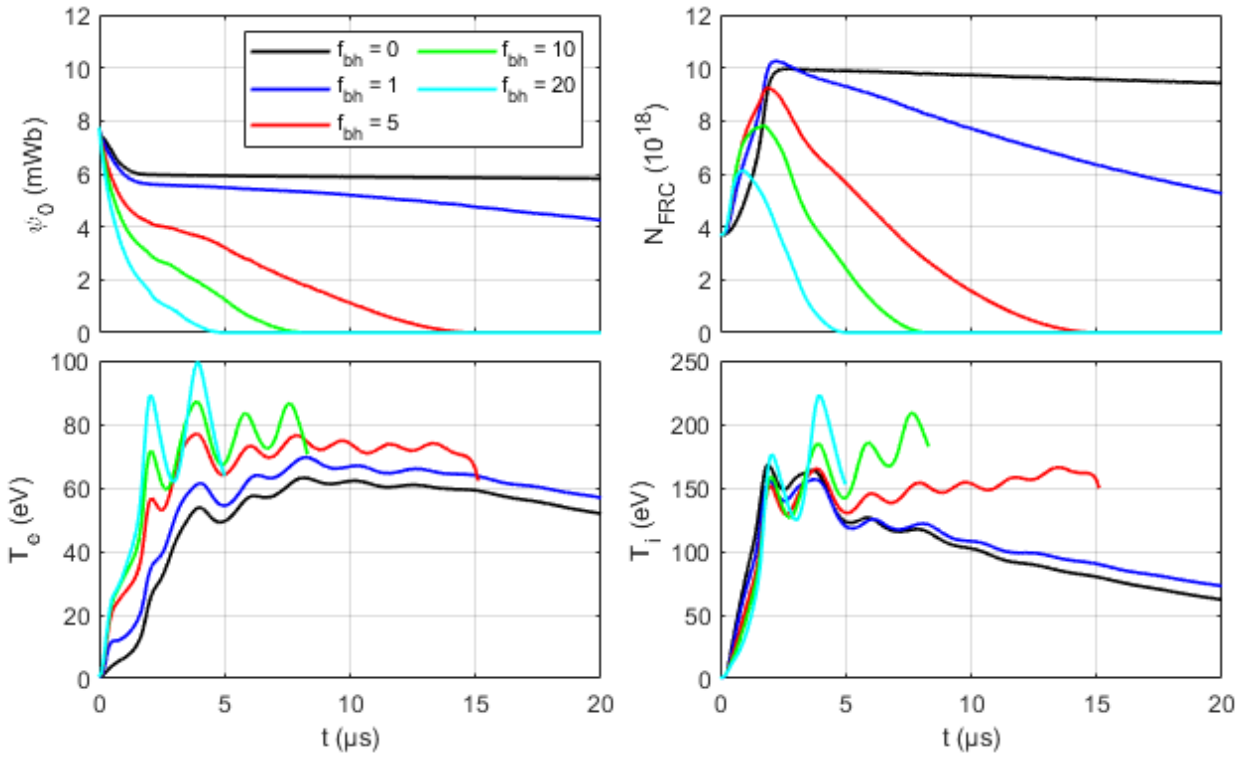

Figure 3.38: The time evolution of the FRC (top left) trapped flux, (top right) trapped particle, (bottom left) volume averaged electron temperature, and (bottom right) volume averaged ion temperature for a sweep of the Bohm multiplier.

resistivity did not lead to major changes in the time dynamics of the volume averaged FRC plasma density, the increase in Bohm resistivity leads to reduction of the volume averaged plasma density. This suggests that the particle loss is faster than the flux loss when using Bohm resistivity.

In summary, similar to the Chodura resistivity, increase in Bohm resistivity leads to smaller FRCs with lower trapped flux and particles. Compared to the Chodura resistivity, more elliptic FRCs are produced. Unlike the Chodura resistivity, the losses associated with Bohm resistivity are persistent throughout the entire simulation. Thus, for the high Bohm case, the FRC decays resistivity before the end of the simulation. In general, the Bohm resistivity leads to larger particle loss compared to flux loss; thus, the rate of the average

density loss in the FRC is enhanced when the Bohm coefficient is increased.

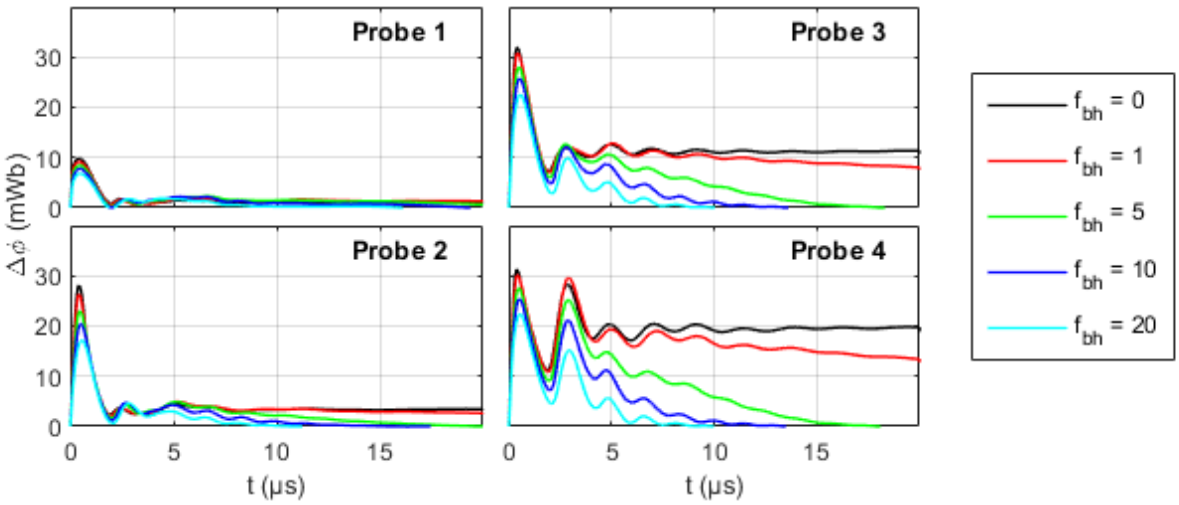

Figure 3.39: The simulation generated excluded flux measurement for a sweep of the Bohm multiplier.

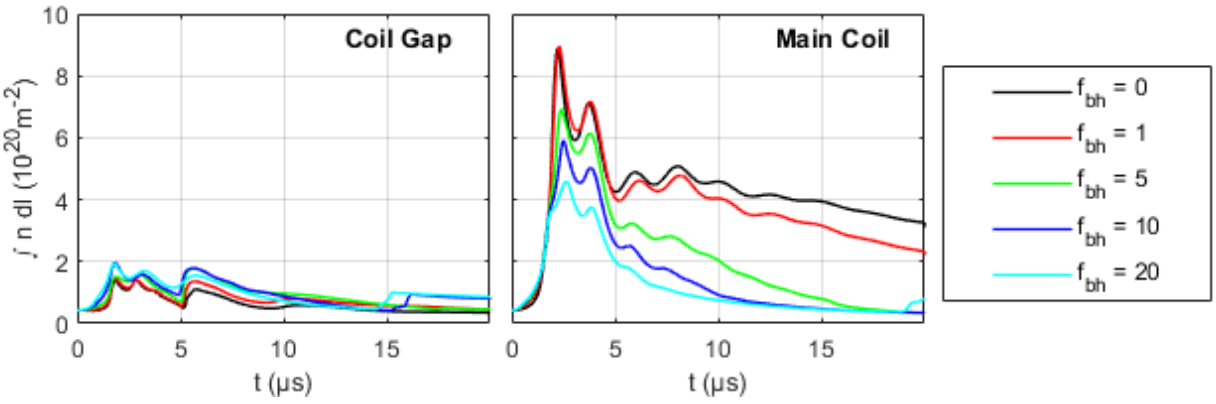

Figure 3.40: The simulation generated line integrated plasma density (NDL) for a sweep of the Bohm multiplier.

3.2.4 Effect of Isotropic Viscosities on FRC Formation

The isotropic viscosity is an important parameter to control the dynamics of the FRC formation process. When the isotropic viscosity is increased, the radial and axial oscillation of the FRC is suppressed and the formation dynamic is less violent. To obtain the influence of

isotropic viscosities in the plasma-neutral model, a sweep of the kinematic isotropic viscosities is performed. Again, the previous uniform 30% ionization case is used as a reference. Note that the viscosity of the plasma in the open field line and that of the neutrals are kept to the same value as the reference case. Only the viscosity in the closed field line region is modified in this test. A sweep of the kinematic isotropic viscosities with 10, 100, 500, 1000, 2000, and 4000 m^2/s is performed.

The resulting FRC separatrix shape at the time of the first minimum excluded flux radius is shown in Fig. 3.41. The time evolution of the FRC relative radius and the separatrix elongation is shown in Fig. 3.42. For the higher viscosity case, the FRC is larger because the implosion velocity is smoothened by the high viscosity. As such, the implosion kinetic energy is converted into thermal energy during the radial implosion, leading to a creation of a larger imploded FRC.

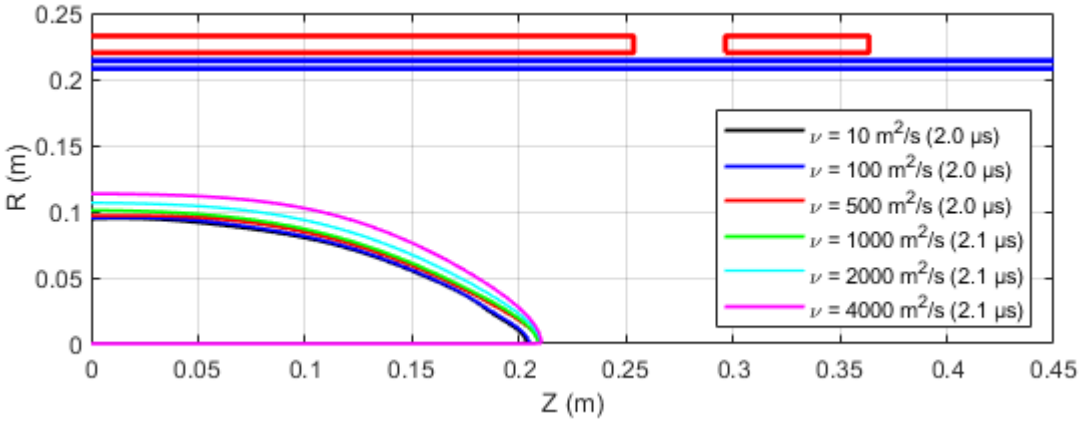

Figure 3.41: The shape of the FRC separatrix at the time of the first minimum excluded flux radius for a sweep of the kinematic isotropic viscosities. Only right half of the separatrix shape is shown due to the symmetry of the result.

As it can be seen in Fig. 3.42, the dynamics of the radial and axial oscillations are significantly dampened for the high viscosity case. In general, their average behavior is unmodified by the increase in the isotropic viscosity. This can also be seen in the time evolution of key FRC parameters computed from the simulation results that is shown in

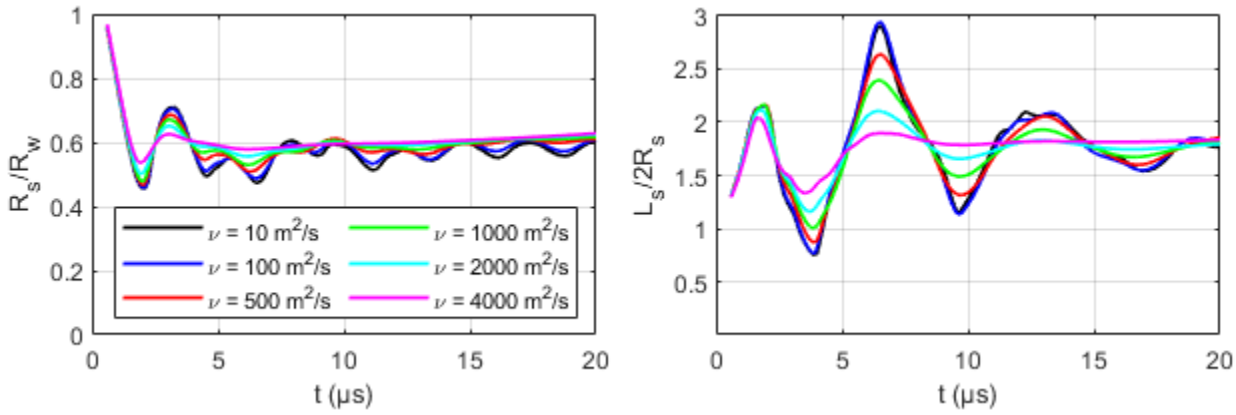

Figure 3.42: The time evolution of the FRC (left) relative radius and (right) separatrix elongation for a sweep of the kinematic isotropic viscosities.

Fig. 3.43. In general, the average behavior of all quantities except for the ion temperature is similar. The reduction in the trapped flux and particles for the low viscosity case is due to the enhanced flux and particle losses during the radial and axial oscillations of the FRC.

The difference in the ion temperature is due to the enhanced conversion of the FRC kinetic energy into the ion thermal energy for the high viscosity case. Since the ion heating in the FRC is caused by the conversion from the FRC kinetic energy, when the viscosity is increased, the energy loss associated with the dynamic oscillation is reduced as it is all converted into ion thermal energy.

The simulation generated excluded flux and NDL signals are shown in Fig. 3.44 and Fig. 3.45, respectively. As it can be seen, the signal for the high viscosity case is smooth with negligible FRC oscillation in the excluded flux signal. Note that the lift-off flux is largely the same for all cases. This is due to the fact that at the time of the wall lift-off, the plasma has not gained much kinetic energy on which the viscosity can influence. After the lift-off, the excluded flux is larger for the high viscosity case, which reflects the fact that the produced FRC is larger.

From the NDL, one can see that the higher viscosity leads to a flatter behavior due to less violent radial implosion. As such there are no NDL signal amplification due to density

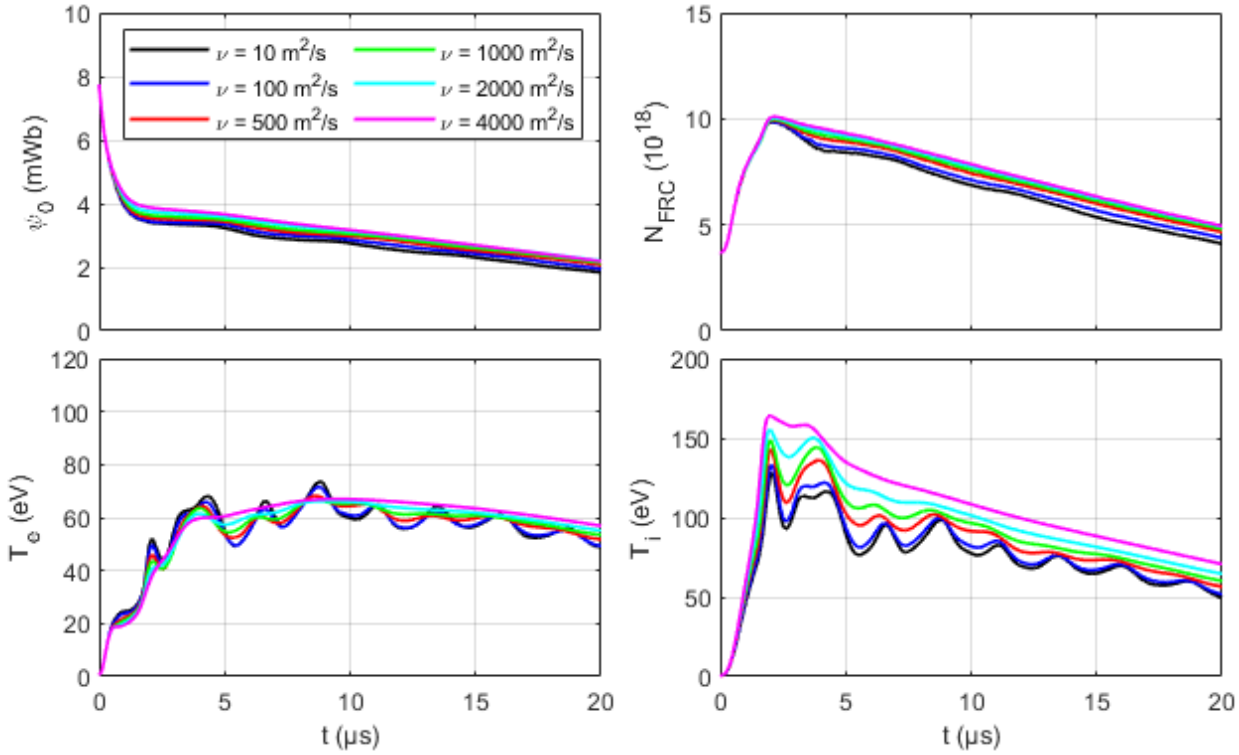

Figure 3.43: The time evolution of the FRC (top left) trapped flux, (top right) trapped particle, (bottom left) volume averaged electron temperature, and (bottom right) volume averaged ion temperature for a sweep of the kinematic isotropic viscosities.

pileup near the axis. Thus, while higher viscosity case generally has slightly more particle inventory, the NDL signal is smaller early in time. In the later time when the FRC reaches quiescent state, the NDL signal is largely the same for all cases, which reflects the fact that the resulting FRC density is unmodified by the choice of the isotropic viscosities.

In summary, adjusting isotropic viscosity used in the simulation can modify the resulting post-implosion oscillatory dynamics of the FRC. Besides the ion temperature, the remaining FRC parameters are largely uninfluenced by the isotropic viscosity, thus it can typically be adjusted independently of other transport coefficients.

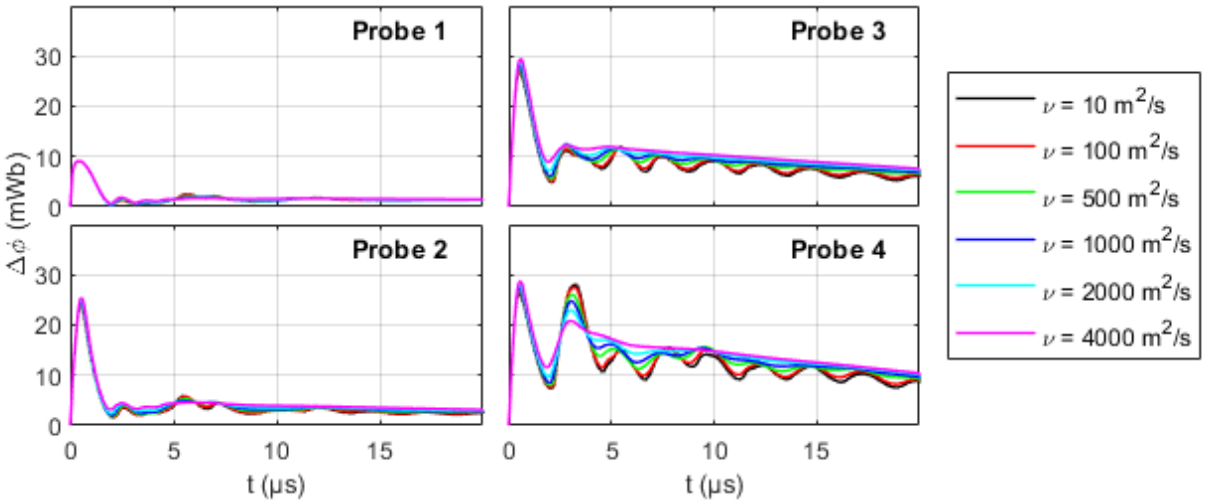

Figure 3.44: The simulation generated excluded flux measurement for a sweep of the kinematic isotropic viscosities.

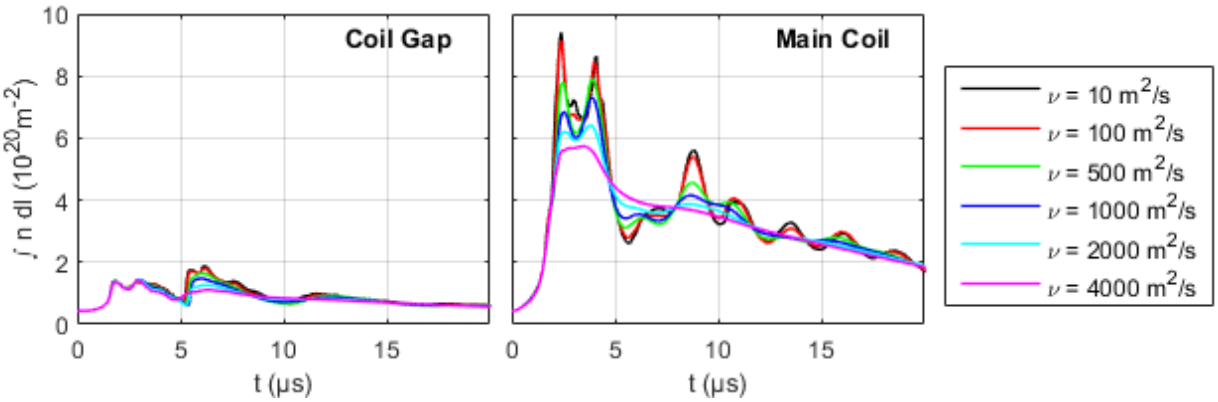

Figure 3.45: The simulation generated line integrated plasma density (NDL) for a sweep of the kinematic isotropic viscosities.

3.2.5 Effect of Anisotropic Viscosities on FRC Formation

Due to the presence of the local magnetic field, an anisotropy is introduced to the local transport. To investigate the effect of the anisotropic viscosity in the FRC formation process, a sweep of various anisotropic viscosity conditions is performed. In the sweep, following anisotropic viscosity conditions are performed: perpendicular kinematic viscosity of $10^2\,\mathrm{m}^2/\mathrm{s}$

and parallel kinematic viscosity of $10^3\,\mathrm{m}^2/\mathrm{s}$ ($\nu = 10^2$-10^3), perpendicular kinematic viscosity of $10^3\,\mathrm{m}^2/\mathrm{s}$ and parallel kinematic viscosity of $10^3\,\mathrm{m}^2/\mathrm{s}$ ($\nu = 10^3$-10^3), perpendicular kinematic viscosity of $10^2\,\mathrm{m}^2/\mathrm{s}$ and parallel kinematic viscosity of $10^4\,\mathrm{m}^2/\mathrm{s}$ ($\nu = 10^2$-10^4), perpendicular kinematic viscosity of $10^3\,\mathrm{m}^2/\mathrm{s}$ and parallel kinematic viscosity of $10^4\,\mathrm{m}^2/\mathrm{s}$ ($\nu = 10^3$-10^4), and Braginskii viscosity.

The resulting FRC separatrix shape at the time of the first minimum excluded flux radius is shown in Fig. 3.46. The time evolution of the FRC relative radius and the separatrix elongation is shown in Fig. 3.47. It can be seen that at the time of the maximum radial implosion, the resulting FRC length is controlled by the value of the parallel viscosity; the influence due to the perpendicular viscosity seems to be largely negligible at this time.

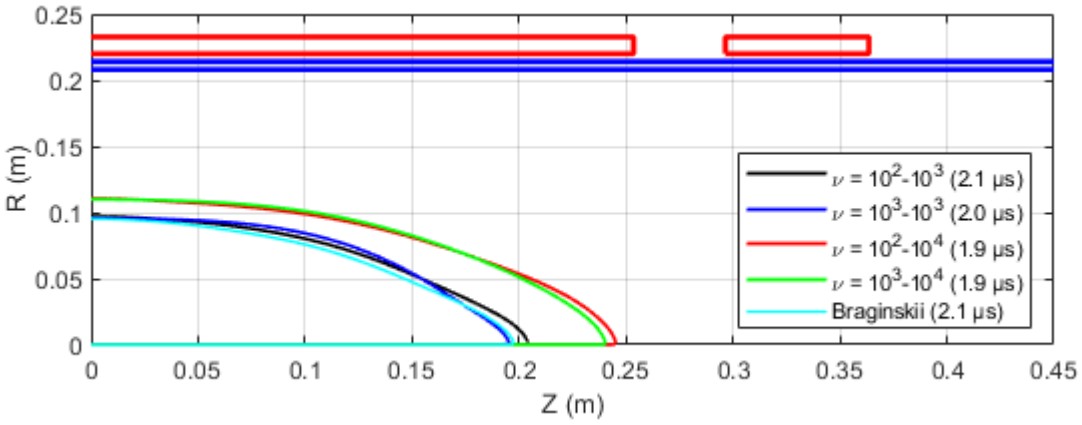

Figure 3.46: The shape of the FRC separatrix at the time of the first minimum excluded flux radius for a sweep of the anisotropic viscosities. Only right half of the separatrix shape is shown due to the symmetry of the result.

As it can be seen in Fig. 3.47, the modification in viscosity does not affect the long time behavior of the FRCs. For all cases, the FRC relative radius and elongation all converge to the same value. Unlike the shape of the FRC at the time of the maximum radial implosion, the time dependent behavior of the FRC elongation seems to be governed by both the parallel and perpendicular viscosity, as there are no clear separation of the elongation results based on either the parallel or perpendicular value.

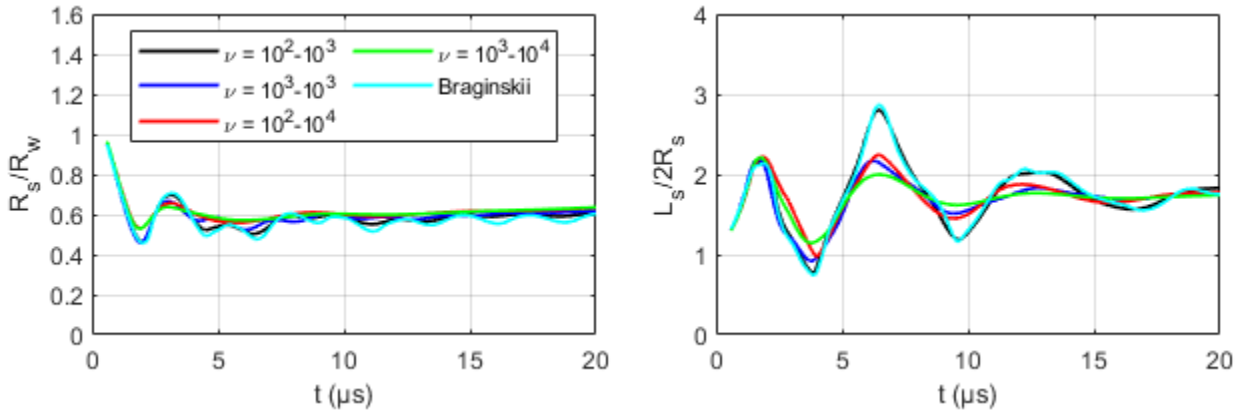

Figure 3.47: The time evolution of the FRC (left) relative radius and (right) separatrix elongation.

The time evolution of key FRC parameters computed from the simulation results is shown in Fig. 3.48. Again, same general behavior observed for the isotropic viscosity is seen for the anisotropic viscosity: when the viscosity is increased, the FRC oscillations are reduced. As observed in the time evolution of the FRC geometry, the value of the parallel viscosity has the greatest effect in smoothing FRC dynamics. In general, the Braginskii viscosity case shows the least viscous behavior, as it has the lowest ion temperature, trapped flux, and particle inventory.

The simulation generated excluded flux and NDL signals are shown in Fig. 3.49 and Fig. 3.50, respectively. Again, similar dampening effects can be seen for the high viscosity case. In the excluded flux signal, effects of the anisotropic viscosities are minor. The global average profile is largely set by the parallel viscosity while the perpendicular viscosity modifies the oscillation frequency of the dynamics. The NDL signal does not offer much distinction between the anisotropic viscosity cases other than modifications in some of the peaks. Again, the results suggest that Braginskii viscosity for the simulated problem is less viscous compared with the lowest viscosity case tested (10^2-10^3) but is comparable.

In summary, anisotropic viscosity shows similar effects as the isotropic viscosity tested in the previous section. Depending on the choice of anisotropy, the oscillation behavior of the

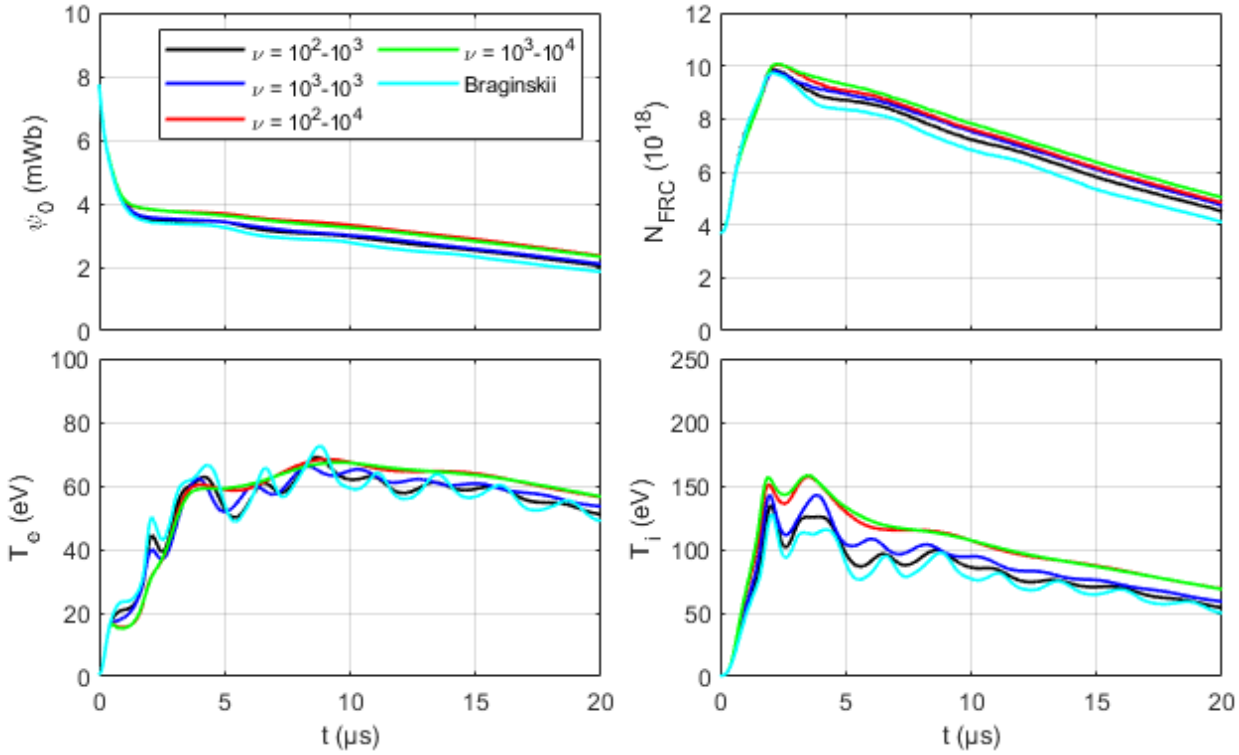

Figure 3.48: The time evolution of the FRC (top left) trapped flux, (top right) trapped particle, (bottom left) volume averaged electron temperature, and (bottom right) volume averaged ion temperature for a sweep of the anisotropic viscosities.

FRC after the radial implosion can be controlled. The shape of the FRC at the time of the maximum radial implosion seems to be only controlled by the parallel viscosity. While the anisotropic viscosity offers more control of the FRC dynamics, in most cases when matching experimental results, isotropic viscosities are sufficient. Since there are many unknowns that can potentially influence the experimentally measured excluded flux and NDL signal, the general goal in selecting viscosity value in the simulation is to match the damping profile of the FRC oscillation post implosion. Thus, for this purpose, isotropic viscosities are more useful as their behaviors are better understood than the anisotropic case.

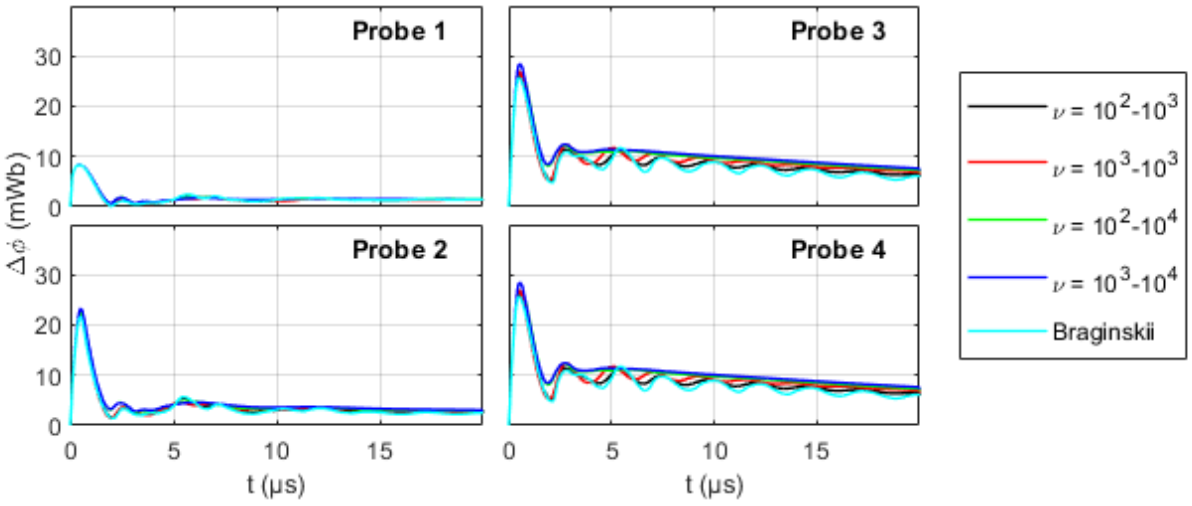

Figure 3.49: The simulation generated excluded flux measurement for a sweep of the anisotropic viscosities.

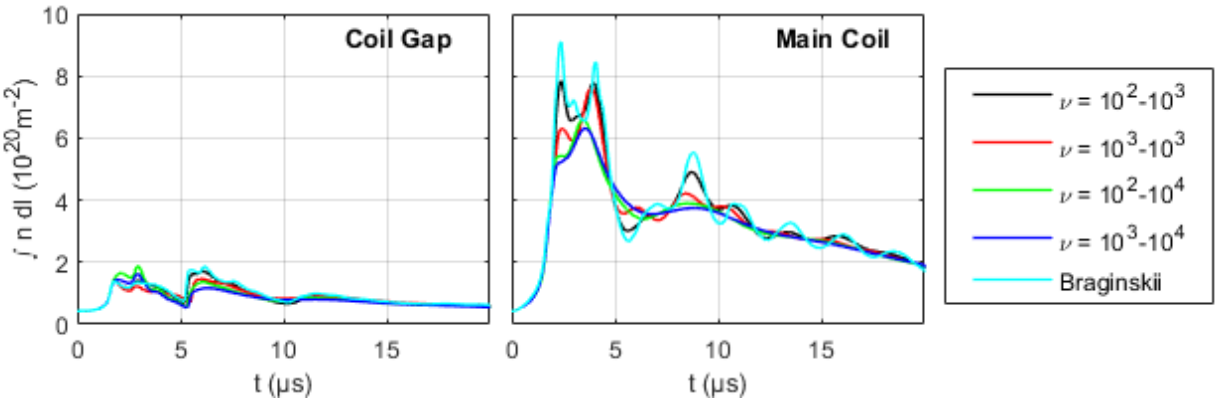

Figure 3.50: The simulation generated line integrated plasma density (NDL) for a sweep of the anisotropic viscosities.

3.3 FRC Formation and Translation with Dynamic Formation

In order to understand effects of neutrals in the dynamic formation process of FRCs, a series of FRC formation and translation simulations is performed with the initial ionization level varied similar to Section 3.1. Similar to the previous calculations, the initial plasma density in the formation chamber is initialized after the bias flux is imbedded in the preionized

plasma in the formation section.

Again, the idealized problem is set up to be simple but reasonable for typical dynamic FRC formation and translation processes. To simulate the dynamic formation process, the formation chamber geometry from Section 3.1 is modified by replacing the long formation coil with five discrete coils with the same dimension as the two trigger coils. A long cylindrical coil is attached to one end of the formation section, where the dynamically formed FRC is translated into. The geometry of the system used for this problem is shown in Fig. 3.51. The initial magnetic flux topology at the start of the simulation is also shown on the same figure.

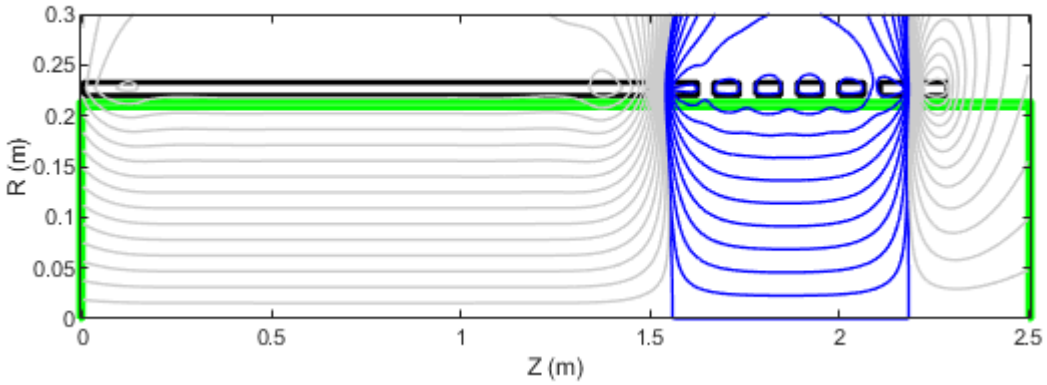

Figure 3.51: Simplified formation and translation chamber geometry used for the simulation. The initial magnetic flux topology due to the bias fields are shown with the negative flux shown in blue.

The last formation coil furthest from the translation section is initialized with a forward flux of 14 mWb, while the remaining six formation coils are initialized with a reversed flux of 11 mWb. The translation coil is initialized with a forward flux of 20 mWb. In essence, the last formation coil and translation coil serve as the trigger coils for this simulation to produce an initial cusp field. The same circuit used in Section 3.1 is used for the formation coils. A flux swing of 60 mWb is used for the last formation coil, while that of 55 mWb is used for the remaining formation coils. The last two formation coils furthest from the

translation section are fired at the start of the simulation, and each subsequent coil is fired 0.2 µs apart, working its way towards the translation coil. The translation coil is never fired, so the initial bias flux is maintained throughout the simulation.

Two cases are investigated in this section, first is a case where the formation and translation section are statically filled with a uniform density of gas. The initial preionization is assumed to occur only in the formation section, so the remainder of the device is initialized with neutrals. The second is a case where the formation chamber is dynamically filled with a uniform density of gas. For this case, only the formation chamber begins with a uniform gas block and the remainder of the device is assumed to be under vacuum. For both cases, fill density of $3.5 \times 10^{20}\,\mathrm{m}^{-3}$ is used where gas exists. A sweep of the initial ionization levels in the formation section of 100%, 90%, 70%, 50%, 30%, and 10% ionization is performed. The remaining simulation setup is the same as what was described previously in Section 3.1.

The separatrix shape of the FRC at the time 3 µs into the simulation is shown in Fig. 3.52. In the dynamic formation process, it is hard to define a single time where the FRC reaches maximum radial implosion; thus, 3 µs is selected as a reasonable time where the FRC is formed and is translating for all simulated cases. Since the gas fill in the formation section is equivalent for both the static and the dynamic fill case, the formed FRCs are similar in profile. Due to the additional background neutrals, there is additional drag in the formation process caused by additional ionizations. As such, the formed FRC has a longer tail in the static fill case. In addition, since there are no upstream neutrals impeding the translation of the formed FRC in the dynamic fill case, the front of the FRC extends further into the translation section.

For both simulations, once the formed FRC enters the translation section, the FRC reaches a quiescent state with a finite bulk FRC geometry. Thus, to compare the FRC profile in the translation section, the separatrix shape at the time 15 µs into the simulation is shown in Fig. 3.53. In general, the FRC is farther back in the translation section for the static fill case, as the neutral background provides a drag to the translating FRC. As a result of this drag force, the FRC is shorter in length for the static fill case. In addition, the front

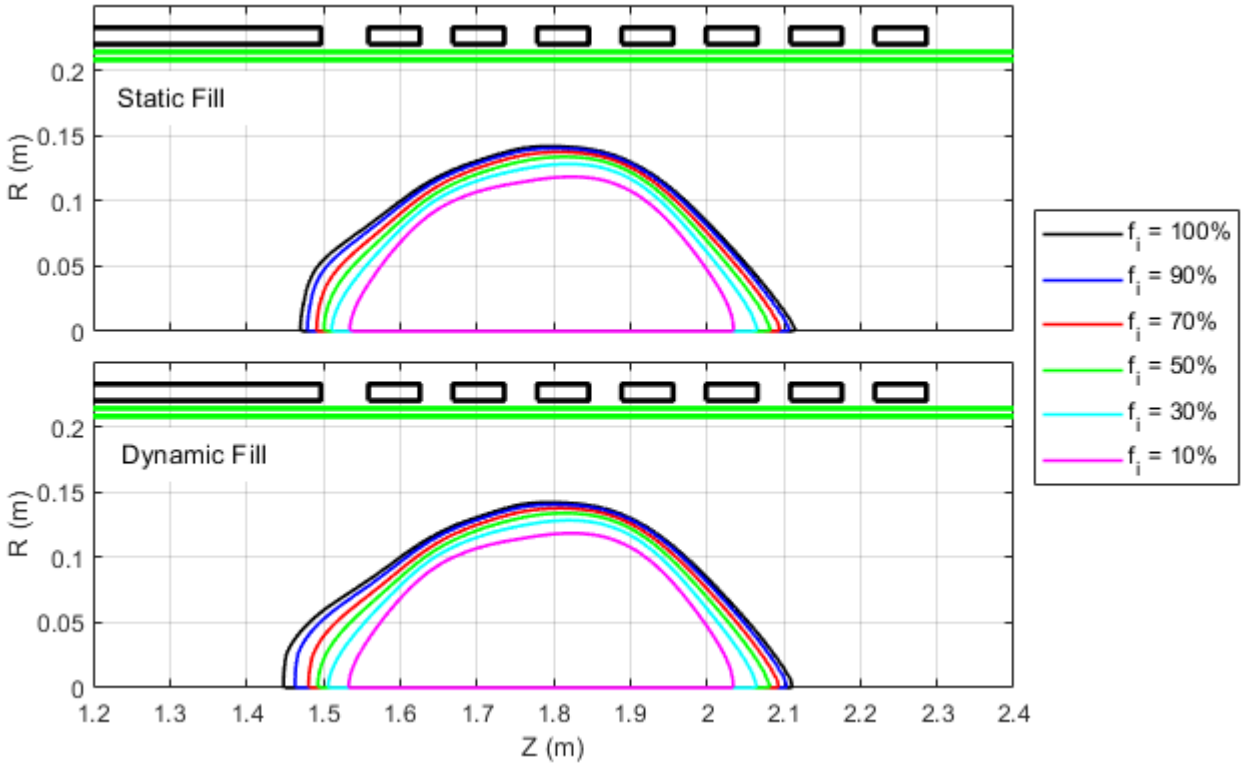

Figure 3.52: The shape of the FRC separatrix in the formation section at 3 μs for (top) static fill and (bottom) dynamic fill case for dynamic FRC formation.

of the FRC is more elliptic with a flat profile near the back due to the neutral interaction. On the other hand, for the dynamic fill case, since there are no initial neutral gas in the translation section, the translating FRC is more symmetric in its shape.

The time evolution of the FRC relative radius and separatrix elongation is shown in Fig. 3.54. As noted earlier, the FRC length is longer in the dynamic fill case as the elongation is generally larger. The radius of the FRC is similar for the two cases, but the static fill case is slightly larger later in time in the translation section. Note that the two cases agree reasonably with each other until later in time when the FRC enters the translation section. As such, the differences in the FRC geometry are caused by the presence of the background neutrals in the translation section.

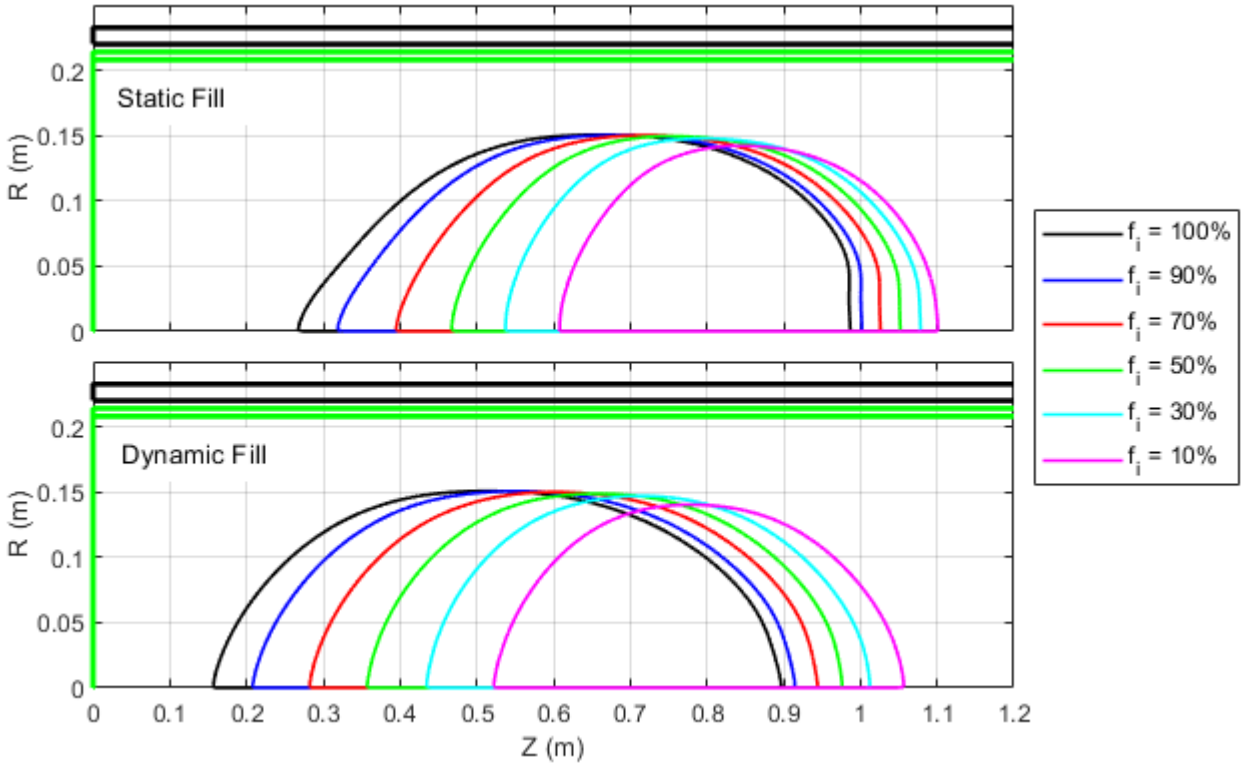

Figure 3.53: The shape of the FRC separatrix in the translation section at 15 µs for (top) static fill and (bottom) dynamic fill case for dynamic FRC formation.

The time evolution of the FRC volume averaged velocity and temperature is shown in Fig. 3.55. The drag effect from the background neutrals in the translation section is clear, as the velocity for the static fill case decreases once it reaches maximum in the translation section; for the dynamic fill case, the velocity remains mostly constant. For the case with lower initial ionization in the formation section, the final velocity in the translation section is lower. This is caused by two effects. First, when the FRC is being formed dynamically, a larger FRC is produced for the case with higher ionization. As such, the FRC couples better to the external circuit inductively, and the magnetic field is more efficient at transferring axial momentum to the FRC.

Second, when the FRC is entering the translation section, due to the difference in the

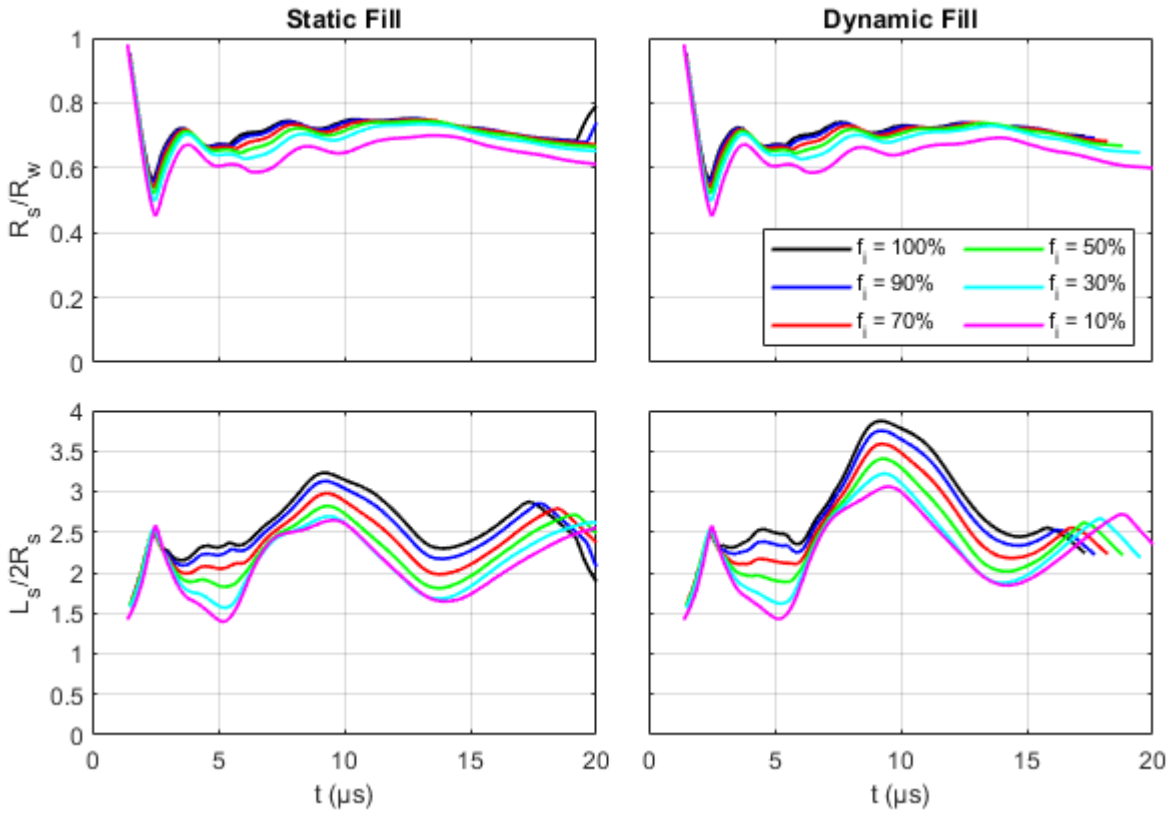

Figure 3.54: The time evolution of the FRC (top) relative radius and (bottom) separatrix elongation for (left) static fill and (right) dynamic fill case.

magnetic field magnitude for this simulation setup, the FRC expands to reach equilibrium with the local axial field. As such, the FRC thermal energy is converted into kinetic energy when entering the translation section. This effect can be seen in Fig. 3.55, as the ion temperature decreases as the FRC velocity increases. Since the higher initial ionization cases begins in a more energetic state when entering the translation section, it is able to gain more kinetic energy from its thermal energy during the entry process.

The time evolution of the trapped flux and particles in the FRC is shown in Fig. 3.56. As it can be seen, the trapped flux in the FRC is almost equivalent for both the static and dynamic fill case. The static fill case has slightly higher trapped flux, but it is negligible compared with the change due to initial ionization levels. The sudden drop in the trapped

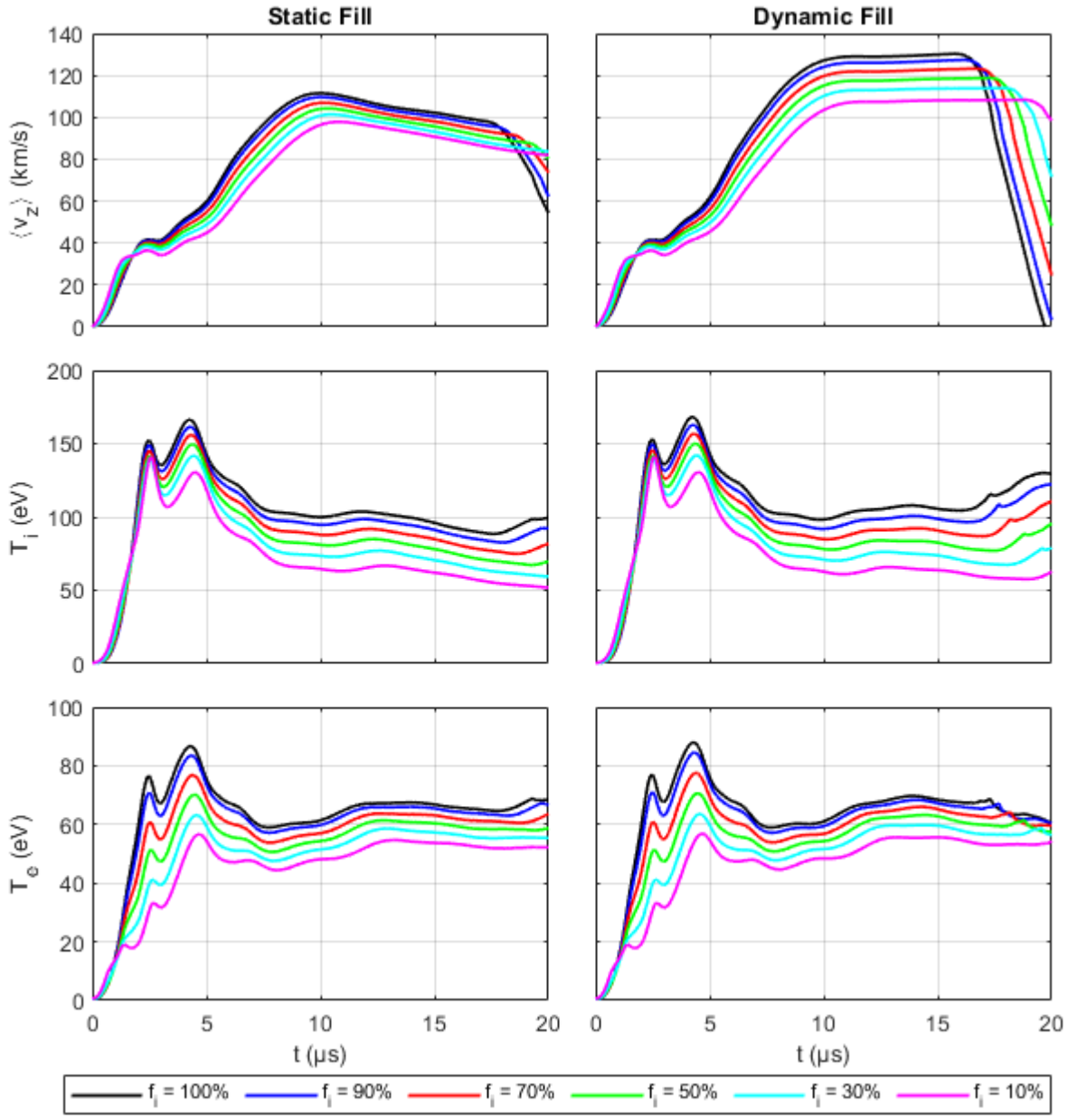

Figure 3.55: The time evolution of the FRC volume averaged (top) axial velocity, (middle) ion temperature, and (bottom) electron temperature for (left) static fill and (right) dynamic fill case.

flux around 7 μs is caused by the injection into the translation section. It can be seen that while the initial particle inventory of the formed FRC is same for both static and dynamic

fill case, the particle decay rate is lower for the static case than the dynamic case. This is due to the fact that as the FRC is translating in the translation section, the background neutrals in the translation section are ionized and help sustain the FRC.

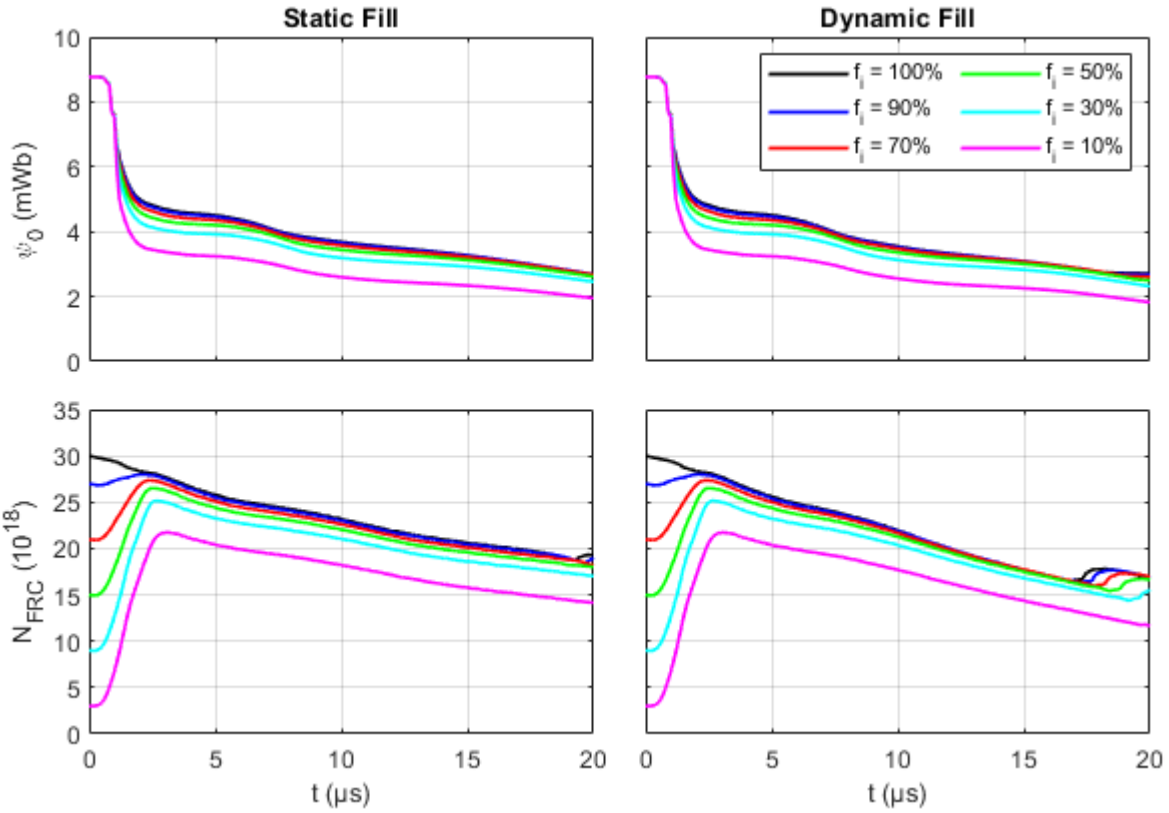

Figure 3.56: The time evolution of the FRC volume averaged (top) axial velocity, (middle) ion temperature, and (bottom) electron temperature for (left) static fill and (right) dynamic fill case.

Note that the particle sustainment in the static fill case is not caused by the neutral beam sustainment effects, i.e., neutral particles penetrating into the closed field region and ionizing. Due to the upstream plasma that exists outside of the closed field region, there is an ionization layer that forms ahead of the FRC in the open field line region. Thus, there are no significant population of the neutral species near the separatrix of the FRC.

As an example, the contour of an ionization fraction at time 15 μs for 30% ionized static

fill case is shown in Fig. 3.57. As it can be seen, the region near the separatrix of the FRC is fully ionized, and due to the closed field structure of the FRC, the plasma produced in the open field line region will not effectively penetrate the FRC to sustain it. The reason for the improved particle confinement for the static fill cases is due to the increased population of the plasma near the separatrix (in the scrape-off-layer) that reduces the particle diffusion from the FRC.

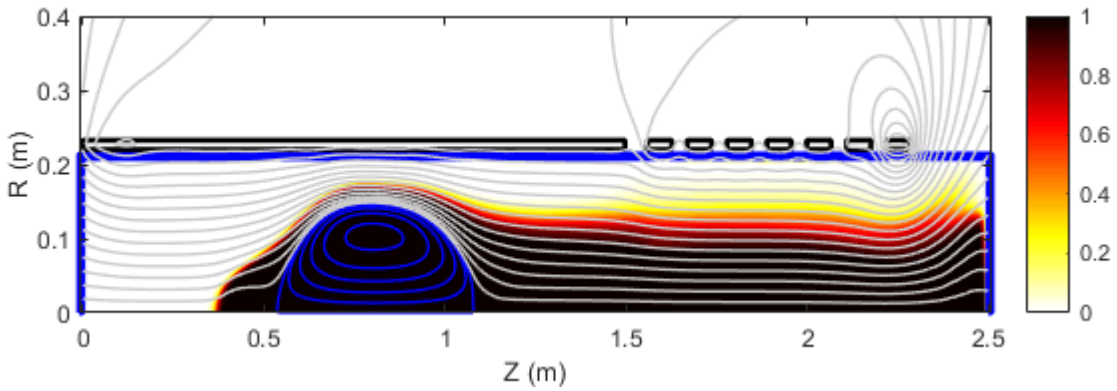

Figure 3.57: The ionization fraction at 15 µs from the start of the simulation for the case with 30% initial ionization in a static fill condition. An ionization layer forms upstream to the FRC, and near the FRC and in its wake, the gas is fully ionized.

The lack of background neutral penetration into the FRC is also evident from the time evolution of FRC electron temperature in Fig. 3.55. If there are significant population of neutrals penetrating into the FRC and then ionizing, the volume averaged FRC electron temperature will be rapidly decreasing in the translation section due to the energy loss associated with the effective ionization potential. However, in Fig. 3.55, the electron temperature for both the static and dynamic fill cases are largely equivalent. Thus, this further confirms inability for the background neutrals to penetrate into translating FRCs.

3.4 Concluding Remarks for Sample Problems

This chapter explored the change in behaviors of the FRC when the initial ionization condition and transport coefficients are modified. In general, good understanding of the initial condition and transport coefficients are crucial in optimizing the simulation results to agree with the experimental measurements. It is shown that various combination of input parameters can lead to similar modifications in the experimental excluded flux and NDL measurements. Thus, unless a good understanding of the initial condition and expected transport scaling is known a priori, it is easy to misinterpret the experimental results from the standard diagnostics available in FRC experiments. Nevertheless, qualitative experimental observations can often help determine the initial condition and transport setting that allow simulated results to agree with experimental measurements.

Chapter 4

SIMULATING VENTI-FORMATION EXPERIMENTAL CONDITIONS

The Cygnus code with the two-fluid plasma-neutral model of Meier and Shumlak is used to model FRC formation conditions encountered in the Venti-Formation experiment. The results from Cygnus are compared to the experimental results from the Venti-Formation device to determine whether the Cygnus model is suitable for capturing additional physics associated with the plasma-neutral interaction processes.

For this study, three experimental shots are selected for comparison with the simulated results: shot 938, 974, and 3275. These three shots are selected, because they were determined to be "good shots" during the experiment, meaning that the experiment proceeded without any anomalies and the result indicated production of a well behaving FRC.

In addition, the selected shots are associated with distinct operating conditions for FRC formation. This allows testing the robustness of Cygnus at capturing the plasma-neutral interaction physics that are important in FRC formation. Besides the differences in the initial gas fill and the external circuits configuration, the biggest difference between the selected shots is the preionization technique used for the experiment. Shot 938 uses a ringing theta-pinch ionization; shot 974 uses a multistage ringing barrier ionization method; shot 3275 uses an unassisted ringing barrier ionization method.

4.1 Initial Plasma and Neutral Fill Condition

In the Venti Formation device, pulsed gas-puffs are used to inject the diatomic deuterium gas into the formation chamber. A sample geometry of the Venti Formation device used for Cygnus calculations are shown in Fig. 4.1, with the location of the gas-puffs and formation

coils shown. Since the experiment is performed using the dynamic fill process, where the formation processes are started before the injected gas reaches static equilibrium in the chamber, the understanding of the initial neutral gas distribution in the chamber is crucial for generating the initial condition in the simulation that closely mimic the experimental initial conditions.

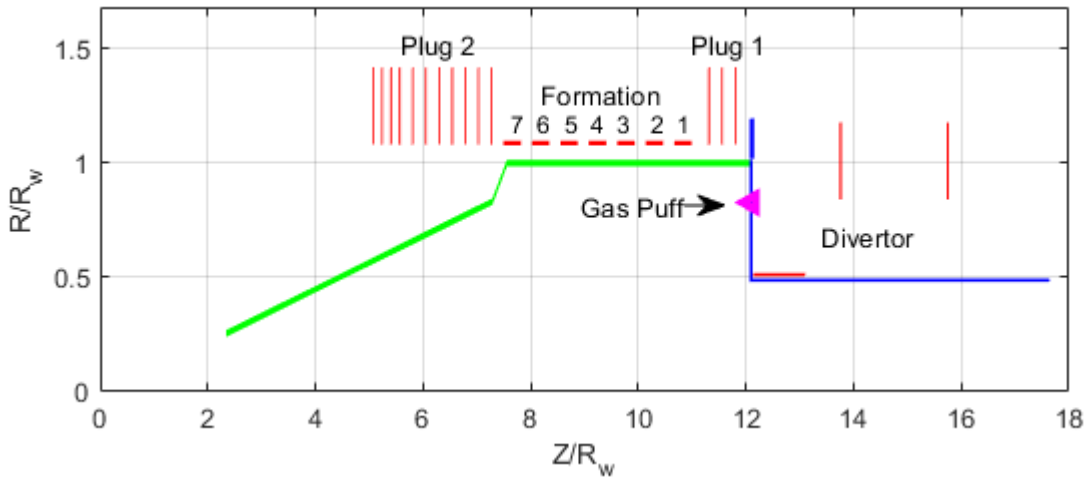

Figure 4.1: Truncated and simplified geometry of the Venti Formation device used for simulations. The length are normalized with respect to the chamber wall radius.

In order to configure the initial plasma and neutral conditions for Cygnus simulations, prior pressure measurements from the Venti Formation experiment using Fast Ion Gauge (FIG) and static pressure probe are used to reconstruct the approximate Cygnus initial condition that agrees with the measured data. The static pressure probe gives an absolute pressure measurement of the Venti Formation chamber long after the initially injected gas comes to an approximate equilibrium. On the other hand, the FIG provides pressure measurements on a short time scale, but it is typically influenced by a signal drift with shot-to-shot variations. Thus, the FIG data obtained from the Venti Formation device is only a relative pressure measurement for a specific shot [65]. The typical results obtained from the static pressure gauge are shown in Fig. 4.2, while the results obtained from FIG are shown

in Fig. 4.3.

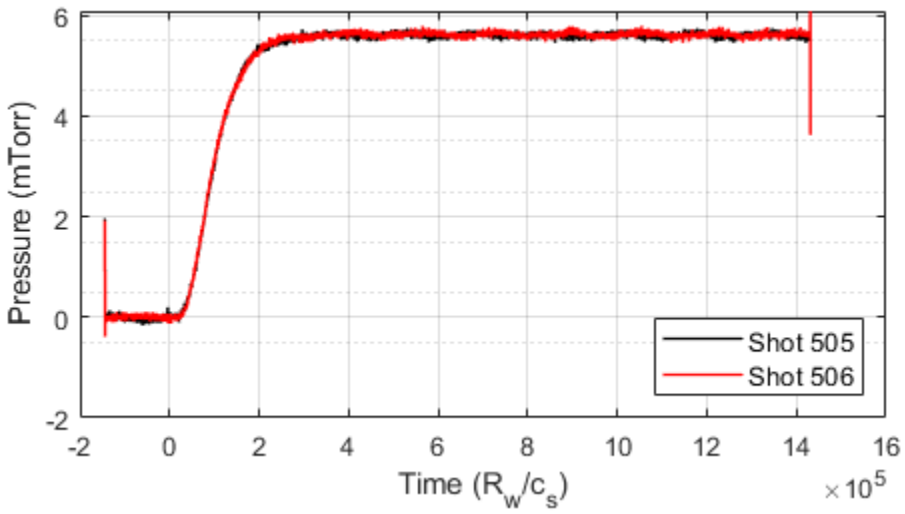

Figure 4.2: Static pressure measurements from the Venti Formation device for gas-puff valves fired with 400 µs opening and 30 psig upstream line pressure [65].

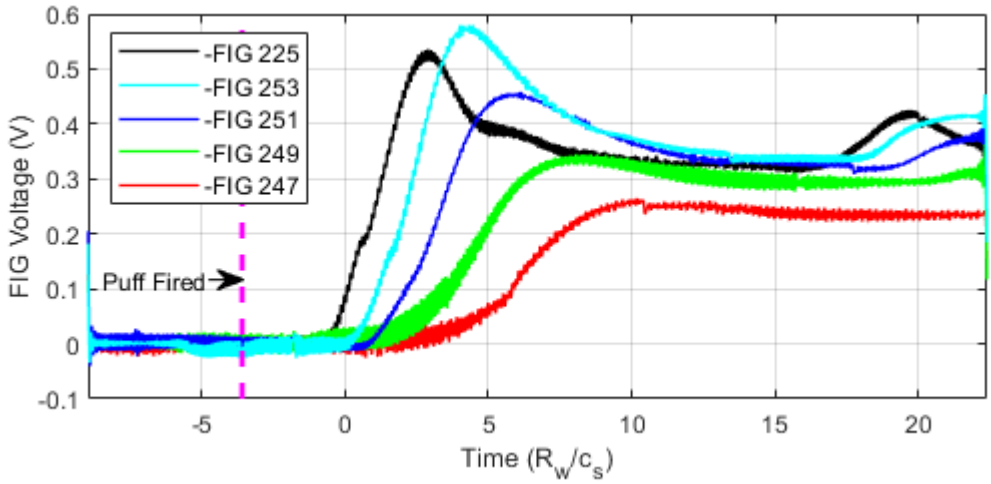

Figure 4.3: FIG measurements from the Venti Formation device for gas-puff valves fired with 400 µs opening. The measurements are taken at five axial positions spaced approximately 1.5 times the chamber radius [65]. The time of the measurement is normalized with a sound velocity of a room temperature molecular deuterium gas and the chamber radius.

From the static pressure measurement, an approximate equilibrium gas density in the chamber can be calculated. Given the measured pressure, the number density of the injected molecular deuterium gas can be calculated using the ideal gas law as:

$$n_{D_2} = \frac{p}{kT_0} \tag{4.1}$$

where p is the measured pressure and T_0 is the equilibrium gas temperature that can be approximated to be the room temperature. For the case shown in Fig. 4.2, the measured chamber pressure is 5.5 mTorr. Thus, the equilibrium number density of the diatomic deuterium is approximately $1.83 \times 10^{20}\,\mathrm{m}^{-3}$. For Cygnus, since atomic species are assumed in the plasma-neutral model, the reference number density for the simulation is approximately $n_D \approx 3.66 \times 10^{20}\,\mathrm{m}^{-3}$, which is the equivalent atomic deuterium number density in the chamber.

From the FIG data, the approximate velocity of the injected gas from the puff valves can be estimated. Let the time at which the magnitude of the FIG signal reaches half of its peak value as a reasonable reference time at which the bulk of the injected gas from the puff valves arrives to the FIG probe location. Using this data, an approximate velocity of the injected gas can be obtained by performing a linear fit. The estimated time of arrival measured at each testing location in the Venti Formation device is shown in Fig. 4.4 together with a best fit to the given data. A Mach number of 1.07 ± 0.06 is obtained from the linear fit, where the Mach number is referenced to the sound speed of the room temperature deuterium molecule. This result is reasonable, as one generally expects the gas ejected from the gas-puffs into a low-pressure background to be approximately equal to its sonic velocity. Thus, based on the FIG data, the gas Mach number of 1.07 is assumed for calculation purposes.

Because the radial variations of the injected gas were not measured in the experiment, only the axial density variations are considered. In order to obtain the axial density profile for Cygnus simulations, consider the results from the FIG measurements. Since the main formation coils are fired before one expects gas reflection from the cone section at the end of

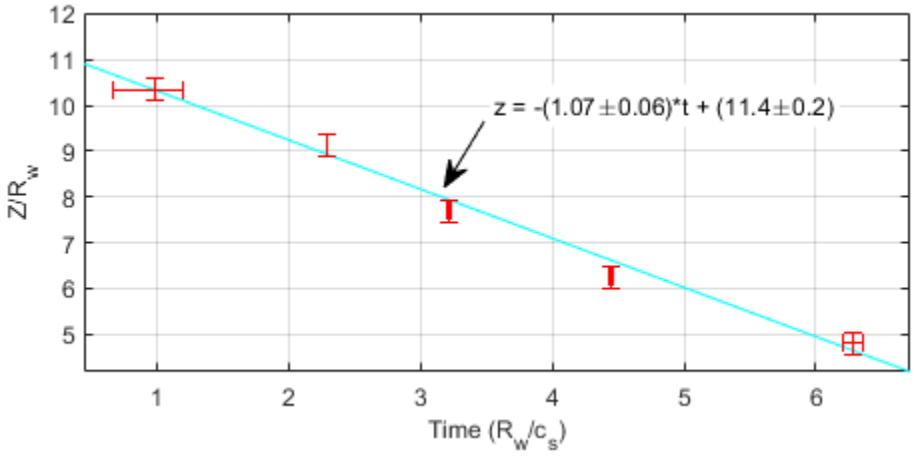

Figure 4.4: Time of arrival of the injected gas at various position in the Venti Formation Chamber estimated from the FIG measurement [65]. The units are normalized with a sound velocity of a room temperature molecular deuterium gas and the chamber radius.

the formation section based on the device size and the computed gas Mach number, the gas build-up near the end of the formation section can be neglected. As such, if one assumes that a wave pulse generated by the puff valves simply translates through the formation chamber at a constant speed, then the axial density distribution can be approximated as

$$n(z) \approx n(z_0 + v_0 t)$$

where z_0 is a reference position and v_0 is the bulk gas velocity.

With this assumption, one can transform the time axis of the FIG data by scaling it with the bulk gas velocity and translating the result to the correct spatial position that the FIG probes are located to obtain relative pressure data as a function of the spatial position in the formation chamber. To account for the voltage drifts in the FIG signals, the signals are normalized with respect to its plateau region of the FIG signal. This is a crude approximation, but a reasonable profile that matches the local FIG measurement can be generated.

Based on the long time FIG measurement taken in the experiment, the plateau region of

the early time FIG data approximately corresponds to 120% of the equilibrium pressure value measured by the static pressure probe [65]. Thus, the axial distribution obtained using the FIG measurements can be scaled with the measurement from the pressure probe to obtain a density distribution suitable for each simulation. Since a relative voltage drift of a factor of two was observed in the FIG data, the error from this analysis can be as large as this value. Since no radial sweep of the FIG measurements were taken in the experiment, the error in the initial density profile computed from this analysis could be even larger.

4.2 Shot 938: Ringing Theta-Pinch Ionization

Shot 938 from the Venti Formation experiment was a static FRC formation test using a ringing theta-pinch ionization. The geometry of the Venti Formation device with a coil system suitable for shot 938 condition is shown in Fig. 4.1. Total of seven formation coils are used for the programed formation of the FRCs. The two plug coils are used to produce the initial cusp field during the formation process. Excluded flux probes are positioned under each formation coil and few plug coils. No interferometer was present for this shot, but a single unfiltered visual light diagnostic was present to measure the light intensity from the formation process. The excluded flux results are vacuum referenced to shot 936. The summary of the diagnostic results from this experiment is shown in Fig. 4.5.

Since the external coil geometry is represented internally with segments in Cygnus, in order to account for the proper geometry of the coils, each coil is given a sufficient number of segments to capture the magnetic field profile during the simulation. Since the pulse time of the experiment is short compared with the magnetic field diffusion timescale of the solid coils, the seven formation coils are represented as a series of segments surrounding the perimeter of the coils. For the plug coils, since the thickness of the coils is sufficiently small, segments are placed at the center of the plug coil geometry in the vertical direction. For the divertor coils, since these coils are highly inductive and slow, segments are placed at the center of the divertor coil geometry in a horizontal direction.

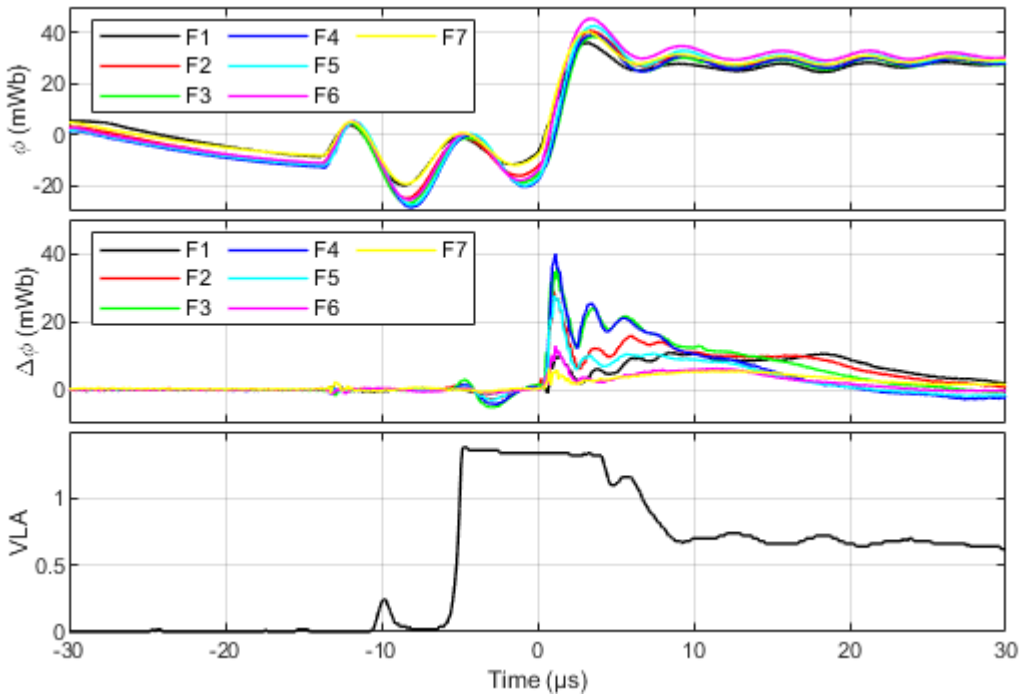

Figure 4.5: The summary of the diagnostic results from Venti Formation shot 938 [65]; (top) magnetic flux; (middle) excluded flux (vacuum referenced to shot 936); and (bottom) unfiltered visual light intensity.

4.2.1 Circuit Configuration for Shot 938

Since the vacuum reference shot associated with shot 938 is shot 936, the circuit model in Cygnus is constructed to best match the flux probe measurements from shot 936 and the measured circuit values from the experiment [65]. The circuit models used in Cygnus for the formation and plug coils for shot 936 are shown in Fig. 4.6 and Fig. 4.7, respectively. For the divertor coils, a constant current carrying coil is assumed in the Cygnus model.

Each formation coil is driven by an independent circuit. The three coils associated with the plug 1 coil are driven in parallel by a common circuit. For the plug 2 coil, the first five coils closest to the formation coils are driven in parallel by a common circuit, and the remaining coils are open and not powered.

The flux probe measurements for the vacuum shot 936 from the experiment and Cygnus

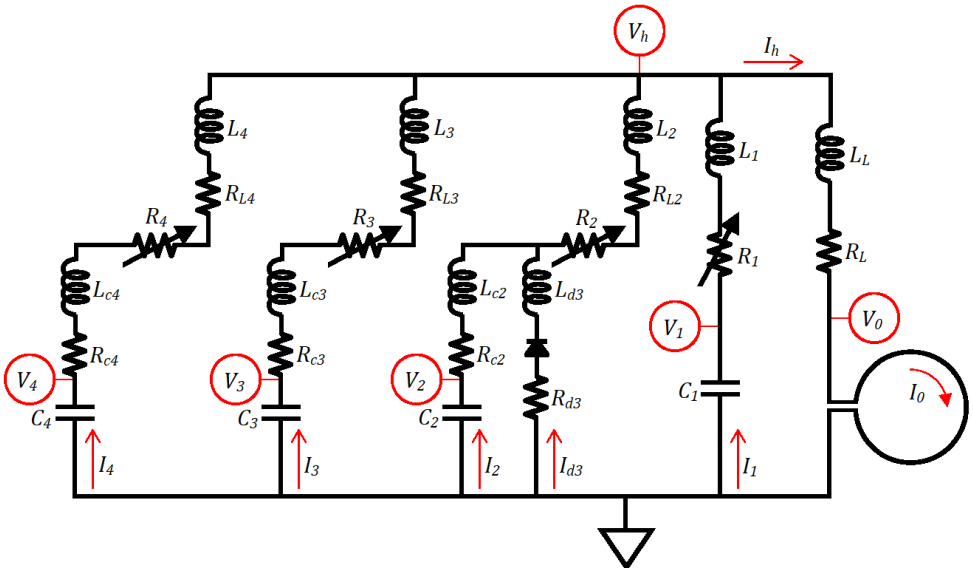

Figure 4.6: Cygnus circuit model for the formation coils in shot 936. Circuit segment 2 corresponds to the main formation bank, segment 3 corresponds to the ringing theta bank, segment 4 corresponds to the formation bias bank, and segment 1 is for numerical stabilization.

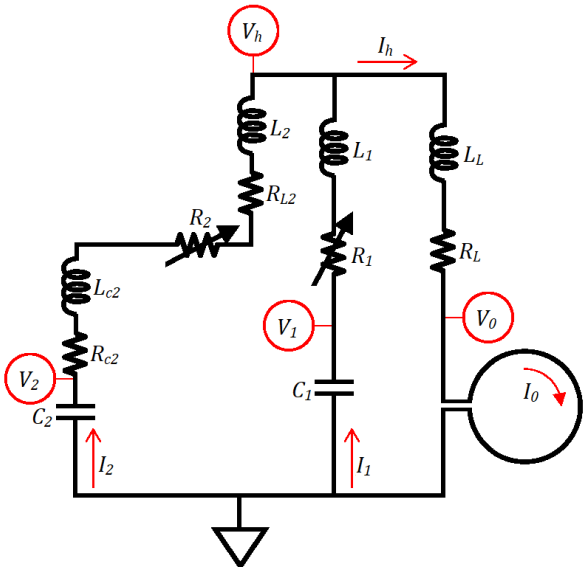

Figure 4.7: Cygnus circuit model for the plug coils in shot 936. Circuit segment 2 corresponds to the plug bank, and segment 1 is for numerical stabilization.

simulation are shown in Fig. 4.8 and Fig. 4.9. A reasonable agreement between the measured and simulated values is obtained. Care is made to ensure good agreement in the flux data for the formation coils during the initial bias, ringer ring down, and up to the first peak of the main bank firing, as these are the times when the neutral effects are important.

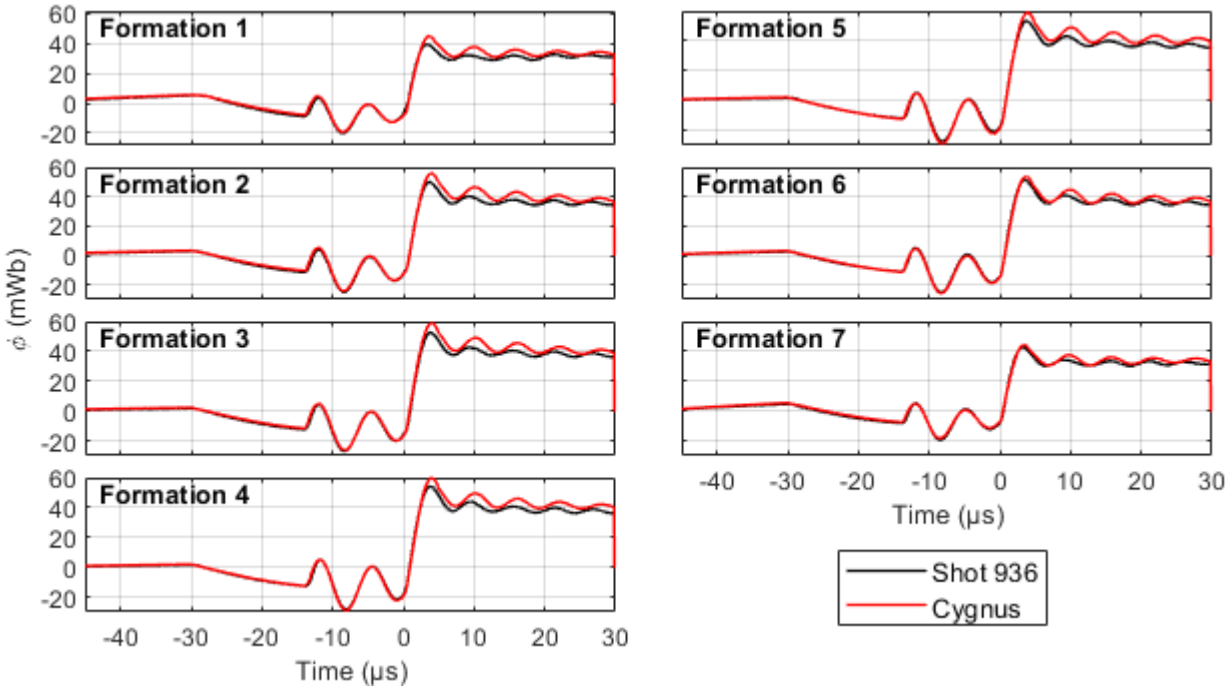

Figure 4.8: Magnetic flux measured under each formation coils from Venti Formation shot 936 [65] and Cygnus simulation.

4.2.2 Simulation Setup for Shot 938

From Fig. 4.5, it can be seen that the ringing theta-pinch starts at -14 μs. Since no ionization occurs until the ringing theta-pinch begins, there are no interaction between the magnetic field and the injected gas in the fluid domain. Thus, the fluid simulation is started at -14 μs. It can be seen from the experimental visual light diagnostic that a blip of light is first observed near -11 to -10 μs, slightly after the first magnetic zero-crossing. A significant light signal begins near -5 μs, and the excluded flux signal also begins to show plasma diamagnetism;

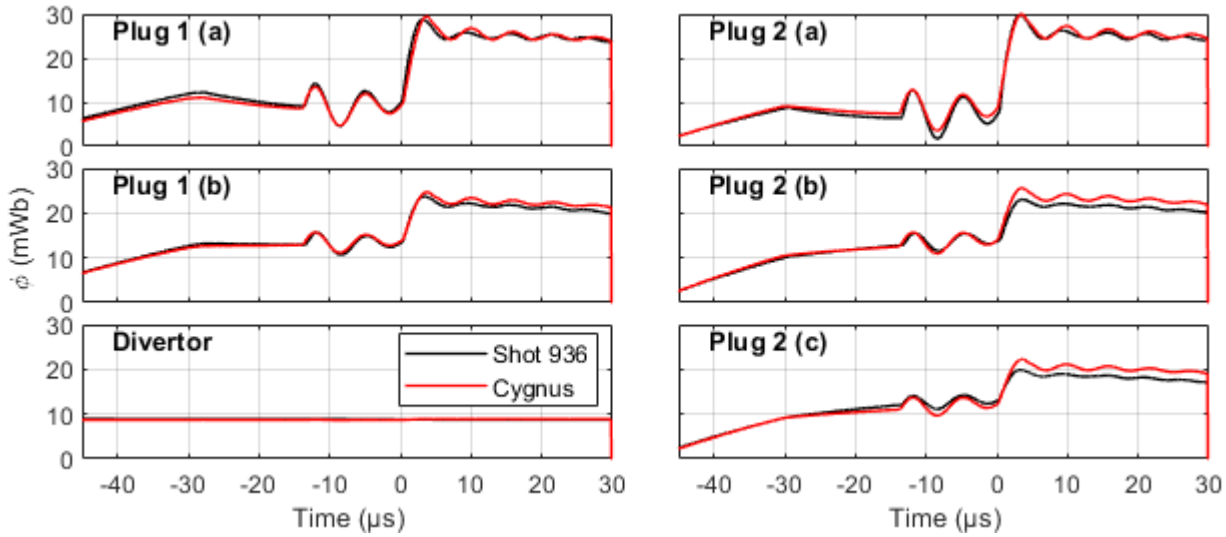

Figure 4.9: Magnetic flux measured under plug and divertor coils from Venti Formation shot 936 [65] and Cygnus simulation.

this approximately corresponds to the second magnetic zero-crossing, suggesting significant ionization occurring at this time.

The initial density profile used in the Cygnus simulation is computed using the procedure discussed in Section 4.1. Based on the static pressure probe measurement, an equilibrium chamber density of $1.83 \times 10^{20}\,\mathrm{m}^{-3}$ for diatomic deuterium is computed assuming room temperature; this leads to an effective atomic deuterium density of $3.66 \times 10^{20}\,\mathrm{m}^{-3}$. Using this equilibrium chamber density value, the density scaling factor computed from the FIG data is used to obtain the axial density variation of the injected neutral density. The density profile is then discretized into a finite number of constant density blocks for Cygnus input. The resulting axial density profile used for the simulation is shown in Fig. 4.10.

In the real experiment, the breakdown process in the ringing theta-pinch ionization method is initialized by the local high electric field generated due to the edge fields. Since this effect cannot be modeled, the simulation is initialized with a small but finite initial ionization. The initial gas in the chamber is initialized with an ionization fraction of 0.1%. The ion and electron temperatures are both initialized to 0.5 eV, while the neutral temperature

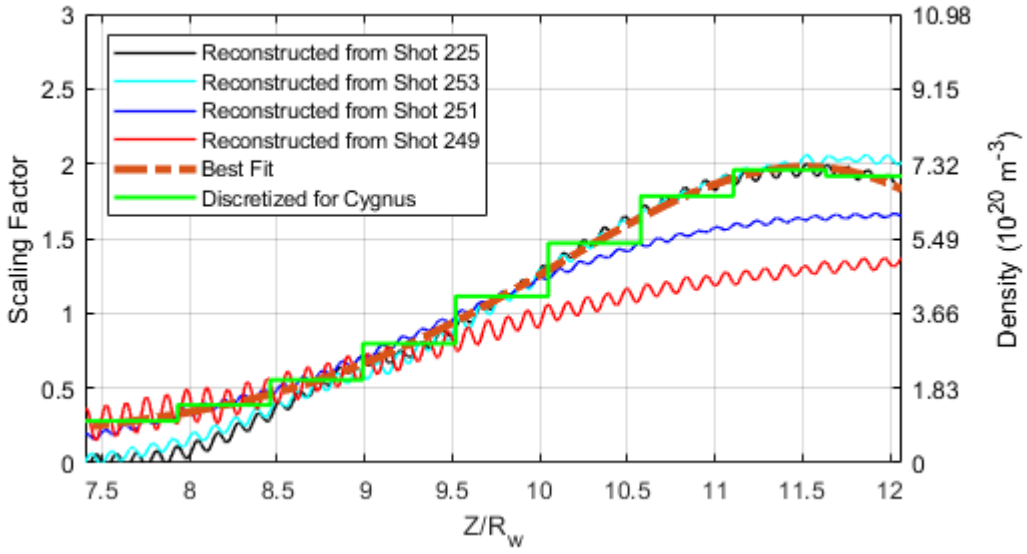

Figure 4.10: Axial density profiled used for shot 938. The best fit curve is obtained by fitting an 8th order polynomial using the weighted reconstructed FIG signal [65]. The discretized fit is based on a discrete volume averaged best fit curve data.

is initialized to 0.025 eV. The neutral species is initialized with an initial axial velocity of 1.07 times the sonic speed of the room temperature diatomic deuterium towards the cone section.

For both electrons and ions, the Braginskii thermal conductivities are used with the parallel diffusivity capped from 10^2 to $10^6\,m^2/s$ and the perpendicular diffusivity capped from 1 to $10^2\,m^2/s$. The neutral thermal conductivity is based on the hard sphere collision model for atomic deuterium, and it is capped from 10^3 to $10^9\,m^2/s$. The limits on the thermal conductivities are placed to ensure a reasonable behavior of the fluid dynamics during the radial implosion process. Without the limits, unphysical temperature spike may form, which results in a generation of large pressure gradients that evacuate the formation chamber prior to the main formation coil firing.

Both Spitzer and the electron-neutral collision resistivities are used by default. The anomalous resistivities are tuned to match the experimental results. Similarly, the isotropic

viscosities are tuned. In general, the anomalous resistivities and isotropic viscosities are used to match the experimental results. Since the anomalous transport is expected to be vastly different before and after the main bank firing, separate transport settings are used during the ringing theta-pinch preionization and FRC formation. Based on the results from parametric sweeps in Chapter 3, the values of the anomalous transport coefficients are chosen to best match the experimental data. The process is iterated until a reasonable agreement is obtained.

After the iteration process, for the ringing theta-pinch preionization phase, anomalous Chodura resistivity with $C_c = 0.6$ and $f_c = 3$ is chosen to be reasonable for the flux loss in the ringing process. Since in the real experiment, the initial ionization level is far below 0.1% (as the experiment starts with a fully neutral gas), the anomalous Bohm resistivity is used to reduce the plasma-field interaction. A Bohm multiplier of 50 gives reasonable suppression of the excluded flux signal during the preionization. For isotropic viscosity, value of $200\,\mathrm{m}^2/\mathrm{s}$ is used for both plasma and neutrals. This allows the plasma diamagnetism observed in the excluded flux signal caused by the ringing field to be captured.

During the FRC formation phase, the anomalous Chodura resistivity with $C_c = 0.5$ and $f_c = 3$ is used. This value of Chodura resistivity gives reasonable agreement with the lift-off flux seen in the excluded flux signal. The Bohm resistivity is disabled during the formation phase, as rapid ionization is expected to occur once the main bank is fired and the plasma confinement in the reversed field region is expected to be good (i.e., not neutral transport dominant). In order to match the post implosion oscillation in the excluded flux signal, isotropic viscosity of $2000\,\mathrm{m}^2/\mathrm{s}$ is used for both plasma and neutrals.

4.2.3 Simulation Results for Shot 938

The resulting excluded flux signal from shot 938 and from Cygnus simulation is shown in Fig. 4.11. The dynamic temperature dependent effective ionization potential is used in the simulation. A reasonable agreement with the experimental results can be observed in the ringing theta-pinch. The simulation computed lift-off flux are in reasonable agreement except

under formation coil 4 and 7. At the time of the maximum radial implosion, the simulation generated excluded flux are generally lower than experimental measurements. This is caused by the lower density of initial gas in the downstream region of the formation chamber. As a result, shorter FRC is produced with the centroid located towards the upstream section.

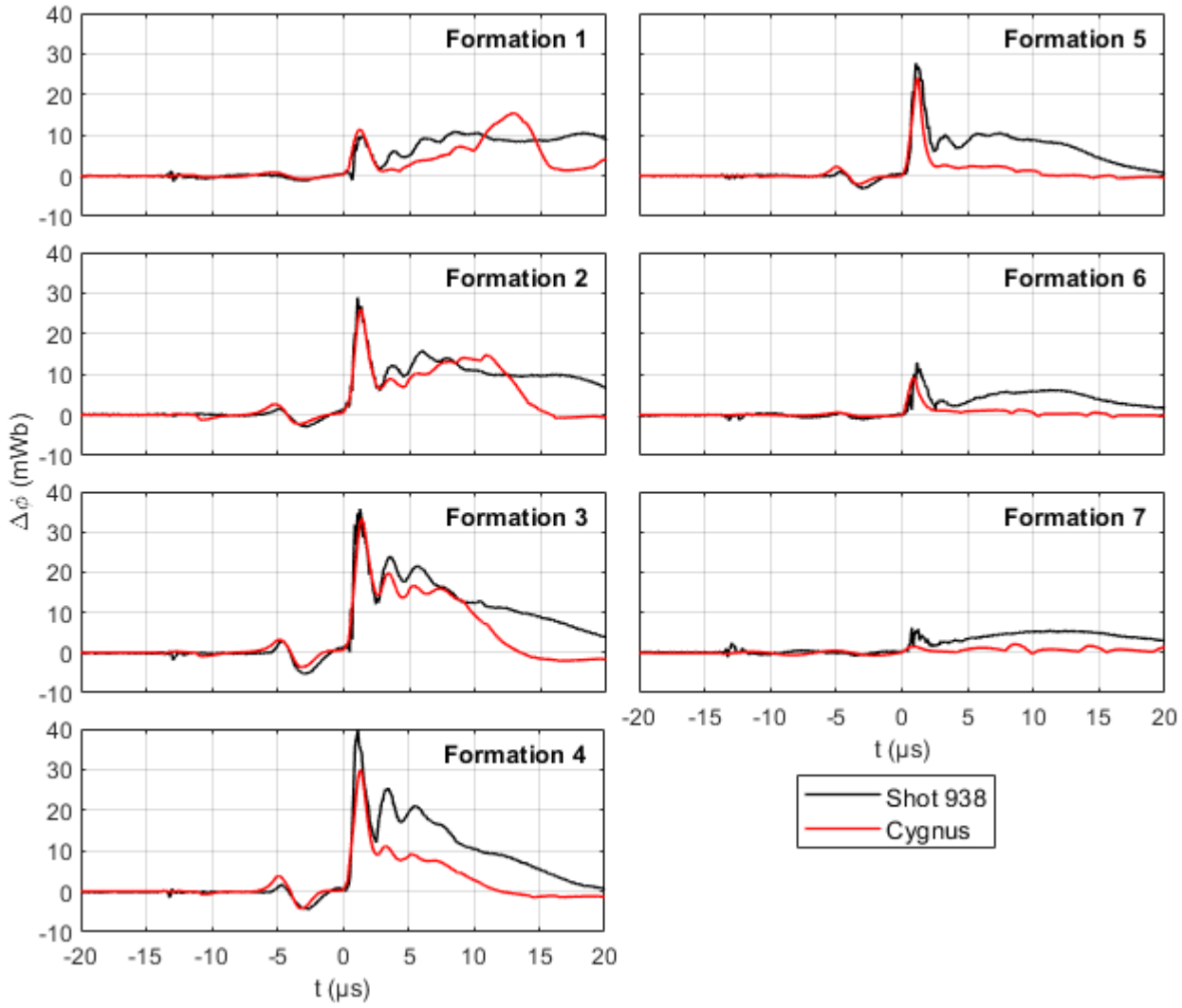

Figure 4.11: The experimental [65] and the simulation generated excluded flux signal under the formation coils for Venti Formation shot 938.

After the first radial implosion, the agreement between the experiment and simulation is quite poor. This is due to the axial drift of the formed FRC in the simulation towards

the upstream divertor section of the device. Since there were no mirror fields applied in the experiment for this shot, the formed FRC is neutrally stable in the formation chamber. In series of simulations with varying initial conditions, it was seen that the formed FRC always had a tendency to drift axially, and it was not possible to stabilize the formed FRC with much success. Thus, while the late time behavior could not be modeled, the simulation with the most agreement early in time is selected as the best numerical solution for this shot.

The FRC dynamics in the experiment and simulation can be compared with more clarity by comparing the snapshot of the excluded flux radius at various time in the FRC formation process. Fig. 4.12 shows a plot of the excluded flux radii overlaid on the Venti Formation geometry at various point in time during the FRC formation process. As it can be seen, during the ringing theta-pinch ionization (up to 0 µs), the disagreement in the excluded flux radii between the experiment and simulation is small. The slight difference at -1.5 µs is due to a minor phase difference in the radial dynamics. In general, the plasma diamagnetism is being captured reasonably well by the simulation, where the anomalous Bohm resistivity is used to enhance the local resistivity of the preionized plasma.

During the radial implosion (1.5 µs), it can be seen that the simulation and the experimental results begin to diverge. Due to the high concentration of the density upstream in the formation chamber, as suggested by the FIG measurements, the simulation generated excluded flux radii in the upstream formation coils (coils 1–3) lag behind the experimental values. On the other hand, since the downstream density is low in the simulation, the simulation excluded flux radii in the downstream region implode faster than the experimental values. As a result, the formed FRC in the simulation is shorter with the centroid located further upstream compared with the experiment, as it can be seen at 3 µs.

For the simulation generated FRC, it gains axial velocity towards the upstream divertor section. As it can be seen from time 4.5–10.5 µs, the simulation formed FRC slowly drifts upstream with negligible flux decay. On the other hand, the experimental excluded flux radii suggest a stationary FRC with flattening profile as time passes. Due to the difference in the axial dynamics, the simulation diverges from the experiment late in time. Eventually the

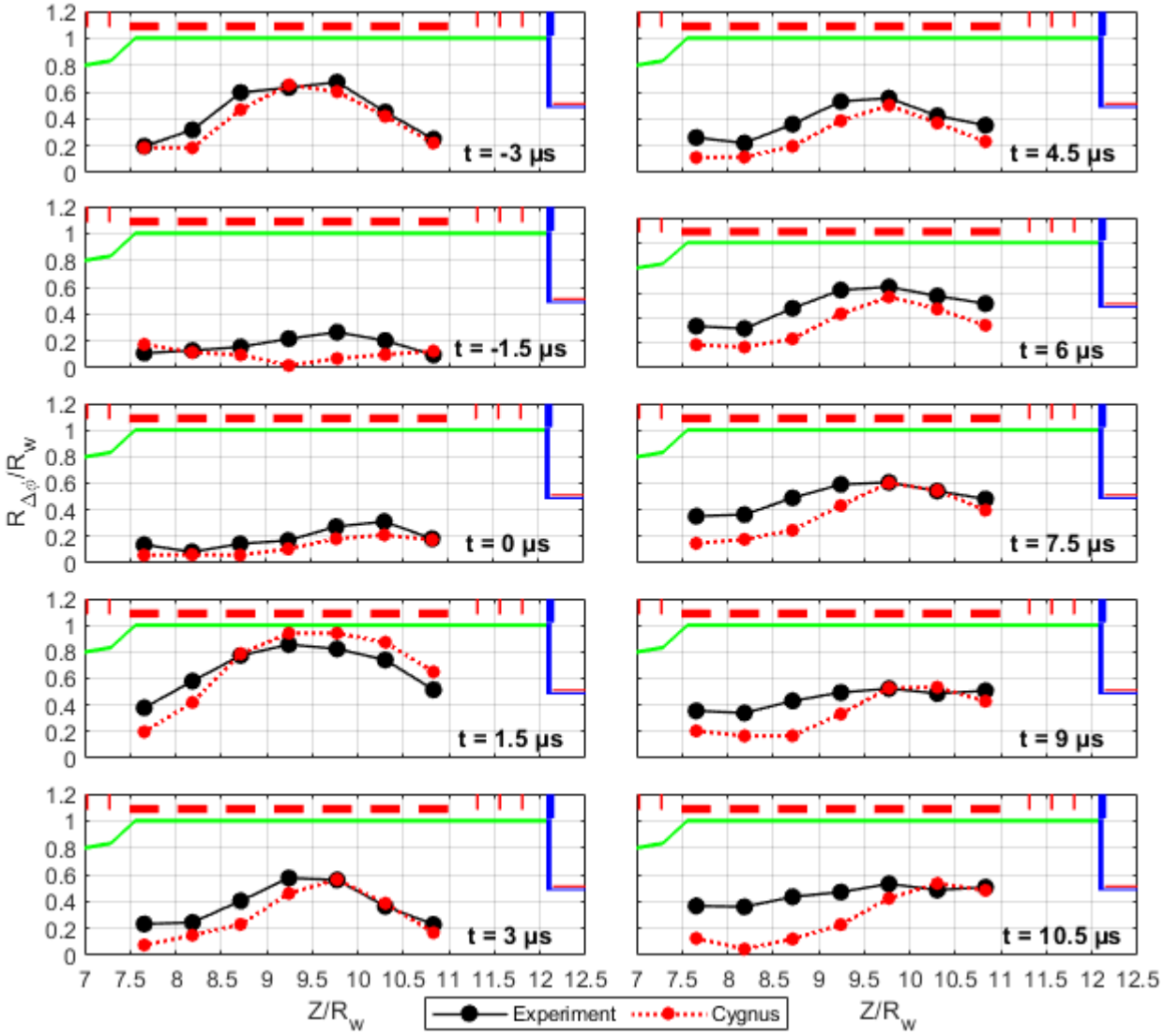

Figure 4.12: The experimental [65] and the simulation generated excluded flux radii for Venti Formation shot 938. The coils geometry is also shown in the same figure.

FRC in the simulation collides with the upstream wall and decays away.

Since there are no mirror fields applied for shot 938, minor errors in the circuit configurations and couplings can bias the FRC upstream or downstream of the device. In other words, small errors in the circuit are amplified as the neutrally stable FRC is given a finite axial velocity with no mechanism to dampen its axial motion. Since the magnetic topology is

in an anti-mirror magnetic configuration at the ends, once the FRC is displaced sufficiently from the center of the formation chamber where the magnetic field is roughly uniform, the tail of the FRC finds the lower magnetic field region in the divertor or the cone section and the drifting FRC is accelerated towards the lower field.

Since the vacuum magnetic flux signals from both the experiment and simulation agree with each other and the circuit values used in the simulation agree with the expected values measured from the experiment, the Cygnus circuit is already tuned as best as possible to the experimental circuit values. Since there are minor shot-to-shot variation in the experimental circuits and some components have non-linear impedance values, disagreements caused by the axial translation of the FRC is not surprising for shot 938, given its neutrally stable magnetic topology.

What is more concerning is the disagreement between the experimental and the simulation results during the radial implosion (1.5 µs). The experimental excluded flux radii suggest that there may be more gas downstream in the device, which disagrees with the neutral gas density measured using FIGs. One possibility is that the FIG measurement is inaccurate near the downstream region and lower gas density were being measured. Considering the factor of two error in the FIG data, it is possible that the disagreement is caused by the use of the incorrect initial density profile. However, based on the excluded flux signal, no significant plasma diamagnetism is observed for the downstream probes during the ringing theta-pinch. Thus, it is hard to imagine a higher gas density downstream in the device, as that should result in a stronger diamagnetism signal similar to the upstream coils.

Another possibility is the radial dependence of the initial gas profile in the formation chamber that was neglected in the simulation. Depending on the radial density profile, it is possible that more gas exists downstream, but it does not show up in a plasma diamagnetic signal during the preionization. Since the FIG measurements were only taken near the axis of the device, there are no experimental measurements to support or deny the radial profile of the initial gas fill. Thus, more experimental measurements are required before this effect can be explored methodically.

Finally, it is possible that there are insufficient ionization occurring in the simulation during the preionization and radial implosion processes. If insufficient neutrals are ionized in the reverse field region, the particle inventory of the resulting FRC will be low. As a result, a smaller and shorter FRC is produced. Based on the simulation results, roughly half of the particles originally inside the bias field region are lost after the formation. The particle loss is not caused by the ringing theta-pinch, as the particle inventory after the ringing theta-pinch at 0 µs is largely same as the original value before the ringer activation. Thus, roughly half of the particles are lost in radial implosion.

To test this hypothesis, the Cygnus simulation is repeated with a more optimistic estimate for the effective ionization potential. As it was shown in Section 3.2.1, since the ionization is driven by the electron temperature, if one reduces the losses associated with electron temperature, the ionization process is enhanced. Note that the dynamic effective ionization potential case behaves similar to the constant effective ionization potential of 150 eV, as shown in Section 3.2.1. Thus, two additional simulations with a constant effective ionization potential of 13.6 eV (theoretical minimum) and 100 eV are performed, and the results are compared to the case with a dynamic effective ionization potential.

The resulting excluded flux radii are shown in Fig. 4.13. For both the 13.6 eV and 100 eV case, a larger FRC is generated at 3 µs, as expected. For 13.6 eV, the produced FRC is larger than what is suggested based on the experimental results. Again, all cases diverge from the experimental result later in time due to the axial drift towards the divertor section. It can be seen that when a more optimistic value of the effective ionization potential is used, the produced FRC is much longer, and there are sufficient ionization in the downstream low-density region. However, there are too much diamagnetism during the ringing theta-pinch, and the agreement before 0 µs is made worse.

To compare the efficiency of the ionization process for the varying level of the effective ionization potential in the simulation, the particle inventory in the reversed field region is tracked during the ringing theta-pinch ionization and FRC formation processes. The result is shown in Fig. 4.14. As it can be seen, when the effective ionization potential is reduced to

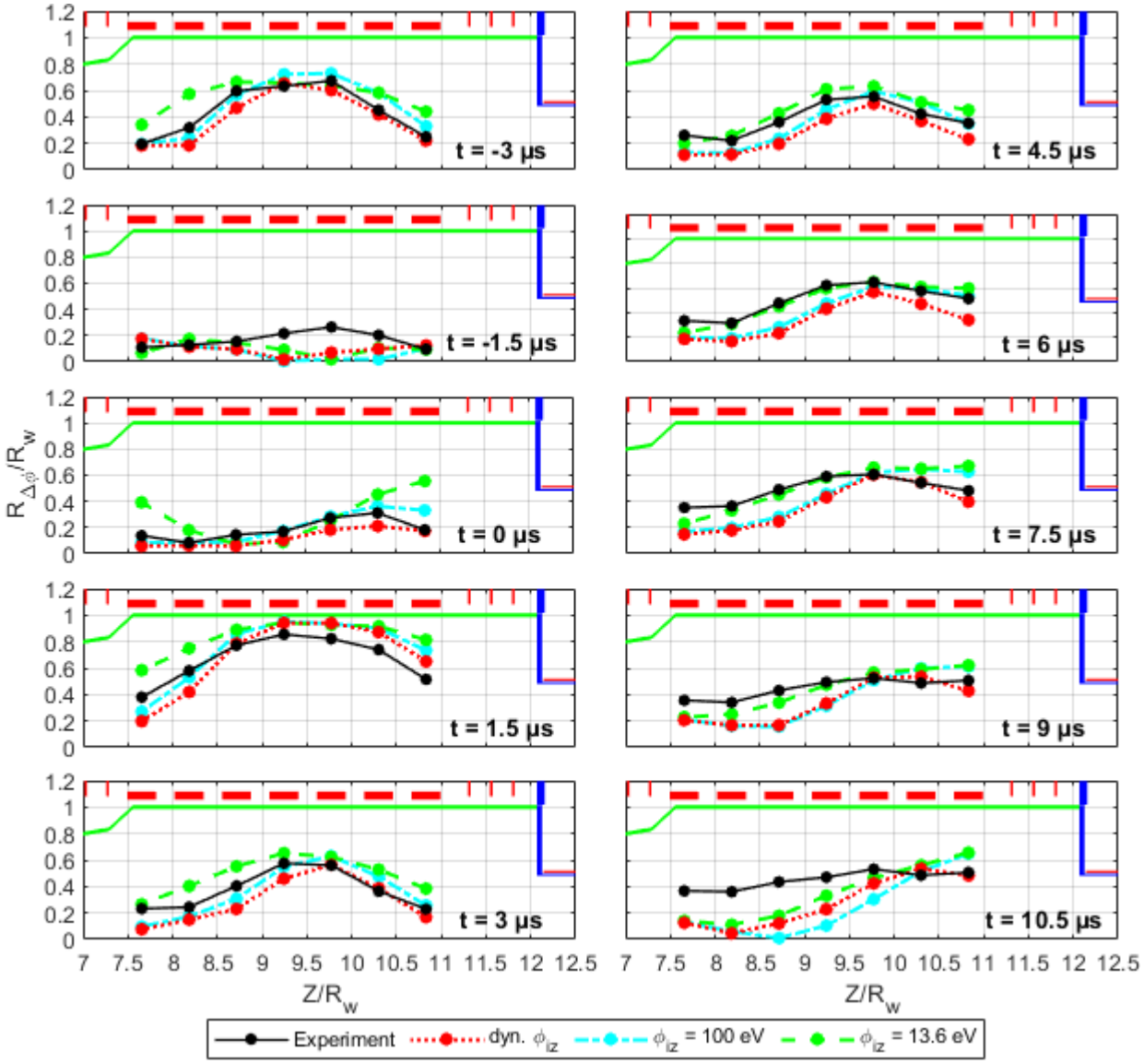

Figure 4.13: The experimental [65] and the simulation generated excluded flux radii for Venti Formation shot 938. Three simulations are performed with different effective ionization potentials.

13.6 eV, the ringing theta-pinch completely ionizes the gas in the reversed field region. Thus, ionization is negligible during the radial implosion. On the other hand, for the dynamic and 100 eV case, only a partial ionization of the gas is achieved with the ringing field, and there are ionization taking placing during the radial implosion. A volume averaged ionization

fraction of 40% and 12% is obtained for the 100 eV and dynamic effective ionization potential case, respectively.

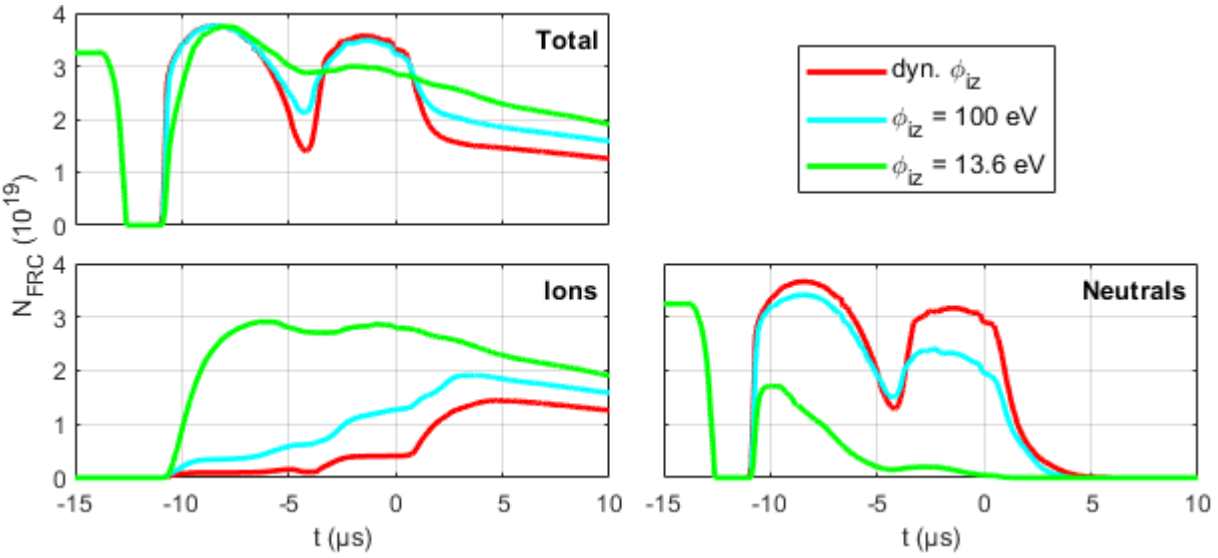

Figure 4.14: The number of particles trapped in the reversed field region during the ringing theta-pinch ionization and FRC formation for Venti Formation shot 938 simulation.

Since there were no NDL measurements for this shot, the density data is not available to judge whether the enhanced ionization is the cause of the disagreement. Based on the visual light diagnostic shown in Fig. 4.5, most signal is obtained after -6 μs. Thus, there should not be significant ionization occurring prior to this point. Thus, at least early in time, the ionization potential must be higher than the theoretical minimum value of 13.6 eV. Additional experimental measurements are required to fully answer this issue.

The simulation generated trapped flux and volume averaged FRC temperatures are shown in Fig. 4.15. Based on the simulation results from the three cases, once the formation process is complete and the ionization process is completed within the FRC (at roughly 5 μs), roughly 5.1–6.2 mWb of flux is trapped in the FRC; the electron temperature is roughly 60–90 eV, and the ion temperature is roughly 150–200 eV. Since the experimental excluded flux result lies within the three simulation results, the FRC trapped flux and temperatures are expected

to lie within these ranges. The particle inventory has significant variation between the three simulated cases, so more experimental diagnostics are required before useful estimate can be made, as discussed previously.

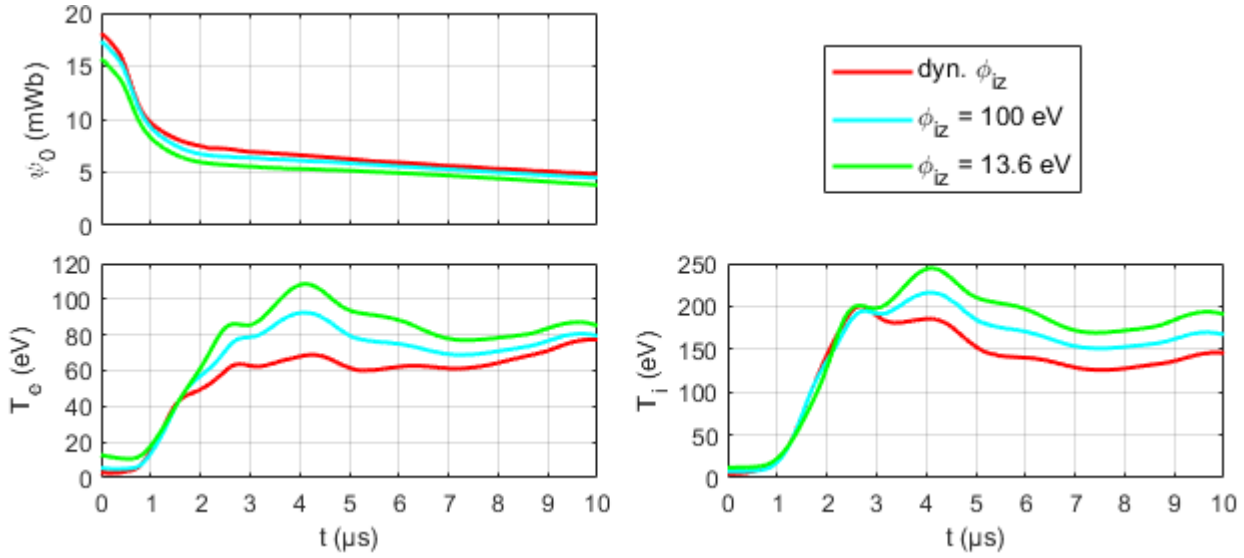

Figure 4.15: The time evolution of the FRC (top left) trapped flux, (bottom left) volume averaged electron temperature, and (bottom right) volume averaged ion temperature for Venti Formation shot 938 simulation.

4.3 Shot 974: Multistage Ringing Barrier Ionization

Shot 974 from the Venti Formation experiment was a static FRC formation test using a multistage ringing barrier ionization. The geometry of the Venti Formation device with the coil system suitable for shot 974 is the same as shot 938 and it is shown in Fig. 4.1. A total of seven formation coils are used for the programed formation of the FRCs. For this shot, the first and the last formation coils are used as the trigger coils to produce the initial cusp field during the formation process. They also serve as mirror coils to center the formed FRC. A HeNe two-pass interferometer system was active in the experiment with the laser positioned between the formation coil 4 and 5. There were no active visual light diagnostics for this shot. The excluded flux results are vacuum referenced to shot 973. The summary of the

diagnostic results from this experiment is shown in Fig. 4.16.

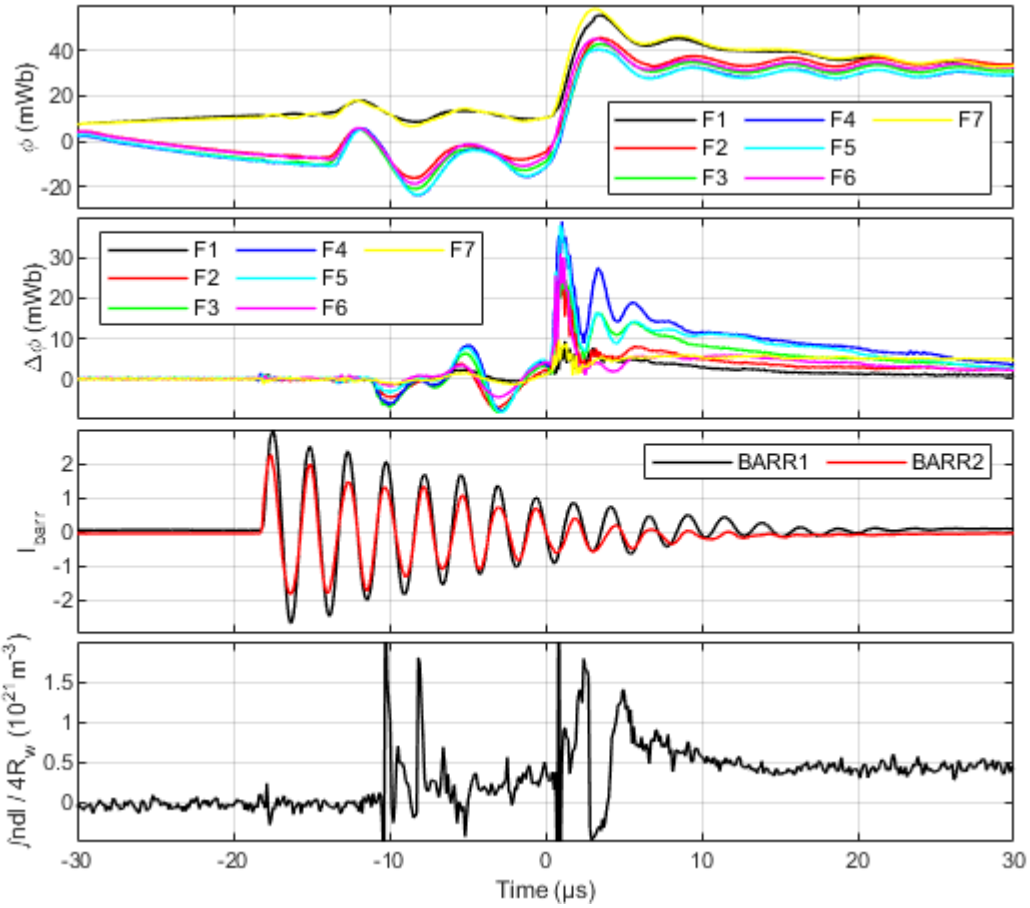

Figure 4.16: Summary of the diagnostic result from shot 974 [65]; (top) magnetic flux; (middle top) excluded flux (vacuum referenced to shot 973); (middle bottom) normalized current in the barrier coils and (bottom) NDL normalized by the path length through the chamber.

The geometry of the Venti Formation device was not modified from shot 938 to shot 974. Only modifications to the diagnostic system and operational circuit conditions were changed. Thus, the same geometry used in the Cygnus simulation for shot 938 can be used for this case.

4.3.1 Circuit Configuration for Shot 974

Since the vacuum reference shot associated with shot 974 is shot 973, the circuit model in Cygnus is constructed to best match the flux probe measurements from shot 973 and the measured circuit values from the experiment [65]. Since the circuit system was not changed from shot 936 to 973, the circuit models shown in Fig. 4.6 and Fig. 4.7 are also used for this shot. The general circuit setup in Cygnus is the same as what is discussed in Section 4.2.1, except with the capacitor voltages and coil firing timings modified. The resulting measured values from the flux probes from the vacuum shot 973 and those calculated from Cygnus are shown in Fig. 4.17 and Fig. 4.18. A reasonable agreement between the experimentally measured and simulated values is obtained.

4.3.2 Simulation Setup for Shot 974

From Fig. 4.16, it can be seen that while the ringing barrier field is initialized at -18 µs that is before the ringing theta-pinch at -14 µs, there are no evidence to suggest ionization from the ringing barrier field until the magnetic zero-crossing of the ringing theta-pinch occurs near -11 µs. This can be verified in both the excluded flux and NDL signals. This is a well-known feature of the ringing barrier field ionization process, where the ringing barrier field cannot ionize gas in the formation chamber when there are significant bias magnetic field as discussed in Section 1.2.3. Thus, a rapid ionization from the ringing barrier field only occurs near the magnetic zero-crossing where the bias field is nullified by the ringing theta-pinch.

Since the ionization due to the ringing barrier field is azimuthally dependent and localized near the formation chamber wall due to its multi-pole field characteristics, it cannot be modeled precisely in an axisymmetric model. However, since the resulting FRC generally does not exhibit azimuthally dependent characteristics, the azimuthal variation can be neglected by assuming that it is smoothed out in the formation process. Furthermore, since the ionization from the ringing barrier field only occurs when the bias magnetic field is

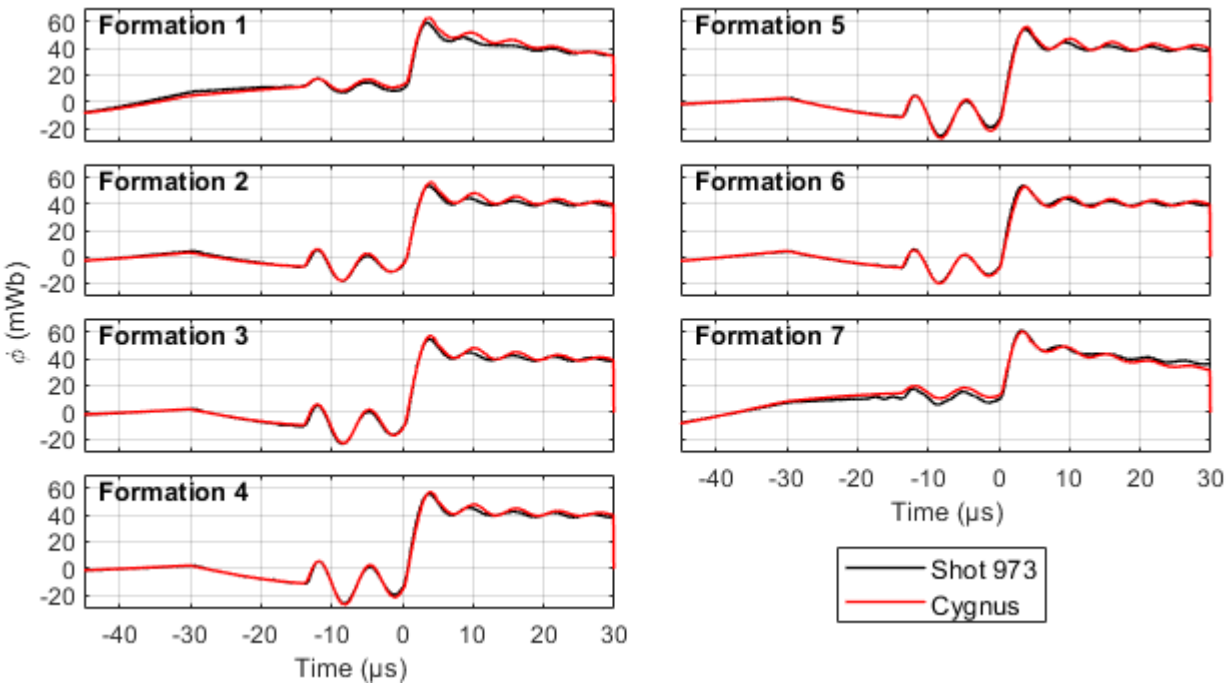

Figure 4.17: Flux measured under each formation coils from shot 973 [65] and Cygnus calculation.

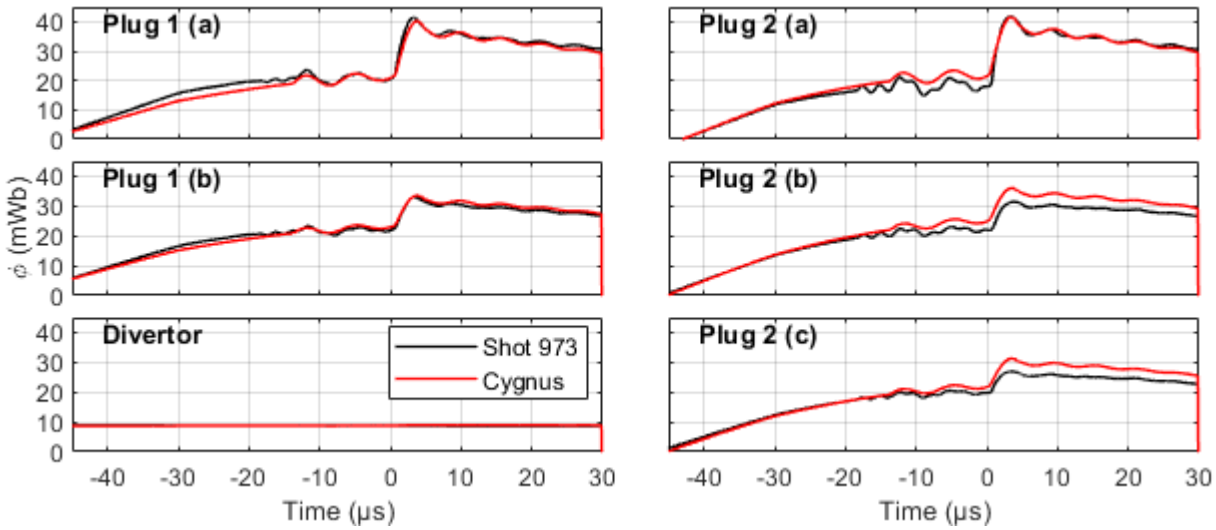

Figure 4.18: Flux measured under plug and divertor coils from shot 973 [65] and Cygnus calculation.

small, the ionization contribution from the ringing barrier field is quenched when the ringing theta-pinch reverses direction after the magnetic zero-crossing. Thus, the effect of the ringing barrier field is to introduce a layer of an ionized plasma near the formation chamber wall during the time of magnetic zero-crossing.

The initial density profile used in the Cygnus simulation is computed using the procedure discussed in Section 4.1. Based on the static pressure probe measurement, an equilibrium chamber density of $1.16 \times 10^{20}\,\mathrm{m}^{-3}$ for the diatomic deuterium is computed; this leads to an effective atomic deuterium density of $2.32 \times 10^{20}\,\mathrm{m}^{-3}$. Using this equilibrium chamber density value, the density scaling factor computed from the FIG data is used to obtain the axial density variation of the injected neutral density. The density profile is then discretized into a finite number of constant density blocks for Cygnus input. The resulting axial density profile used for the simulation is shown in Fig. 4.19.

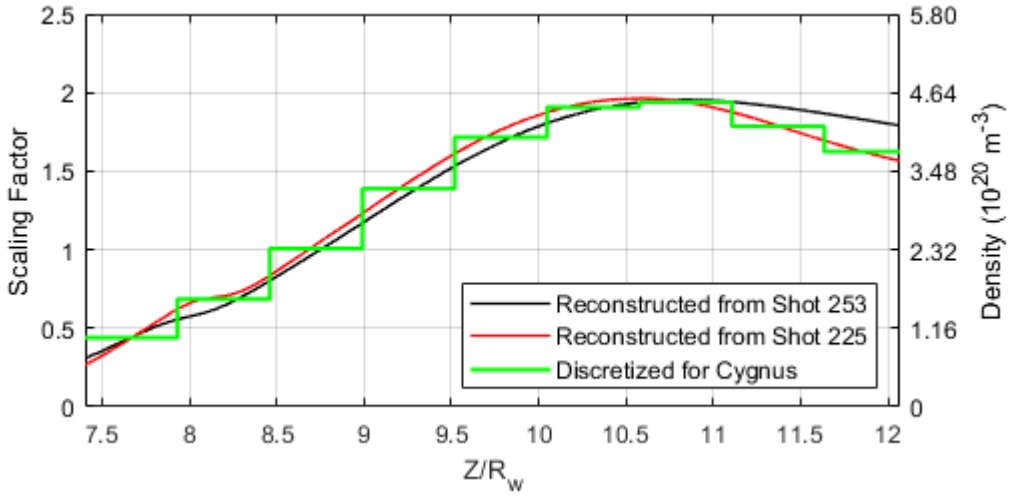

Figure 4.19: The axial density profile used for shot 974.

In order to model the initial ionization due to the barrier field, consider initializing the gas density with an ionization layer at time -11 µs. The simulation is started at -11 µs where the excluded flux and NDL signal first shows sign of plasma. While the NDL data is quite noisy, an approximate chord averaged plasma density of $6.0 \pm 4.5 \times 10^{19}\,\mathrm{m}^{-3}$ can be estimated

at -11 µs with an error bar confidence level of 70%.

Using this knowledge, the radial density profile for this case is modeled similar to the wall localized preionization from previous chapter (Section 3.1.2). For this simulation, the plasma layer is initialized with a 99% ionization while the rest of the gas is initialized with a 1% ionization. A plasma layer with a thickness of 12% chamber wall radius is found to produce a reasonable chord averaged plasma density of $4.6 \times 10^{19}\,\mathrm{m}^{-3}$. Considering the multipole nature of the ringing barrier field, this plasma layer thickness is reasonable considering the radial decay of the local magnetic field magnitude from the multipole coils.

Since the ringing barrier field enhances the electron temperature in the plasma layer, the electron temperature of 10 eV is used in the plasma layer as an estimate for this effect. Elsewhere in the chamber, the electron temperature of 0.5 eV is used. The ion temperature is initialized everywhere to 0.5 eV, as the ringing barrier field is too fast to impart significant momentum to ions. The neutral temperature is initialized to 0.025 eV, close to the room temperature. The neutral species is initialized with an initial axial velocity of 1.07 times the sonic speed of the room temperature diatomic deuterium towards the cone section.

For both electrons and ions, the Braginskii thermal conductivities are used with the parallel diffusivity capped from 10^2 to $10^6\,\mathrm{m}^2/\mathrm{s}$ and the perpendicular diffusivity capped from 1 to $10^2\,\mathrm{m}^2/\mathrm{s}$. The neutral thermal conductivity is based on the hard sphere collision model for atomic deuterium, and it is capped from 10^3 to $10^9\,\mathrm{m}^2/\mathrm{s}$. The limits on the thermal conductivities are placed to ensure a reasonable behavior of the fluid dynamics during the radial implosion process.

Both Spitzer and the electron-neutral collision resistivities are used by default. Both the anomalous resistivities and isotropic viscosities are tuned to match the experimental results. Since the anomalous transport is expected to be different before and after the main bank firing, separate transport settings are used during the ringing theta-pinch and FRC formation. The values of the anomalous transport coefficients are chosen to best match the experimental data, and it is iterated until a reasonable convergence is reached.

After the iteration process, the final transport setting for this simulation is obtained. For

the ringing theta-pinch phase, the anomalous Chodura resistivity with $C_c = 2$ and $f_c = 3$ is chosen to obtain reasonable losses in the ringing process. Since in the real experiment, there are azimuthal variations in the ionized plasma layer, the flux penetration rate in the chamber is higher than the penetration rate through the azimuthally symmetric layer. Thus, an anomalous Bohm resistivity with Bohm multiplier of 30 is used to improve the flux penetration into the gas in order to match the experimental excluded flux signals. For isotropic viscosity, a value of $1000\,\mathrm{m}^2/\mathrm{s}$ is used for both plasma and neutrals. This allows the plasma dynamics to be captured during the ringing theta-pinch.

During the FRC formation phase, the anomalous Chodura resistivity with $C_c = 0.5$ and $f_c = 3$ is used. This is the value of the Chodura resistivity that was found to produce a reasonable match in the past with the fully ionized MHD version of Cygnus [26]. Bohm resistivity is disabled during the formation phase, as the azimuthal variation in the plasma layer is expected to be smoothened by the time the main banks are fired. In order to match the implosion dynamics of the produced FRC, the isotropic viscosity of $100\,\mathrm{m}^2/\mathrm{s}$ is used until 3.6 µs. After this point, the isotropic viscosity is increased to $2000\,\mathrm{m}^2/\mathrm{s}$ to match the post-implosion damping of the FRC dynamics observed in the excluded flux signal.

4.3.3 Simulation Results for Shot 974

The resulting excluded flux signal from shot 974 and Cygnus simulation is shown in Fig. 4.20. The results calculated using both the dynamic temperature dependent effective ionization potential and the constant effective ionization potential of 13.6 eV are shown in the figure. A reasonable agreement with the experimental results can be observed for both cases. The agreement in the ringing theta-pinch phase is similar for both cases. Post FRC formation, the 13.6 eV case shows better agreement under most coils. For the temperature dependent case, the simulation generated excluded flux signal is lower than the experimental measurement in general.

In order to compare the shape of the FRC between the experiment and simulation, excluded flux radii at various times in the FRC formation process are compared. Fig. 4.21

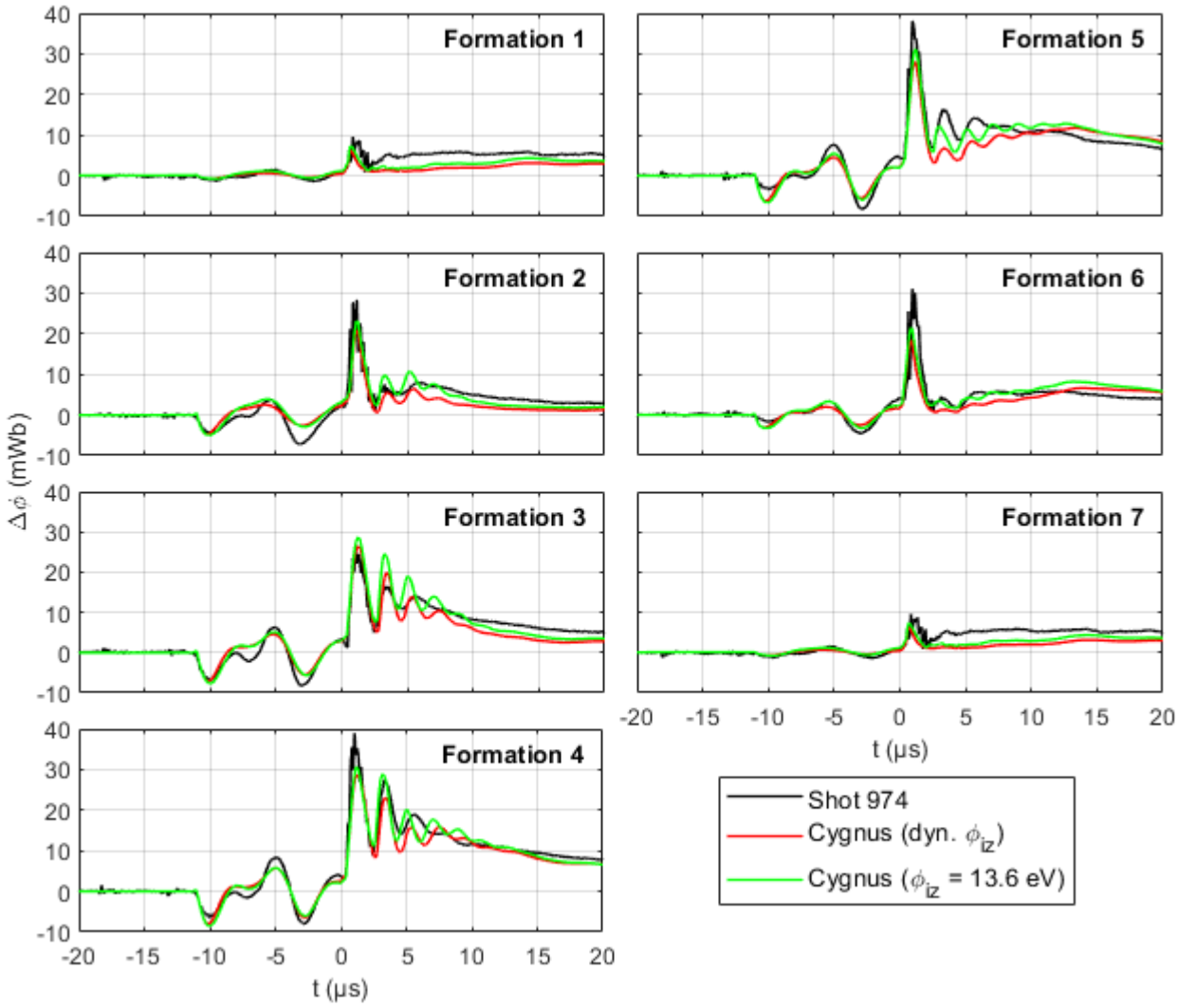

Figure 4.20: The experimental [65] and the simulation generated excluded flux signal under the formation coils for Venti Formation shot 974.

shows a plot of the excluded flux radii overlaid on the Venti Formation geometry at various point in time during the FRC formation process. In general, decent agreements are seen between the experimental and simulation results for all times. The simulation case with the dynamic effective ionization potential tends to form a shorter and smaller FRC compared with the experiment. The case with the optimistic 13.6 eV effective ionization potential has an FRC shape that better agrees with the experiment.

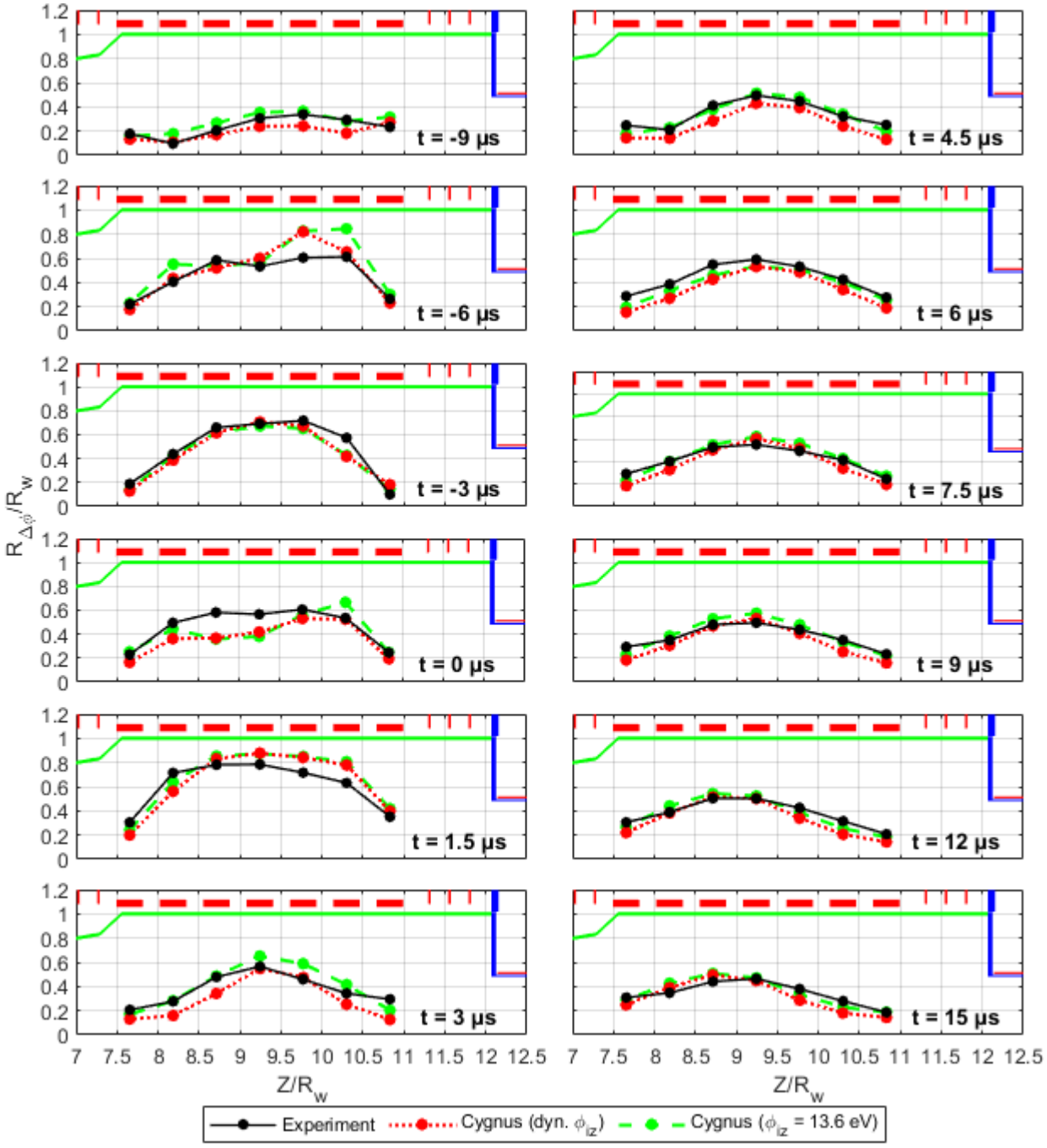

Figure 4.21: The experimental [65] and the simulation generated excluded flux radii for Venti Formation shot 974. The coils geometry is also shown in the same figure.

Since there are electron energy loss associated with electron impact excitation of neutrals

for the case of the dynamic effective ionization potential, the ionization efficiency is lower than the case of 13.6 eV where there are no such loss. Thus, one can conclude that in the experiment, more ionization is occurring than expected, which lowers the effective ionization potential down close to the theoretical minimum. As a result, when the electron impact excitation losses are neglected, better agreements are obtained in the excluded flux results.

In order to verify that a lack of ionization is the cause of the disagreement for the case of the dynamic effective ionization potential, the resulting NDL signal can be compared. Fig. 4.22 shows a plot of the NDL signal measured from the experiment and that calculated from the simulation. At the start of the simulation at -11 µs, the simulation agrees reasonably with the experiment. As it can be seen, for the case with the dynamic effective ionization potential, the measured NDL prior to the main bank firing at 0 µs is far lower than what is suggested from the experimental measurement. On the other hand, for the 13.6 eV case, the computed NDL signal matches the experiment well from -5 to 0 µs; from -11 to -5 µs, the computed NDL signal is too large, suggesting that there are too much ionization occurring during this time for the 13.6 eV case. Nevertheless, the 13.6 eV case produces initial conditions before the main bank firing that agrees with the experimental measurement.

After the main bank firing, the agreement of the simulated to experimental result is not as conclusive. Since there is large noise at about 1 µs and another around 3 to 4 µs, the experimental results during these times are not reliable. It can be seen that in the late time after 10 µs, the 13.6 eV case agrees well with the experiment measurement. On the other hand, the dynamic effective ionization potential case disagrees due to its smaller volume. Again, the 13.6 eV case agrees better with the experiment, though it has too much ionization from -11 to 5 µs.

The particle inventory in the reversed field region computed from the simulation is shown in Fig. 4.23. It can be seen that for the 13.6 eV case, significantly more ionization occurs during the ringing theta-pinch. By -5 µs, the ionization is complete, and remaining simulation behaves as the fully ionized case. On the other hand, the case with the dynamic effective ionization potential has neutrals left over after the ringing theta-pinch, and rapid ionization

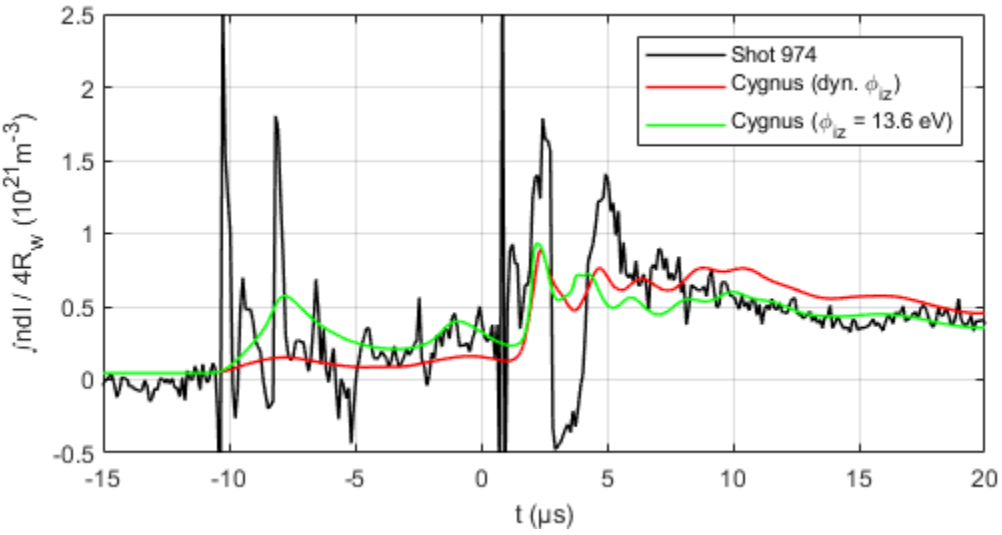

Figure 4.22: The experimental [65] and the simulation generated NDL signal for Venti Formation shot 974. The NDL signal is normalized by the path length through the chamber.

occurs during the radial implosion process. The volume averaged ionization level in the reversed field region is roughly 50%. It is interesting to note, however, that the resulting particle inventory in the FRC is similar for both cases.

The simulation generated trapped flux and volume averaged FRC temperatures are shown in Fig. 4.24. Since the dynamic effective ionization potential case gives less ideal estimate for the FRC condition than the 13.6 eV case, the expected trapped flux, particle inventory, and temperatures can be bounded and estimated. Consider the time when the formation and ionization process is completed within the FRC at roughly 5 μs. At this time, roughly 4–4.5 mWb of flux is trapped with a particle inventory of roughly 1.4×10^{19} atomic deuterium ions. The electron temperature is roughly 60–90 eV, with ion temperature ranging from 150–180 eV.

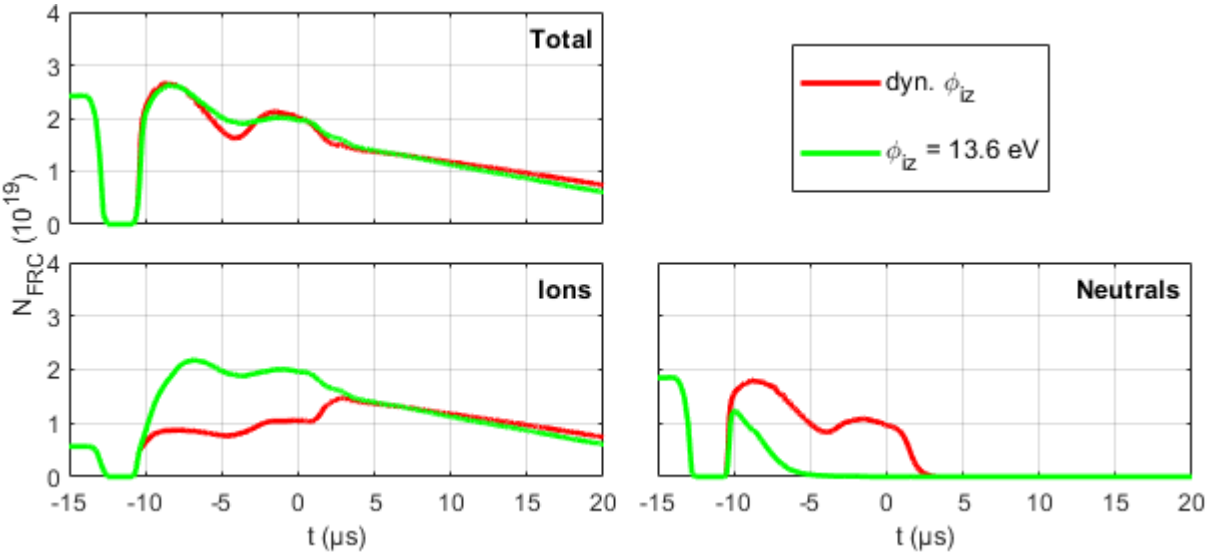

Figure 4.23: The number of particles trapped in the reversed field region during the ringing theta-pinch ionization and FRC formation for Venti Formation shot 974 simulation.

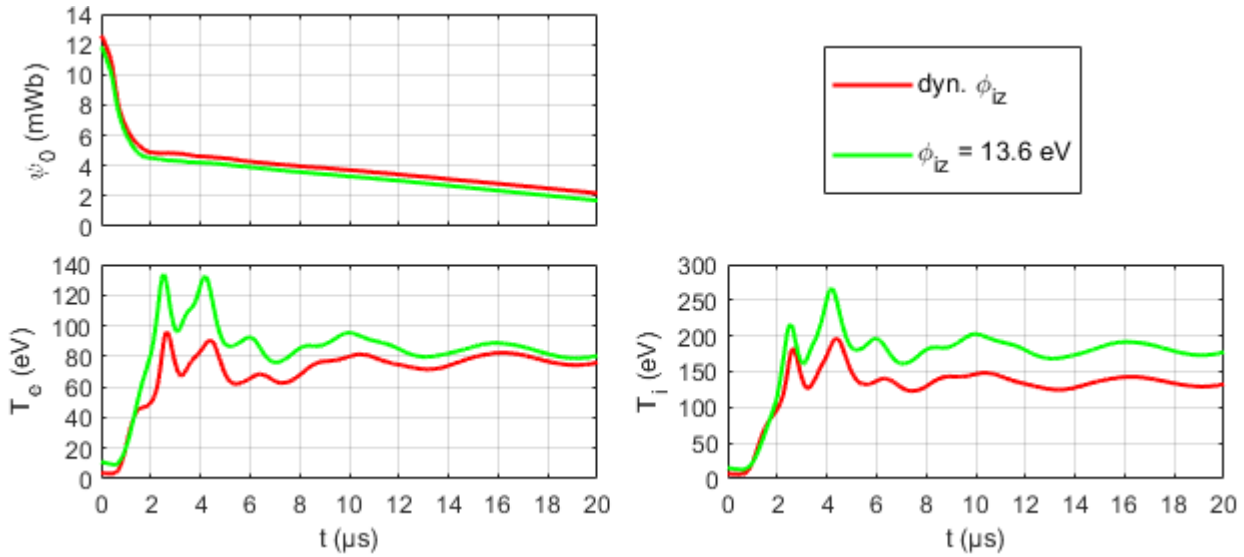

Figure 4.24: The time evolution of the FRC (top left) trapped flux, (bottom left) volume averaged electron temperature, and (bottom right) volume averaged ion temperature for Venti Formation shot 974 simulation.

4.4 Shot 3275: Unassisted Ringing Barrier Ionization

Shot 3725 from Venti Formation experiment was a dynamic FRC formation test using an unassisted ringing barrier ionization. The geometry of the Venti Formation device for shot 3275 was modified from that for Shot 938, with the addition of nine coils in the cone section to imitate the accelerator coils for the Venti device. The plug 2 coil was also be modified by removing all but the first two upstream coils from the assembly. The remaining coils geometry is the same as shot 938. The geometry of the Venti Formation device suitable for shot 3275 is shown in Fig. 4.25

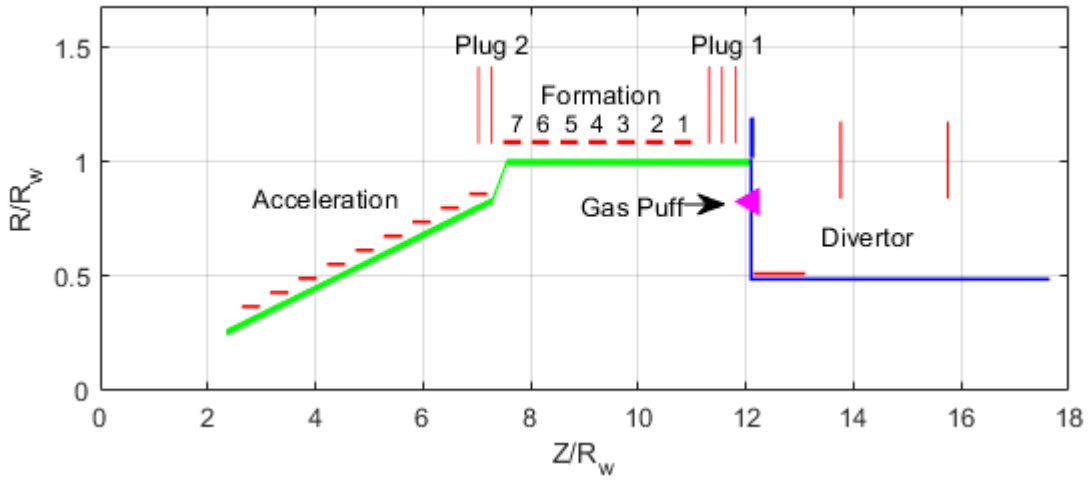

Figure 4.25: Truncated and simplified geometry of Venti Formation device for shot 3275. The length are normalized with respect to the chamber radius.

The seven formation coils are used for the dynamic formation of the FRC with the firing time staggered to gently push the formed FRC into the cone section. The nine accelerator coils are driven together in parallel to act as a flux conserver to hinder the translated FRC from contacting the cone wall. An infrared two-pass interferometer system was active in the experiment with the laser positioned between the formation coil 5 and 6. Multiple visual light diagnostics were present for this shot, but the signals were all filtered to measure

Bremsstrahlung emissions, so no useful data were collected for ionization. The excluded flux results are vacuum referenced to shot 3274. A summary of the diagnostic results from this experiment is shown in Fig. 4.26.

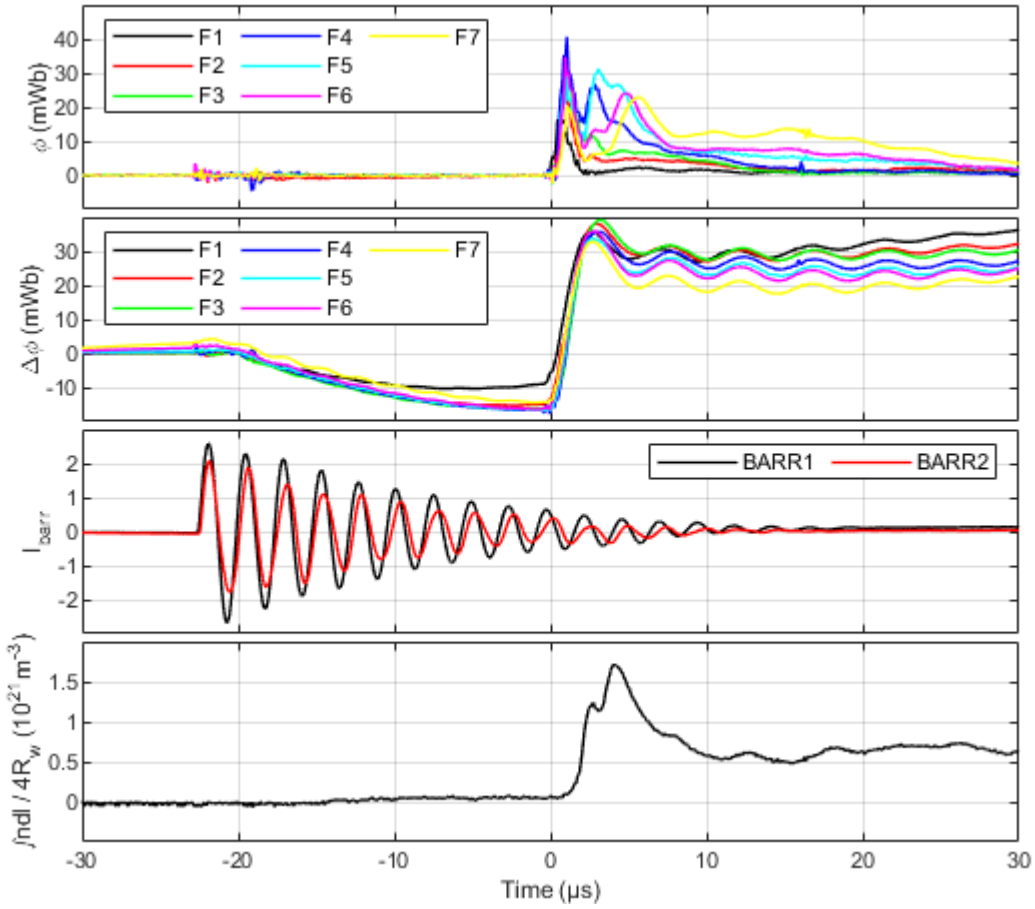

Figure 4.26: Summary of diagnostic result from shot 3275 [65]; (top) magnetic flux; (middle top) excluded flux (vacuum referenced to shot 3274); (middle bottom) barrier coil normalized current and (bottom) NDL normalized by the path length through the chamber.

4.4.1 Circuit Configuration for Shot 3275

Since the vacuum reference shot associated with shot 3275 is shot 3274, the circuit model in Cygnus is constructed to best match the measurements from the flux probes in shot 3275

and from circuit values measured a priori from the experiment [65]. For the formation coils and plug coils, the general circuit structures were not changed from shot 936 to this shot. Thus, the circuit models shown in Fig. 4.6 and Fig. 4.7 are also used for this shot. However, additional accelerator coils were added for this shot. The circuit model used in Cygnus for the accelerator coils is shown in Fig. 4.27. All nine accelerator coils are connected in parallel and driven by a single circuit.

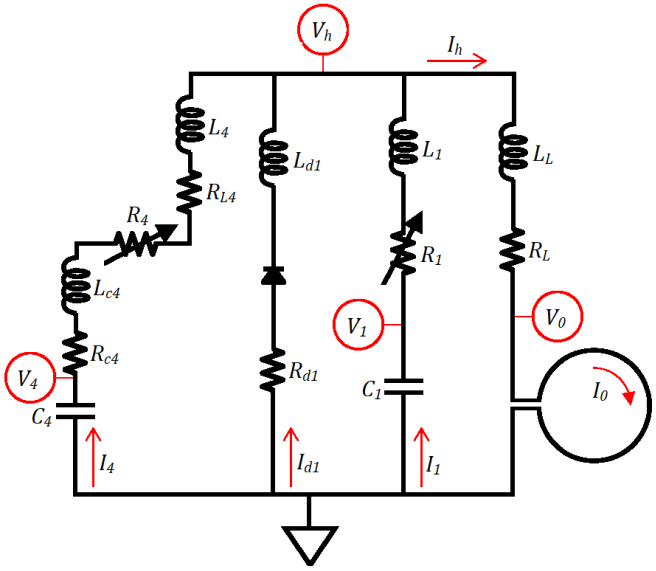

Figure 4.27: Cygnus circuit model for the accelerator coils in shot 3274. Circuit segment 4 corresponds to acceleration bias capacitor and segment 1 is for numerical stabilization

The resulting measured values from the flux probes from the vacuum shot 3274 and those calculated from Cygnus is shown in Fig. 4.28. Note that plug 2 coils were not fired in this shot, and the excluded flux probes for the plug and divertor coils were not active for this shot. For the accelerator coil, since all nine coils are driven together, only one flux loop is used to measure the flux on the coil. A reasonable agreement between the measured and simulated value is obtained.

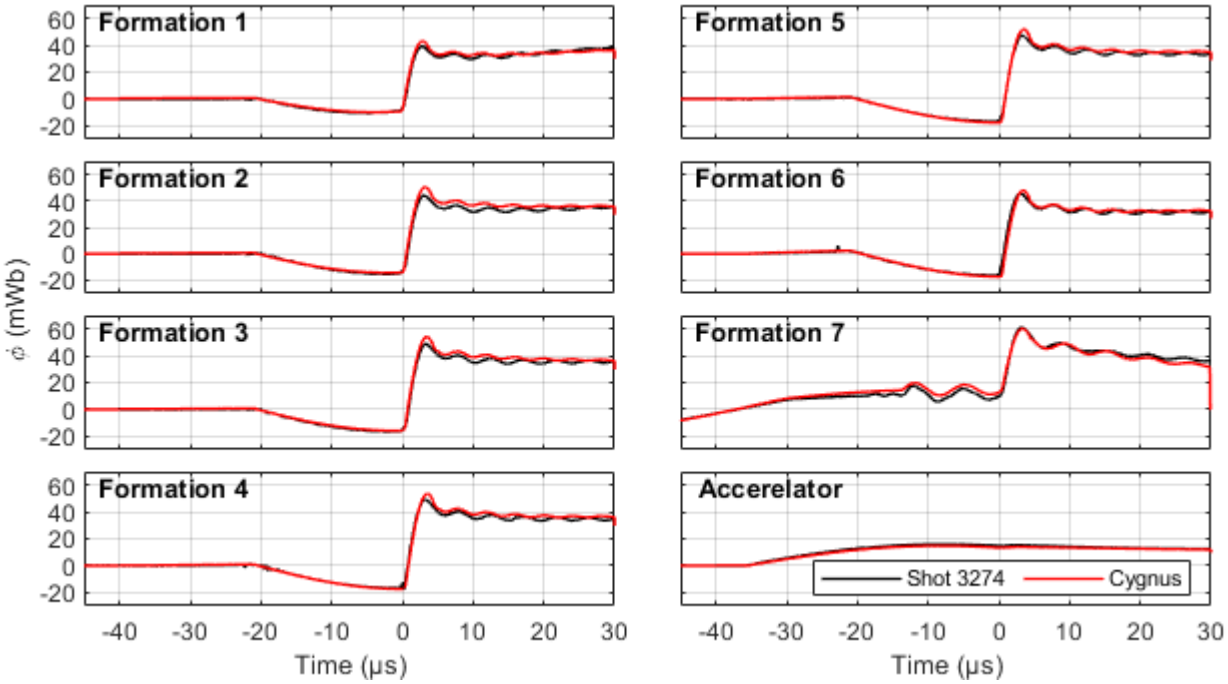

Figure 4.28: Flux measured under each formation coils from shot 3274 [65] and Cygnus calculation.

4.4.2 Simulation Setup for Shot 3275

From Fig. 4.26, it can be seen that the ringing barrier field is started at approximately -23 μs, which is 2 μs before the formation bias firing. Thus, it allows few oscillations of the barrier field for ionization before the bias field becomes too large and hinders the ionization from the ringing barrier coils. Based on the excluded flux signal, there are enhanced noise from -23 to -16 μs, suggesting either ionization events or noise pickups from the barrier coils. The NDL from the interferometer does not begin to show signal from the preionized plasma until after -14 μs.

Similar to the multistage ringing barrier ionization case, the effect of the ringing barrier field is to introduce an ionized plasma layer near the formation chamber wall. For the unassisted case, the plasma layer is produced before the bias field injection, and the additional ionization is quenched when the local bias field becomes larger. Again, the azimuthal profile

of the ringing barrier ionization is neglected, and an axisymmetric plasma layer is assumed. Thus, the initial ionization due to the barrier field can be modeled by initializing a gas density with an ionization layer at time -21 µs, which is the time when the bias flux injection begins. Similar to the multistage ringing barrier ionization case, a layer thickness of 12% formation chamber wall radius is a reasonable approximation for the multipole system used in the device.

For shot 3275, because the time delay between the gas-puff firing and the experimental start times was increased, one can no longer neglect the gas reflection effects from the end of the formation and cone section. As such, the simple density reconstruction method discussed in Section 4.1 is no longer applicable. The effect of the gas reflection is to smoothen the density profile within the formation chamber, as the distinct pulse like dynamic profiles is reduced. For this reason, the gas density is assumed to be constant in the formation section as a simple approximation from this smoothening effect.

Based on the static pressure probe measurement, an equilibrium chamber density of $1.66 \times 10^{20}\,\mathrm{m}^{-3}$ for the diatomic deuterium is computed; this leads to an effective atomic deuterium density of $3.32 \times 10^{20}\,\mathrm{m}^{-3}$. Since the chamber does not reach complete equilibrium at the time when the coils are fired, the gas density at the start of the formation process is larger than this value in the formation section. Based on the FIG measurement, the formation section effective atomic deuterium density can be as high as $6.64 \times 10^{20}\,\mathrm{m}^{-3}$, but the averaged value is closer to $4.85 \times 10^{20}\,\mathrm{m}^{-3}$.

Based on the FIG data average, the atomic deuterium total density of $4.85 \times 10^{20}\,\mathrm{m}^{-3}$ is used in the simulation. The radial density profile is modeled similar to the wall localized preionization from the previous chapter (Section 3.1.2). Early in the bias field injection phase, the infrared interferometer is unable to pick up any signal due to insufficient signal strength. Thus, the initial ionization in the plasma layer is configured to gives a reasonable agreement with the NDL signal at time 0 µs right before the main formation banks are fired; a reasonable agreement is obtained with the initial ionization fraction of 50%. The remaining gas is initialized with 1% ionization.

Based on the initial ionization fraction, initial electron temperature of 1.5 eV is used [66]. The ion temperature is initialized everywhere to 0.5 eV, as the ringing barrier field is too fast to impart significant momentum to ions. The neutral temperature is initialized to 0.025 eV. Since the gas is now assumed to be reflected from the end of the formation chamber, the initial neutral velocity is set to zero.

For both electrons and ions, the Braginskii thermal conductivities are used with the parallel diffusivity capped from 10^2 to $10^6\,\mathrm{m}^2/\mathrm{s}$ and the perpendicular diffusivity capped from 1 to $10^2\,\mathrm{m}^2/\mathrm{s}$. The neutral thermal conductivity is based on the hard sphere collision model for atomic deuterium, and it is capped from 10^3 to $10^9\,\mathrm{m}^2/\mathrm{s}$. The limits on the thermal conductivities are placed to ensure reasonable fluid dynamics behavior during the radial implosion process.

Both Spitzer and the electron-neutral collision resistivities are used by default. Both the anomalous resistivities and isotropic viscosities are tuned to match the experimental results. Again, separate anomalous transport values are used before and after the main bank firing. The values of the anomalous transport coefficients are chosen to best match the experimental data, and it is iterated until a reasonable convergence is reached.

After the iteration process, prior to the main coil firing, the anomalous Chodura resistivity with $C_c = 2$ and $f_c = 3$ is used as a reasonable value for bias flux injection. Similar to the multistage ringing barrier case, an anomalous Bohm resistivity with a Bohm multiplier of 30 is used to improve the flux penetration into the plasma layer to account for the enhanced transport due to azimuthal variation in the ionization plasma layer. For isotropic viscosity, the value of $4000\,\mathrm{m}^2/\mathrm{s}$ is used for both plasma and neutrals to account for negligible excluded flux dynamics in the bias injection phase.

During the FRC formation phase, the anomalous Chodura resistivity with $C_c = 2$ and $f_c = 3$, and isotropic plasma and neutral viscosity of $200\,\mathrm{m}^2/\mathrm{s}$ is used until 2.2 µs where the initial radial implosion occurs. After this time, the anomalous Chodura resistivity is reduced to $C_c = 0.5$ and $f_c = 3$, and the isotropic viscosity is increased to $2000\,\mathrm{m}^2/\mathrm{s}$ for the plasma in the closed field line region. The neutral and open field plasma viscosities are reduced to

$20\,\mathrm{m}^2/\mathrm{s}$. The neutral and open field plasma viscosities are reduced to assist the translation of the FRC into the cone section.

4.4.3 Simulation Results for Shot 3275

The resulting excluded flux signal from shot 3275 and Cygnus simulation is shown in Fig. 4.29. The result calculated using both the dynamic temperature dependent effective ionization potential and the 13.6 eV constant ionization potential are shown in the figure. A reasonable agreement is seen with the experimental results, but neither cases are perfect. In general, the 13.6 eV cases matches better but not conclusively. Both cases has issue later in time due to disagreement in the FRC size and translation velocity.

In order to compare the shape of the FRC between the experiment and simulation, excluded flux radii at various times in the FRC formation process are compared. Fig. 4.30 shows a plot of the excluded flux radii overlaid on the Venti Formation geometry at various point in time during the FRC formation. The agreement with the experiment is not terrible, but some noticeable disagreements can be seen. In general, the simulation generated FRCs are shorter and smaller. This is especially true for the dynamic effective ionization potential case. The general translation behavior of the FRC from the simulation has reasonable agreement with the behavior observed in the experiment.

The NDL signal from the experiment and simulation is shown in Fig. 4.31. A reasonable agreement in the NDL signal can be seen prior to the main bank firing for both calculations, though the 13.6 eV case has slightly higher plasma density than what the experiment suggests. Both simulation cases agree decently during the first radial implosion; however, the experimental density increases more rapidly compared with the two simulations. The agreement beyond the first radial implosion is poor. For the dynamic effective ionization potential case, the NDL signal is far wider compared with the experiment. The 13.6 eV case captures the basic shape of the experimental signal, but it does not capture the magnitude of the second NDL peak. For both cases, the signal in the plateau regions of the NDL signal does not agree well.

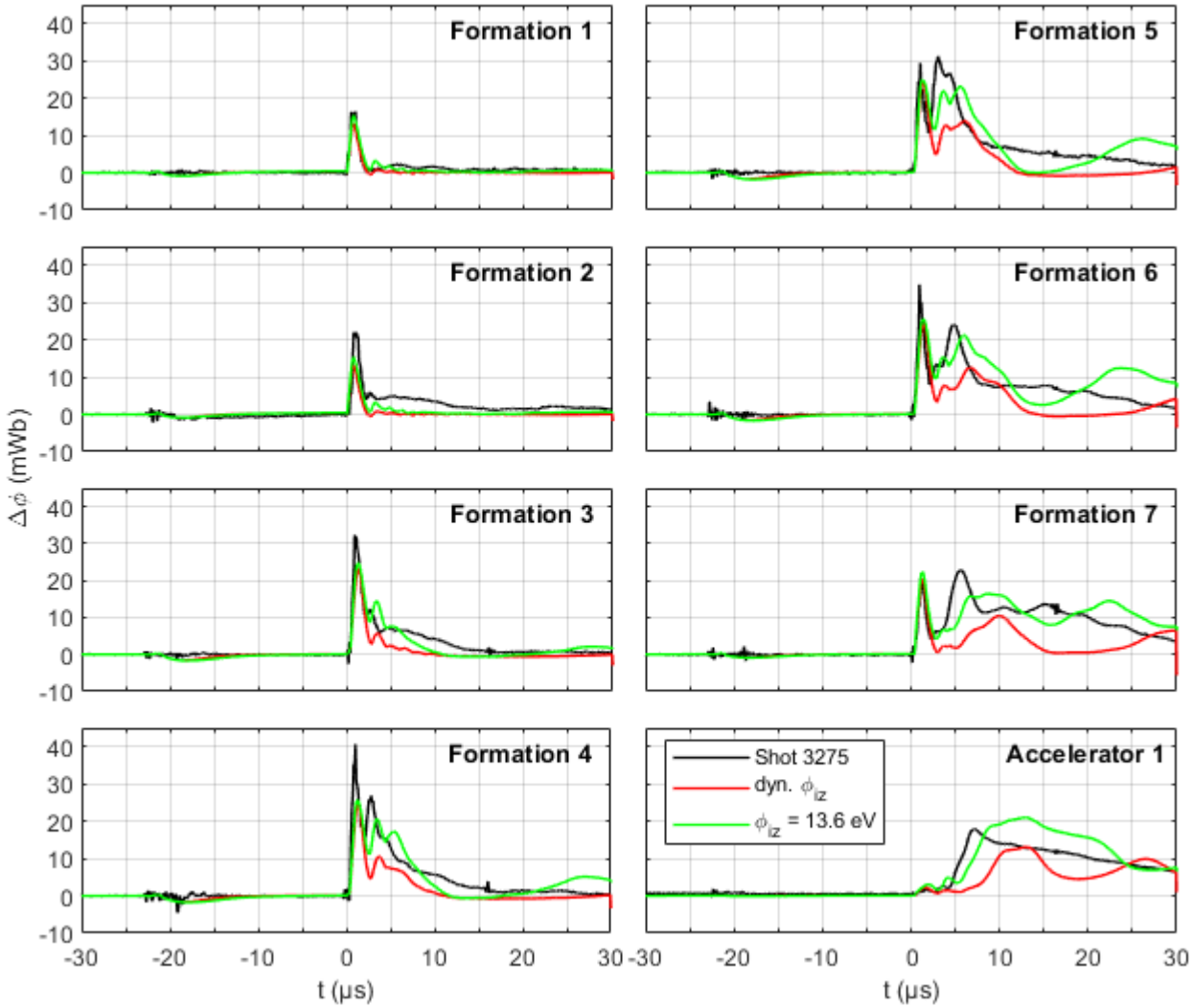

Figure 4.29: The experimental [65] and the simulation generated excluded flux signal under the formation coils for Venti Formation shot 3275.

The disagreement in the rate of the NDL increase during the radial implosion suggests that more ionization is occurring in the experiment. The disagreements beyond the first peak are influenced by many factors. One, because the FRC is translating into the cone section of the device, slight disagreement in the translation speed leads to large change in the NDL signal. The late time disagreement in the NDL signal is most likely caused by the smaller FRC computed from the simulation.

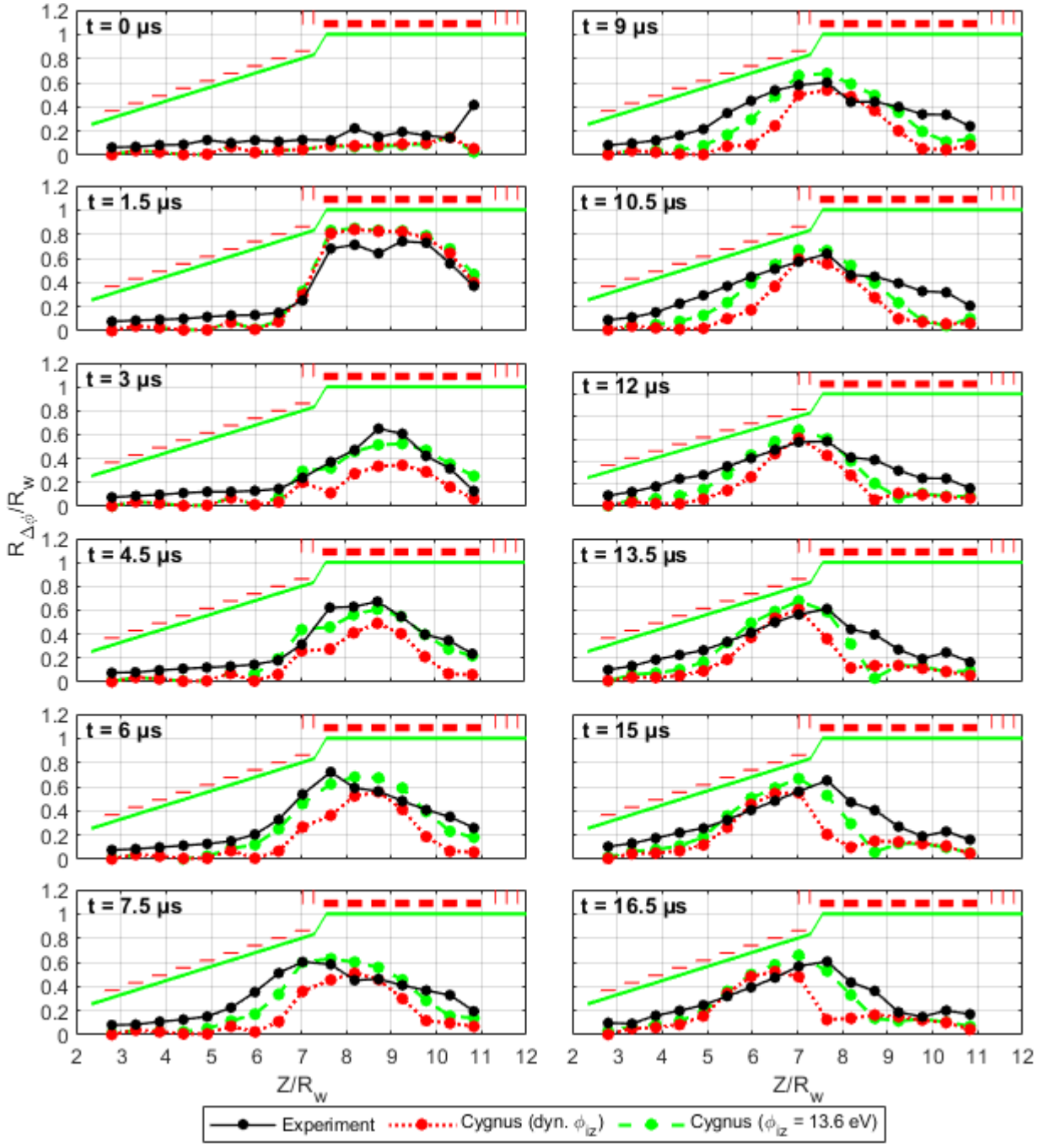

Figure 4.30: The experimental [65] and the simulation generated excluded flux radii for Venti Formation shot 3275. The coils geometry is also shown in the same figure.

The particle inventory in the reversed field region computed from the simulation is shown

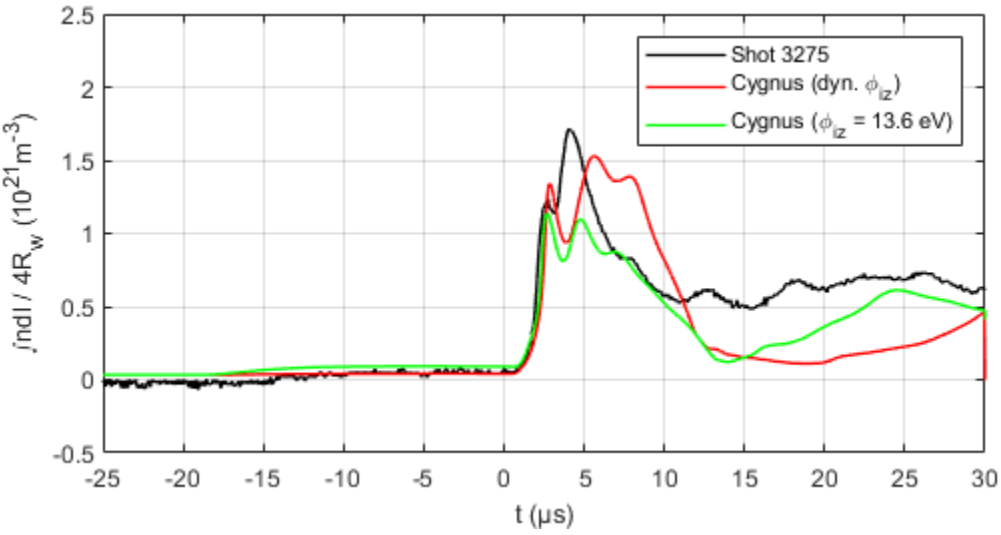

Figure 4.31: The experimental [65] and the simulation generated NDL signal for Venti Formation shot 3275. The NDL signal is normalized by the path length through the chamber.

in Fig. 4.32. It can be seen that slightly more ionization occurs during the bias flux injection in the 13.6 eV case. Right before the main bank is fired, the volume averaged ionization level in the reversed field region is roughly 13% for the dynamic effective ionization potential case and 24% for the 13.6 eV case. Furthermore, during the radial implosion, the 13.6 eV case is able to ionize the remaining gas more rapidly than the dynamic effective ionization potential case, leading to a higher particle inventory at the end of the formation process.

The simulation generated trapped flux and volume averaged FRC temperatures are shown in Fig. 4.33. Since the dynamic effective ionization potential case gives less ideal estimate for the FRC condition than the 13.6 eV case, the expected trapped flux, particle inventory, and temperatures can be estimated. Consider 10 μs when the formation and ionization process is completed and FRC is moving towards the cone section. At this time, roughly 2.2–3.1 mWb of flux is trapped with a particle inventory of roughly 2.3–2.8$\times 10^{19}$ atomic deuterium ions. The electron temperature is roughly 30–70 eV, with the ion temperature ranging from 30–80 eV. For both cases, the peak translational velocity is roughly 0.28 chamber wall radii per microsecond.

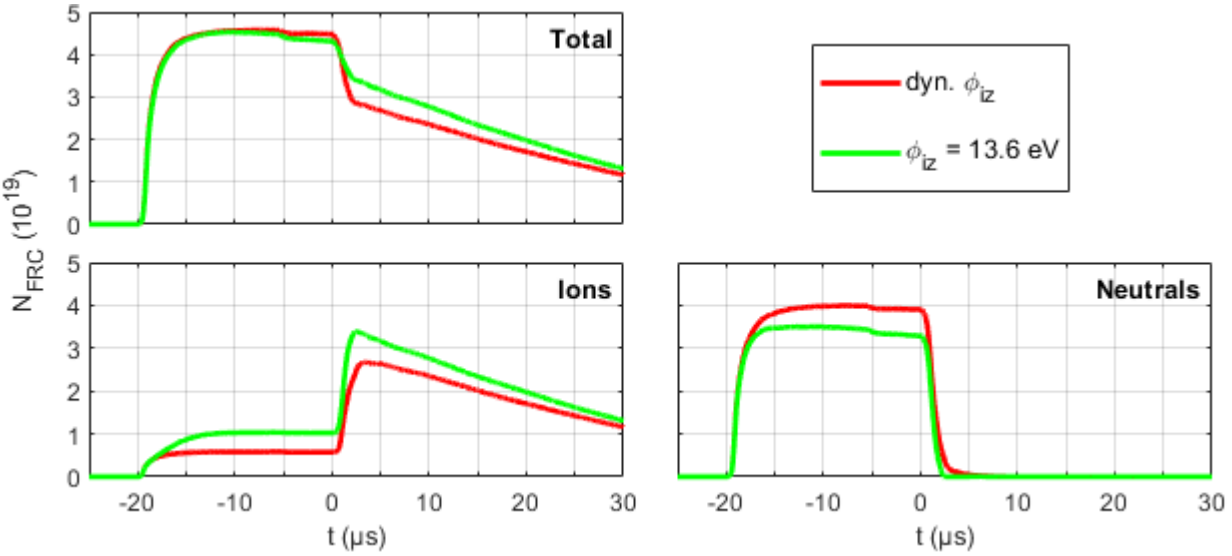

Figure 4.32: The number of particles trapped in the reversed field region during the ringing theta-pinch ionization and FRC formation for Venti Formation shot 3275 simulation.

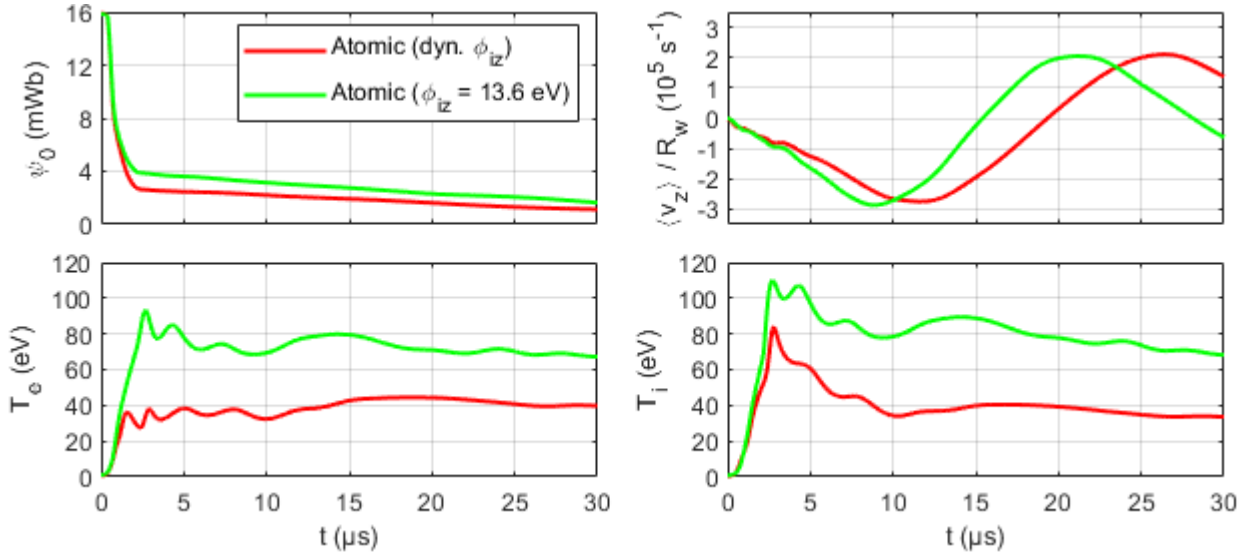

Figure 4.33: The time evolution of the FRC (top left) trapped flux, (bottom left) volume averaged electron temperature, and (bottom right) volume averaged ion temperature for Venti Formation shot 3275 simulation.

4.5 Concluding Remarks for Venti Formation Simulations

Using the plasma-neutral model implemented in the Cygnus code, it is seen that a reasonable agreement between the experimental and simulation results is obtained after sufficient tuning is performed to set reasonable anomalous transport coefficients. From the three cases tested, using temperature dependent dynamic effective ionization potential based on Lieberman and Lichtenberg [58] resulted in poorer agreement with the experiment. Using the theoretical minimum value of 13.6 eV generally resulted in better agreement, through too much ionization were seen early in the simulation during the preionization phase. In general, significant iterations were necessary for tuning the simulation results to the experimental one. Improvements in the experimental diagnostics as well as better knowledge of the exact initial condition in the formation chamber are expected to accelerate the tuning process in the future.

Chapter 5

DISCUSSION OF POSSIBLE SOURCES OF DISCREPANCY WITH THE EXPERIMENT

In the previous chapter, the results from the experiment and simulation were compared. The simulated results showed reasonable match with the experimental measurements, but it was observed that the match is not perfect or that the match required significant tuning of the transport variables and initial conditions.

In this chapter, possible sources of the disagreement for the simulated results and experimental measurements are considered. In the previous chapter, some experiment specific reason for the disagreement were already discussed, e.g., lack of good understanding of the initial condition of the preionized gas in the formation chamber and lack of diagnostic to obtain data that are useful for monitoring ionization level in the formation process. Here, the attention is paid to the possible source of discrepancy due to missing physics in the model. In particular, following four effects are considered: 1) three-dimensional effects, 2) multi-step ionization processes, 3) molecular species effects, and 4) kinetic effects.

5.1 Three-Dimensional Effects

The ionization process is a complex three-dimensional phenomena, especially when a ringing barrier field is used. Due to the azimuthal dependence of the ringing multi-pole barrier field, the ionization events occur locally near the wall with a spatial azimuthal mode of the multipole. Thus, it is possible that azimuthal magnetic islands and local plasma filamentation can occur during the preionization process, which leads to plasma production, but with no pickup in the excluded flux arrays due to the fact that it cannot conduct any azimuthal current. This effect may also not be picked up by a single-chord interferometer, as the laser

may miss the local region where it occurs. It is also possible that the feature of interests is too close to the wall such that the pickup by the interferometer is small.

The ringing barrier field also opens the closed field-line structure generated by the bias field and the cusp fields. As such, the outer magnetic field layer of the initial imbedded magnetic field has a complex three-dimensional structure that is not captured by a axisymmetric model. This three-dimensional structure of the magnetic field may lead to modifications in the plasma transport process, especially that of the electrons that are energized by the ringing barrier field to enhance electron impact ionization processes. In order to capture these effects, a three-dimensional model with a complete description of the external conductors including the barrier coils are necessary.

5.2 Multi-Step Ionization

In the previous chapter, it was observed that the agreement with the experiment was improved when the effective ionization potential was reduced and the ideal optimum value was used for the simulation. In particular, using the dynamic temperature dependent effective ionization potential with a form suggested by Lieberman and Lichtenberg resulted in too much electron cooling, that significantly reduced the efficiency of the ionization process during the radial implosion. This suggests that not all energy that is spent exciting neutral atoms is lost through the radiation. As such, the excited state neutrals can be further ionized with a multi-step ionization process.

The multi-step ionization process occurs in the FRC formation due to the time scale of the formation and implosion processes. If the ionization time scale of the excited states are much shorter than the time scale of the radiative decay back down to a deexcited state, then the energy absorbed by the neutrals cannot be lost from the system through the radiative deexcitation process. As such, it remains as excited neutrals that have much lower threshold energy for ionization. In addition, if the initial neutral gas density is sufficiently dense such that it is optically thick to the radiation produced by the decay, then the energy loss through the radiative deexcitation process is prevented indefinitely.

The importance of the multi-step ionization process was known in the past for the numerical modeling of theta-pinches. For example, Duchs and Griem developed a multi-component fluid model with the excited neutral states tracked [67]. The gas state is characterized with three states: ground state, excited state, and continuum (ion) state. In the excited state, the $n = 2$ state of the hydrogen is tracked. For states with $n \geq 3$, it is treated as being an ion, since the collisional transition to a true continuum state has large cross sections with small energy gaps. The metastable $2s$ state is not distinguished from the excited $2p$ state, as the hydrogen in $2s$ states are excited to $2p$ state very effectively. With this, fluid equations for three gas states and electrons can be derived; given appropriate reaction rates and cross sections, the ionization process can be modeled numerically with Duchs and Griem's model.

Significantly simplified version of the Duchs and Griem's model was developed by Sgro, which is applicable to many cases where a sufficiently high electron temperature exists to maintain an efficient ionization process during the radial implosion [32]. Sgro's simplification removes the requirement to keep track of the excited neutral states separately, and instead, treats the effect of the excited state neutrals by using a modified ionization rate that includes contributions from the multi-step ionization processes. Sgro argues that for typical condition encountered in the implosion of high voltage theta-pinches, the rate of ionization of the excited state species are very rapid compared with the implosion time scale, such that it can be considered as a single step process to greatly simplify the numerical model.

In both models, the reason for the inclusion of the first excited state ($n = 2$) hydrogen is due to the excitation cross section that is comparable to the ionization. In addition, the $n = 2$ state does not radiatively decay back down to the ground state in the time scale of the implosion process, as the Ly-α from the decay process is strongly re-absorbed. This condition is met as long as the neutral gas is optically thick to Ly-α. Based on Sgro, the neutral gas will remain optically thick to Ly-α in a machine with a 0.1 m radius as long as $n_n \gtrsim 2 \times 10^{18} T_e^{1/2} \mathrm{m}^{-3}$ where T_e is in eV [32]. Thus, for many FRC formation problems, Sgro's condition is met, and multi-step ionization processes must be included.

The use of the optimistic value of the effective ionization potential in the simulation is thus

justified by the presence of the multi-step ionization process. As a future work, the effective ionization potential model based on Lieberman and Lichtenberg should be replaced with the Sgro's model. Similar to the theta-pinches modeled by Sgro, for typical FRC formation problems, radiative recombination processes are negligible in the time scale of the formation process. Thus, the ionization model of Sgro is more appropriate for FRC modelings than that of Lieberman and Lichtenberg. For now, optimistic value of the effective ionization potential is used to account for the reduced energy loss in the excitation process due to the multi-step ionization process.

5.3 Molecular Effects

In many experiments for fusion energy, the starting gas species is diatomic deuterium that is stable and storable. In many cases for FRC formation, the diatomic deuterium gas is injected directly into the formation chamber and the preionization process is started. In some devices, the gas may be assisted with a pre-preionization step that breaks down the gas prior to the preionization process, but for the Venti Formation device, no pre-preionization step exists so the gas starts as a molecular species. Thus, depending on the formation method used, the preionization and bias flux injection phase may be affected by the molecular species.

Since the initial gas fill is diatomic neutrals, the modification in the neutral gas behavior due to the presence of the diatomic molecules must be considered. For one, there are additional energy expended in ionizing the neutrals. For example, for diatomic hydrogen molecule, the dissociation reaction begins at the threshold energy of 8.8 eV as the repulsive $^3\Sigma_u^+$ state is excited and two fast atomic hydrogen fragments each carrying 2.2 eV are produced [58]. Thus, additional electron energy loss is required in addition to the required ionization potential. At higher threshold energy, dissociative ionizations to atomic ions and neutrals and ionizations to molecular ions are possible. In addition, due to the complexity of the molecular species, additional excited states are possible, which results in modified cross sections for ionizations, dissociations, and recombinations.

Second major change to plasma-neutral interactions when the molecular species are

present is the development of the non-resonant charge-exchange processes. When there are multiple species of ions and neutrals present, depending on the ground state energy of the interacting neutral and ion species, energy deficit that hinders the charge-exchange process is present [68]. For the non-resonant (asymmetric) charge exchange between the two gas species, the charge exchange reaction is given as

$$A^+ + B \rightarrow A + B^+ + \Delta E \tag{5.1}$$

where the energy deficit $\Delta E = \varphi_{iz}^A - \varphi_{iz}^B$ is the difference in the ionization potentials of gas species A and B. When the energy deficit is positive, then the reaction is exothermic, and the reaction is quasi-resonant where the reaction rates are similar to the resonant cases. When the energy deficit is negative, then the reaction is endothermic, and the reaction is non-resonant. For the non-resonant case, when the impact energy is low, the charge exchange cross section is significantly reduced from the resonant value as computed by Rapp and Francis [68]. For high impact energy, the non-resonant case generally converges to the resonant value.

Due to the modification in the ionization and charge exchange process when the molecular species are considered, when a device with a non-negligible initial molecular neutral fill is modeled, effects of molecular species must be included in the model. Since the Venti Formation device had no pre-preionization system installed, the weakly ionized gas fill in the formation chamber during the preionization and radial implosion contained non-negligible population of molecular neutrals. Thus, to improve the modeling of the FRC formation process in the Venti Formation device, effects of molecular deuterium species should be added to the numerical model.

5.4 Kinetic Effects

The preionization and formation phase of the FRC are violent and turbulent phenomena, and the detailed physics of the preionization and formation is not well understood both theoretically and experimentally. It is possible that there are formation of both global and

micro turbulences that cause instabilities in the mixed partially ionized gas in the formation chamber. As a result, the local distribution function for ions, electrons, and neutrals may be far removed from the Maxwellian distribution on which the collision and reaction terms are based. In this section, the term kinetic effects is used to refer to all phenomena that are caused by the non-Maxwellian nature of the local distribution function, irrespective of the source of such non-Maxwellian development.

The plasma-neutral fluid model is more susceptible to the non-Maxwellian effect compared with the typical fully ionized MHD model. In the model, all reactions assume Maxwellian distribution, but some reaction cross sections (e.g., ionization) are sharply peaked at a specific impact energy. Thus, if the local distribution is removed from the Maxwellian distribution, the reaction rate will not be computed accurately for reactions with sharply peaked cross sections.

To see this more clearly, consider a kinetic description of the species governed by the Boltzmann equation. The Boltzmann equation for species α is given to be

$$\frac{\partial f_\alpha}{\partial t} + \mathbf{v}_\alpha \cdot \boldsymbol{\nabla}_{\mathbf{x}} f_\alpha + \left[\frac{e_\alpha}{m_\alpha}\left(\mathbf{E} + \mathbf{v}_\alpha \times \mathbf{B}\right)\right] \cdot \boldsymbol{\nabla}_{\mathbf{v}} f_\alpha = \frac{\delta f_\alpha}{\delta t}$$

where e_α and m_α are the species charge and mass, respectively, $\mathbf{E}$ and $\mathbf{B}$ are the electric and magnetic field, respectively, that depends only on the spatial coordinates, and the right-hand-side term is associated with the time change of the species distribution function due to collision and reaction processes.

To obtain the fluid description, moments of the Boltzmann equation are taken, and the infinite chain of the moment equations is obtained. The infinite chain of the moment equation fully captures the original Boltzmann equation as the distribution function can be reconstructed from the tensorial series sum of the moment variables given as

$$f_\alpha\left(\mathbf{r}, \mathbf{v}, t\right) = f_\alpha^{(0)}\left(\mathbf{r}, \mathbf{v}, t\right) \sum_{n=0}^{\infty} \sum_{m=0}^{\infty} \sigma_{mn} a^{mn}_{\alpha, r_1 \cdots r_m}\left(\mathbf{r}, t\right) H^{mn}_{\alpha, r_1 \cdots r_m}\left(\boldsymbol{\xi}\right)$$

where $\boldsymbol{\xi} = \gamma_\alpha^{1/2}\mathbf{c}_\alpha$ is the normalized random velocity, $\mathbf{c}_\alpha = \mathbf{v} - \mathbf{u}_\alpha$ is the random velocity, $\gamma_\alpha = m_\alpha/kT_\alpha$ is the inverse of the thermal speed squared, $a^{mn}_{\alpha,r_1\cdots r_m}$ are the moment variables, and $H^{mn}_{\alpha,r_1\cdots r_m}$ is the irreducible tensorial Hermite polynomials [57].

Consider the zeroth, first, and the second order moment of the Boltzmann equation that are typically considered for the fluid models. They are given to be as follows:

$$\frac{\partial n_\alpha}{\partial t} + \boldsymbol{\nabla}\cdot(n_\alpha \mathbf{u}_\alpha) = \frac{\delta N_\alpha}{\delta t}$$

$$\frac{\partial}{\partial t}(m_\alpha n_\alpha \mathbf{u}_\alpha) + \boldsymbol{\nabla}\cdot\left(m_\alpha n_\alpha \mathbf{u}_\alpha\mathbf{u}_\alpha + p_\alpha \overleftrightarrow{\mathrm{I}} + \overleftrightarrow{\Pi}_\alpha\right) - n_\alpha e_\alpha(\mathbf{E} + \mathbf{u}_\alpha\times\mathbf{B}) = \frac{\delta \mathbf{M}_\alpha}{\delta t}$$

$$\frac{\partial p_\alpha}{\partial t} + \boldsymbol{\nabla}\cdot(p_\alpha\mathbf{u}_\alpha) + \frac{2}{3}\left(p_\alpha\boldsymbol{\nabla}\cdot\mathbf{u}_\alpha + \overleftrightarrow{\Pi}_\alpha\boldsymbol{\nabla}\mathbf{u}_\alpha + \boldsymbol{\nabla}\cdot\mathbf{q}_\alpha\right) = \frac{\delta E_\alpha}{\delta t}$$

where n_α, $\mathbf{u}_\alpha$, p_α, $\overleftrightarrow{\Pi}_\alpha$, and $\mathbf{q}_\alpha$ are the moment variables, where $\overleftrightarrow{\Pi}_\alpha$ and $\mathbf{q}_\alpha$ are the higher order moment terms. The right-hand-side term represents the moment of the $\delta f_\alpha/\delta t$ term. Since the $\delta f_\alpha/\delta t$ term is a function of the local distribution function itself, the right-hand-side terms in the fluid equation are functions of all of the moment variables in general.

5.4.1 Special Case for Single Species Fully Ionized Plasma

Consider the special case of the fully ionized fluid with a single ion species with no internal states and no reactions. In this special case, a series of physics-based argument can be made to simplify the right-hand-side collision terms in the fluid equation without assuming the form of the local distribution function itself. First, consider the continuity equation. Since the system is assumed to be fully ionized with no reactions, there will be no production or destruction of ions or electrons from the system. As such, since the collision processes cannot modify the local number density due to the conservation of mass, the right-hand-side of the continuity equation for both ions and electrons is exactly equal to zero, irrespective of the number of particles participating in such a collision process. Thus, the continuity equation

becomes

$$\frac{\partial n_i}{\partial t} + \boldsymbol{\nabla} \cdot (n_i \mathbf{u}_i) = 0$$
$$\frac{\partial n_e}{\partial t} + \boldsymbol{\nabla} \cdot (n_e \mathbf{u}_e) = 0$$

From the above form of the continuity equations, one can obtain two equations in the center-of-mass of the two fluid to bring it to the form similar to the MHD.

$$\frac{\partial \rho_m}{\partial t} + \boldsymbol{\nabla} \cdot (\rho_m \mathbf{u}) = 0$$
$$\frac{\partial \rho_c}{\partial t} + \boldsymbol{\nabla} \cdot \mathbf{J} = 0$$

where $\rho_m = m_i n_i + m_e n_e$ is the center-of-mass mass density, $\mathbf{u} = \rho_m^{-1} (m_i n_i \mathbf{u}_i + m_e n_e \mathbf{u}_e)$ is the center-of-mass velocity, $\rho_c = Z e n_i - e n_e$ is the charge density, $J = Z n_i \mathbf{u}_i - e n_e \mathbf{u}_e$ is the current density, and Z is the ionization number of the ions.

Next, consider the momentum equation. Again, since there are no reactions, there are no momentum production due to creation or destruction of the particles. Since there are two species (ions and electrons), they can now exchange momentum with each other through the collision process. However, regardless of the number of ion and electron particles that interacted within the collision event, the total momentum of the system will be conserved. Thus, the right-hand-side term in the ion and electron momentum equation will be equal and opposite to each other. The momentum equation becomes

$$\frac{\partial}{\partial t} (m_i n_i \mathbf{u}_i) + \boldsymbol{\nabla} \cdot \left(m_i n_i \mathbf{u}_i \mathbf{u}_i + p_i \overleftrightarrow{\mathrm{I}} + \overleftrightarrow{\Pi}_i \right) - n_i Z e (\mathbf{E} + \mathbf{u}_i \times \mathbf{B}) = \frac{\delta \mathbf{M}}{\delta t}$$
$$\frac{\partial}{\partial t} (m_e n_e \mathbf{u}_e) + \boldsymbol{\nabla} \cdot \left(m_e n_e \mathbf{u}_e \mathbf{u}_e + p_e \overleftrightarrow{\mathrm{I}} + \overleftrightarrow{\Pi}_e \right) - n_e e (\mathbf{E} + \mathbf{u}_e \times \mathbf{B}) = -\frac{\delta \mathbf{M}}{\delta t}$$

Using the center-of-mass fluid variables, the momentum equation for the combined system

becomes the following:

$$\frac{\partial}{\partial t}\left(\rho_m \mathbf{u}\right) + \boldsymbol{\nabla}\cdot\left(\rho_m \mathbf{u}\mathbf{u} + p\overleftrightarrow{\mathrm{I}} + \overleftrightarrow{\Pi}^*\right) - \rho_c \mathbf{E} - \mathbf{J}\times\mathbf{B} = 0$$

where

$$\overleftrightarrow{\Pi}^* = \overleftrightarrow{\Pi} + \frac{m_i m_e}{Ze^2\rho_m}\frac{\mathbf{J}\mathbf{J} - \rho_c\left(\mathbf{u}\mathbf{J} + \mathbf{J}\mathbf{u}\right) + \rho_c^2\mathbf{u}\mathbf{u}}{\left(1 + r_m r_c\right)\left(1 - r_c\right)}$$

$r_m = Zm_e/m_i$, $r_c = m_i\rho_c/\left(Ze\rho_m\right)$, $p = p_i + p_e$ is the total pressure, and $\overleftrightarrow{\Pi} = \overleftrightarrow{\Pi}_i + \overleftrightarrow{\Pi}_e$ is the total viscous stress tensor. The equation for the advance of the current density is given to be the following:

$$\left[1 - r_c\left(1 - r_m\right)\right]\mathbf{E} + \mathbf{u}\times\mathbf{B} = \mathbf{R}^* + \frac{m_i}{Ze\rho_m}\left(1 - r_m\right)\mathbf{J}\times\mathbf{B}$$

where

$$\begin{aligned}\mathbf{R}^* = \mathbf{R} &- \frac{m_i}{Ze\rho_m}\left(1 + r_m\right)\boldsymbol{\nabla}\cdot\left(p_e\overleftrightarrow{\mathrm{I}} + \overleftrightarrow{\Pi}_e\right) \\ &+ \frac{m_i m_e}{Ze^2\rho_m}\left\{\frac{\partial\mathbf{J}}{\partial t} + \boldsymbol{\nabla}\cdot\left[\frac{\mathbf{J}\mathbf{u} + \mathbf{u}\mathbf{J} - \left(m_i/Ze\rho_m\right)\mathbf{J}\mathbf{J} - \rho_c\mathbf{u}\mathbf{u}}{1 - r_c} + \frac{Ze}{m_i}\left(p\overleftrightarrow{\mathrm{I}} + \overleftrightarrow{\Pi}^*\right)\right]\right\}\end{aligned}$$

and

$$\mathbf{R} = -\frac{m_i}{Ze\rho_m}\left(1 + r_m\right)\frac{\delta\mathbf{M}}{\delta t}$$

is the term associated with collisions between ions and electrons.

Finally, consider the pressure equation. Since the species is assumed to have no internal states, the species pressure equation can be written as an energy equation with the total energy density of the species defined to be $\varepsilon_\alpha = m_\alpha n_\alpha u_\alpha^2/2 + 3p_\alpha/2$. Since the system is fully ionized, there are no energy production due to creation or destruction of the particles from reactions. Since there are two species (ions and electrons), the two species can now exchange energy with each other through the collision process. However, regardless of the number of ion and electron particles that interacted within the collision event, the total energy of

the system will be conserved, although the partition of the energy in the two fluid will be modified. Thus, the right-hand-side term in the ion and electron energy equation will be equal and opposite to each other. The energy equation becomes

$$\frac{\partial \varepsilon_i}{\partial t} + \boldsymbol{\nabla} \cdot \left[\varepsilon_i \mathbf{u}_i + \mathbf{u}_i \cdot \left(p_i \overleftrightarrow{\mathrm{I}} + \overleftrightarrow{\Pi}_i \right) + \mathbf{q}_i \right] - n_i Z e \mathbf{u}_i \cdot \mathbf{E} = \frac{\delta \tilde{E}}{\delta t}$$
$$\frac{\partial \varepsilon_e}{\partial t} + \boldsymbol{\nabla} \cdot \left[\varepsilon_e \mathbf{u}_e + \mathbf{u}_e \cdot \left(p_e \overleftrightarrow{\mathrm{I}} + \overleftrightarrow{\Pi}_e \right) + \mathbf{q}_e \right] + n_e e \mathbf{u}_e \cdot \mathbf{E} = -\frac{\delta \tilde{E}}{\delta t}$$

Using the center-of-mass fluid variables, the energy equation for the combined system becomes the following:

$$\frac{\partial \varepsilon}{\partial t} + \boldsymbol{\nabla} \cdot \Bigg\{ \varepsilon \mathbf{u} + \frac{m_e \varepsilon}{e \rho_m} \frac{\mathbf{J} - \rho_c \mathbf{u}}{1 + r_m r_c} - \left[\frac{1}{2} \frac{m_e}{e} \frac{\left| \mathbf{u} - m_i \mathbf{J} / Z e \rho_m \right|^2}{1 - r_c} \right] \frac{\mathbf{J} - \rho_c \mathbf{u}}{(1 + r_m r_c)(1 - r_c)}$$
$$+ \frac{\mathbf{u} + m_e \mathbf{J} / e \rho_m}{1 + r_m r_c} \cdot \left(p \overleftrightarrow{\mathrm{I}} + \overleftrightarrow{\Pi} \right) - \frac{(1 + r_m)(m_i \mathbf{J} / Z e \rho_m - r_c \mathbf{u})}{(1 + r_m r_c)(1 + r_c)} \cdot \left(\frac{5}{2} p_e \overleftrightarrow{\mathrm{I}} + \overleftrightarrow{\Pi}_e \right)$$
$$+ \mathbf{q} \Bigg\} - \mathbf{J} \cdot \mathbf{E} = 0$$

where $\mathbf{q} = \mathbf{q}_i + \mathbf{q}_e$ and

$$\varepsilon = \frac{1}{2} \rho_m u^2 + \frac{3}{2} p + \frac{1}{2} \frac{m_i m_e}{Z e^2 \rho_m} \frac{\left| \mathbf{J} - \rho_c \mathbf{u} \right|^2}{(1 + r_m r_c)(1 - r_c)}$$

Note that in general, one must still advance electron pressure equation together with the total energy equation to fully reproduce the original set of continuity, momentum, and the energy equations for the ion and electron species. The electron pressure advance is given to be

$$\frac{\partial p_e}{\partial t} + \boldsymbol{\nabla} \cdot (p_e \mathbf{u}_e) + \frac{2}{3} \left[p_e \boldsymbol{\nabla} \cdot \mathbf{u}_e + \overleftrightarrow{\Pi}_e : \boldsymbol{\nabla} \mathbf{u}_e + \boldsymbol{\nabla} \cdot \mathbf{q}_e \right] = -\frac{2}{3} \left(Q + n e \mathbf{u}_e \cdot \mathbf{R} \right)$$

where $Q = \delta E / \delta t$ is the energy transferred from electrons to ions due to the collision processes.

From what has been shown up to this point, one can see that the right-hand-side col-

lision and reaction contribution to the center-of-mass continuity, momentum, and energy equation are exactly equal to zero from physical arguments alone, and the detail of the local distribution function is not required. For the higher order moment terms and the remaining collision terms, there are no conservation law that allows further simplification. Thus, the explicit dependence on the local distribution function is contained in those transport terms that has well understood physical meaning. These transport terms are viscosities, thermal conductivity, electrical resistivity, and heat transfer.

To obtain MHD equations, further assumptions can be made, that are applicable in many physically relevant cases. First, one can assume quasi-neutrality and set $\rho_c \approx 0$. Unless very strong external electric or magnetic field is applied in the plasma system, the assumptions of quasi-neutrality is generally valid due to large Coulomb forces between ions and electrons. Second, for typical fusion experiments, one can assumes hydrogenic species, and set $Z = 1$. Third, since the electron inertia is much smaller than the ion inertia, the terms multiplied by the electron inertia can be neglected. Finally, the electromagnetic radiation effects can be largely neglected for typical conditions. With these assumptions, the fluid equations reduces to the following:

$$\frac{\partial n}{\partial t} + \boldsymbol{\nabla} \cdot (n\mathbf{u}) = 0$$

$$\frac{\partial}{\partial t}(mn\mathbf{u}) + \boldsymbol{\nabla} \cdot (mn\mathbf{u}\mathbf{u}) + \boldsymbol{\nabla} p - \mathbf{J} \times \mathbf{B} = -\boldsymbol{\nabla} \cdot \overleftrightarrow{\Pi}$$

$$\frac{\partial \varepsilon}{\partial t} + \boldsymbol{\nabla} \cdot [(\varepsilon + p)\,\mathbf{u}] - \mathbf{J} \cdot \mathbf{E} = -\boldsymbol{\nabla} \cdot \left(\mathbf{q}^* + \mathbf{u} \cdot \overleftrightarrow{\Pi}\right)$$

$$\mathbf{E} + \mathbf{u} \times \mathbf{B} = \mathbf{R}^* + \frac{1}{en}\mathbf{J} \times \mathbf{B}$$

$$\boldsymbol{\nabla} \times \mathbf{E} = -\frac{\partial \mathbf{B}}{\partial t}$$

$$\boldsymbol{\nabla} \times \mathbf{B} = \mu_0 \mathbf{J}$$

$$\frac{\partial p_e}{\partial t} + \frac{5}{3}\boldsymbol{\nabla} \cdot \left[p_e \left(\mathbf{u} - \frac{\mathbf{J}}{en}\right)\right] = -\frac{2}{3}\left[Q^* + (en\mathbf{u} - \mathbf{J}) \cdot \mathbf{R}^*\right]$$

where

$$\mathbf{q}^* = \mathbf{q} - \frac{\mathbf{J}}{en} \cdot \left(\frac{5}{2} p_e \overleftrightarrow{\mathrm{I}} + \overleftrightarrow{\Pi}_e \right)$$

$$\mathbf{R}^* = \mathbf{R} - \frac{1}{en} \boldsymbol{\nabla} \cdot \left(p_e \overleftrightarrow{\mathrm{I}} + \overleftrightarrow{\Pi}_e \right)$$

$$Q^* = Q + \boldsymbol{\nabla} \cdot \mathbf{q}_e + \boldsymbol{\nabla} \cdot \left[\overleftrightarrow{\Pi}_e \cdot \left(\mathbf{u} - \frac{\mathbf{J}}{ne} \right) \right]$$

and $\varepsilon = mnu^2/2 + 3p/2$ is the total energy density for the plasma. It can be seen that there are four transport related terms that are dependent on the local distribution function (i.e. dependent on all of the moment variables). They are the viscous stress tensor for the combined fluid $\overleftrightarrow{\Pi}$, the effective heat flow vector for the combined fluid $\mathbf{q}^*$, the dissipative decay of the magnetic field $\mathbf{R}^*$ and the effective heat generation for the electron fluid Q^*. As it can be seen, all transport variables have well understood physical meanings.

Fundamentally, one only needs to know the exact form of these four transport variables to obtain solutions from the above equation that agrees with that computed from the Boltzmann equation. Note that in the above form of equations, quasi-neutrality is assumed so the spatial length scale must be larger than the Debye length, and a negligible electron inertia is assumed so the high frequency effects on electron inertial time scale are not captured. However, no assumption was made on the exact form of the local distribution function. Thus, the assumption of the locally Maxwellian distribution function is not required to generate the above form of the fluid equation, and rather, such assumptions are typically used to generate a closure for the transport terms.

Historically, MHD model has been shown to be applicable to surprisingly wide range of applications, one of which is FRC modeling, where based on the traditional criteria is outside the region of validity for the MHD model. As shown in this derivation, the key to the success of the MHD based model is that the basic equations of MHD are applicable to the system that is far from equilibrium as long as reasonable form of the transport coefficient is used to capture the non-Maxwellian feature of the local distribution function. This does not mean that the solution from the MHD equation captures the full form of the local distribution

function. Rather, it simply ensures that the fluid variables computed by advancing the MHD equation with an exact and accurate transport terms will exactly match the fluid variables computed by directly advancing the Boltzmann equation and taking fluid moments.

In the MHD modeling of the FRCs, typically, following anomalous corrections are made to the transport variables to obtain result that matches the experimental results. In order to obtain a correct magnetic flux decay profile that matches experimental measurements, empirically tunable Chodura resistivity is employed (e.g. to capture the effect of microturbulent electron dynamics [54]). To match the radial implosion and axial contraction dynamic in the FRC formation with the experiment, viscosity is modified. The heat flow is limited to ensure that the heat flow rate from the separatrix is reasonable compared with the experimental observation (e.g. as discussed by Steinhauer, the electron thermal loss along the field line is limited to its convective rates and not the larger parallel thermal conduction rates [12]). Furthermore, the heat generation for electrons is often adjusted to obtain FRC temperature that matches experimental results (e.g. anomalous resistive heating due to microinstabilities typically goes into the ion heating rather than the electron heating, as discussed by Milroy and Brackbill [53]). In essence, by tuning these simulation parameters to match experimental results, one implicitly add kinetic corrections (corrections due to non-Maxwellian features of the local distribution function) to the MHD equation, allowing the MHD equation to capture phenomena that cannot be explained by assuming a locally Maxwellian distribution functions.

Note that the form of the closure must be known a priori, either theoretically or through experimental observations. Thus, the MHD model with the transport terms modified to match experimental results does not result in a predictive simulation from fundamental physics. Rather, one generally hopes that the set of the modified transport terms have correct scaling characteristics such that the transport that was applicable to one experimental condition are applicable to other similar experiments. In order to capture physics from the kinetic effect based on fundamental physics, one must resort to a numerical model that solves the kinetic Boltzmann equation directly, such as the Particle-in-Cell method.

5.4.2 Meier-Shumlak Two-Fluid Model

Now consider the two-fluid plasma-neutral model of Meier and Shumlak. In the Meier and Shumlak's two-fluid model, the quasi-neutral plasma species of ions and electrons and the neutral fluid is included. Due to the presence of the neutral fluid, species conversion due to reactions is now allowed in addition to the collision interactions. Assuming quasi-neutrality, negligible electron inertia, and negligible electromagnetic radiation from the beginning, the continuity equation for the three-species model is given to be

$$\begin{aligned} \frac{\partial n}{\partial t} + \boldsymbol{\nabla} \cdot (n\mathbf{u}) &= S^* \\ \frac{\partial n_n}{\partial t} + \boldsymbol{\nabla} \cdot (n_n \mathbf{u}_n) &= -S^* \end{aligned}$$

where S^* is the species conversion rate from neutrals to ions. Due to conservation of mass, the rate of ion generation is equal to the rate of neutral destruction.

Already from the continuity equation, one can observe the weakness of the two-fluid plasma-neutral model. Due to the fact reactions are allowed, the right-hand-side of the continuity equation is no longer equal to zero as it was the case for the two species fully ionized model. While the total number density of the combined species is still conserved, the partition between the two species is dependent on the right-hand-side collision and reaction term. As such, a term that has coupling to every other moments of the distribution function is introduced in the continuity equation. A transport coefficient must be introduced into the continuity equation that depends on the local distribution function.

For the remaining equations, the details of the derivations are skipped, but similar argument based on the global macroscopic conservation laws can be used alongside the moment equation to obtain the results presented. The remaining equations are the followings:

$$\begin{aligned} \frac{\partial}{\partial t}(mn\mathbf{u}) + \boldsymbol{\nabla} \cdot (mn\mathbf{u}\mathbf{u}) + \boldsymbol{\nabla} p - \mathbf{J} \times \mathbf{B} &= -\boldsymbol{\nabla} \cdot \overleftrightarrow{\Pi} + \mathbf{M}^* \\ \frac{\partial}{\partial t}(mn_n\mathbf{u}_n) + \boldsymbol{\nabla} \cdot (mn_n\mathbf{u}_n\mathbf{u}_n) + \boldsymbol{\nabla} p_n &= -\boldsymbol{\nabla} \cdot \overleftrightarrow{\Pi}_n - \mathbf{M}^* \end{aligned}$$

$$\mathbf{E} + \mathbf{u} \times \mathbf{B} = \mathbf{R}^* + \frac{1}{en}\mathbf{J} \times \mathbf{B}$$

$$\frac{\partial \varepsilon}{\partial t} + \boldsymbol{\nabla} \cdot [(\varepsilon + p)\,\mathbf{u}] - \mathbf{J} \cdot \mathbf{E} = -\boldsymbol{\nabla} \cdot \left(\mathbf{q}^* + \mathbf{u} \cdot \overleftrightarrow{\Pi}\right) + W^*$$

$$\frac{\partial \varepsilon_n}{\partial t} + \boldsymbol{\nabla} \cdot [(\varepsilon_n + p_n)\,\mathbf{u}_n] = -\boldsymbol{\nabla} \cdot \left(\mathbf{q}_n + \mathbf{u}_n \cdot \overleftrightarrow{\Pi}_n\right) - W^*$$

$$\frac{\partial p_e}{\partial t} + \frac{5}{3}\boldsymbol{\nabla} \cdot \left[p_e \left(\mathbf{u} - \frac{\mathbf{J}}{en}\right)\right] = -\frac{2}{3}\left[Q^* + (en\mathbf{u} - \mathbf{J}) \cdot \mathbf{R}^*\right]$$

where $\overleftrightarrow{\Pi}_n$ is the viscous stress tensor for the neutral species, $\mathbf{q}_n$ is the heat flow vector for the neutral species, and $\mathbf{M}^*$ and W^* are the momentum transfer rate and energy transfer rate, respectively, from the neutral species to the combined ion and electron center-of-mass plasma species that account for both collision and reaction contributions. Note that the dissipative decay of the magnetic field $\mathbf{R}^*$ and the effective heat generation for the electron fluid Q^* now include effects of the neutral species.

It can be seen that five additional unique transport terms are required to describe the plasma-neutral system: the neutral viscous stress tensor $\overleftrightarrow{\Pi}_n$ and the neutral heat flow vector $\mathbf{q}_n$ that are the transport coefficients associated with the neutral species; the particle transfer rate S^*, the momentum transfer rate $\mathbf{M}^*$, and the energy transfer rate W^* between the two fluids that describe the interaction of the plasma and neutral species.

In essence, one can view the two-fluid model of Meier and Shumlak as a closure relation for the additional transport variables introduced when neutral fluid are considered with three common reactions: ionization, recombination, and charge exchange. Unfortunately, since the closure by Meier and Shumlak assumes locally Maxwellian distribution function for the plasma-neutral interaction involving reactions, their model is only applicable to systems where the deviation of the local distribution function from the Maxwellian is negligible.

Since in the typical FRC modeling, anomalous modification to the transports is necessary to match experimental results, local distribution function is non-Maxwellian. As a result, in order to capture FRC dynamics well, one must come up with a suitable anomalous correction to the transport variables introduced when the neutral species are considered. In order to

obtain such anomalous correction, either more experimental data involving plasma-neutral interaction or a kinetic model that includes the necessary physics for reactions are required to obtain scaling for the anomalous terms.

This conclusion suggests that unless suitable forms of closures that resolve kinetic effects can be determined a priori, kinetic simulations are required to capture behavior of the FRC when neutral effects are considered. In order to capture reactions accurately, all three species (ions, electrons, and neutrals) must be treated kinetically. In particular, electron species cannot be treated as a fluid as commonly done in hybrid simulations of FRCs, as details of the electron distribution function are crucial for obtaining correct ionization and recombination reaction rates.

5.5 Summary of Possible Source of Discrepancy with the Experiment

In this chapter few missing physics in the present implementation of Cygnus were discussed. While neglecting three-dimensional and kinetic effects are likely big sources of solution disagreements, these two effects cannot be tested easily using the framework of the Cygnus code and require complete re-writing of Cygnus or development of a new code. Thus, exploration of these two effects is outside the scope of this project.

On the other hand, molecular and multi-step ionization effects can be tested within the existing framework of Cygnus if certain simplifications are made to the multi-fluid model. For example, the simple ionization model by Sgro can be included trivially in the plasma-neutral model [32]. In order to quantify the potential significance of molecular effects in the FRC formation process, a simplified molecular model was developed and implemented in Cygnus. Effects of the multi-step ionization process are neglected for now in the model to allow independent testing of the molecular effects. Details of the molecular extension of the Meier and Shumlak's plasma-neutral model are discussed in the next chapter.

Chapter 6

FLUID MODEL FOR FRC FORMATION WITH DIATOMIC DEUTERIUM NEUTRAL

6.1 Introduction

In the FRC formation processes for fusion applications, the most commonly used gas species is deuterium. In the pulsed dynamic formation of the FRCs, one often injects molecular deuterium gas into the formation chamber using an array of gas-puffs. The preionization process is initialized after some time to allow the gas to populate the formation chamber. Then, the bias magnetic field is injected into the weakly ionized plasma. The main formation bank is subsequently fired, which causes rapid ionization of any remaining neutral species in the formation chamber while producing an FRC.

As discussed in the previous section, one possible source of the disagreement with the experimental results is the presence of molecular deuterium species. When molecular species are present, the charge exchange process is no longer resonant due to the existence of energy deficits [68], and the charge exchange rate computed by the model of Meier and Shumlak will be too excessive. In the preionization phase, since the ionization fraction is sufficiently weak, the resonant charge exchange frequency dominates over all other scattering or reaction processes. Because of this, if there are significant population of molecular neutrals hindering charge exchange processes, the physics of the preionization process can be significantly altered by allowing other reaction processes to play a more dominant role. In this case, the prediction based on the Meier and Shumlak's model will be incorrect due to the assumption of resonant charge exchange.

Rates of molecular dissociation and ionization govern whether the resonant or non-resonant charge exchange processes occur in the preionization process. Since the injected

deuterium gas is initially a diatomic molecule, if the gas is incompletely dissociated before it is ionized, non-negligible population of the diatomic neutrals can exist during the preionization and formation processes. Thus, to explore this effect, a simple extension to the Meier and Shumlak's model that includes molecular deuterium effects is developed to test for the influence of molecular species on the FRC formation process.

It should be noted that there exists a more general model developed by Zhdanov and Stepanenko for a partially ionized reactive plasma, which account for internal degrees of freedom of species with arbitrary reactions [69]. In their model, the binary collision integral is written in the Wang-Chang and Uhlenbeck form [70], and the chemical collision integral is defined for the bimolecular and trimolecular reactions. The generalized chemical collision integral of Giovangigli and Graille allows inclusion of any arbitrary reactions in the model [71]. Details of the transport due to binary collisions are given in great details by Zhdanov [57]. However, one issue with this model is its complexity. As such, in order to obtain a simple extension to the plasma-neutral model, a derivation using the classical collision model is used here.

6.2 Model Assumptions and Fluid Equations

In order to develop a simple extension to the two-fluid plasma-neutral model of Meier and Shumlak, first, a minimum number of the fluid species that must be included to capture the effects of the diatomic deuterium molecules is considered. Initially, when the deuterium gas is injected into the formation chamber, one can assume that the molecular deuterium is largely in its ground state. While it is possible for the higher order vibrational modes to be populated at the room temperature, because the injected gas is expanded into a low pressure formation chamber, it can be assumed that the adiabatic expansion process sufficiently cools the gas and brings it to a vibrational and rotational ground state [58].

Following Lieberman and Lichtenberg, consider the following time scale ordering for the

electron-molecule collision processes:

$$t_{at} \sim t_c \ll \tau_{vib} \sim \tau_{dis} \ll \tau_{rad} \ll \tau_c$$

where t_{at} is a time scale for the electron motion in the molecule, t_c is the collisional interaction time for the electron with the molecule, τ_{vib} is the vibration time for the molecule, τ_{dis} is the dissociation time for the molecule, τ_{rad} is the transition time for electric dipole radiations, and τ_c is the mean free time between collision for the electron and molecule [58]. Similarly, the heavy particle collision time scale can be ordered as the following:

$$t_{at} \ll t_{cp} \sim \tau_{vib} \ll \tau_{rad} \ll \tau_c$$

where t_{cp} is the interaction time for collision between two heavy particles [58].

With the assumed time scale ordering, the ground state condition for all species can be assumed in the fluid collision time scale. As such the collisional excitation process can be modeled with a simple energy loss mechanism. In essence, any collisional excitation reaction of the form

$$A + B \rightarrow A + B^*$$

is assumed to be immediately followed by a deexcitation reaction

$$B^* \rightarrow B + h\nu$$

such that only ground state species are present. Note that the species with the superscript, $*$, denotes excited states. While this assumption can be poor for molecular species due to the existence of the meta-stable electronic states, vibrational states, and rotation states, it significantly simplifies the modeling of the species in the fluid model.

During the FRC preionization process, electrons are generated to enhance the electron impact ionization process. For a diatomic deuterium molecule in the ground state, following

interaction paths with an electron are possible:

$$\begin{aligned} e + D_2(X^1\Sigma_g^+) &\rightarrow \text{Momentum Transfer (Elastic Scattering)} \\ &\rightarrow \text{Ionization } (D_2^+) \\ &\rightarrow \text{Dissociative Ionization } (D^+ + D) \\ &\rightarrow \text{Dissociation } (D + D) \\ &\rightarrow \text{Excitation } (D_2^*) \end{aligned}$$

Thus, by adding the diatomic deuterium species in the model, following species must be tracked: atomic deuterium neutrals (D), diatomic deuterium neutrals (D_2), atomic deuterium ions (D^+), diatomic deuterium ions (D_2^+), and electrons (e). In addition, the low energy heavy particle collision process between the diatomic deuterium ions and diatomic deuterium neutrals has a potential path for the formation of the stable triatomic deuterium ions (D_3^+). In the typical energy range encountered in the FRC formation process, the formation of the negative ions are largely negligible. Thus, if the diatomic deuterium neutrals are included in the fluid model, following six species must be tracked: e, D, D_2, D^+, D_2^+, and D_3^+.

The reactions that are included in the model is selected based on the strength of their reaction cross-sections in typical FRC formation conditions. The reactions involving excited species states are neglected due to the assumption of the ground state dominance. The following reactions are included in the model:

Electron Impact Ionization:

$$e + D \rightarrow e + D^+ + e \qquad \text{(EL 1)}$$

$$e + D_2 \rightarrow e + D_2^+ + e \qquad \text{(EL 2)}$$

Electron Impact Dissociative Ionization:

$$e + D_2 \rightarrow e + D^+ + D + e \quad \text{(EL 3)}$$

$$e + D_2^+ \rightarrow e + D^+ + D^+ + e \quad \text{(EL 4)}$$

Electron Impact Dissociation:

$$e + D_2 \rightarrow e + D + D \quad \text{(EL 5)}$$

Electron Impact Dissociative Excitation:

$$e + D_2^+ \rightarrow e + D^+ + D \quad \text{(EL 6)}$$

$$e + D_3^+ \rightarrow e + D^+ + D + D \quad \text{(EL 7)}$$

Electron Impact Dissociative Recombination:

$$e + D_2^+ \rightarrow D + D \quad \text{(EL 8)}$$

$$e + D_3^+ \rightarrow D_2 + D \quad \text{(EL 9)}$$

$$e + D_3^+ \rightarrow D + D + D \quad \text{(EL 10)}$$

Electron Impact Radiative Recombination:

$$e + D^+ \rightarrow D + h\nu \quad \text{(EL 11)}$$

Charge Exchange:

$$D^+ + D \rightarrow D + D^+ \quad \text{(HP 1)}$$

$$D^+ + D_2 \rightarrow D + D_2^+ \quad \text{(HP 2)}$$

$$D_2^+ + D \rightarrow D_2 + D^+ \quad \text{(HP 3)}$$

$$D_2^+ + D_2 \rightarrow D_2 + D_2^+ \quad \text{(HP 4)}$$

Triatomic Deuterium Ion Production

$$D_2^+ + D_2 \rightarrow D_3^+ + D \qquad \text{(HP 5)}$$

In addition to the above reactions, the elastic scattering collisions between all species are also included.

For simplicity, cross sections for hydrogens are used to judge the dominant reaction processes, since significantly more theoretical and experimental data exist in literature for hydrogens compared with deuteriums. Note that the elastic cross section of deuterium and hydrogen is equivalent. The cross sections with greatest disagreement between the deuterium and hydrogen are those associated with the excited states. This is due to the difference in the vibrational and rotational states of the deuterium and hydrogen molecule. The isotope effects are especially important in the low energy regime where the internal state of the molecule is more important [72]. Since the ground state is assumed for all species and the species temperatures during the FRC formation process are generally above 1 eV, errors due to using the hydrogen reaction cross sections for deuterium should be small.

If the derivation of the multi-fluid model used by Meier and Shumlak is followed to generate fluid equations for all six species, the model will become far too complex and intractable for practical problems involving FRCs. As such, in order to simplify the model and reduce the required number of the fluid equations, several simplifying assumptions are made to reduce the model to a form similar to the Meier and Shumlak's two-fluid model.

First, the temperatures of all neutral species (D and D_2) are assumed to be equal to each other such that only a single neutral temperature T_n has to be tracked. Similarly, the temperatures of all ions (D^+, D_2^+, and D_3^+) are assumed to be equal to each other such that only a single ion temperature T_i has to be tracked. The use of the ion and neutral temperatures in the model implicitly assumes that the thermal equilibration time for neutrals and that for ions are sufficiently short compared with the time scale of the problem. Single temperature model for heavy particles is a common assumption made in a typical multi-component plasma-neutral model (e.g. Zhdanov [57]), so this assumption is reasonable. The

distinction between the ion and neutral temperatures is made here to retain the structure of the Meier-Shumlak model and also to account for the difference in the thermal equilibration time scale between the Coulomb collisions for the ions and the hard sphere collisions for the neutrals.

Second, the diffusion velocities of each neutral species with respect to the center of mass neutral fluid velocity and the diffusion velocities of each ion species with respect to the center of mass ion fluid velocity are assumed to be negligible and equal to zero. In essence, all neutrals have a fluid velocity equal to the neutral center of the mass velocity, and all ions have a fluid velocity equal to the ion center of the mass velocity. Thus, neutrals and ions behave as a single independent fluid when in motion. A relative motion is only allowed between the neutral and ion fluids. This simplification assumes that the momentum transfer collision process amongst neutral species and amongst ion species dominates, leading to a bulk fluid motion. It is assumed that the species are sufficiently collisional such that the error introduced by this assumption is not the dominant error in the system.

Finally, the typical MHD assumptions of negligible electron inertia, negligible displacement current, quasi-neutrality, and Maxwellian distribution function for all species are assumed. With these assumptions, one obtains a quasi-two-fluid model of the six species mixture given with a following set of equations:

Continuity:

$$\frac{\partial n}{\partial t} + \boldsymbol{\nabla} \cdot (n\mathbf{u}) = \frac{\delta n_{D^+}}{\delta t} + \frac{\delta n_{D_2^+}}{\delta t} + \frac{\delta n_{D_3^+}}{\delta t} \tag{6.1}$$

$$\frac{\partial n_n}{\partial t} + \boldsymbol{\nabla} \cdot (n_n \mathbf{u}_n) = \frac{\delta n_D}{\delta t} + \frac{\delta n_{D_2}}{\delta t} \tag{6.2}$$

Species Partition:

$$\frac{\partial f_{di}}{\partial t} + \mathbf{u} \cdot \boldsymbol{\nabla} f_{di} = \frac{1}{n}\left[(1 - f_{di})\frac{\delta n_{D_2^+}}{\delta t} - f_{di}\left(\frac{\delta n_{D^+}}{\delta t} + \frac{\delta n_{D_3^+}}{\delta t}\right)\right] \tag{6.3}$$

$$\frac{\partial f_{ti}}{\partial t} + \mathbf{u} \cdot \boldsymbol{\nabla} f_{ti} = \frac{1}{n}\left[(1 - f_{ti})\frac{\delta n_{D_3^+}}{\delta t} - f_{ti}\left(\frac{\delta n_{D^+}}{\delta t} + \frac{\delta n_{D_2^+}}{\delta t}\right)\right] \tag{6.4}$$

$$\frac{\partial f_{dn}}{\partial t} + \mathbf{u}_n \cdot \boldsymbol{\nabla} f_{dn} = \frac{1}{n_n}\left[(1 - f_{dn})\,\frac{\delta n_{D_2}}{\delta t} - f_{dn}\frac{\delta n_D}{\delta t}\right] \tag{6.5}$$

Momentum:

$$\frac{\partial}{\partial t}\left(m\tilde{n}\mathbf{u}\right) + \boldsymbol{\nabla}\cdot\left(m\tilde{n}\mathbf{u}\mathbf{u} + p\overleftrightarrow{\mathrm{I}} + \overleftrightarrow{\Pi}\right) - \mathbf{J}\times\mathbf{B} = \frac{\delta\mathbf{M}}{\delta t} \tag{6.6}$$

$$\frac{\partial}{\partial t}\left(m\tilde{n}_n\mathbf{u}_n\right) + \boldsymbol{\nabla}\cdot\left(m\tilde{n}_n\mathbf{u}_n\mathbf{u}_n + p_n\overleftrightarrow{\mathrm{I}} + \overleftrightarrow{\Pi}_n\right) = \frac{\delta\mathbf{M}_n}{\delta t} \tag{6.7}$$

Generalized Ohm:

$$\mathbf{E} + \mathbf{u}\times\mathbf{B} - \frac{1}{ne}\left(\mathbf{J}\times\mathbf{B} - \boldsymbol{\nabla}p_e - \boldsymbol{\nabla}\cdot\overleftrightarrow{\Pi}_e\right) = \frac{1}{ne}\frac{\delta\mathbf{M}_e}{\delta t} \tag{6.8}$$

Energy:

$$\frac{3}{2}\left[\frac{\partial p}{\partial t} + \boldsymbol{\nabla}\cdot(p\mathbf{u})\right] + p\boldsymbol{\nabla}\cdot\mathbf{u} + \boldsymbol{\nabla}\cdot\mathbf{q} + \overleftrightarrow{\Pi} : \boldsymbol{\nabla}\mathbf{u} = \frac{\delta E}{\delta t} - \frac{\mathbf{J}}{ne}\cdot\left[\boldsymbol{\nabla}\cdot\left(p_e\overleftrightarrow{\mathrm{I}} + \overleftrightarrow{\Pi}_e\right)\right] \tag{6.9}$$

$$\frac{3}{2}\left[\frac{\partial p_n}{\partial t} + \boldsymbol{\nabla}\cdot(p_n\mathbf{u}_n)\right] + p_n\boldsymbol{\nabla}\cdot\mathbf{u}_n + \boldsymbol{\nabla}\cdot\mathbf{q}_n + \overleftrightarrow{\Pi}_n : \boldsymbol{\nabla}\mathbf{u}_n = \frac{\delta E_n}{\delta t} \tag{6.10}$$

$$\frac{3}{2}\left[\frac{\partial p_e}{\partial t} + \boldsymbol{\nabla}\cdot(p_e\mathbf{u}_e)\right] + p_e\boldsymbol{\nabla}\cdot\mathbf{u}_e + \boldsymbol{\nabla}\cdot\mathbf{q}_e + \overleftrightarrow{\Pi}_e : \boldsymbol{\nabla}\mathbf{u}_e = \frac{\delta E_e}{\delta t} \tag{6.11}$$

where $n = n_{D^+} + n_{D_2^+} + n_{D_3^+}$ is the plasma number density, $\tilde{n} = (1 + f_{di} + 2f_{ti})n$ is the modified plasma number density, $n_n = n_D + n_{D_2}$ is the neutral number density, $\tilde{n}_n = (1 + f_{dn})n_n$ is the modified neutral number density, $f_{di} = n_{D_2^+}/n$ is the fraction of the diatomic ion number density with respect to the plasma number density, $f_{ti} = n_{D_3^+}/n$ is the fraction of the triatomic ion number density with respect to the plasma number density, $f_{dn} = n_{D_2}/n_n$ is the fraction of the diatomic neutral number density with respect to the neutral number density, $p = nk(T_i + T_e)$ is the plasma pressure, $p_e = nkT_e$ is the electron temperature, $p_n = n_n kT_n$ is the neutral pressure, $\overleftrightarrow{\Pi} = \overleftrightarrow{\Pi}_{D^+} + \overleftrightarrow{\Pi}_{D_2^+} + \overleftrightarrow{\Pi}_{D_3^+} + \overleftrightarrow{\Pi}_e$ is the plasma viscous stress tensor, $\overleftrightarrow{\Pi}_n = \overleftrightarrow{\Pi}_D + \overleftrightarrow{\Pi}_{D_2}$ is the neutral viscous stress tensor, $\mathbf{q} = \mathbf{q}_{D^+} + \mathbf{q}_{D_2^+} + \mathbf{q}_{D_3^+} + \mathbf{q}_e - \frac{\mathbf{J}}{ne}(\frac{5}{2}p_e\overleftrightarrow{\mathrm{I}} + \overleftrightarrow{\Pi}_e)$ is the plasma heat flow vector, $\mathbf{q}_n = \mathbf{q}_D + \mathbf{q}_{D_2}$ is the neutral heat flow vector, and m is the

mass of the deuterium atom. The collision and the reaction related terms are defined as

$$\frac{\delta n_\alpha}{\delta t} \equiv \int \frac{\delta f_\alpha}{\delta t}\, \mathrm{d}^3 v$$

$$\frac{\delta \mathbf{M}_\alpha}{\delta t} \equiv m_\alpha \int \mathbf{v} \frac{\delta f_\alpha}{\delta t}\, \mathrm{d}^3 v$$

$$\frac{\delta E_\alpha}{\delta t} \equiv \frac{1}{2} m_\alpha \int |\mathbf{v} - \mathbf{u}_\alpha|^2 \frac{\delta f_\alpha}{\delta t}\, \mathrm{d}^3 v$$

where $\frac{\delta f_\alpha}{\delta t}$ is the collisional and reaction right-hand-side contribution in the Boltzmann equation. Note that in the above equation, following definition are made for the sum of the collision reaction terms

$$\frac{\delta \mathbf{M}}{\delta t} = \frac{\delta \mathbf{M}_{D^+}}{\delta t} + \frac{\delta \mathbf{M}_{D_2^+}}{\delta t} + \frac{\delta \mathbf{M}_{D_3^+}}{\delta t} + \frac{\delta \mathbf{M}_e}{\delta t}$$

$$\frac{\delta \mathbf{M}_n}{\delta t} = \frac{\delta \mathbf{M}_D}{\delta t} + \frac{\delta \mathbf{M}_{D_2}}{\delta t}$$

$$\frac{\delta E}{\delta t} = \frac{\delta E_{D^+}}{\delta t} + \frac{\delta E_{D_2^+}}{\delta t} + \frac{\delta E_{D_3^+}}{\delta t} + \frac{\delta E_e}{\delta t}$$

$$\frac{\delta E_n}{\delta t} = \frac{\delta E_D}{\delta t} + \frac{\delta E_{D_2}}{\delta t}$$

The fluid variables are defined as

$$n_\alpha = \int f_\alpha\, \mathrm{d}^3 v$$

$$\mathbf{u}_\alpha = \frac{1}{n_\alpha} \int \mathbf{v} f_\alpha\, \mathrm{d}^3 v$$

$$p_\alpha = \frac{1}{3} m_\alpha \int |\mathbf{v} - \mathbf{u}_\alpha|^2 f_\alpha\, \mathrm{d}^3 v$$

$$\overleftrightarrow{\Pi}_\alpha = m_\alpha \int (\mathbf{v} - \mathbf{u}_\alpha)(\mathbf{v} - \mathbf{u}_\alpha) f_\alpha\, \mathrm{d}^3 v - p_\alpha \overleftrightarrow{\mathrm{I}}$$

$$\mathbf{q}_\alpha = \frac{1}{2} m_\alpha \int |\mathbf{v} - \mathbf{u}_\alpha|^2 (\mathbf{v} - \mathbf{u}_\alpha) f_\alpha\, \mathrm{d}^3 v$$

for $\alpha = D, D_2, D^+, D_2^+, D_3^+,$ and e.

Because of the simplifying assumptions, there are only three additional equations introduced to the original set of the fluid equations from the Meier and Shumlak's model. These three equations correspond to the partition of the species in the neutral and the ion fluid. The above set of equation has been written in a form where the left-hand-side closely mimics the original form of the plasma-neutral model for single atomic species neutrals and ions. This allows the additional species contributions to be treated as a right-hand-side source term in the preexisting implementation of the plasma-neutral model in Cygnus.

With the above form of the fluid equations defined, what is required next is the specific form of the right-hand-side collision and reaction terms $\frac{\delta n_\alpha}{\delta t}$, $\frac{\delta \mathbf{M}_\alpha}{\delta t}$, and $\frac{\delta E_\alpha}{\delta t}$. In addition, closures for transport variables $\overleftrightarrow{\Pi}$, $\overleftrightarrow{\Pi}_n$, $\overleftrightarrow{\Pi}_e$, $\mathbf{q}$, $\mathbf{q}_n$, and $\mathbf{q}_e$ are also required.

Note that the collision contribution to the energy equation is written in a non-conservative form using the moment with respect to the random velocity. To obtain the conservative form of the collision contribution to the energy equation defined to be

$$\frac{\delta \tilde{E}_\alpha}{\delta t} \equiv \frac{1}{2} m_\alpha \int v^2 \frac{\delta f_\alpha}{\delta t} \, \mathrm{d}^3 v$$

it can be related to the non-conservative form as

$$\frac{\delta \tilde{E}_\alpha}{\delta t} = \frac{\delta E_\alpha}{\delta t} + \mathbf{u}_\alpha \cdot \frac{\delta \mathbf{M}_\alpha}{\delta t} - \frac{1}{2} m_\alpha u_\alpha^2 \frac{\delta n_\alpha}{\delta t}$$

The conservative form of the energy equation can then be written as the followings:

$$\frac{\partial \tilde{\varepsilon}}{\partial t} + \boldsymbol{\nabla} \cdot \left[\tilde{\varepsilon} \mathbf{u} + \mathbf{u} \cdot \left(p \overleftrightarrow{\mathrm{I}} + \overleftrightarrow{\Pi} \right) + \mathbf{q} \right] - \mathbf{J} \cdot \mathbf{E} = \frac{\delta \tilde{E}}{\delta t} \tag{6.12}$$

$$\frac{\partial \tilde{\varepsilon}_n}{\partial t} + \boldsymbol{\nabla} \cdot \left[\tilde{\varepsilon}_n \mathbf{u}_n + \mathbf{u}_n \cdot \left(p_n \overleftrightarrow{\mathrm{I}} + \overleftrightarrow{\Pi}_n \right) + \mathbf{q}_n \right] = \frac{\delta \tilde{E}_n}{\delta t} \tag{6.13}$$

where $\tilde{\varepsilon} \approx \frac{1}{2} m \tilde{n} u^2 + \frac{3}{2} p$ is the plasma energy density and $\tilde{\varepsilon}_n = \frac{1}{2} m \tilde{n}_n u_n^2 + \frac{3}{2} p_n$ is the neutral

energy density. The collision contributions are given as the followings:

$$\frac{\delta\tilde{E}}{\delta t} \approx \frac{\delta E}{\delta t} + \mathbf{u}\cdot\frac{\delta\mathbf{M}}{\delta t} - \frac{1}{2}mu^2\left(\frac{\delta n_{D^+}}{\delta t} + 2\frac{\delta n_{D_2^+}}{\delta t} + 3\frac{\delta n_{D_3^+}}{\delta t}\right)$$

$$\frac{\delta\tilde{E}_n}{\delta t} \approx \frac{\delta E_n}{\delta t} + \mathbf{u}_n\cdot\frac{\delta\mathbf{M}_n}{\delta t} - \frac{1}{2}mu_n^2\left(\frac{\delta n_D}{\delta t} + 2\frac{\delta n_{D_2}}{\delta t}\right)$$

In the subsequent sections, the form of the right-hand-side collision contributions to the fluid equations is discussed.

6.3 Elastic Collision Integral

In this section, collision contributions to the fluid equations due to the elastic scattering are considered. Contributions due to reactions are discussed in the next section.

For the elastic scattering collisions, assume that the collision is a hard sphere collision when it is between neutral species or when it is between the neutral species and the ion species; assume that the collision is a Coulomb collision when it is between the charged species. Assuming Maxwellian distribution for all species, the collision contributions to the fluid equations can be expressed as the followings as shown by Schunk and Nagy:

$$\frac{\delta n_\alpha}{\delta t} = 0$$

$$\frac{\delta\mathbf{M}_\alpha}{\delta t} = \sum_\beta n_\alpha m_\alpha \nu_{\alpha\beta}\left(\mathbf{u}_\beta - \mathbf{u}_\alpha\right)\Phi_{\alpha\beta}$$

$$\frac{\delta E_\alpha}{\delta t} = \sum_\beta \frac{n_\alpha m_\alpha \nu_{\alpha\beta}}{m_\alpha + m_\beta}\left[3k\left(T_\beta - T_\alpha\right)\Psi_{\alpha\beta} + m_\beta\left|\mathbf{u}_\alpha - \mathbf{u}_\beta\right|^2\Phi_{\alpha\beta}\right]$$

where $\nu_{\alpha\beta} = n_\beta m_\beta K_{\alpha\beta}/(m_\alpha + m_\beta)$ is the momentum transfer collision frequency, $K_{\alpha\beta}$ is the effective reaction rate, and $\Phi_{\alpha\beta}$ and $\Psi_{\alpha\beta}$ are the velocity correction factor that is different for the type of the collision processes [50]. For the Coulomb collision process,

$$\Phi_{\alpha\beta} = \frac{3\sqrt{\pi}}{4}\lambda_{\alpha\beta}^{-3/2}\,\mathrm{erf}\left(\lambda_{\alpha\beta}^{1/2}\right) - \frac{3}{2}\lambda_{\alpha\beta}^{-1}\,e^{-\lambda_{\alpha\beta}}$$

$$\Psi_{\alpha\beta} = e^{-\lambda_{\alpha\beta}}$$

$$K_{\alpha\beta} = \frac{16\sqrt{\pi}}{3}\left(2k\overline{T}_{\alpha\beta}\right)^{-3/2}\left(\frac{e_\alpha e_\beta}{4\pi\varepsilon_0\mu_{\alpha\beta}}\right)^2 \ln\Lambda_{\alpha\beta}$$

and for the hard sphere collision process,

$$\Phi_{\alpha\beta} = \frac{3\sqrt{\pi}}{32}\lambda_{\alpha\beta}^{-3/2}\left(4\lambda_{\alpha\beta}^2 + 4\lambda_{\alpha\beta} - 1\right)\mathrm{erf}\left(\lambda_{\alpha\beta}^{1/2}\right) + \frac{3}{16}\lambda_{\alpha\beta}^{-1}\left(2\lambda_{\alpha\beta}+1\right)e^{-\lambda_{\alpha\beta}}$$

$$\Psi_{\alpha\beta} = \frac{\sqrt{\pi}}{4}\lambda_{\alpha\beta}^{-1/2}\left(2\lambda_{\alpha\beta}+1\right)\mathrm{erf}\left(\lambda_{\alpha\beta}^{1/2}\right) + \frac{1}{2}e^{-\lambda_{\alpha\beta}}$$

$$K_{\alpha\beta} = \frac{8}{3\sqrt{\pi}}(2k\overline{T}_{\alpha\beta})^{1/2}(\pi r_{\alpha\beta}^2)$$

where $\lambda_{\alpha\beta} = u_{\alpha\beta}^2/\left(2k\overline{T}_{\alpha\beta}\right)$ is the ratio of the reduced relative kinetic energy divided by the reduced thermal energy, $\mathbf{u}_{\alpha\beta} = \mathbf{u}_\alpha - \mathbf{u}_\beta$ is the relative velocity, $\overline{T}_{\alpha\beta} = T_\alpha/m_\alpha + T_\beta/m_\beta$ is the reduced temperature divided by the reduced mass, $\mu_{\alpha\beta} = m_\alpha m_\beta/(m_\alpha + m_\beta)$ is the reduced mass, and $r_{\alpha\beta}$ is the sum of the radii of the colliding particles [50].

The elastic scattering collision contribution to the species number density is all equal to zero. For the collisions involving electrons, due to the small electron inertia, $\lambda_{\alpha\beta}$ is small, and $\Psi_{\alpha\beta} \approx \Psi_{\alpha\beta} \approx 1$. Note that because of the assumption of a single velocity and temperature for the ions, the Coulomb collisions between the ions have no influence in the fluid equation (they are assumed to be large such that temperature and velocity difference for different ion species are kept low). Likewise, the hard sphere collisions between two neutral species have no influence in the fluid equations for the same reason. Note that for Coulomb collisions involving electrons, the Coulomb logarithm is largely independent of the species masses for the typical FRC conditions and the species mass dependence can be neglected.

Applying all of the assumptions made thus far, after some simplifications, the momentum

contributions are given to be the followings:

$$\frac{\delta \mathbf{M}}{\delta t} = -mnn_n\mathbf{u}_{in}\Bigg\{(1-f_{di}-f_{ti})\left[\frac{1}{2}(1-f_{dn})K_{DD^+}\Phi_{DD^+}+\frac{2}{3}f_{dn}K_{D_2D^+}\Phi_{D_2D^+}\right] + f_{di}\left[\frac{2}{3}(1-f_{dn})K_{DD_2^+}\Phi_{DD_2^+}+f_{dn}K_{D_2D_2^+}\Phi_{D_2D_2^+}\right] + f_{ti}\left[\frac{3}{4}(1-f_{dn})K_{DD_3^+}\Phi_{DD_3^+}+\frac{6}{5}f_{dn}K_{D_2D_3^+}\Phi_{D_2D_3^+}\right]\Bigg\} \quad (6.14)$$

$$\frac{\delta \mathbf{M}_n}{\delta t} = -\frac{\delta \mathbf{M}}{\delta t} \quad (6.15)$$

$$\frac{1}{ne}\frac{\delta \mathbf{M}_e}{\delta t} = \frac{m_e}{e^2}\left\{K_{sp}\mathbf{J}+\frac{n_n}{n}\left[(1-f_{dn})K_{eD}+f_{dn}K_{eD_2}\right](\mathbf{J}-ne\mathbf{u}_{in})\right\} \quad (6.16)$$

where $\mathbf{u}_{in} = \mathbf{u} - \mathbf{u}_n$ and

$$K_{sp} = \frac{4\sqrt{2\pi}}{3}\frac{e^{5/2}\,\ln(\Lambda)}{(4\pi\varepsilon_0)^2\,m_e^{1/2}}\left(\frac{kT_e}{e}\right)^{-3/2}$$

is the Coulomb collision reaction rate. The energy contributions are given to be the followings:

$$\frac{\delta E}{\delta t} = \frac{3}{2}nn_nk(T_n-T_i)\Bigg\{(1-f_{di}-f_{ti})\left[\frac{1}{2}(1-f_{dn})K_{DD^+}\Psi_{DD^+}+\frac{4}{9}f_{dn}K_{D_2D^+}\Psi_{D_2D^+}\right] + f_{di}\left[\frac{4}{9}(1-f_{dn})K_{DD_2^+}\Psi_{DD_2^+}+\frac{1}{2}f_{dn}K_{D_2D_2^+}\Psi_{D_2D_2^+}\right] + f_{ti}\left[\frac{3}{8}(1-f_{dn})K_{DD_3^+}\Psi_{DD_3^+}+\frac{12}{25}f_{dn}K_{D_2D_3^+}\Psi_{D_2D_3^+}\right]\Bigg\} + \frac{1}{2}mnn_nu_{in}^2\Bigg\{(1-f_{di}-f_{ti})\left[\frac{1}{2}(1-f_{dn})K_{DD^+}\Phi_{DD^+}+\frac{8}{9}f_{dn}K_{D_2D^+}\Phi_{D_2D^+}\right] + f_{di}\left[\frac{4}{9}(1-f_{dn})K_{DD_2^+}\Phi_{DD_2^+}+f_{dn}K_{D_2D_2^+}\Phi_{D_2D_2^+}\right] + f_{ti}\left[\frac{3}{8}(1-f_{dn})K_{DD_3^+}\Phi_{DD_3^+}+\frac{24}{25}f_{dn}K_{D_2D_3^+}\Phi_{D_2D_3^+}\right]\Bigg\} \quad (6.17)$$

$$\frac{\delta E_n}{\delta t} = \frac{3}{2} n n_n k (T_i - T_n) \Bigg\{ (1 - f_{di} - f_{ti}) \left[\frac{1}{2}(1 - f_{dn}) K_{DD^+} \Psi_{DD^+} + \frac{4}{9} f_{dn} K_{D_2D^+} \Psi_{D_2D^+} \right] + f_{di} \left[\frac{4}{9}(1 - f_{dn}) K_{DD_2^+} \Psi_{DD_2^+} + \frac{1}{2} f_{dn} K_{D_2D_2^+} \Psi_{D_2D_2^+} \right] + f_{ti} \left[\frac{3}{8}(1 - f_{dn}) K_{DD_3^+} \Psi_{DD_3^+} + \frac{12}{25} f_{dn} K_{D_2D_3^+} \Psi_{D_2D_3^+} \right] \Bigg\} + \frac{1}{2} m n n_n u_{in}^2 \Bigg\{ (1 - f_{di} - f_{ti}) \left[\frac{1}{2}(1 - f_{dn}) K_{DD^+} \Phi_{DD^+} + \frac{4}{9} f_{dn} K_{D_2D^+} \Phi_{D_2D^+} \right] + f_{di} \left[\frac{8}{9}(1 - f_{dn}) K_{DD_2^+} \Phi_{DD_2^+} + f_{dn} K_{D_2D_2^+} \Phi_{D_2D_2^+} \right] + f_{ti} \left[\frac{9}{8}(1 - f_{dn}) K_{DD_3^+} \Phi_{DD_3^+} + \frac{36}{25} f_{dn} K_{D_2D_3^+} \Phi_{D_2D_3^+} \right] \Bigg\} \quad (6.18)$$

$$\frac{\delta E_e}{\delta t} = 3 n^2 \frac{m_e}{m} k \left(T_i - T_e \right) \left(3 - \frac{3}{2} f_{di} - 2 f_{ti} \right) K_{sp} + 3 n n_n \frac{m_e}{m} k \left(T_n - T_e \right) \left[\left(1 - f_{dn} \right) K_{eD} + \frac{1}{2} f_{dn} K_{eD_2} \right] + \frac{m_e}{e^2} K_{sp} J^2 + n n_n m_e \left| \mathbf{u}_{in} - \mathbf{J}/ne \right|^2 \left[\left(1 - f_{dn} \right) K_{eD} + f_{dn} K_{eD_2} \right] \quad (6.19)$$

In addition, the energy conservative form of the energy transfer term is given as the following:

$$\begin{aligned}\frac{\delta\tilde{E}}{\delta t} = \frac{3}{2}nn_nk\left(T_n - T_i\right)\Bigg\{&\left(1-f_{di}-f_{ti}\right)\left[\frac{1}{2}\left(1-f_{dn}\right)K_{DD^+}\Psi_{DD^+} + \frac{4}{9}f_{dn}K_{D_2D^+}\Psi_{D_2D^+}\right]\\ &+ f_{di}\left[\frac{4}{9}\left(1-f_{dn}\right)K_{DD_2^+}\Psi_{DD_2^+} + \frac{1}{2}f_{dn}K_{D_2D_2^+}\Psi_{D_2D_2^+}\right]\\ &+ f_{ti}\left[\frac{3}{8}\left(1-f_{dn}\right)K_{DD_3^+}\Psi_{DD_3^+} + \frac{12}{25}f_{dn}K_{D_2D_3^+}\Psi_{D_2D_3^+}\right]\Bigg\}\\ + \frac{1}{2}mnn_n\Bigg\{&\left(1-f_{di}-f_{ti}\right)\left[\frac{1}{4}\left(1-f_{dn}\right)\left(u_n^2-u^2\right)K_{DD^+}\Phi_{DD^+}\right.\\ &\left.+\frac{2}{9}f_{dn}\left(2u_n^2-u^2-\mathbf{u}\cdot\mathbf{u}_n\right)K_{D_2D^+}\Phi_{D_2D^+}\right]\\ &+ f_{di}\left[\frac{2}{9}\left(1-f_{dn}\right)\left(u_n^2+\mathbf{u}\cdot\mathbf{u}_n-2u^2\right)K_{DD_2^+}\Phi_{DD_2^+}\right.\\ &\left.+\frac{1}{2}f_{dn}\left(u_n^2-u^2\right)K_{D_2D_2^+}\Phi_{D_2D_2^+}\right]\\ &+ f_{ti}\left[\frac{3}{16}\left(1-f_{dn}\right)\left(u_n^2+2\mathbf{u}\cdot\mathbf{u}_n-3u^2\right)K_{DD_3^+}\Phi_{DD_3^+}\right.\\ &\left.+\frac{6}{25}f_{dn}\left(2u_n^2+\mathbf{u}\cdot\mathbf{u}_n-3u^2\right)K_{D_2D_3^+}\Phi_{D_2D_3^+}\right]\Bigg\}\end{aligned} \tag{6.20}$$

$$\frac{\delta\tilde{E}_n}{\delta t} = -\frac{\delta\tilde{E}}{\delta t} \tag{6.21}$$

6.4 Derivation of the Reaction Collision Integral

In this section, collision contributions to the fluid equations due to the reactions are considered. For reaction processes, a general form of the reaction can be given by

$$A + B \rightarrow C + \cdots + \Delta E$$

where in the above, ΔE represents energy released by the reaction (positive for exothermic reactions and negative for endothermic reactions). For the reaction given above, in order to generalize the form of the collision operator used by Meier and Shumlak [11], consider a

general collision operator of the form

$$C_{\delta}^{\alpha\beta} = f_{\alpha}(\mathbf{v}) \int g\sigma(g) f_{\beta}(\mathbf{v}') \, \mathrm{d}^3 v' \tag{6.22}$$

which represents the collision operator for species δ due to a bimolecular reaction involving species α and β with species δ as the product. In the above collision operator, $\mathbf{g} = \mathbf{v} - \mathbf{v}'$ is the relative collisional velocity of the two species, $f_{\alpha}(\mathbf{v})$ and $f_{\beta}(\mathbf{v}')$ are assumed to be a Maxwellian distribution of form

$$f_i(\mathbf{v}) = n_i \left(\frac{m_i}{2\pi k T_i} \right)^{3/2} \exp\left(-\frac{m_i c_i^2}{2kT_i} \right) \tag{6.23}$$

for $i = \alpha, \beta$, $\mathbf{c}_i = \mathbf{v} - \mathbf{u}_i$ is the random velocity of species i, and $\mathbf{u}_i$ is the bulk fluid velocity of species i.

With the general collision operator defined in Eq. 6.22, the collision operator for the product C from a bimolecular reaction with reactants A and B can be expressed as

$$C_C = \frac{m_A C_C^{AB} + m_B C_C^{BA}}{m_A + m_B} \tag{6.24a}$$

and that for the reactant A and B can be expressed as

$$C_A = -C_A^{AB} \tag{6.24b}$$

$$C_B = -C_B^{BA} \tag{6.24c}$$

Note that the above form of the collision integral ensures the conservation of mass, momentum, and energy after the reaction process.

In a fluid model for species A, B, and C, one typically needs moments of the collision operator with respect to its species random velocity. Consider the general collision integral that was given before. The resulting collision integral given for the m-th order moment can

be expressed as

$$R^{\alpha\beta,\,m}_{\delta,\,r_1\cdots r_m} = \int [\mathbf{c}^m_\delta]_{r_1\cdots r_m} C^{\alpha\beta}_\delta \,\mathrm{d}^3 v \tag{6.25}$$

where $[\mathbf{c}^m_\delta]_{r_1\cdots r_m}$ is a tensor of the order m produced by a dyadic product of m number of $\mathbf{c}_\delta$, and $R^{\alpha\beta,\,m}_{\delta,\,r_1\cdots r_m}$ is a tensor collision integral of order m. Note that $\mathbf{c}_\delta$ can be expressed as $\mathbf{c}_\delta = \mathbf{c}_\alpha + \mathbf{u}_{\alpha\delta}$, where $\mathbf{u}_{\alpha\delta} = \mathbf{u}_\alpha - \mathbf{u}_\delta$. With this substitution, the collision integral can be expressed as

$$R^{\alpha\beta,\,m}_{\delta,\,r_1\cdots r_m} = \iint [(\mathbf{c}_\alpha + \mathbf{u}_{\alpha\delta})^m]_{r_1\cdots r_m} f_\alpha(c_\alpha) f_\beta(c_\beta) g\sigma(g) \,\mathrm{d}^3 c_\alpha \,\mathrm{d}^3 c_\beta \tag{6.26}$$

To make progress, consider the conversion of the six-dimensional space defined by $\mathbf{c}_\alpha$ and $\mathbf{c}_\beta$ to a new coordinate space defined by $\mathbf{c}_*$ and $\mathbf{g}_*$ which is defined to be

$$\mathbf{c}_* = \mathbf{v}_c - \mathbf{u}_c - \beta \mathbf{u}_{\alpha\beta} + \beta \mathbf{g}$$

$$\mathbf{g}_* = -\mathbf{g} + \mathbf{u}_{\alpha\beta}$$

where

$$\mathbf{v}_c = \frac{m_\alpha \mathbf{v}_\alpha + m_\beta \mathbf{v}_\beta}{m_\alpha + m_\beta}$$

$$\mathbf{u}_c = \frac{m_\alpha \mathbf{u}_\alpha + m_\beta \mathbf{u}_\beta}{m_\alpha + m_\beta}$$

$$\beta = \frac{\mu_{\alpha\beta}}{m_\alpha + m_\beta} \frac{T_\beta - T_\alpha}{T_{\alpha\beta}}$$

$$\mu_{\alpha\beta} = \frac{m_\alpha m_\beta}{m_\alpha + m_\beta}$$

$$T_{\alpha\beta} = \frac{m_\alpha T_\beta + m_\beta T_\alpha}{m_\alpha + m_\beta}$$

From this coordinate transformation, one can obtain

$$\mathbf{c}_\alpha = \mathbf{c}_* - \psi_{\alpha\beta} \mathbf{g}_*$$

$$\mathbf{c}_\beta = \mathbf{c}_* + (1 - \psi_{\alpha\beta})\mathbf{g}_*$$

where

$$\psi_{\alpha\beta} = \frac{m_\beta T_\alpha}{m_\beta T_\alpha + m_\alpha T_\beta}$$

and the product of the two Maxwellian distribution is simplified to the following:

$$f_\alpha(c_\alpha) f_\beta(c_\beta) = n_\alpha n_\beta \left(\frac{\gamma_{\alpha\beta}}{2\pi}\right)^{3/2} \left(\frac{\gamma_\alpha + \gamma_\beta}{2\pi}\right)^{3/2} \exp\left[-\frac{1}{2}(\gamma_\alpha + \gamma_\beta)c_*^2 - \frac{1}{2}\gamma_{\alpha\beta} g_*^2\right] \tag{6.27}$$

where $\gamma_i = m_i/kT_i$ and $\gamma_{\alpha\beta} = \gamma_\alpha\gamma_\beta/(\gamma_\alpha + \gamma_\beta)$. Note that $\psi_{\alpha\beta} = \gamma_{\alpha\beta}/\gamma_\alpha$. The details of the process of conversion to the six-dimensional space defined by $\mathbf{c}_*$ and $\mathbf{g}_*$ can be found in standard textbooks covering transport derivations such as Schunk and Nagy [50] and Zhdanov [57].

After the coordinate transformation, the collision integral in Eq. 6.26 becomes

$$R^{\alpha\beta,\,m}_{\delta,\,r_1\cdots r_m} = n_\alpha n_\beta \left(\frac{\gamma_{\alpha\beta}}{2\pi}\right)^{3/2} \left(\frac{\gamma_\alpha + \gamma_\beta}{2\pi}\right)^{3/2} \iint \left[(\mathbf{c}_* + \psi_{\alpha\beta}\mathbf{g} + \mathbf{u}_\Delta)^m\right]_{r_1\cdots r_m} \times g\sigma(g) \exp\left[-\frac{1}{2}\left(\gamma_\alpha + \gamma_\beta\right) c_*^2\right] \exp\left[-\frac{1}{2}\gamma_{\alpha\beta}\left|\mathbf{g} - \mathbf{u}_{\alpha\beta}\right|^2\right] \mathrm{d}^3 c_* \, \mathrm{d}^3 g \tag{6.28}$$

where $\mathbf{u}_\Delta = \mathbf{u}_{\alpha\delta} - \psi_{\alpha\beta}\mathbf{u}_{\alpha\beta}$. To make additional progress and to simplify the tensor product, define

$$\left[(\mathbf{c}_\alpha + \psi_{\alpha\beta}\mathbf{g} + \mathbf{u}_\Delta)^m\right]_{r_1\cdots r_m} = \sum_{r=0}^{m} \sum_{s=0}^{m-r} \psi_{\alpha\beta}^r \left[\mathbf{c}_*^s \mathbf{g}^r \mathbf{u}_\Delta^{m-s-r}\right]^{\mathrm{all}}_{r_1\cdots r_m} \tag{6.29}$$

where $[\mathbf{a}^m\mathbf{b}^n\mathbf{c}^p]^{\mathrm{all}}$ is defined to be the sum of all possible and unique $(m+n+p)$ order tensor that is constructed from the dyadic products of m number of vector $\mathbf{a}$, n number of vector $\mathbf{b}$, and p number of vector $\mathbf{c}$. For example

$$\left[\mathbf{a}^2\mathbf{b}^2\mathbf{c}^0\right]^{\mathrm{all}} = \mathbf{aabb} + \mathbf{abab} + \mathbf{abba} + \mathbf{baab} + \mathbf{baba} + \mathbf{bbaa}$$

where the dyadic product is assumed for all vector products. With this notation, the collision

integral can be expressed as

$$R^{\alpha\beta,\,m}_{\delta,\,r_1\cdots r_m} = n_\alpha n_\beta \left(\frac{\gamma_{\alpha\beta}}{2\pi}\right)^{3/2} \left(\frac{\gamma_\alpha+\gamma_\beta}{2\pi}\right)^{3/2} \sum_{r=0}^{m}\sum_{s=0}^{m-r} \psi^r_{\alpha\beta} \int g\sigma(g) \exp\left[-\frac{1}{2}\gamma_{\alpha\beta}\left|\mathbf{g}-\mathbf{u}_{\alpha\beta}\right|^2\right] \times \left\{\int \left[\mathbf{c}^s_* \mathbf{g}^r \mathbf{u}^{m-s-r}_\Delta\right]^{\text{all}}_{r_1\cdots r_m} \exp\left[-\frac{1}{2}(\gamma_\alpha+\gamma_\beta)c^2_*\right] \mathrm{d}^3 c_*\right\} \mathrm{d}^3 g \quad (6.30)$$

First, consider the inner integral over $\mathbf{c}_*$. The integral over $\mathbf{c}_*$ has an analytical solution of the following form:

$$\left(\frac{\gamma_\alpha+\gamma_\beta}{2\pi}\right)^{3/2} \int \mathbf{c}^s_* \exp\left(-\frac{\gamma_\alpha+\gamma_\beta}{2}c^2_*\right) \mathrm{d}^3 c_* = \begin{cases} \left(\gamma_\alpha+\gamma_\beta\right)^{-s/2} \boldsymbol{\delta}^{s/2} & \text{if } s \text{ is even} \\ 0 & \text{if } s \text{ is odd} \end{cases} \quad (6.31)$$

where $\boldsymbol{\delta}^m$ is defined to be the symmetric sum of the m number of Kronecker delta dyadic products following the convention of Grad; e.g., $\boldsymbol{\delta}^2 = \delta_{rs}\delta_{tl} + \delta_{rt}\delta_{sl} + \delta_{rl}\delta_{st}$, where δ_{ij} is the Kronecker delta [49]. Due to the inner integral, all contributions from the odd s vanish, and the above collision integral simplifies to the following:

$$R^{\alpha\beta,\,m}_{\delta,\,r_1\cdots r_m} = n_\alpha n_\beta \left(\frac{\gamma_{\alpha\beta}}{2\pi}\right)^{3/2} \sum_{r=0}^{m} \sum_{s=0}^{\left[\frac{1}{2}(m-r)\right]_f} \frac{\psi^r_{\alpha\beta}}{\left(\gamma_\alpha+\gamma_\beta\right)^s} T^{\text{sym}}_{r_1\cdots r_m}\left\{\left[\boldsymbol{\delta}^s\right]_{r_1\cdots r_{2s}}, G^{(r)}_{r_1\cdots r_r}, \left[\mathbf{u}^t_\Delta\right]_{r_1\cdots r_t}\right\} \quad (6.32)$$

where $t = m - 2s - r$ and $\left[\frac{1}{2}p\right]_f$ is defined to be the largest integer not exceeding $\frac{1}{2}p$ as defined by Grad [49]. The tensor function $G^{(r)}_{r_1\cdots r_r}$ is defined as

$$G^{(m)}_{r_1\cdots r_m} = \int g\left[\mathbf{g}^m\right]_{r_1\cdots r_m} \sigma(g) \exp\left(-\frac{1}{2}\gamma_{\alpha\beta}\left|\mathbf{g}-\mathbf{u}_{\alpha\beta}\right|^2\right) \mathrm{d}^3 g \quad (6.33)$$

The tensor operator $T^{\text{sym}}_{r_1\cdots r_{m+n+p}}\left\{A_{r_1\cdots r_m}, B_{s_1\cdots s_n}, C_{t_1\cdots t_p}\right\}$ is defined to be equal to the $(m+n+p)$ order tensor that is generated from $[\hat{\mathbf{x}}^m_r \hat{\mathbf{x}}^n_s \hat{\mathbf{x}}^p_t]^{\text{all}}_{r_1\cdots r_{m+n+p}}$ by replacing the m order tensor formed by the dyadic product of the m number of $\hat{\mathbf{x}}_r$ (i.e. $\hat{\mathbf{x}}_{r_1}\cdots\hat{\mathbf{x}}_{r_m}$) with the m order

tensor $A_{r_1\cdots r_m}$, the n order tensor formed by the dyadic product of the n number of $\hat{\mathbf{x}}_s$ (i.e. $\hat{\mathbf{x}}_{s_1}\cdots\hat{\mathbf{x}}_{s_n}$) with the n order tensor $B_{s_1\cdots s_n}$, and the p order tensor formed by the dyadic product of the p number of $\hat{\mathbf{x}}_t$ (i.e. $\hat{\mathbf{x}}_{t_1}\cdots\hat{\mathbf{x}}_{t_p}$) with the p order tensor $C_{t_1\cdots t_p}$. For example:

$$T^{\text{sym}}_{ijkl}\{\overleftrightarrow{A},\overleftrightarrow{B},1\} = A_{ij}B_{kl} + A_{ik}B_{jl} + A_{il}B_{jk} + A_{jk}B_{il} + A_{jl}B_{ik} + A_{kl}B_{ij}$$

Next, consider the integral over $\mathbf{g}$. In order to solve for $G^{(m)}_{r_1\cdots r_m}$, transform into a spherical coordinate system with the vector $\mathbf{u}_{\alpha\beta}$ taken along the polar axis. Then,

$$\hat{\mathbf{g}} = \sin\theta\cos\phi\,\hat{\mathbf{x}}_1 + \sin\theta\sin\phi\,\hat{\mathbf{x}}_2 + \cos\theta\,\hat{\mathbf{x}}_3$$

where $\hat{\mathbf{g}} = \mathbf{g}/g$ and $\hat{\mathbf{x}}_3 = \mathbf{u}_{\alpha\beta}/u_{\alpha\beta}$. Then, the expression for $G^{(m)}_{r_1\cdots r_m}$ simplifies to the following:

$$G^{(m)}_{r_1\cdots r_m} = \exp\left(-\frac{1}{2}\gamma_{\alpha\beta}u^2_{\alpha\beta}\right)\int_0^\infty g^{m+3}\sigma(g)\Theta^{(m)}_{r_1\cdots r_m}\exp\left(-\frac{1}{2}\gamma_{\alpha\beta}g^2\right)\mathrm{d}g \tag{6.34}$$

where

$$\Theta^{(m)}_{r_1\cdots r_m} = \int_0^\pi \sin\theta\exp\left(\gamma_{\alpha\beta}u_{\alpha\beta}g\cos\theta\right)\left[\int_0^{2\pi}\left[\hat{\mathbf{g}}^m\right]_{r_1\cdots r_m}\mathrm{d}\phi\right]\mathrm{d}\theta \tag{6.35}$$

To simplify the angular integral terms, note that from the orthogonality of the trigonometric function, one has the following relationship:

$$\int_0^{2\pi}\sin^n(\phi)\cos^m(\phi)\,\mathrm{d}\phi = \begin{cases} \frac{2\pi\,m!\,n!}{2^{n+m}(n/2)!\,(m/2)!\,[(m+n)/2]!} & \text{if } n \text{ and } m \text{ are even} \\ 0 & \text{otherwise} \end{cases}$$

Thus, all terms that contain odd tensorial product of $\hat{\mathbf{x}}_1$ and $\hat{\mathbf{x}}_2$ are zero. This result is simply a consequence of the the azimuthal invariance of the collision integral. Using the

above result, the integral over the azimuthal coordinate is given to be

$$\int_0^{2\pi} [\hat{\mathbf{g}}^m]_{r_1\cdots r_m}\,\mathrm{d}\phi = \sum_{r=0}^{p} \frac{2\pi}{4^{p-r}\,(p-r)!}\cos^{m-2(p-r)}(\theta)\,\sin^{2(p-r)}(\theta) \times \sum_{s=0}^{p-r} \frac{[2\,(p-r-s)]!\;(2s)!}{(p-r-s)!\,s!}\left[\hat{\mathbf{x}}_1^{2s}\,\hat{\mathbf{x}}_2^{2(p-r-s)}\,\hat{\mathbf{x}}_3^{m-2p+2r}\right]^{\text{all}}_{r_1\cdots r_m} \tag{6.36}$$

where $p = [\frac{1}{2}m]_f$.

Using the result from above, the polar integration can now be applied. Defining $a = \gamma_{\alpha\beta}u_{\alpha\beta}g$, the angular integral term becomes

$$\Theta^{(m)}_{r_1\cdots r_m} = \frac{8\pi\;(p+1)!}{[2\,(p+1)]!}\sum_{r=0}^{p}\sum_{s=0}^{p-r}\frac{(2r)!\;[2\,(p-r-s)]!\;(2s)!}{r!\;(p-r-s)!\,s!} \times F_{rp}(a)\left[\hat{\mathbf{x}}_1^{2s}\,\hat{\mathbf{x}}_2^{2(p-r-s)}\hat{\mathbf{x}}_3^{2r}\right]^{\text{all}}_{r_1\cdots r_m} \tag{6.37a}$$

for even m and

$$\Theta^{(m)}_{r_1\cdots r_m} = \frac{8\pi\;(p+1)!}{[2\,(p+1)]!}\sum_{r=0}^{p}\sum_{s=0}^{p-r}\frac{(2r)!\;[2\,(p-r-s)]!\;(2s)!}{r!\;(p-r-s)!\,s!} \times \frac{2r+1}{a}\left[F_{r+1p}(a) - F_{rp}(a)\right]\left[\hat{\mathbf{x}}_1^{2s}\,\hat{\mathbf{x}}_2^{2(p-r-s)}\hat{\mathbf{x}}_3^{2r+1}\right]^{\text{all}}_{r_1\cdots r_m} \tag{6.37b}$$

for odd m. In the above equation,

$$F_{rp}(a) = {}_1F_2\left(\tfrac{1}{2}+r;\;\tfrac{1}{2},\;\tfrac{3}{2}+p;\;\tfrac{1}{4}a^2\right)$$

where ${}_pF_q(a_1,\ldots,a_p;\,b_1,\ldots,b_q;\,x)$ is the generalized hypergeometric function.

From the recursion relationship for the generalized hypergeometric function, ${}_1F_2$, there exists a recursion relationship of the form

$$F_p(a) = {}_0F_1\left(;\;\tfrac{3}{2}+p;\;\tfrac{1}{4}a^2\right)$$

and

$$F_{1p}(a) - F_p(a) = \frac{a^2}{3+2p} F_{p+1}(a)$$

where $F_p(a) = F_{0p}(a)$ and ${}_0F_1$ is the confluent hypergeometric limit function. Thus, using the recursion relationship and the knowledge of the F_{rp} function at the $r = 0$, one can express solution to the polar integral as a sum of the confluent hypergeometric limit functions. First few values of F_p are given as the following:

$$\begin{aligned}
F_0(a) &= \frac{1}{a}\sinh(a) \\
F_1(a) &= \frac{3}{a^3}\left[a\cosh(a) - \sinh(a)\right] \\
F_2(a) &= \frac{15}{a^5}\left[\left(3+a^2\right)\sinh(a) - 3a\cosh(a)\right] \\
F_3(a) &= \frac{105}{a^7}\left[a\left(15+a^2\right)\cosh(a) - 3\left(5+2a^2\right)\sinh(a)\right] \\
F_4(a) &= \frac{945}{a^9}\left[\left(105+45a^2+a^4\right)\sinh(a) - 5a\left(21+2a^2\right)\cosh(a)\right] \\
F_5(a) &= \frac{10395}{a^{11}}\left[a\left(945+105a^2+a^4\right)\cosh(a) - 15\left(63+28a^2+a^4\right)\sinh(a)\right]
\end{aligned}$$

While it is not obvious at the first glance, due to the symmetry of the tensor $\hat{\mathbf{g}}^m$, the resulting solution from the angular integral will result in a tensor with the same symmetry characteristics. From these observations, one can construct an ansatz that the tensor structure of $\Theta^{(m)}_{r_1\cdots r_m}$ is of form

$$\Theta^{(m)}_{r_1\cdots r_m} = \sum_{r=0}^{p} a_r \left[\boldsymbol{\delta}^{p-r}\hat{\mathbf{u}}^{m-2p+2r}_{\alpha\beta}\right]^{\text{sym}}_{r_1\cdots r_m}$$

where a_r is some constant and $[\mathbf{a}^m\mathbf{b}^n]^{\text{sym}}_{r_1\cdots r_{m+n}}$ represents a symmetric sum of the dyadic products of m number of $\mathbf{a}$ and n number of $\mathbf{b}$. Since $\boldsymbol{\delta}$ is an isotropic tensor and $\mathbf{u}_{\alpha\beta}$ has been written in a general vector form without any specified coordinate system, the solution for $\Theta^{(m)}_{r_1\cdots r_m}$ is coordinate invariant, even though a specific spherical coordinate system was chosen to carry out the integration. Note that in the spherical coordinate system chosen for

the integration, $\boldsymbol{\delta} = \hat{\mathbf{x}}_1\hat{\mathbf{x}}_1 + \hat{\mathbf{x}}_2\hat{\mathbf{x}}_2 + \hat{\mathbf{x}}_3\hat{\mathbf{x}}_3$ and $\hat{\mathbf{u}}_{\alpha\beta} = \hat{\mathbf{x}}_3$.

To construct the coordinate invariant form of the angular integral, first consider the case of the even m as expressed before. First note that

$$\left[\boldsymbol{\delta}^{p-t}\hat{\mathbf{u}}_{\alpha\beta}^{2t}\right]^{\text{sym}}_{r_1\cdots r_m} = \sum_{r=0}^{p-t}\sum_{s=0}^{p-t-r}\frac{(2r+2t)!\,[2\,(p-t-r-s)]!\,(2s)!}{2^{p-t}\,(2t)!\,r!\,(p-t-r-s)!\,s!}\left[\hat{\mathbf{x}}_1^{2s}\,\hat{\mathbf{x}}_2^{2(p-t-r-s)}\,\hat{\mathbf{x}}_3^{2(r+t)}\right]^{\text{all}}_{r_1\cdots r_m}$$

where $0 \leq t \leq p$. One can see that the tensorial contribution to the solution of the angular integral for the even m case can be isolated into a sum of the coordinate invariant tensorial contributions through the tedious series manipulation,

$$\sum_{r=0}^{p} F_r(a)a_r = F_0(a)\sum_{r=0}^{p} a_r + \sum_{r=1}^{p}[F_r(a) - F_0(a)]a_r$$

which can be recursively applied to isolate the coordinate invariant tensorial contribution.

After the recursive application of the above series manipulation, one obtains a coordinate invariant solution for the angular integral for the even m case is given to be

$$\Theta^{(m)}_{r_1\cdots r_m} = \frac{8\pi\,(p+1)!\,2^p}{[2\,(p+1)]!}\sum_{r=0}^{p}\frac{(2r)!}{2^r}\alpha_r[\boldsymbol{\delta}^{p-r}\hat{\mathbf{u}}_{\alpha\beta}^{2r}]^{\text{sym}}_{r_1\cdots r_m}$$

where α_r is defined with a recursive relationship of the form

$$\alpha_0 = F_p(a)$$
$$\alpha_1 = F_{1p}(a) - F_p(a)$$

and

$$\alpha_r = \frac{1}{r!}\left[F_{rp}(a) - F_p(a)\right] - \sum_{n=1}^{r-1}\frac{\alpha_n}{(r-n)!}$$

for $r > 1$. The recursive relationship given above for α_r can be greatly simplified using the

recursion relationship for F_{rp}. After some simplification, one obtains

$$\alpha_r = \frac{a^{2r}\,\Gamma\left(\frac{3}{2}+p\right)}{(2r)!\,\Gamma\left(\frac{3}{2}+p+n\right)} F_{p+r}(a)$$

where $\Gamma(x)$ is the gamma function. With this simplification, the coordinate invariant form of the angular integral for the even m case becomes the following:

$$\Theta^{(m)}_{r_1\cdots r_m} = 8\pi \sum_{r=0}^{p} \frac{2^{p+r}\ (p+r+1)!}{[2\,(p+r+1)]!} a^{2r} F_{p+r}(a)\left[\boldsymbol{\delta}^{p-r}\hat{\mathbf{u}}^{2r}_{\alpha\beta}\right]^{\text{sym}}_{r_1\cdots r_m}$$

For the odd m, first note that

$$\left[\boldsymbol{\delta}^{p-t}\hat{\mathbf{u}}^{2t+1}_{\alpha\beta}\right]^{\text{sym}}_{r_1\cdots r_m} = \sum_{r=0}^{p-t}\sum_{s=0}^{p-t-r} \frac{(2r+2t)!\ [2\,(p-t-r-s)]!\ (2s)!}{2^{p-t}\ (2t)!\,r!\ (p-t-r-s)!\,s!} \left[\hat{\mathbf{x}}_1^{2s}\,\hat{\mathbf{x}}_2^{2(p-t-r-s)}\,\hat{\mathbf{x}}_3^{2(r+t)}\right]^{\text{all}}_{r_1\cdots r_m}$$

where $0 \le t \le p$. One can carry out an equivalent procedure as done before for the even m to manipulate the series solution to obtain a coordinate invariant solution for the angular integral of the odd m case as

$$\Theta^{(m)}_{r_1\cdots r_m} = \frac{8\pi\ (p+1)!\,2^p}{a\ [2\,(p+1)]!} \sum_{r=0}^{p} \frac{(2r+1)!}{2^r} \beta_r \left[\boldsymbol{\delta}^{p-r}\hat{\mathbf{u}}^{2r+1}_{\alpha\beta}\right]^{\text{sym}}_{r_1\cdots r_m}$$

where β_r is defined with a recursive relationship of the form

$$\beta_0 = F_{1p}(a) - F_p(a)$$
$$\beta_1 = [F_{2p}(a) - F_{1p}(a)] - [F_{1p}(a) - F_p(a)]$$

and

$$\beta_r = \frac{1}{r!}\left\{[F_{r+1p}(a) - F_{rp}(a)] - [F_{1p}(a) - F_p(a)]\right\} - \sum_{n=1}^{r-1} \frac{\beta_n}{(r-n)!}$$

for $r > 1$. Similar to the even m case, the recursive relationship given above for β_r can be

greatly simplified using the recursion relationship for $F_{rp}(a)$. After some simplification, one obtains

$$\beta_r = \frac{a^{2r+1}\,\Gamma\left(\frac{3}{2}+p\right)}{2\;(2r+1)!\,\Gamma\left(\frac{5}{2}+p+n\right)} F_{p+r+1}(a)$$

With this simplification, the coordinate invariant form of the angular integral for the odd m case becomes the following:

$$\Theta^{(m)}_{r_1\cdots r_m} = 8\pi \sum_{r=0}^{p} \frac{2^{p+r+1}\;(p+r+2)!}{[2\,(p+r+2)]!} a^{2r+1} F_{p+r+1}(a)\left[\boldsymbol{\delta}^{p-r}\hat{\mathbf{u}}^{2r+1}_{\alpha\beta}\right]^{\mathrm{sym}}_{r_1\cdots r_m}$$

Finally, after some additional simplifications, the angular integral term that is applicable for all m becomes the following:

$$\Theta^{(m)}_{r_1\cdots r_m} = 8\pi \sum_{r=0}^{p} \frac{2^{m-p+r}\;(m-p+r+1)!}{[2\,(m-p+r+1)]!} \left(\gamma_{\alpha\beta} g\right)^{2r+m-2p} \times F_{m-p+r}\left(\gamma_{\alpha\beta} u_{\alpha\beta} g\right)\left[\boldsymbol{\delta}^{p-r}\hat{\mathbf{u}}^{2r+m-2p}_{\alpha\beta}\right]^{\mathrm{sym}}_{r_1\cdots r_m} \quad (6.41)$$

With the coordinate invariant form of the angular integral defined, after further simplification, the expression, $G^{(m)}_{r_1\cdots r_m}$, simplifies to the following:

$$G^{(m)}_{r_1\cdots r_m} = 16\left(\frac{2\pi}{\gamma_{\alpha\beta}}\right)^{3/2} \sum_{r=0}^{p} \frac{4^{m+r-p}\;(m+r-p+1)!}{\gamma^{p-r}_{\alpha\beta}\;[2\,(m+r-p+1)]!} \overline{\Omega}^{(m+r-p)}_{\alpha\beta}\left[\boldsymbol{\delta}^{p-r}\mathbf{u}^{2r+m-2p}_{\alpha\beta}\right]^{\mathrm{sym}}_{r_1\cdots r_m} \quad (6.42)$$

where $\overline{\Omega}^{(p)}_{\alpha\beta}$ is a generalized collision integral defined to be

$$\overline{\Omega}^{(p)}_{\alpha\beta} = \frac{\gamma^{p+3/2}_{\alpha\beta}}{(2\pi)^{1/2}\,2^{p+2}} e^{-\frac{1}{2}\gamma_{\alpha\beta}u^2_{\alpha\beta}} \int_0^\infty g^{2p+3}\sigma(g) F_p(\gamma_{\alpha\beta}u_{\alpha\beta}g) e^{-\frac{1}{2}\gamma_{\alpha\beta}g^2}\,\mathrm{d}g \quad (6.43)$$

The generalized collision integral $\overline{\Omega}^{(p)}_{\alpha\beta}$ can also be expressed as an infinite series of the Chapman-Cowling collision integral as

$$\overline{\Omega}^{(p)}_{\alpha\beta} = \sum_{l=0}^{\infty} \frac{4^l\;[2\,(p+1)]!\;(p+l+1)!}{l!\;(p+1)!\;[2\,(p+l+1)]!} \left(\frac{1}{2}\gamma_{\alpha\beta}u^2_{\alpha\beta}\right)^l \Omega^{(p+l)}_{\alpha\beta} e^{-\frac{1}{2}\gamma_{\alpha\beta}u^2_{\alpha\beta}} \quad (6.44)$$

where $\Omega_{\alpha\beta}^{(p)}$ is the Chapman-Cowling collision integral defined as the following [52]:

$$\Omega_{\alpha\beta}^{(p)} = \frac{\gamma_{\alpha\beta}^{p+3/2}}{(2\pi)^{1/2}\, 2^{p+2}} \int_0^\infty g^{2p+3} \sigma(g) e^{-\frac{1}{2}\gamma_{\alpha\beta} g^2} \, \mathrm{d}g \tag{6.45}$$

The above series expression for the collision integral may sometimes be more useful, as one can separate the contribution due to the species temperature ($\gamma_{\alpha\beta}$) and the contribution due to the relative velocity of the reacting fluids ($u_{\alpha\beta}$). This allows one to obtain the Chapman-Cowling collision integrals for the specified reaction as a function of the $\gamma_{\alpha\beta}$, and use this result to obtain the approximation of $\overline{\Omega}_{\alpha\beta}^{(p)}$ for the specified fluid relative velocity.

The final expression for the collision integral simplifies to the following:

$$\begin{aligned} R_{\delta,\, r_1 \cdots r_m}^{\alpha\beta,\, m} = 16 n_\alpha n_\beta \sum_{r=0}^{m} \sum_{s=0}^{n} \sum_{q=0}^{p} & \frac{4^{r+q-p}\ (r+q-p+1)!}{[2\,(r+q-p+1)]!} \frac{\gamma_\beta^r}{\gamma_{\alpha\beta}^{p-q}\,(\gamma_\alpha+\gamma_\beta)^{s+r}} \overline{\Omega}_{\alpha\beta}^{(r+q-p)} \\ & \times T_{r_1 \cdots r_m}^{\mathrm{sym}} \left\{ \left[\boldsymbol{\delta}^s\right]_{r_1 \cdots r_{2s}}, \left[\boldsymbol{\delta}^{p-q} \mathbf{u}_{\alpha\beta}^{2q-2p+r}\right]_{r_1 \cdots r_r}^{\mathrm{sym}}, \left[\mathbf{u}_\Delta^{m-2s-r}\right]_{r_1 \cdots r_{m-2s-r}} \right\} \end{aligned} \tag{6.46}$$

Note that $\mathbf{u}_\Delta = (\gamma_\alpha \mathbf{u}_\alpha + \gamma_\beta \mathbf{u}_\beta)/(\gamma_\alpha + \gamma_\beta) - \mathbf{u}_\delta$, $n = [\frac{1}{2}(m-r)]_f$, and $p = [\frac{1}{2} r]_f$. As soon as the cross section for the reaction is defined, the generalized collision integral $\overline{\Omega}_{\alpha\beta}^{(p)}$ for the reaction can be determined, and the above expression can be used to derive the collision and reaction contribution to the fluid equations.

6.4.1 Electron Impact Reaction Process

Consider the special case of the electron impact reaction process given as

$$e + A \rightarrow B + \cdots + \Delta E$$

where the reactant species A is assumed to be a heavy species with a significant mass difference compared with the electrons, i.e. $m_A \gg m_e$. For this case, additional simplifications can be made due to the small electron inertia compared with the heavier species. Assuming

that $m_e/m_A \ll T_e/T_A$, where m_e is the electron inertia, m_A is the reactant heavy particle inertia, T_e is the electron temperature, and T_A is the reactant heavy particle temperature, one obtains following approximations:

$$\gamma_\alpha + \gamma_\beta \approx \frac{m_A}{kT_A} = \gamma_A$$

$$\gamma_{\alpha\beta} \approx \frac{m_e}{kT_e} = \gamma_e$$

Note that in the above approximation, it has not been specified to which of the two species, α and β, the electron species corresponds. The requirement is that it is a bimolecular reaction involving an electron and heavy species.

Next, assume that $\gamma_e^{-1} \gg |\mathbf{u}_e - \mathbf{u}_A|^2$, where γ_e^{-1} is the electron thermal velocity squared, $\mathbf{u}_e$ is the electron velocity, and $\mathbf{u}_A$ is the reactant heavy species velocity. This assumption is generally valid, since the reduced impact kinetic energy is generally small compared with the electron thermal energy due to the small electron inertia. Then, the generalized collision integral can be greatly simplified as

$$\overline{\Omega}^{(p)}_{\alpha\beta} \approx \Omega^{(p)}_{\alpha\beta}$$

as all of the high order term in $\gamma_{\alpha\beta} u^2_{\alpha\beta}$ vanishes in the series expansion. Thus, the generalized collision integral reduces to the Chapman-Cowling collision integral. The Chapman-Cowling collision integral can further be simplified as

$$\Omega^{(p)}_{eA} \approx \sqrt{\frac{kT_e}{8\pi m_e}} \left[\frac{1}{kT_e} \int_0^\infty \left(\frac{E}{kT_e} \right)^{p+1} \sigma(E) e^{-E/kT_e} \, \mathrm{d}E \right] \tag{6.47}$$

where $E = \frac{1}{2} m_e g^2$ is the electron impact energy. In addition, following approximation can be made:

$$\mathbf{u}_\Delta \approx \mathbf{u}_A - \mathbf{u}_\delta = \mathbf{u}_{A\delta}$$

For a typical 5-moment fluid model, zeroth, first, and second order moments are of

importance. For the zeroth order moment, one obtains the following result:

$$R_{\delta}^{\alpha\beta,\,0} \approx 8 n_e n_A \Omega_{eA}^{(0)} \tag{6.48}$$

For the first order moment, one obtains the following result:

$$\mathbf{R}_{\delta}^{\alpha\beta,\,1} \approx 8 n_e n_A \Omega_{eA}^{(0)} \left(\mathbf{u}_{A\delta} + \frac{2}{3} \frac{m_\beta}{m_A} \frac{\Omega_{eA}^{(1)}}{\Omega_{eA}^{(0)}} \mathbf{u}_{\alpha\beta} \right) \tag{6.49}$$

Finally, for the second order moment case, one obtains the following result:

$$\begin{aligned} \overleftrightarrow{R}_{\delta}^{\alpha\beta,\,2} \approx 8 n_e n_A \Omega_{eA}^{(0)} \left(\mathbf{u}_{A\delta}\mathbf{u}_{A\delta} + \frac{kT_A}{m_A} \overleftrightarrow{\mathrm{I}} \right) + \frac{16}{3} n_e n_A \frac{m_\beta}{m_A} \frac{T_A}{T_\beta} \Omega_{eA}^{(1)} \left(\mathbf{u}_{\alpha\beta}\mathbf{u}_{A\delta} + \mathbf{u}_{A\delta}\mathbf{u}_{\alpha\beta} + \frac{kT_\alpha}{m_\alpha} \overleftrightarrow{\mathrm{I}} \right) \\ + \frac{32}{15} n_e n_A \left(\frac{m_\beta}{m_A} \frac{T_A}{T_\beta} \right)^2 \Omega_{eA}^{(2)} \mathbf{u}_{eA}\mathbf{u}_{eA} \end{aligned} \tag{6.50}$$

As it can be seen from the above result, for the 5-moment fluid model, zeroth, first, and second order Chapman-Cowling collision integrals for the electron impact reactions are required. In practice, only the zeroth and the first order Chapman-Cowling collision integrals are needed due to the fact that the term associated with the second order Chapman-Cowling collision integral vanishes due to the small electron inertia assumption once the species specific collision integrals for the fluid equations are constructed.

6.4.2 Heavy Species Collision Reaction Processes

For the heavy species collisional reaction processes, the simplifications that were possible for the electron impact collision processes are not possible. However, the collision integral can be simplified to some degree for the case of the first three moments.

First, note that in general, the heavy species collisional reaction cross section is defined as a function of the specific impact energy (generally in units of eV/amu). Thus, the generalized

collision integral may be written in terms of the specific energy as the following:

$$\overline{\Omega}_{\alpha\beta}^{(p)} = \sqrt{\frac{k\overline{T}_{\alpha\beta}}{8\pi}} \left[\frac{1}{k\overline{T}_{\alpha\beta}} \int_0^\infty \left(\frac{\overline{E}}{k\overline{T}_{\alpha\beta}} \right)^{p+1} \sigma(\overline{E}) F_p \left(2\sqrt{\frac{\overline{E}\lambda_{\alpha\beta}}{k\overline{T}_{\alpha\beta}}} \right) e^{-(\overline{E}/k\overline{T}_{\alpha\beta} + \lambda_{\alpha\beta})} \, \mathrm{d}\overline{E} \right] \tag{6.51}$$

where $\overline{E}$ is the specific impact energy, $\overline{T}_{\alpha\beta} = T_\alpha/m_\alpha + T_\beta/m_\beta$ is the specific reduced temperature (the reduced temperature divided by the reduced mass), and $\lambda_{\alpha\beta} = u_{\alpha\beta}^2/(2k\overline{T}_{\alpha\beta})$ is the specific impact kinetic energy divided by the specific reduced temperature. In a series form, the generalized collision integral can be expressed as

$$\overline{\Omega}_{\alpha\beta}^{(p)} = \sum_{l=0}^{\infty} \frac{4^l \, [2\,(p+1)]! \, (p+l+1)!}{l! \, (p+1)! \, [2\,(p+l+1)]!} \lambda_{\alpha\beta}^l \Omega_{\alpha\beta}^{(p+l)} e^{-\lambda_{\alpha\beta}} \tag{6.52}$$

where the Chapman-Cowling collision integral is defined as

$$\Omega_{\alpha\beta}^{(p)} = \sqrt{\frac{k\overline{T}_{\alpha\beta}}{8\pi}} \left[\frac{1}{k\overline{T}_{\alpha\beta}} \int_0^\infty \left(\frac{\overline{E}}{k\overline{T}_{\alpha\beta}} \right)^{p+1} \sigma(\overline{E}) e^{-\overline{E}/k\overline{T}_{\alpha\beta}} \, \mathrm{d}\overline{E} \right] \tag{6.53}$$

Thus, the collision integral is parametrized by two independent variables for a given collision cross section: $\overline{T}_{\alpha\beta}$ and $\lambda_{\alpha\beta}$.

For a typical 5-moment fluid model, zeroth, first, and second order moments are important. For the zeroth order moment, one obtains the following result:

$$R_\delta^{\alpha\beta,\,0} = 8 n_\alpha n_\beta \overline{\Omega}_{\alpha\beta}^{(0)} \tag{6.54}$$

For the first order moment, one obtains the following result:

$$\mathbf{R}_\delta^{\alpha\beta,\,1} = 8 n_\alpha n_\beta \overline{\Omega}_{\alpha\beta}^{(0)} \left(\mathbf{u}_\Delta + \frac{2}{3} \frac{\gamma_{\alpha\beta}}{\gamma_\alpha} \frac{\overline{\Omega}_{\alpha\beta}^{(1)}}{\overline{\Omega}_{\alpha\beta}^{(0)}} \mathbf{u}_{\alpha\beta} \right) \tag{6.55}$$

Finally, for the second order moment case, one obtains the following result:

$$\overleftrightarrow{R}_{\delta}^{\alpha\beta,\,2} = 8n_\alpha n_\beta \overline{\Omega}_{\alpha\beta}^{(0)} \left(\mathbf{u}_\Delta \mathbf{u}_\Delta + \frac{\gamma_{\alpha\beta}}{\gamma_\alpha \gamma_\beta} \overleftrightarrow{\mathrm{I}} \right) + \frac{16}{3} n_\alpha n_\beta \frac{\gamma_{\alpha\beta}}{\gamma_\alpha} \overline{\Omega}_{\alpha\beta}^{(1)} \left(\mathbf{u}_{\alpha\beta} \mathbf{u}_\Delta + \mathbf{u}_\Delta \mathbf{u}_{\alpha\beta} + \gamma_\alpha^{-1} \overleftrightarrow{\mathrm{I}} \right) + \frac{32}{15} n_\alpha n_\beta \left(\frac{\gamma_{\alpha\beta}}{\gamma_\alpha} \right)^2 \overline{\Omega}_{\alpha\beta}^{(2)} \mathbf{u}_{\alpha\beta} \mathbf{u}_{\alpha\beta} \quad (6.56)$$

As it can be seen from the above result, for the 5-moment fluid model, zeroth, first, and second order generalized collision integral for the heavy species collisional reactions are required.

6.4.3 Special Case for a Constant Cross Section

For the special case when the cross section is a constant value given as σ_0, there is a closed form analytical solution for the generalized collision integral given to be the following:

$$\overline{\Omega}_{\alpha\beta}^{(p)} = \sigma_0 (p+1)! \left(\frac{k\overline{T}_{\alpha\beta}}{8\pi} \right)^{1/2} \Phi_{\alpha\beta}^{(p)} \quad (6.57)$$

where $\Phi_{\alpha\beta}^{(p)}$ is a velocity correction function defined to be

$$\Phi_{\alpha\beta}^{(p)} = {}_1F_1 \left(-\tfrac{1}{2};\, \tfrac{3}{2} + p;\, -\lambda_{\alpha\beta} \right) \quad (6.58)$$

where ${}_1F_1$ is the confluent hypergometric function of the first kind. First few values of the velocity correction function are given to be the followings:

$$\Phi_{\alpha\beta}^{(0)} = \frac{1}{4} \left[2e^{-\lambda_{\alpha\beta}} + \sqrt{\pi} \lambda_{\alpha\beta}^{-1/2} \left(2\lambda_{\alpha\beta} + 1 \right) \mathrm{erf} \left(\lambda_{\alpha\beta}^{1/2} \right) \right]$$

$$\Phi_{\alpha\beta}^{(1)} = \frac{3}{32\lambda_{\alpha\beta}} \left[2 \left(2\lambda_{\alpha\beta} + 1 \right) e^{-\lambda_{\alpha\beta}} + \sqrt{\pi} \lambda_{\alpha\beta}^{-1/2} \left(4\lambda_{\alpha\beta}^2 + 4\lambda_{\alpha\beta} - 1 \right) \mathrm{erf} \left(\lambda_{\alpha\beta}^{1/2} \right) \right]$$

$$\Phi_{\alpha\beta}^{(2)} = \frac{5}{128\lambda_{\alpha\beta}^2} \left[2 \left(4\lambda_{\alpha\beta}^2 + 4\lambda_{\alpha\beta} - 3 \right) e^{-\lambda_{\alpha\beta}} + \sqrt{\pi} \lambda_{\alpha\beta}^{-1/2} \left(8\lambda_{\alpha\beta}^3 + 12\lambda_{\alpha\beta}^2 - 6\lambda_{\alpha\beta} + 3 \right) \mathrm{erf} \left(\lambda_{\alpha\beta}^{1/2} \right) \right]$$

6.4.4 Special Case for Maxwell Molecule Cross Section

Consider the special case of the Maxwell molecules discussed in Schunk and Nagy, which has a cross section that scales as $\sigma = \sigma_0(\overline{E}_0/\overline{E})^{1/2}$ where σ_0 and $\overline{E}_0$ are some constants [50]. For this case, there is a simple closed form analytical solution for the generalized collision integral given to be the following:

$$\overline{\Omega}^{(p)}_{\alpha\beta} = \sigma_0 \Gamma(\tfrac{3}{2} + p)\sqrt{\frac{\overline{E}_0}{k\overline{T}_{\alpha\beta}}} \tag{6.60}$$

Thus, the dependence on the impact velocity vanishes for the special case of the Maxwell molecules.

6.4.5 Special Case for the Inverse-Power Inter-particle Force Law Cross Section

Consider the special case of the cross section governed by an inverse-power inter-particle force law of the form $F = K_{\alpha\beta}/r^{\alpha}$. As discussed in Schunk and Nagy, there exists a closed form solution for the Chapman-Cowling collision integral of the following form:

$$\Omega^{(l,p)}_{\alpha\beta} = \frac{\sqrt{\pi}}{2} A_l \left(\frac{K_{\alpha\beta}}{\mu_{\alpha\beta}}\right)^{2/(a-1)} \left(2k\overline{T}_{\alpha\beta}\right)^{(a-5)/[2(a-1)]} \Gamma\left(p + 2 - \frac{2}{a-1}\right) \tag{6.61}$$

where $A_l = \int_0^{\infty} \hat{b}_0(1 - \cos^l(\theta))\, \mathrm{d}\hat{b}_0$, θ is the scattering angle, and $\hat{b}_0$ is the non-dimensional impact parameter [50]. The generalized collision integral then becomes

$$\overline{\Omega}^{(l,p)}_{\alpha\beta} = \frac{\sqrt{\pi}}{2} A_l \left(\frac{K_{\alpha\beta}}{\mu_{\alpha\beta}}\right)^{2/(a-1)} (2k\overline{T}_{\alpha\beta})^{(a-5)/[2(a-1)]} \Gamma\left(p + 2 - \frac{2}{a-1}\right) \Phi^{(p)}_{\alpha\beta} \tag{6.62}$$

where $\Phi^{(p)}_{\alpha\beta}$ is a velocity correction function defined to be

$$\Phi^{(p)}_{\alpha\beta} = e^{-\lambda_{\alpha\beta}} {}_1F_1\left(p + 2 - \frac{2}{a-1};\, \frac{3}{2} + p;\, \lambda_{\alpha\beta}\right) \tag{6.63}$$

where ${}_1F_1$ is the confluent hypergometric function of the first kind.

For the special case of the Coulomb potential which corresponds to $a = 2$ and $K_{\alpha\beta} = e_\alpha e_\beta/(4\pi\varepsilon_0)$, the generalized collision integral simplifies to the following:

$$\overline{\Omega}_{\alpha\beta}^{(p)} = \sqrt{\pi}(p-1)!\,(2k\overline{T}_{\alpha\beta})^{-3/2}\left(\frac{e_\alpha e_\beta}{4\pi\varepsilon_0\mu_{\alpha\beta}}\right)^2 \frac{A_l}{2}\Phi_{\alpha\beta}^{(p)} \tag{6.64}$$

where

$$\Phi_{\alpha\beta}^{(p)} = {}_1F_1\left(\tfrac{3}{2};\ \tfrac{3}{2}+p;\ -\lambda_{\alpha\beta}\right) \tag{6.65}$$

For the special case when $l = 1$, which corresponds to the momentum transfer cross section, $A_1 = 2\ln\Lambda$, and the generalized collision integral for the Coulomb collision simplifies to the following:

$$\overline{\Omega}_{\alpha\beta}^{(p)} = \sqrt{\pi}(p-1)!\,(2k\overline{T}_{\alpha\beta})^{-3/2}\left(\frac{e_\alpha e_\beta}{4\pi\varepsilon_0\mu_{\alpha\beta}}\right)^2 \ln(\Lambda)\,\Phi_{\alpha\beta}^{(p)} \tag{6.66}$$

where Λ is the Coulomb logarithm. The first few values of the velocity correction function are given to be the followings:

$$\begin{aligned}
\Phi_{\alpha\beta}^{(0)} &= e^{-\lambda_{\alpha\beta}} \\
\Phi_{\alpha\beta}^{(1)} &= \frac{3}{4\lambda_{\alpha\beta}}\left[\sqrt{\pi}\lambda_{\alpha\beta}^{-1/2}\,\mathrm{erf}\left(\lambda_{\alpha\beta}^{1/2}\right) - 2e^{-\lambda_{\alpha\beta}}\right] \\
\Phi_{\alpha\beta}^{(2)} &= \frac{15}{16\lambda_{\alpha\beta}^2}\left[\sqrt{\pi}\lambda_{\alpha\beta}^{-1/2}\,(2\lambda_{\alpha\beta}-3)\,\mathrm{erf}\left(\lambda_{\alpha\beta}^{1/2}\right) + 6e^{-\lambda_{\alpha\beta}}\right]
\end{aligned}$$

6.4.6 Application to the Boltzmann Collision Integral

The collision integrals derived for the reactions are quite general, and the formalism of the generalized collision integral can be applied to the Boltzmann collision integral that is typically used for elastic collision processes. For the Boltzmann collision integral of form

$$\frac{\delta f_\alpha}{\delta t} = \iint g\sigma_{\alpha\beta}\,(g,\theta)\left(f'_\alpha f'_\beta - f_\alpha f_\beta\right)\,\mathrm{d}\Omega\,\mathrm{d}^3v'$$

the collision contribution to the fluid equation for the 5-moment Maxwellian distribution function can be expressed as the following as given by Schunk and Nagy [50]:

$$\frac{\delta n_\alpha}{\delta t} = 0$$

$$\frac{\delta \mathbf{M}_\alpha}{\delta t} = -\mu_{\alpha\beta} \iint g f_\alpha f_\beta \left[\mathbf{g} Q^{(1)}_{\alpha\beta}\right] \, \mathrm{d}^3 c_\alpha \, \mathrm{d}^3 c_\beta$$

$$\frac{\delta E_\alpha}{\delta t} = -\mu_{\alpha\beta} \iint g f_\alpha f_\beta \left[\mathbf{g} \cdot (\mathbf{v}_c - \mathbf{u}_\alpha) \, Q^{(1)}_{\alpha\beta}\right] \, \mathrm{d}^3 c_\alpha \, \mathrm{d}^3 c_\beta$$

where

$$Q^{(1)}_{\alpha\beta} = \int \sigma_{\alpha\beta}(g, \theta) \, (1 - \cos\theta) \, \mathrm{d}\Omega$$

is the momentum transfer cross section.

Carrying out the coordinate transformation to the $\mathbf{c}_*$ and $\mathbf{g}_*$ space as done before and integrating, the collision contribution to the momentum and the energy equation can be expressed as the following:

$$\frac{\delta \mathbf{M}_\alpha}{\delta t} = -\mu_{\alpha\beta} n_\alpha n_\beta \left(\frac{\gamma_{\alpha\beta}}{2\pi}\right)^{3/2} \mathbf{G}^{(1)}$$

$$\frac{\delta E_\alpha}{\delta t} = \frac{\mu_{\alpha\beta}}{m_\alpha + m_\beta} n_\alpha n_\beta \left(\frac{\gamma_{\alpha\beta}}{2\pi}\right)^{3/2} \left[k(T_\beta - T_\alpha)\gamma_{\alpha\beta} \left(\overleftrightarrow{\mathrm{I}} : \overleftrightarrow{G}^{(2)}\right) + (m_\alpha + m_\beta) \frac{\gamma_{\alpha\beta}}{\gamma_\alpha} \left(\mathbf{u}_{\alpha\beta} \cdot \mathbf{G}^{(1)}\right)\right]$$

where $G^{(m)}_{r_1 \cdots r_m}$ is the same as what was defined previously with the cross section σ replaced with the momentum transfer cross section $Q^{(1)}_{\alpha\beta}$.

After some algebra, it can be shown that the collision contribution to the momentum and energy equations simplifies to the followings:

$$\frac{\delta \mathbf{M}_\alpha}{\delta t} = -\frac{16}{3} \frac{m_\alpha m_\beta}{m_\alpha + m_\beta} n_\alpha n_\beta \overline{\Omega}^{(1)}_{\alpha\beta} \mathbf{u}_{\alpha\beta} \tag{6.68}$$

$$\frac{\delta E_\alpha}{\delta t} = \frac{16}{3}\frac{m_\alpha m_\beta}{(m_\alpha + m_\beta)^2} n_\alpha n_\beta \Bigg\{ 3k(T_\beta - T_\alpha) \left[\left(1 - \frac{2}{3}\lambda_{\alpha\beta} \right) \overline{\Omega}^{(1)}_{\alpha\beta} + \frac{4}{15}\lambda_{\alpha\beta}\overline{\Omega}^{(2)}_{\alpha\beta} \right] + m_\beta u^2_{\alpha\beta} \overline{\Omega}^{(1)}_{\alpha\beta} \Bigg\} \quad (6.69)$$

It can be verified after some simple algebra that for the special case of the hard sphere and Coulomb collision processes, the above expression reduces to the result shown in the previous section for the elastic collision integral. The energy conservative form of the collision contribution to the energy equation can be expressed as

$$\frac{\delta \tilde{E}_\alpha}{\delta t} = \frac{16}{3}\frac{m_\alpha m_\beta}{(m_\alpha + m_\beta)^2} n_\alpha n_\beta \Bigg\{ 3k(T_\beta - T_\alpha) \left[\left(1 - \frac{2}{3}\lambda_{\alpha\beta} \right) \overline{\Omega}^{(1)}_{\alpha\beta} + \frac{4}{15}\lambda_{\alpha\beta}\overline{\Omega}^{(2)}_{\alpha\beta} \right] + \left[(m_\alpha - m_\beta)\mathbf{u}_\alpha \cdot \mathbf{u}_\beta + m_\beta u^2_\beta - m_\alpha u^2_\alpha \right] \overline{\Omega}^{(1)}_{\alpha\beta} \Bigg\} \quad (6.70)$$

6.5 Specific Form of the Collision Integral for the Electron Impact Reactions

Specific form of the collision integral for the electron impact reactions considered in this model is covered in this section. The collision integrals for the heavy species impact reactions are considered in the next section.

In what follows the contribution to the fluid equation due to the electron impact ionization required for the model is given. In particular, the contribution to $\frac{\delta n_\alpha}{\delta t}$, $\frac{\delta \mathbf{M}}{\delta t}$, $\frac{\delta \mathbf{M}_n}{\delta t}$, $\frac{\delta \mathbf{M}_e}{\delta t}$, $\frac{\delta E}{\delta t}$, $\frac{\delta E_n}{\delta t}$, and $\frac{\delta E_e}{\delta t}$ are given. Note that the electron inertia is assumed to be negligible in all collision contribution to the fluid equations except for the $\frac{\delta \mathbf{M}_e}{\delta t}$ term where the first dominant contribution term is of order m_e.

The required Chapman-Cowling collision integrals for each reaction are numerically integrated using the cross sections for each reactions tabulated in literatures. The resulting Chapman-Cowling collision integrals are shown for each reaction in their respective sections. Note that $\Omega^{(0)}_{eA}$ term is directly associated with the reaction rate parameter $\langle \sigma_{eA} v_e \rangle$ commonly

tabulated for electron impact reaction process through the relationship

$$\langle \sigma_{eA} v_e \rangle = 8\Omega_{eA}^{(0)}$$

6.5.1 (EL 1) Electron Impact Ionization: $e + D \rightarrow e + D^+ + e$

The electron impact ionization of the deuterium atom is given as

$$e + D \rightarrow e + D^+ + e - \phi_{EL1} \tag{6.71}$$

where ϕ_{EL1} is the effective ionization potential that includes the ionization threshold energy of 13.6 eV and additional energy losses due to excitations and radiations from the electron impact process. For this reaction, the collision operators for e, D, and D^+ can be represented as

$$\begin{aligned} C_{D^+} &= \frac{m_e C_{D^+}^{eD} + m_D C_{D^+}^{De}}{m_e + m_D} \\ C_e &= 2\frac{m_e C_e^{eD} + m_D C_e^{De}}{m_e + m_D} - C_e^{eD} \\ C_D &= -C_D^{De} \end{aligned}$$

The collision terms required for the fluid equation can be expressed as follows:

Continuity:

$$\begin{aligned} \frac{\delta n_{D^+}}{\delta t} &= \frac{m_e R_{D^+}^{eD,0} + m_D R_{D^+}^{De,0}}{m_e + m_D} \\ \frac{\delta n_e}{\delta t} &= 2\frac{m_e R_e^{eD,0} + m_D R_e^{De,0}}{m_e + m_D} - R_e^{eD,0} \\ \frac{\delta n_D}{\delta t} &= -R_D^{De,0} \end{aligned}$$

Momentum:

$$\frac{\delta \mathbf{M}}{\delta t} = m_{D^+} \frac{m_e \left(\mathbf{R}_{D^+}^{eD,\,1} + R_{D^+}^{eD,\,0} \mathbf{u}_{D^+} \right) + m_D \left(\mathbf{R}_{D^+}^{De,\,1} + R_{D^+}^{De,\,0} \mathbf{u}_{D^+} \right)}{m_e + m_D} + \frac{\delta \mathbf{M}_e}{\delta t}$$

$$\frac{\delta \mathbf{M}_e}{\delta t} = m_e \left[2 \frac{m_e \left(\mathbf{R}_e^{eD,\,1} + R_e^{eD,\,0} \mathbf{u}_e \right) + m_D \left(\mathbf{R}_e^{De,\,1} + R_e^{De,\,0} \mathbf{u}_e \right)}{m_e + m_D} - \left(\mathbf{R}_e^{eD,\,1} + R_e^{eD,\,0} \mathbf{u}_e \right) \right]$$

$$\frac{\delta \mathbf{M}_n}{\delta t} = -m_D \left(\mathbf{R}_D^{De,\,1} + R_D^{De,\,0} \mathbf{u}_D \right)$$

Energy:

$$\frac{\delta E}{\delta t} = \frac{1}{2} m_{D^+} \left(\frac{m_e \overleftrightarrow{R}_{D^+}^{eD,\,2} + m_D \overleftrightarrow{R}_{D^+}^{De,\,2}}{m_e + m_D} \right) : \overleftrightarrow{\mathrm{I}} + \frac{\delta E_e}{\delta t}$$

$$\frac{\delta E_e}{\delta t} = \frac{1}{2} m_e \left(2 \frac{m_e \overleftrightarrow{R}_e^{eD,\,2} + m_D \overleftrightarrow{R}_e^{De,\,2}}{m_e + m_D} - \overleftrightarrow{R}_e^{eD,\,2} \right) : \overleftrightarrow{\mathrm{I}}$$

$$\frac{\delta E_n}{\delta t} = -\frac{1}{2} m_D \overleftrightarrow{R}_D^{De,\,2} : \overleftrightarrow{\mathrm{I}}$$

After neglecting electron inertia and simplifying, the collision terms required for the fluid equations from this reaction are obtained to be the followings:

Continuity:

$$\frac{\delta n_{D^+}}{\delta t} = \frac{\delta n_e}{\delta t} = -\frac{\delta n_D}{\delta t} \approx 8 n n_n (1 - f_{dn}) \Omega_{EL1}^{(0)} \tag{6.76}$$

Momentum:

$$\frac{\delta \mathbf{M}}{\delta t} = -\frac{\delta \mathbf{M}_n}{\delta t} \approx 8 n n_n (1 - f_{dn}) \Omega_{EL1}^{(0)} m \mathbf{u}_n \tag{6.77a}$$

$$\frac{1}{ne} \frac{\delta \mathbf{M}_e}{\delta t} \approx \frac{16}{3} (1 - f_{dn}) \frac{n_n}{n} \frac{m_e}{e^2} \Omega_{EL1}^{(1)} \left[\mathbf{J} - ne \left(\mathbf{u}_{in} - \frac{3}{2} \frac{\Omega_{EL1}^{(0)}}{\Omega_{EL1}^{(1)}} \mathbf{u}_n \right) \right] \tag{6.77b}$$

Energy:

$$\frac{\delta E}{\delta t} \approx 8nn_n(1-f_{dn})\Omega^{(0)}_{EL1}\left(\frac{1}{2}mu^2_{in}+\frac{3}{2}kT_n-\phi_{EL1}\right) \tag{6.78a}$$

$$\frac{\delta E_e}{\delta t} \approx -8nn_n(1-f_{dn})\Omega^{(0)}_{EL1}\left(\phi_{EL1}+\frac{\Omega^{(1)}_{EL1}}{\Omega^{(0)}_{EL1}}kT_e\right) \tag{6.78b}$$

$$\frac{\delta E_n}{\delta t} \approx -8nn_n(1-f_{dn})\Omega^{(0)}_{EL1}\left(\frac{3}{2}kT_n\right) \tag{6.78c}$$

For the Chapman-Cowling collision integral required for this reaction, the recommended cross section data from Janev and Smith for hydrogen is used [73]. No low energy extrapolation is necessary due to the existence of the threshold energy at 13.6 eV. The high energy extrapolation is made by fitting a linear line at the tail of the cross-section in the log-space. The resulting Chapman-Cowling collision integral after the numerical integration of the cross-section data is shown in Fig. 6.1.

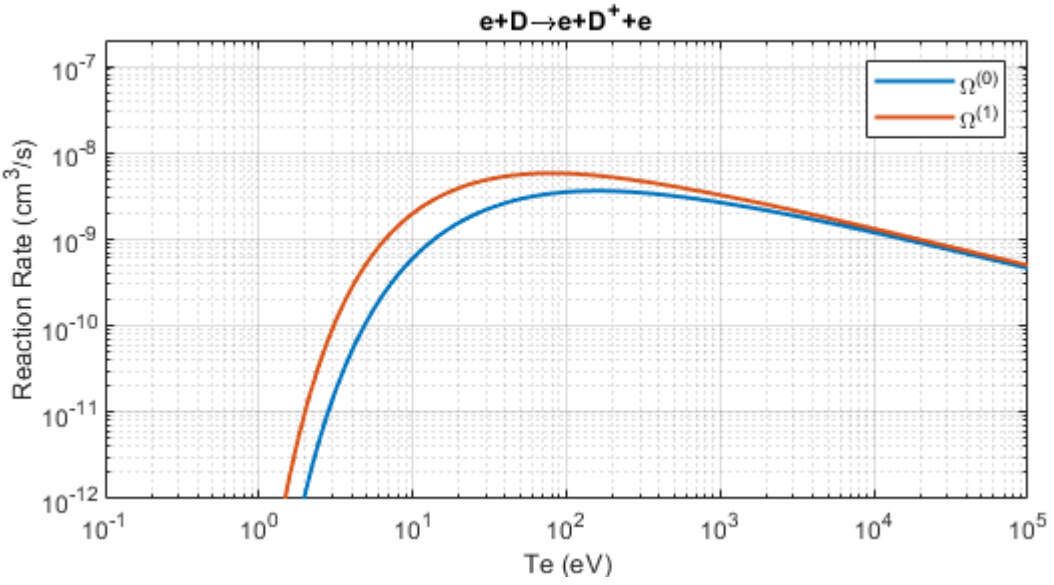

Figure 6.1: Chapman-Cowling collision integral for electron impact ionization of D (EL 1).

6.5.2 (EL 2) Electron Impact Ionization: $e + D_2 \rightarrow e + D_2^+ + e$

The electron impact ionization of the deuterium molecule is given as

$$e + D_2 \rightarrow e + D_2^+ + e - \phi_{EL2} \tag{6.79}$$

where ϕ_{EL2} is the effective ionization potential that includes the ionization threshold energy of 15.4 eV and additional energy losses due to excitations and radiations from the electron impact process. For this reaction, the collision operators for e, D_2, and D_2^+ can be represented as

$$\begin{aligned} C_{D_2^+} &= \frac{m_e C_{D_2^+}^{eD_2} + m_{D_2} C_{D_2^+}^{D_2 e}}{m_e + m_{D_2}} \\ C_e &= 2\frac{m_e C_e^{eD_2} + m_{D_2} C_e^{D_2 e}}{m_e + m_{D_2}} - C_e^{eD_2} \\ C_{D_2} &= -C_{D_2}^{D_2 e} \end{aligned}$$

A similar procedure as done before for reaction EL 1 can be used to obtain the collision terms for the fluid equations for this reaction. After some simplification, the collision terms required for the fluid equations are the followings:

Continuity:

$$\frac{\delta n_{D_2^+}}{\delta t} = \frac{\delta n_e}{\delta t} = -\frac{\delta n_{D_2}}{\delta t} \approx 8 n n_n f_{dn} \Omega_{EL2}^{(0)} \tag{6.81}$$

Momentum:

$$\frac{\delta \mathbf{M}}{\delta t} = -\frac{\delta \mathbf{M}_n}{\delta t} \approx 16 n n_n f_{dn} \Omega_{EL2}^{(0)} m \mathbf{u}_n \tag{6.82a}$$

$$\frac{1}{ne}\frac{\delta \mathbf{M}_e}{\delta t} \approx \frac{16}{3} f_{dn} \frac{n_n}{n} \frac{m_e}{e^2} \Omega_{EL2}^{(1)} \left[\mathbf{J} - ne \left(\mathbf{u}_{in} - \frac{3}{2} \frac{\Omega_{EL2}^{(0)}}{\Omega_{EL2}^{(0)}} \mathbf{u}_n \right) \right] \tag{6.82b}$$

Energy:

$$\frac{\delta E}{\delta t} \approx 8nn_n f_{dn}\Omega^{(0)}_{EL2}\left(mu^2_{in} + \frac{3}{2}kT_n - \phi_{EL2}\right) \tag{6.83a}$$

$$\frac{\delta E_e}{\delta t} \approx -8nn_n f_{dn}\Omega^{(0)}_{EL2}\left(\phi_{EL2} + \frac{\Omega^{(1)}_{EL2}}{\Omega^{(0)}_{EL2}}kT_e\right) \tag{6.83b}$$

$$\frac{\delta E_n}{\delta t} \approx -8nn_n f_{dn}\Omega^{(0)}_{EL2}\left(\frac{3}{2}kT_n\right) \tag{6.83c}$$

For the Chapman-Cowling collision integral required for this reaction, the recommended cross section data from Yoon et al. for hydrogen is used [74]. No low energy extrapolation is necessary due to the existence of the threshold energy at 15.4 eV. The high energy extrapolation is made by fitting a linear line at the tail of the cross-section in the log-space. The resulting Chapman-Cowling collision integral after the numerical integration of the cross-section data is shown in Fig. 6.2.

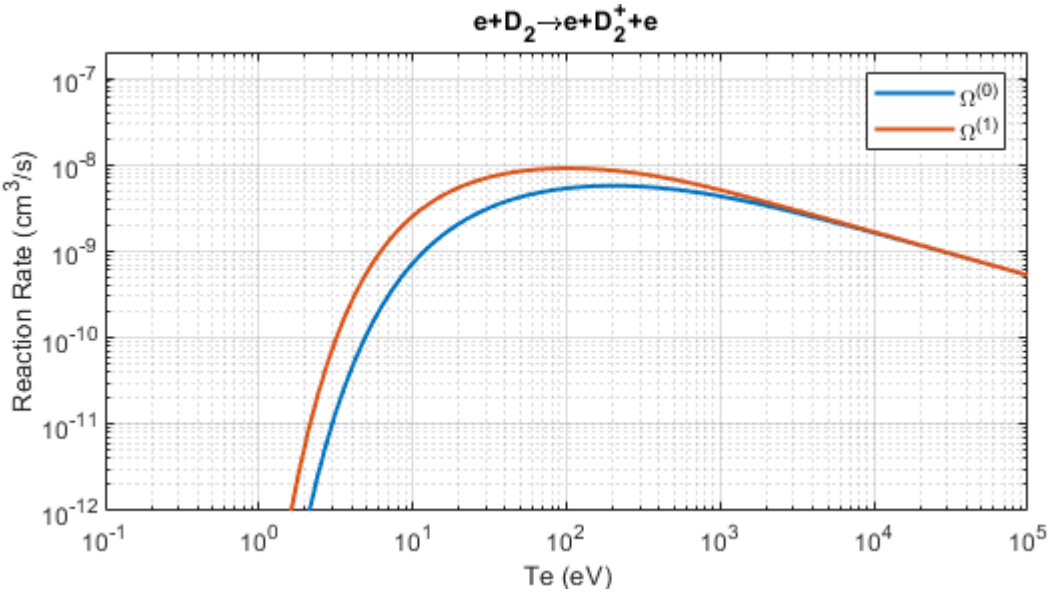

Figure 6.2: Chapman-Cowling collision integral for electron impact ionization of D_2 (EL 2).

6.5.3 (EL 3) Electron Impact Dissociative Ionization: $e + D_2 \rightarrow e + D^+ + D + e$

The electron impact dissociative ionization of the deuterium molecule is given as

$$e + D_2 \rightarrow e + D^+ + D + e - \phi_{EL3} \tag{6.84}$$

where ϕ_{EL3} is the effective dissociative ionization potential of 28.0 eV. For this reaction, the collision operators for e, D, D_2, and D^+ can be represented as

$$\begin{aligned}
C_{D^+} &= \frac{m_e C_{D^+}^{eD_2} + m_{D_2} C_{D^+}^{D_2 e}}{m_e + m_{D_2}} \\
C_e &= 2\frac{m_e C_e^{eD_2} + m_{D_2} C_e^{D_2 e}}{m_e + m_{D_2}} - C_e^{eD_2} \\
C_D &= \frac{m_e C_D^{eD_2} + m_{D_2} C_D^{D_2 e}}{m_e + m_{D_2}} \\
C_{D_2} &= -C_{D_2}^{D_2 e}
\end{aligned}$$

A similar procedure as done before for reaction EL 1 can be used to obtain the collision terms for the fluid equations for this reaction. After some simplification, the collision terms required for the fluid equations are the followings:

Continuity:

$$\frac{\delta n_{D^+}}{\delta t} = \frac{\delta n_e}{\delta t} = \frac{\delta n_D}{\delta t} = -\frac{\delta n_{D_2}}{\delta t} \approx 8 n n_n f_{dn} \Omega_{EL3}^{(0)} \tag{6.86}$$

Momentum:

$$\frac{\delta \mathbf{M}}{\delta t} = -\frac{\delta \mathbf{M}_n}{\delta t} \approx 8 n n_n f_{dn} \Omega_{EL3}^{(0)} m \mathbf{u}_n \tag{6.87a}$$

$$\frac{1}{ne}\frac{\delta \mathbf{M}_e}{\delta t} \approx \frac{16}{3} f_{dn} \frac{n_n}{n} \frac{m_e}{e^2} \Omega_{EL3}^{(1)} \left[\mathbf{J} - ne \left(\mathbf{u}_{in} - \frac{3}{2} \frac{\Omega_{EL3}^{(0)}}{\Omega_{EL3}^{(1)}} \mathbf{u}_n \right) \right] \tag{6.87b}$$

Energy:

$$\frac{\delta E}{\delta t} \approx 8nn_n f_{dn}\Omega^{(0)}_{EL3}\left(\frac{1}{2}mu^2_{in} + \frac{3}{4}kT_n - \phi_{EL3} - \frac{1}{2}\frac{\Omega^{(1)}_{EL3}}{\Omega^{(0)}_{EL3}}kT_e\right) \tag{6.88a}$$

$$\frac{\delta E_e}{\delta t} \approx 8nn_n f_{dn}\Omega^{(0)}_{EL3}\left(-\phi_{EL3} + \frac{\Omega^{(1)}_{EL3}}{\Omega^{(0)}_{EL3}}kT_e\right) \tag{6.88b}$$

$$\frac{\delta E_n}{\delta t} \approx -8nn_n f_{dn}\Omega^{(0)}_{EL3}\left(\frac{3}{4}kT_n - \frac{1}{2}\frac{\Omega^{(1)}_{EL3}}{\Omega^{(0)}_{EL3}}kT_e\right) \tag{6.88c}$$

For the Chapman-Cowling collision integral required for this reaction, the recommended cross section data from Yoon et al. for hydrogen is used [74]. No low energy extrapolation is necessary due to the existence of the threshold energy at 28.0 eV. The high energy extrapolation is made by fitting a linear line at the tail of the cross-section in the log-space. The resulting Chapman-Cowling collision integral after the numerical integration of the cross-section data is shown in Fig. 6.3.

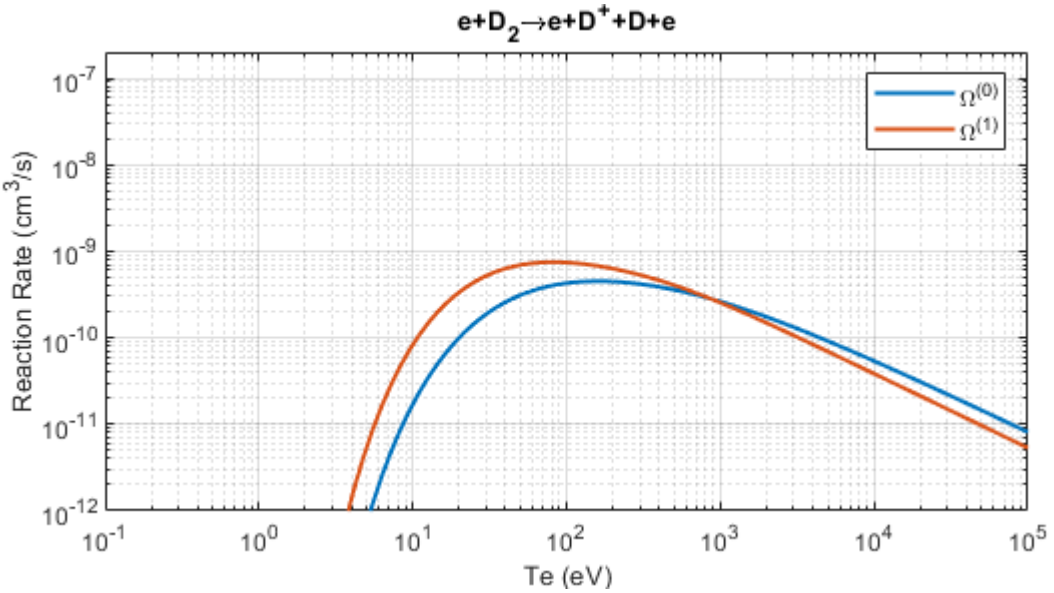

Figure 6.3: Chapman-Cowling collision integral for electron impact dissociative ionization of D_2 (EL 3).

6.5.4 (EL 4) Electron Impact Dissociative Ionization: $e + D_2^+ \rightarrow e + D^+ + D^+ + e$

The electron impact dissociative ionization of the molecular deuterium ion is given as

$$e + D_2^+ \rightarrow e + D^+ + D^+ + e - \phi_{EL4} \tag{6.89}$$

where ϕ_{EL4} is the effective dissociative ionization potential of 14.7 eV. For this reaction, the collision operators for e, D^+, and D_2^+ can be represented as

$$\begin{aligned} C_{D^+} &= 2\frac{m_e C_{D^+}^{eD_2^+} + m_{D_2^+} C_{D^+}^{D_2^+ e}}{m_e + m_{D_2^+}} \\ C_e &= 2\frac{m_e C_e^{eD_2^+} + m_{D_2^+} C_e^{D_2^+ e}}{m_e + m_{D_2^+}} - C_e^{eD_2^+} \\ C_{D_2^+} &= -C_{D_2^+}^{D_2^+ e} \end{aligned}$$

A similar procedure as done before for reaction EL 1 can be used to obtain the collision terms for the fluid equations for this reaction. After some simplification, the collision terms required for the fluid equations are the followings:

Continuity:

$$\frac{\delta n_{D^+}}{\delta t} = 2\frac{\delta n_e}{\delta t} = -2\frac{\delta n_{D_2^+}}{\delta t} \approx 16 n^2 f_{di} \Omega_{EL4}^{(0)} \tag{6.91}$$

Momentum:

$$\frac{\delta \mathbf{M}}{\delta t} = \frac{\delta \mathbf{M}_n}{\delta t} = 0 \tag{6.92a}$$

$$\frac{1}{ne}\frac{\delta \mathbf{M}_e}{\delta t} \approx \frac{16}{3} f_{di} \Omega_{EL4}^{(1)} \frac{m_e}{e^2} \left(\mathbf{J} + \frac{3}{2}\frac{\Omega_{EL4}^{(0)}}{\Omega_{EL4}^{(1)}} ne\mathbf{u} \right) \tag{6.92b}$$

Energy:

$$\frac{\delta E}{\delta t} \approx -8n^2 f_{di} \Omega^{(0)}_{EL4} \phi_{EL4} \tag{6.93a}$$

$$\frac{\delta E_e}{\delta t} \approx -8n^2 f_{di} \Omega^{(0)}_{EL4} \left(\phi_{EL4} - \frac{\Omega^{(1)}_{EL4}}{\Omega^{(0)}_{EL4}} kT_e \right) \tag{6.93b}$$

$$\frac{\delta E_n}{\delta t} = 0 \tag{6.93c}$$

For the Chapman-Cowling collision integral required for this reaction, the cross section data compiled by Janev et al. for hydrogen is used [60]. No low energy extrapolation is necessary due to the existence of the threshold energy at 14.7 eV. The high energy extrapolation is made by fitting a linear line at the tail of the cross-section in the log-space. The resulting Chapman-Cowling collision integral after the numerical integration of the cross-section data is shown in Fig. 6.4.

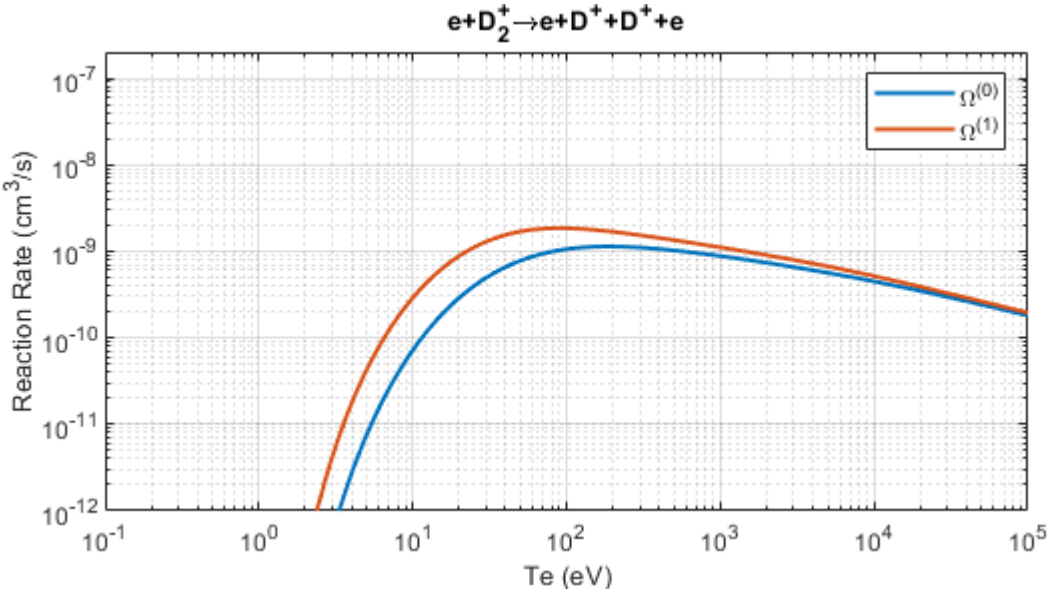

Figure 6.4: Chapman-Cowling collision integral for electron impact dissociative ionization of D_2^+ (EL 4).

6.5.5 (EL 5) Electron Impact Dissociation: $e + D_2 \rightarrow e + D + D$

The electron impact dissociation of the deuterium molecule is given as

$$e + D_2 \rightarrow e + D + D - \phi_{EL5} \tag{6.94}$$

where ϕ_{EL5} is the effective dissociation potential of 8.8 eV. For this reaction, the collision operators for e, D, and D_2 can be represented as

$$\begin{aligned} C_D &= 2\frac{m_e C_D^{eD_2} + m_{D_2} C_D^{D_2 e}}{m_e + m_{D_2}} \\ C_e &= \frac{m_e C_e^{eD_2} + m_{D_2} C_e^{D_2 e}}{m_e + m_{D_2}} - C_e^{eD_2} \\ C_{D_2} &= -C_{D_2}^{D_2 e} \end{aligned}$$

A similar procedure as done before for reaction EL 1 can be used to obtain the collision terms for the fluid equations for this reaction. After some simplification, the collision terms required for the fluid equations are the followings:

Continuity:

$$\frac{\delta n_D}{\delta t} = 2\frac{\delta n_{D_2}}{\delta t} \approx 16 n n_n f_{dn} \Omega_{EL5}^{(0)} \tag{6.96a}$$

$$\frac{\delta n_e}{\delta t} = 0 \tag{6.96b}$$

Momentum:

$$\frac{\delta \mathbf{M}}{\delta t} = \frac{\delta \mathbf{M}_n}{\delta t} = 0 \tag{6.97a}$$

$$\frac{1}{ne}\frac{\delta \mathbf{M}_e}{\delta t} \approx \frac{16}{3} f_{dn} \frac{n_n}{n} \frac{m_e}{e^2} \Omega_{EL5}^{(1)} (\mathbf{J} - ne\mathbf{u}_{in}) \tag{6.97b}$$

Energy:

$$\frac{\delta E}{\delta t} \approx -8nn_n f_{dn}\Omega^{(0)}_{EL5}\left(\phi_{EL5} + \frac{\Omega^{(1)}_{EL5}}{\Omega^{(0)}_{EL5}}kT_e\right) \tag{6.98a}$$

$$\frac{\delta E_e}{\delta t} \approx -8nn_n f_{dn}\Omega^{(0)}_{EL5}\left(\phi_{EL5} + \frac{\Omega^{(1)}_{EL5}}{\Omega^{(0)}_{EL5}}kT_e\right) \tag{6.98b}$$

$$\frac{\delta E_n}{\delta t} \approx 8nn_n f_{dn}\Omega^{(1)}_{EL5}kT_e \tag{6.98c}$$

For the Chapman-Cowling collision integral required for this reaction, the recommended cross section data from Yoon et al. for hydrogen is used [74]. No low energy extrapolation is necessary due to the existence of the threshold energy at 8.8 eV. The high energy extrapolation is made by fitting a linear line at the tail of the cross-section in the log-space. The resulting Chapman-Cowling collision integral after the numerical integration of the cross-section data is shown in Fig. 6.5.

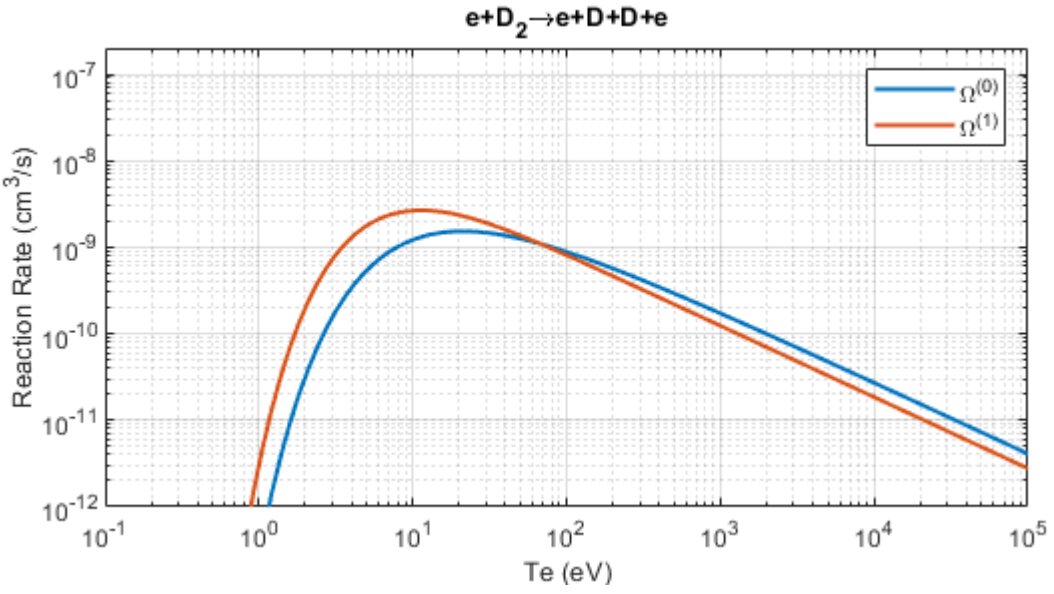

Figure 6.5: Chapman-Cowling collision integral for electron impact dissociation of D_2 (EL 5).

6.5.6 (EL 6) Electron Impact Dissociative Excitation: $e + D_2^+ \rightarrow e + D^+ + D$

The electron impact dissociative excitation of the molecular deuterium ion is given as

$$e + D_2^+ \rightarrow e + D^+ + D - \phi_{EL6} \tag{6.99}$$

where ϕ_{EL6} is the effective dissociative excitation potential of 2.4 eV. For this reaction, the collision operators for e, D, D^+, and D_2^+ can be represented as

$$\begin{aligned}
C_D &= \frac{m_e C_D^{eD_2^+} + m_{D_2^+} C_D^{D_2^+ e}}{m_e + m_{D_2^+}} \\
C_e &= \frac{m_e C_e^{eD_2^+} + m_{D_2^+} C_e^{D_2^+ e}}{m_e + m_{D_2^+}} - C_e^{eD_2^+} \\
C_{D^+} &= \frac{m_e C_{D^+}^{eD_2^+} + m_{D_2^+} C_{D^+}^{D_2^+ e}}{m_e + m_{D_2^+}} \\
C_{D_2^+} &= -C_{D_2^+}^{D_2^+ e}
\end{aligned}$$

A similar procedure as done before for reaction EL 1 can be used to obtain the collision terms for the fluid equations for this reaction. After some simplification, the collision terms required for the fluid equations are the followings:

Continuity:

$$\frac{\delta n_{D^+}}{\delta t} = -\frac{\delta n_{D_2^+}}{\delta t} = \frac{\delta n_D}{\delta t} \approx 8n^2 f_{di} \Omega_{EL6}^{(0)} \tag{6.101a}$$

$$\frac{\delta n_e}{\delta t} = 0 \tag{6.101b}$$

Momentum:

$$\frac{\delta \mathbf{M}}{\delta t} = -\frac{\delta \mathbf{M}_n}{\delta t} \approx -8n^2 f_{di} \Omega_{EL6}^{(0)} m\mathbf{u} \tag{6.102a}$$

$$\frac{1}{ne}\frac{\delta \mathbf{M}_e}{\delta t} \approx \frac{16}{3} f_{di} \frac{m_e}{e^2} \Omega^{(1)}_{EL6} \mathbf{J} \tag{6.102b}$$

Energy:

$$\frac{\delta E}{\delta t} \approx -4n^2 f_{di} \Omega^{(0)}_{EL6} \left(\frac{3}{2} kT_i + \phi_{EL6} + \frac{\Omega^{(1)}_{EL6}}{\Omega^{(0)}_{EL6}} kT_e \right) \tag{6.103a}$$

$$\frac{\delta E_e}{\delta t} \approx -8n^2 f_{di} \Omega^{(0)}_{EL6} \left(\phi_{EL6} + \frac{\Omega^{(1)}_{EL6}}{\Omega^{(0)}_{EL6}} kT_e \right) \tag{6.103b}$$

$$\frac{\delta E_n}{\delta t} \approx 4n^2 f_{di} \Omega^{(0)}_{EL6} \left(m u_{in}^2 + \frac{3}{2} kT_i + \frac{\Omega^{(1)}_{EL6}}{\Omega^{(0)}_{EL6}} kT_e \right) \tag{6.103c}$$

For the Chapman-Cowling collision integral required for this reaction, the cross section data compiled by Janev et al. for hydrogen is used [60]. No low energy extrapolation is necessary due to the existence of the threshold energy at 2.4 eV. The high energy extrapolation is made by fitting a linear line at the tail of the cross-section in the log-space. The resulting Chapman-Cowling collision integral after the numerical integration of the cross-section data is shown in Fig. 6.6.

6.5.7 (EL 7) Electron Impact Dissociative Excitation: $e + D_3^+ \rightarrow e + D^+ + D + D$

The electron impact dissociative excitation of the molecular deuterium ion is given as

$$e + D_3^+ \rightarrow e + D^+ + D + D - \phi_{EL7} \tag{6.104}$$

where ϕ_{EL7} is the effective dissociative excitation potential of 15 eV. For this reaction, the collision operators for e, D, D^+, and D_3^+ can be represented as

$$C_D = 2\frac{m_e C_D^{eD_3^+} + m_{D_3^+} C_D^{D_3^+ e}}{m_e + m_{D_3^+}}$$

$$C_e = \frac{m_e C_e^{eD_3^+} + m_{D_3^+} C_e^{D_3^+ e}}{m_e + m_{D_3^+}} - C_e^{eD_3^+}$$

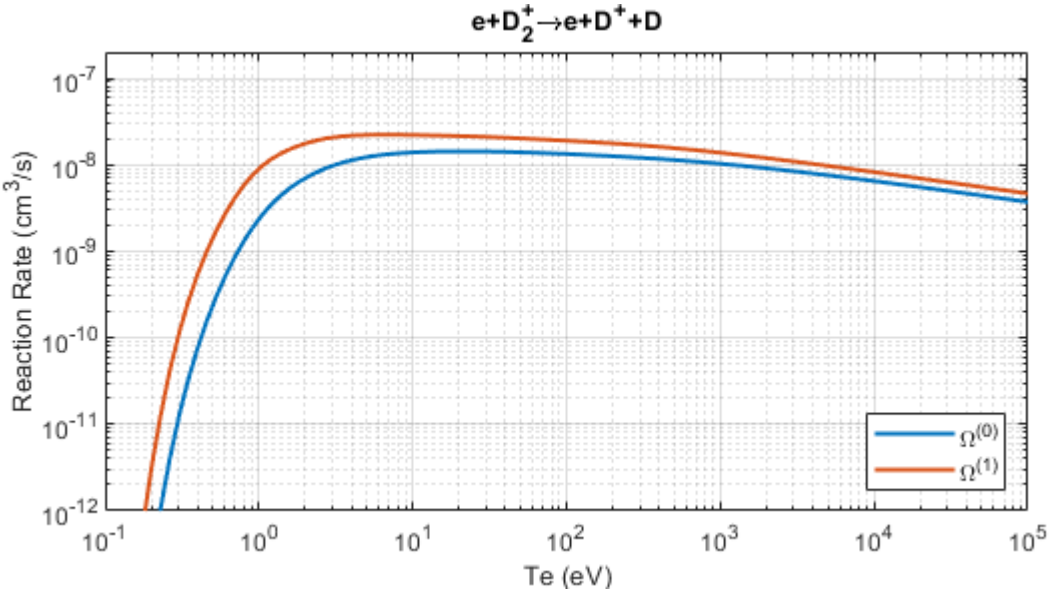

Figure 6.6: Chapman-Cowling collision integral for electron impact dissociative excitation of D_2^+ (EL 6).

$$C_{D^+} = \frac{m_e C_{D^+}^{eD_3^+} + m_{D_3^+} C_{D^+}^{D_3^+ e}}{m_e + m_{D_3^+}}$$
$$C_{D_3^+} = -C_{D_3^+}^{D_3^+ e}$$

A similar procedure as done before for reaction EL 1 can be used to obtain the collision terms for the fluid equations for this reaction. After some simplification, the collision terms required for the fluid equations are the followings:

Continuity:

$$2\frac{\delta n_{D^+}}{\delta t} = -2\frac{\delta n_{D_3^+}}{\delta t} = \frac{\delta n_D}{\delta t} \approx 8n^2 f_{ti} \Omega_{EL7}^{(0)} \tag{6.106a}$$
$$\frac{\delta n_e}{\delta t} = 0 \tag{6.106b}$$

Momentum:

$$\frac{\delta \mathbf{M}}{\delta t} = -\frac{\delta \mathbf{M}_n}{\delta t} \approx -16n^2 f_{ti} \Omega^{(0)}_{EL7} m\mathbf{u} \tag{6.107a}$$

$$\frac{1}{ne}\frac{\delta \mathbf{M}_e}{\delta t} \approx \frac{16}{3} f_{ti} \frac{m_e}{e^2} \Omega^{(1)}_{EL7} \mathbf{J} \tag{6.107b}$$

Energy:

$$\frac{\delta E}{\delta t} \approx -8n^2 f_{ti} \Omega^{(0)}_{EL7} \left(kT_i + \phi_{EL7} + \frac{2}{3}\frac{\Omega^{(1)}_{EL7}}{\Omega^{(0)}_{EL7}} kT_e \right) \tag{6.108a}$$

$$\frac{\delta E_e}{\delta t} \approx -8n^2 f_{ti} \Omega^{(0)}_{EL7} \left(\phi_{EL7} + \frac{\Omega^{(1)}_{EL7}}{\Omega^{(0)}_{EL7}} kT_e \right) \tag{6.108b}$$

$$\frac{\delta E_n}{\delta t} \approx 8n^2 f_{ti} \Omega^{(0)}_{EL7} \left(mu_{in}^2 + kT_i + \frac{2}{3}\frac{\Omega^{(1)}_{EL7}}{\Omega^{(0)}_{EL7}} kT_e \right) \tag{6.108c}$$

For the Chapman-Cowling collision integral required for this reaction, the cross section data measured by Peart and Dolder [75,76] as recommended by Tawara et al. [72] for hydrogen is used. No low energy extrapolation is necessary due to the existence of the threshold energy at 15 eV. The high energy extrapolation is made by fitting a linear line at the tail of the cross-section in the log-space. The resulting Chapman-Cowling collision integral after the numerical integration of the cross-section data is shown in Fig. 6.7.

6.5.8 (EL 8) Electron Impact Dissociative Recombination: $e + D_2^+ \rightarrow e + D + D$

The electron impact dissociative recombination of the molecular deuterium ion is given as

$$e + D_2^+ \rightarrow D + D \tag{6.109}$$

Note that there is no energy loss potential for this reaction due to the fact that there are no threshold energy. For this reaction, the collision operators for e, D, and D_2^+ can be

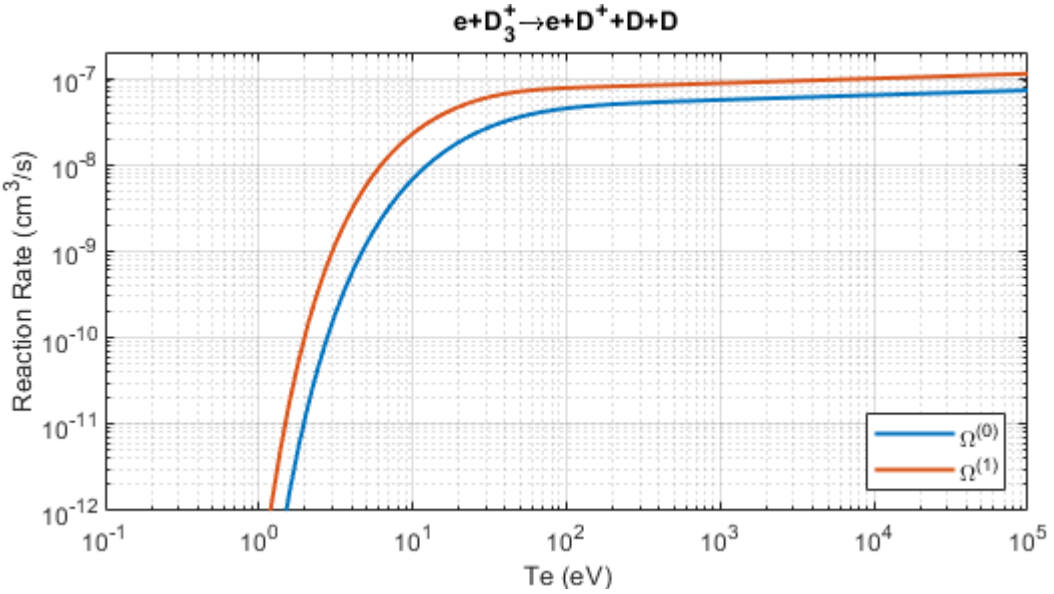

Figure 6.7: Chapman-Cowling collision integral for electron impact dissociative excitation of D_3^+ (EL 7).

represented as

$$C_D = 2\frac{m_e C_D^{eD_2^+} + m_{D_2^+} C_D^{D_2^+ e}}{m_e + m_{D_2^+}}$$
$$C_e = -C_e^{eD_2^+}$$
$$C_{D_2^+} = -C_{D_2^+}^{D_2^+ e}$$

A similar procedure as done before for reaction EL 1 can be used to obtain the collision terms for the fluid equations for this reaction. After some simplification, the collision terms required for the fluid equations are the followings:

Continuity:

$$2\frac{\delta n_{D_2^+}}{\delta t} = 2\frac{\delta n_e}{\delta t} = -\frac{\delta n_D}{\delta t} \approx 16 n^2 f_{di} \Omega_{EL8}^{(0)} \tag{6.111}$$

Momentum:

$$\frac{\delta \mathbf{M}}{\delta t} = -\frac{\delta \mathbf{M}_n}{\delta t} \approx -16 n^2 f_{di} \Omega^{(0)}_{EL8} m \mathbf{u} \tag{6.112a}$$

$$\frac{1}{ne}\frac{\delta \mathbf{M}_e}{\delta t} \approx \frac{16}{3} f_{di} \Omega^{(1)}_{EL8} \frac{m_e}{e^2} \left(\mathbf{J} - \frac{3}{2} \frac{\Omega^{(0)}_{EL8}}{\Omega^{(1)}_{EL8}} ne \mathbf{u} \right) \tag{6.112b}$$

Energy:

$$\frac{\delta E}{\delta t} \approx -8 n^2 f_{di} \Omega^{(0)}_{EL8} \left(\frac{3}{2} k T_i + \frac{\Omega^{(1)}_{EL8}}{\Omega^{(0)}_{EL8}} k T_e \right) \tag{6.113a}$$

$$\frac{\delta E_e}{\delta t} \approx -8 n^2 f_{di} \Omega^{(1)}_{EL8} k T_e \tag{6.113b}$$

$$\frac{\delta E_n}{\delta t} \approx 8 n^2 f_{di} \Omega^{(0)}_{EL8} \left(m u_{in}^2 + \frac{3}{2} k T_i + \frac{\Omega^{(1)}_{EL8}}{\Omega^{(0)}_{EL8}} k T_e \right) \tag{6.113c}$$

For the Chapman-Cowling collision integral required for this reaction, the cross-section data compiled by Janev et al. for hydrogen is used [60]. The cross-section data is fit reasonably well by the following fit:

$$\sigma(E) = \sigma_0 (E/E_0)^{-m}$$

where $\sigma_0 = 7.64 \times 10^{-16}\,\mathrm{cm}^2$, $E_0 = 1\,\mathrm{eV}$, and $m = 1.1046$. Note that the cross section as expressed above can be integrated exactly for the Chapman-Cowling collision integral. The resulting Chapman-Cowling collision integral is given in the following form:

$$\Omega^{(p)} = \sigma_0 \left(\frac{k T_e}{E_0} \right)^{-m} \Gamma(2 + p - m) \left(\frac{k T_e}{8 \pi m_e} \right)^{1/2}$$

The resulting Chapman-Cowling collision integral is shown in Fig. 6.8.

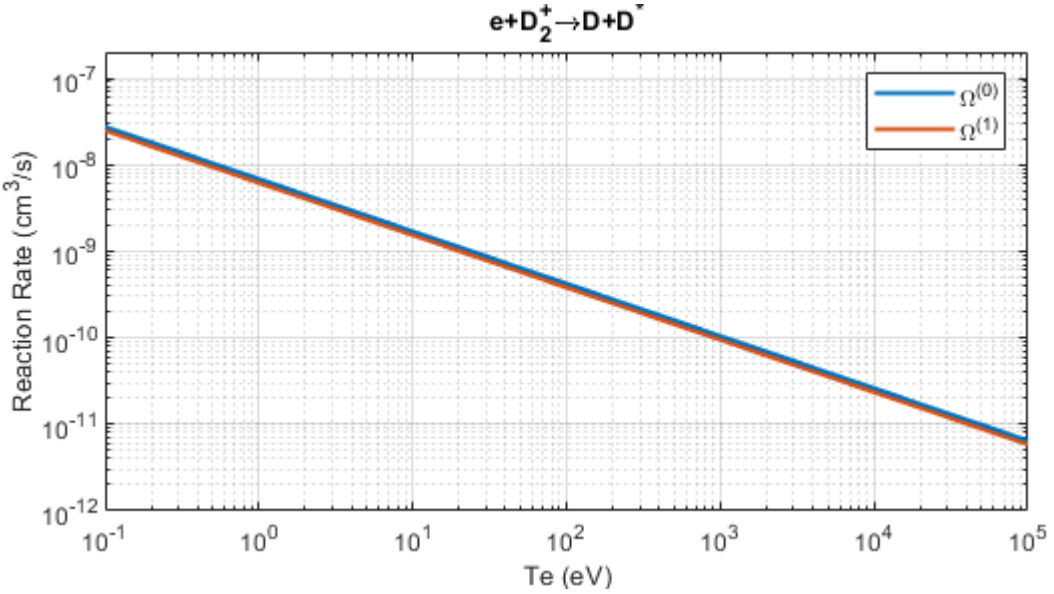

Figure 6.8: Chapman-Cowling collision integral for electron impact dissociative recombination of D_2^+ (EL 8).

6.5.9 (EL 9) Electron Impact Dissociative Recombination: $e + D_3^+ \rightarrow e + D_2 + D$

The electron impact dissociative recombination of the molecular deuterium ion is given as

$$e + D_3^+ \rightarrow D_2 + D \tag{6.114}$$

Note that there is no energy loss potential for this reaction due to the fact there are no threshold energy. For this reaction, the collision operators for e, D, D_2, and D_3^+ can be represented as

$$C_D = 2\frac{m_e C_D^{eD_3^+} + m_{D_3^+} C_D^{D_3^+ e}}{m_e + m_{D_3^+}}$$

$$C_{D_2} = 2\frac{m_e C_{D_2}^{eD_3^+} + m_{D_3^+} C_{D_2}^{D_3^+ e}}{m_e + m_{D_3^+}}$$

$$C_e = -C_e^{eD_3^+}$$

$$C_{D_3^+} = -C_{D_3^+}^{D_3^+ e}$$

A similar procedure as done before for reaction EL1 can be used to obtain the collision terms for the fluid equations for this reaction. After some simplification, the collision terms required for the fluid equations are the followings:

Continuity:

$$\frac{\delta n_{D_3^+}}{\delta t} = \frac{\delta n_e}{\delta t} = -\frac{\delta n_D}{\delta t} = -\frac{\delta n_{D_2}}{\delta t} \approx -8n^2 f_{ti} \Omega_{EL9}^{(0)} \tag{6.116}$$

Momentum:

$$\frac{\delta \mathbf{M}}{\delta t} = -\frac{\delta \mathbf{M}_n}{\delta t} \approx -24n^2 f_{ti} \Omega_{EL9}^{(0)} m\mathbf{u} \tag{6.117a}$$

$$\frac{1}{ne}\frac{\delta \mathbf{M}_e}{\delta t} \approx \frac{16}{3} f_{ti} \frac{m_e}{e^2} \Omega_{EL9}^{(1)} \left(\mathbf{J} - \frac{3}{2} \frac{\Omega_{EL9}^{(0)}}{\Omega_{EL9}^{(1)}} \mathbf{u} \right) \tag{6.117b}$$

Energy:

$$\frac{\delta E}{\delta t} \approx -8n^2 f_{ti} \Omega_{EL9}^{(0)} \left(\frac{3}{2} kT_i + \frac{\Omega_{EL9}^{(1)}}{\Omega_{EL9}^{(0)}} kT_e \right) \tag{6.118a}$$

$$\frac{\delta E_e}{\delta t} \approx -8n^2 f_{ti} \Omega_{EL9}^{(1)} kT_e \tag{6.118b}$$

$$\frac{\delta E_n}{\delta t} \approx 8n^2 f_{ti} \Omega_{EL9}^{(0)} \left(\frac{3}{2} m u_{in}^2 + \frac{3}{2} kT_i + \frac{\Omega_{EL9}^{(1)}}{\Omega_{EL9}^{(0)}} kT_e \right) \tag{6.118c}$$

For the Chapman-Cowling collision integral required for this reaction, the cross-section data compiled by Janev et al. for hydrogen is used [60]. Unfortunately, the cross-section data by Janev does not distinguish between the contribution of the two channels of the dissociative recombination of triatomic hydrogen ions, given as

$$e + H_3^+ \rightarrow H_2 + H \tag{a}$$

and

$$e + H_3^+ \rightarrow H + H + H \qquad \text{(b)}$$

Based on Janev et al., the cross section for the total dissociative recombination for the two channels (a and b) are given well by the following fit [60]:

$$\sigma(E) = \sigma_0 (E/E_0)^{-m}$$

where $\sigma_0 = 6.47 \times 10^{-16}\,\mathrm{cm}^2$, $E_0 = 1\,\mathrm{eV}$, and $m = 0.905$.

The relative dominance of the two dissociative recombination reaction channels are dependent on the impact electron energy. In general, for the low temperature regime, the first channel (a) is more dominant, while for the high temperature regime, the second channel (b) dominates. According to Janev et al., the first channel is favored by roughly 2.5:1 for temperature from 0.1 to 1 eV, while above 1 eV, the theoretical calculations indicates that the second channel is dominant [6].

To obtain a simple partitioning of the reaction path for the dissociative recombination, following simple model is used: for the electron impact energy below 1 eV, it is assumed that the reaction follows the first channel, while for the electron impact energy above 1 eV, it is assumed that all reaction follows the second channel. With this simple model, the cross section for the total electron impact dissociative recombination can be integrated analytically, and one obtains following results for the reaction rates:

$$\Omega_a^{(p)} \approx \sigma_0 \left(\frac{kT_e}{E_0}\right)^{-m} \left[\Gamma(2+p-m) - \Gamma(2+p-m,\, E_0/kT_e)\right] \left(\frac{kT_e}{8\pi m_e}\right)^{1/2}$$

$$\Omega_b^{(p)} \approx \sigma_0 \left(\frac{kT_e}{E_0}\right)^{-m} \Gamma(2+p-m,\, E_0/kT_e) \left(\frac{kT_e}{8\pi m_e}\right)^{1/2}$$

where $\Gamma(s,x)$ is the upper incomplete gamma function. The resulting Chapman-Cowling collision integral for this reaction (channel b) is shown in Fig. 6.9. The resulting Chapman-Cowling collision integral for channel a is given in next sub-section.

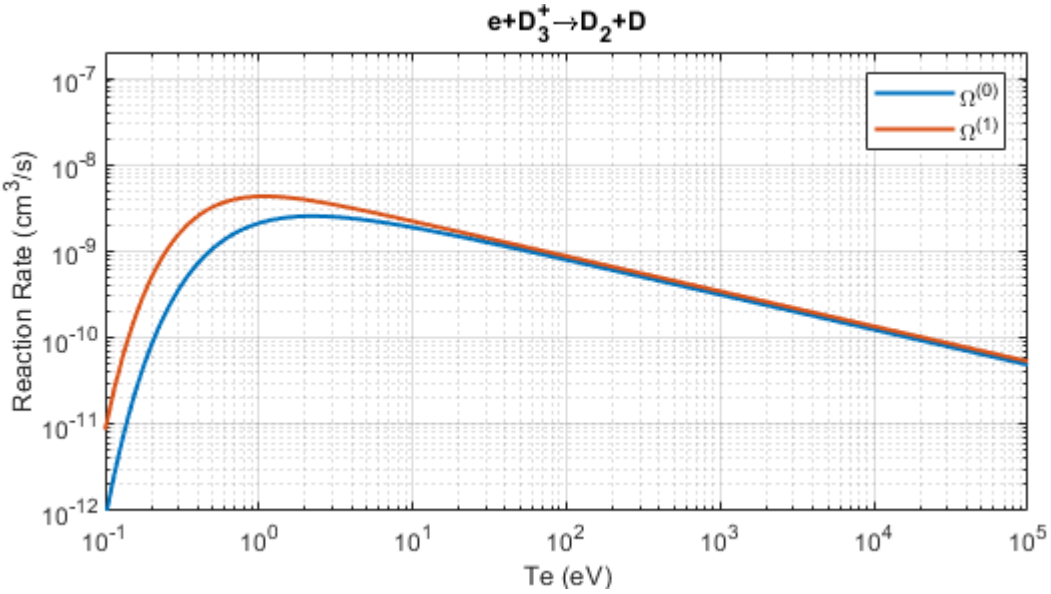

Figure 6.9: Chapman-Cowling collision integral for electron impact dissociative recombination of D_3^+ (EL 9).

6.5.10 (EL 10) Electron Impact Dissociative Recombination: $e + D_3^+ \rightarrow e + D + D + D$

The electron impact dissociative recombination of the molecular deuterium ion is given as

$$e + D_3^+ \rightarrow D + D + D \tag{6.120}$$

Note that there is no energy loss potential for this reaction due to the fact there are no threshold energy. For this reaction, the collision operators for e, D, and D_3^+ can be represented as

$$C_D = 3\frac{m_e C_D^{eD_3^+} + m_{D_3^+} C_D^{D_3^+ e}}{m_e + m_{D_3^+}}$$

$$C_e = -C_e^{eD_3^+}$$

$$C_{D_3^+} = -C_{D_3^+}^{D_3^+ e}$$

A similar procedure as done before for reaction EL 1 can be used to obtain the collision terms for the fluid equations for this reaction. After some simplification, the collision terms required for the fluid equations are the followings:

Continuity:

$$3\frac{\delta n_{D_3^+}}{\delta t} = 3\frac{\delta n_e}{\delta t} = -\frac{\delta n_D}{\delta t} \approx -24n^2 f_{ti}\Omega^{(0)}_{EL10} \tag{6.122}$$

Momentum:

$$\frac{\delta \mathbf{M}}{\delta t} = -\frac{\delta \mathbf{M}_n}{\delta t} \approx -24n^2 f_{ti}\Omega^{(0)}_{EL10} m\mathbf{u} \tag{6.123a}$$

$$\frac{1}{ne}\frac{\delta \mathbf{M}_e}{\delta t} \approx -\frac{16}{3} f_{ti}\frac{m_e}{e^2}\Omega^{(1)}_{EL10}\left(\frac{3}{2}\frac{\Omega^{(0)}_{EL10}}{\Omega^{(1)}_{EL10}} ne\mathbf{u} - \mathbf{J}\right) \tag{6.123b}$$

Energy:

$$\frac{\delta E}{\delta t} \approx -8n^2 f_{ti}\Omega^{(0)}_{EL10}\left(\frac{3}{2}kT_i + \frac{\Omega^{(1)}_{EL10}}{\Omega^{(0)}_{EL10}}kT_e\right) \tag{6.124a}$$

$$\frac{\delta E_e}{\delta t} \approx -8n^2 f_{ti}\Omega^{(1)}_{EL10} kT_e \tag{6.124b}$$

$$\frac{\delta E_n}{\delta t} \approx 8n^2 f_{ti}\Omega^{(0)}_{EL10}\left(\frac{3}{2}mu_{in}^2 + \frac{3}{2}kT_i + \frac{\Omega^{(1)}_{EL10}}{\Omega^{(0)}_{EL10}}kT_e\right) \tag{6.124c}$$

The discussion of the Chapman-Cowling collision integral for this reaction has been covered in the previous sub-section (for reaction EL 9). The resulting Chapman-Cowling collision integral is shown in Fig. 6.10.

6.5.11 (EL 11) Electron Impact Radiative Recombination: $e + D^+ \rightarrow D + h\nu$

The electron impact dissociative recombination of the atomic deuterium ion is given as

$$e + D^+ \rightarrow D + h\nu \tag{6.125}$$

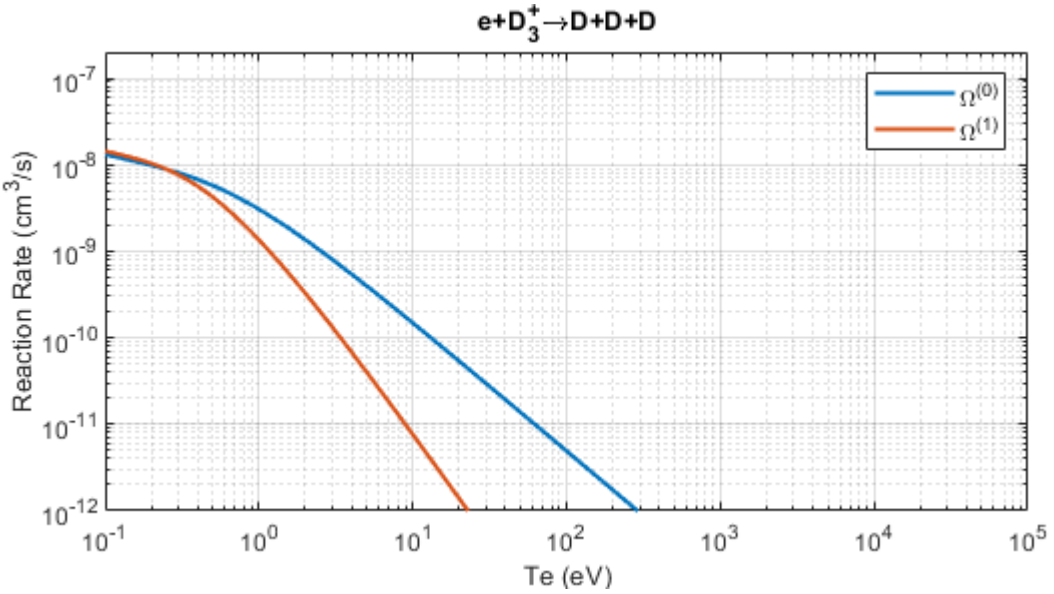

Figure 6.10: Chapman-Cowling collision integral for electron impact dissociative recombination of D_3^+ (EL 10).

Note that there is no energy loss potential for this reaction due to the fact there are no threshold energy. For this reaction, the collision operators for e, D, and D^+ can be represented as

$$C_D = 3\frac{m_e C_D^{eD^+} + m_{D^+} C_D^{D^+e}}{m_e + m_{D^+}}$$
$$C_e = -C_e^{eD^+}$$
$$C_{D^+} = -C_{D^+}^{D^+e}$$

A similar procedure as done before for reaction EL1 can be used to obtain the collision terms for the fluid equations for this reaction. After some simplification, the collision terms required for the fluid equations are the followings:

Continuity:

$$\frac{\delta n_{D^+}}{\delta t} = \frac{\delta n_e}{\delta t} = -\frac{\delta n_D}{\delta t} \approx -8n^2(1 - f_{di} - f_{ti})\Omega^{(0)}_{EL11} \tag{6.127}$$

Momentum:

$$\frac{\delta \mathbf{M}}{\delta t} = -\frac{\delta \mathbf{M}_n}{\delta t} \approx -8n^2(1 - f_{di} - f_{ti})\Omega^{(0)}_{EL11} m\mathbf{u} \tag{6.128a}$$

$$\frac{1}{ne}\frac{\delta \mathbf{M}_e}{\delta t} \approx \frac{16}{3}(1 - f_{di} - f_{ti})\frac{m_e}{e^2}\Omega^{(1)}_{EL11}\left(\mathbf{J} - \frac{3}{2}\frac{\Omega^{(0)}_{EL11}}{\Omega^{(1)}_{EL11}} ne\mathbf{u}\right) \tag{6.128b}$$

Energy:

$$\frac{\delta E}{\delta t} \approx -8n^2(1 - f_{di} - f_{ti})\Omega^{(0)}_{EL11}\left(\frac{3}{2}kT_i + \frac{\Omega^{(1)}_{EL11}}{\Omega^{(0)}_{EL11}}kT_e\right) \tag{6.129a}$$

$$\frac{\delta E_e}{\delta t} \approx -8n^2(1 - f_{di} - f_{ti})\Omega^{(1)}_{EL11}kT_e \tag{6.129b}$$

$$\frac{\delta E_n}{\delta t} \approx 8n^2(1 - f_{di} - f_{ti})\Omega^{(0)}_{EL11}\left(\frac{1}{2}mu^2_{in} + \frac{3}{2}kT_i + \frac{\Omega^{(1)}_{EL11}}{\Omega^{(0)}_{EL11}}kT_e\right) \tag{6.129c}$$

For the Chapman-Cowling collision integral required for this reaction, the analytic formula for the reaction rate of the radiative recombination by Sobelman is used [77]. The analytical formula by Sobelman is of form

$$\langle \sigma_r v_e \rangle = 10^{-14} A Q_r \left|\frac{E_{\gamma 0}}{Ry}\right|^{1/2} \frac{\beta^{3/2}}{\beta + \chi}\,(\mathrm{cm}^3/\mathrm{s})$$

where the parameters A and χ are the fit parameter that depends on the atom and the final recombined state, $\beta = |E_{\gamma 0}|/kT_e$, $E_{\gamma 0}$ is the energy of the final recombined energy level, and Q_r is the factor that depends on quantum numbers of angular momenta; for hydrogen recombining to $1s$ final state, $Q_r = 1$, $A = 3.92$, $\chi = 0.35$, and $|E_{\gamma 0}| = Ry$ [13]. Using the relationship between the reaction rate and the Chapman-Cowling collision integral, $\langle \sigma_r v_e \rangle = 8\Omega^{(0)}$, the zeroth Chapman-Cowling collision integral for this reaction can

be expressed as the following

$$\Omega^{(0)}_{HP11} = (0.49 \times 10^{-14}) \frac{\beta^{3/2}}{\beta + 0.35} \, (\mathrm{cm}^3/\mathrm{s})$$

For the first Chapman-Cowling collision integral, one can consider the analytical form of the cross section for radiative recombination given by Sobelman of the form

$$\sigma_r = 10^{-6} \pi a_0^2 Q_r \frac{\Phi(u)}{u}$$

where $u = E/\left|E_{\gamma 0}\right|$, E is the initial energy of the electron, a_0 is the Bohr radius, and $\Phi(u)$ is a correction factor that depends on the atom, final energy level, and initial electron energy [13]. The tabulated values of $\Phi(u)$ for hydrogen atom with the final recombined state of $1s$ can be found in Sobelman [77]. A more general form of the radiative recombination cross section based on quantum mechanics and be found in the text of Sobelman [77] and Sobelman et al. [78], but a simpler form of the effective radiative recombination cross section is used here.

By using the tabulated values of $\Phi(u)$ and interpolating, the cross section can be numerically integrated to obtain the first Chapman-Cowling collision integral for this reaction. The resulting Chapman-Cowling collision integral is shown in Fig. 6.11.

6.5.12 (EL 12) Electron Elastic Scattering with Atomic Deuterium Neutral

While not technically a reaction, electron impact scattering processes with the atomic deuterium neutrals is not well approximated by the hard sphere collision process. Instead, the electron impact momentum transfer cross section recommended by Itikawa [79] for hydrogen is used to approximate the electron elastic scattering cross section. For the elastic scattering of electrons with neutrals, the required collision integral is that of the momentum transfer that corresponds to the first Chapman-Cowling collision integral. The high energy extrapolation is made by fitting a linear line at the tail of the cross-section in the log-space. The

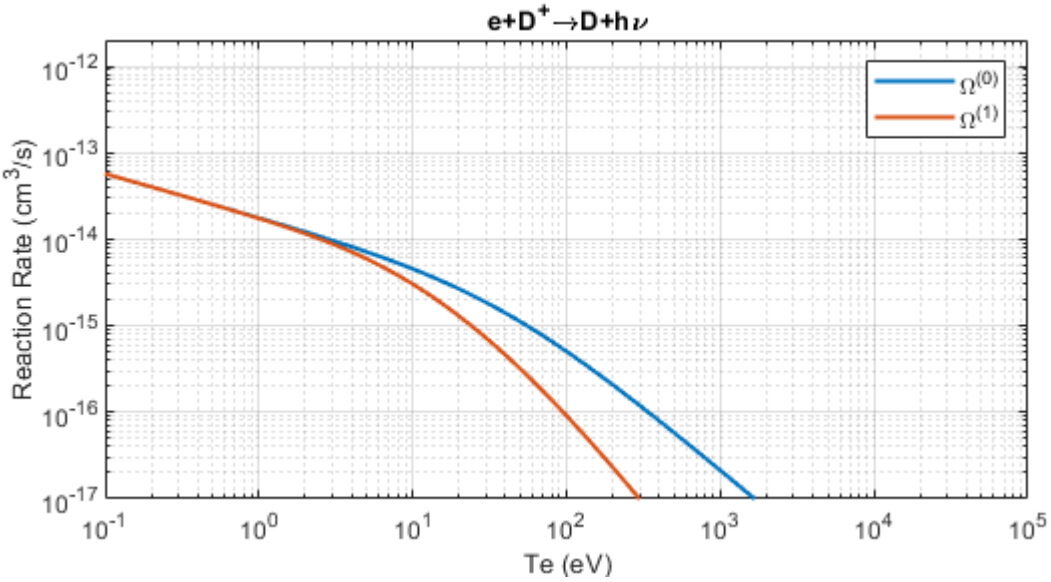

Figure 6.11: Chapman-Cowling collision integral for electron impact radiative recombination of D^+ (EL 11).

resulting Chapman-Cowling collision integral after numerical integration of the cross-section data is shown in Fig. 6.12.

6.5.13 (EL 13) Electron Elastic Scattering with Molecular Deuterium Neutral

While not technically a reaction, the electron impact scattering process with the diatomic deuterium neutrals is not well approximated by the hard sphere collision process. Instead, the electron impact momentum transfer cross section recommended by Yoon et al. [74] for hydrogen molecule is used to approximate the electron elastic scattering cross section. For the elastic scattering of electrons with neutrals, the required collision integral is that of the momentum transfer that corresponds to the first Chapman-Cowling collision integral. The high energy extrapolation is made by fitting a linear line at the tail of the cross-section in the log-space. The resulting Chapman-Cowling collision integral after numerical integration of the cross-section data is shown in Fig. 6.13.

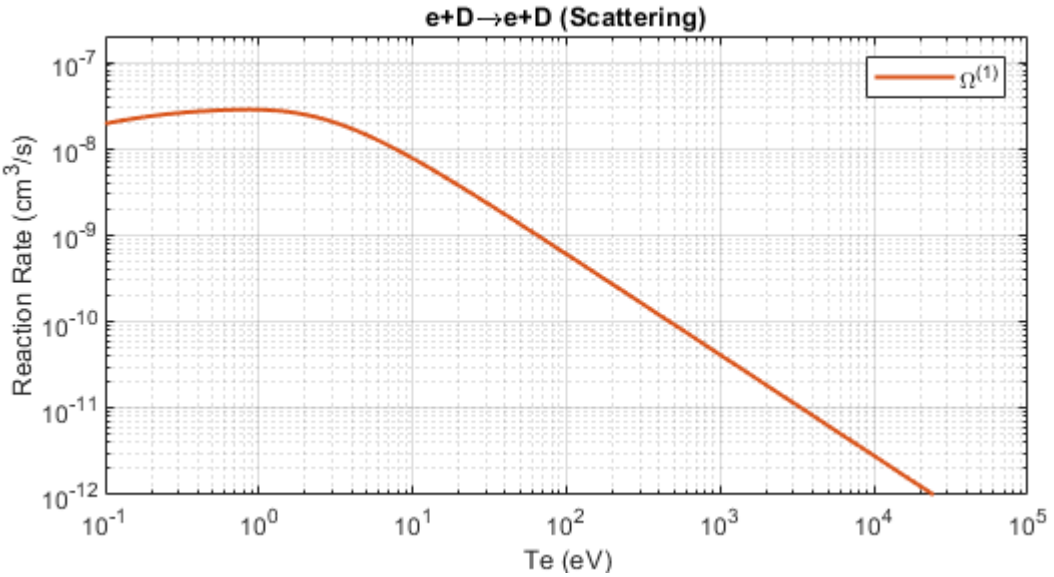

Figure 6.12: Chapman-Cowling collision integral for electron elastic scattering for D (EL 12).

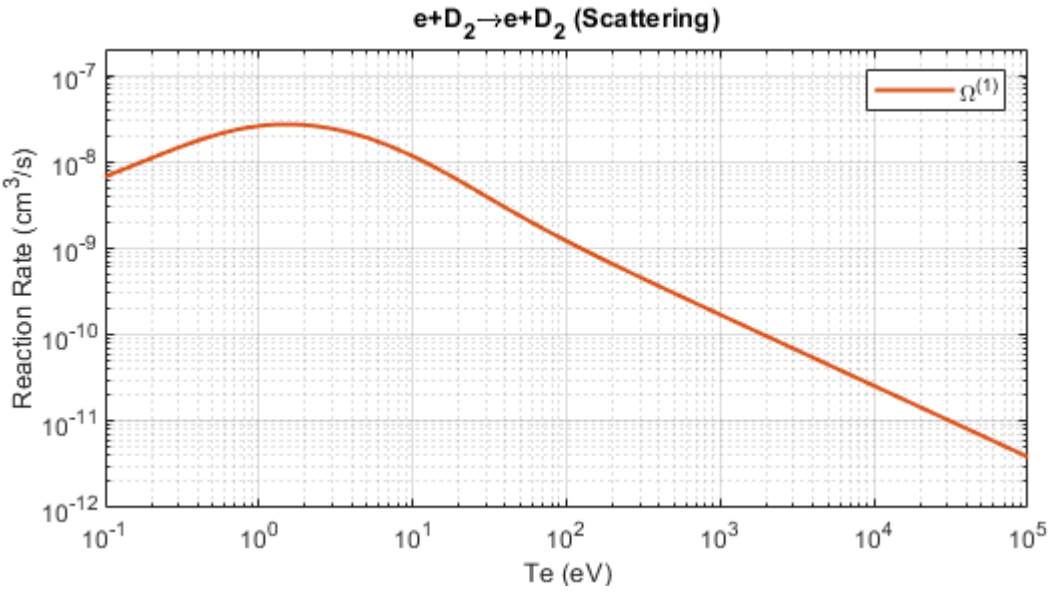

Figure 6.13: Chapman-Cowling collision integral for electron elastic scattering for D_2 (EL 13).

6.6 Specific Form of the Collision Integral for the Heavy Particle Impact Reactions

A specific form of the collision integrals for the heavy particle reactions considered in this model is covered in this section.

6.6.1 (HP 1) Heavy Particle Charge Exchange: $D^+ + D \rightarrow D + D^+$

The resonant charge exchange between atomic deuterium ions and atomic deuterium neutrals is given as

$$D^+ + D \rightarrow D + D^+ \tag{6.130}$$

For this reaction, the collision operators for D, and D^+ can be represented as

$$C_{D^+} = \frac{m_{D^+} C_{D^+}^{D^+D} + m_D C_{D^+}^{DD^+}}{m_{D^+} + m_D} - C_{D^+}^{D^+D}$$
$$C_D = \frac{m_{D^+} C_D^{D^+D} + m_D C_D^{DD^+}}{m_{D^+} + m_D} - C_D^{DD^+}$$

After some simplification, the collision term required for the fluid equations from this reaction are the following:

Continuity:

$$\frac{\delta n_{D^+}}{\delta t} = \frac{\delta n_D}{\delta t} = 0 \tag{6.132}$$

Momentum:

$$\frac{\delta \mathbf{M}}{\delta t} = -\frac{\delta \mathbf{M}_n}{\delta t} \approx -\frac{8}{3}(1 - f_{di} - f_{ti})(1 - f_{dn}) n n_n \overline{\Omega}_{HP1}^{(1)} m \mathbf{u}_{in} \tag{6.133}$$

Energy:

$$\frac{\delta E}{\delta t} = \frac{4}{3}(1-f_{di}-f_{ti})(1-f_{dn})nn_n\Bigg\{3k(T_n-T_i)\Bigg[\left(1-\frac{2}{3}\lambda_{DD^+}\right)\overline{\Omega}^{(1)}_{HP1} + \frac{4}{15}\lambda_{DD^+}\overline{\Omega}^{(2)}_{HP1}\Bigg] + mu_{in}^2\overline{\Omega}^{(1)}_{HP1}\Bigg\} \tag{6.134a}$$

$$\frac{\delta E}{\delta t} = -\frac{4}{3}(1-f_{di}-f_{ti})(1-f_{dn})nn_n\Bigg\{3k(T_n-T_i)\Bigg[\left(1-\frac{2}{3}\lambda_{DD^+}\right)\overline{\Omega}^{(1)}_{HP1} + \frac{4}{15}\lambda_{DD^+}\overline{\Omega}^{(2)}_{HP1}\Bigg] - mu_{in}^2\overline{\Omega}^{(1)}_{HP1}\Bigg\} \tag{6.134b}$$

For the generalized collision integral required for this reaction, the analytical fit for the cross section from Ito et al. [80] for hydrogen is used. Because the fit function behaves normally in both the low energy region and high energy tail, the fit function is used to extrapolate in both low energy and high energy region for numerical integration. The resulting generalized collision integral after the numerical integration of the cross-section data is shown in Fig. 6.14–6.16 for the zeroth, first, and second collision integral.

6.6.2 (HP 2) Heavy Particle Charge Exchange: $D^+ + D_2 \rightarrow D + D_2^+$

The non-resonant charge exchange between atomic deuterium ions and diatomic deuterium neutrals is given as

$$D^+ + D_2 \rightarrow D + D_2^+ - \phi_{HP2} \tag{6.135}$$

where ϕ_{HP2} is the effective threshold potential for the non-resonant charge exchange process that includes both the threshold energy of 2.5 eV as well as additional losses from excitation reaction from atomic deuterium ions colliding with diatomic deuterium neutrals. For this

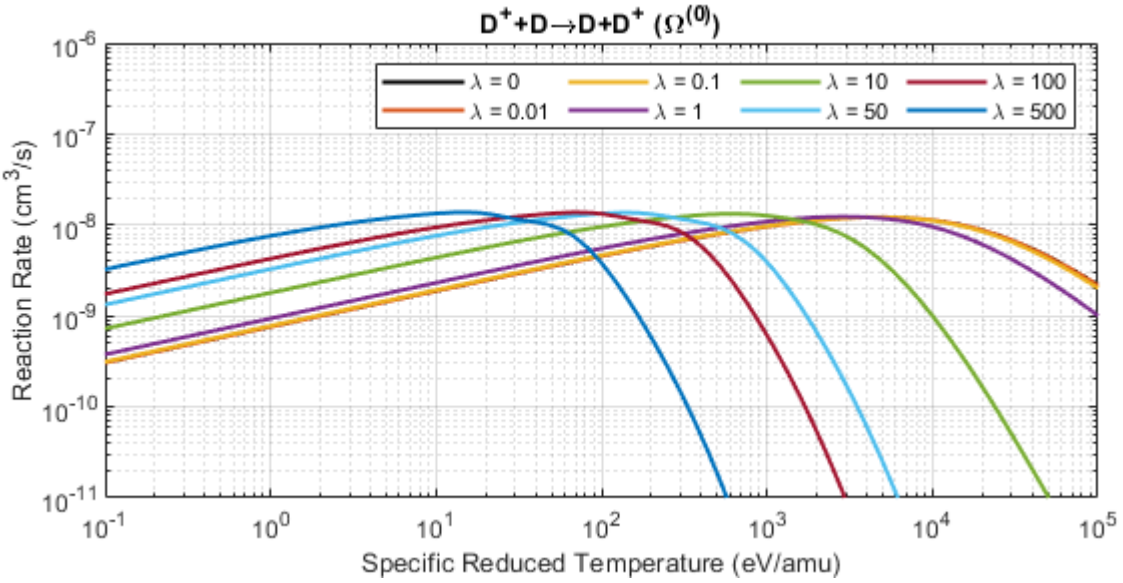

Figure 6.14: Zeroth generalized collision integral $\overline{\Omega}^{(0)}$ for resonant charge exchange of D^+ (HP 1).

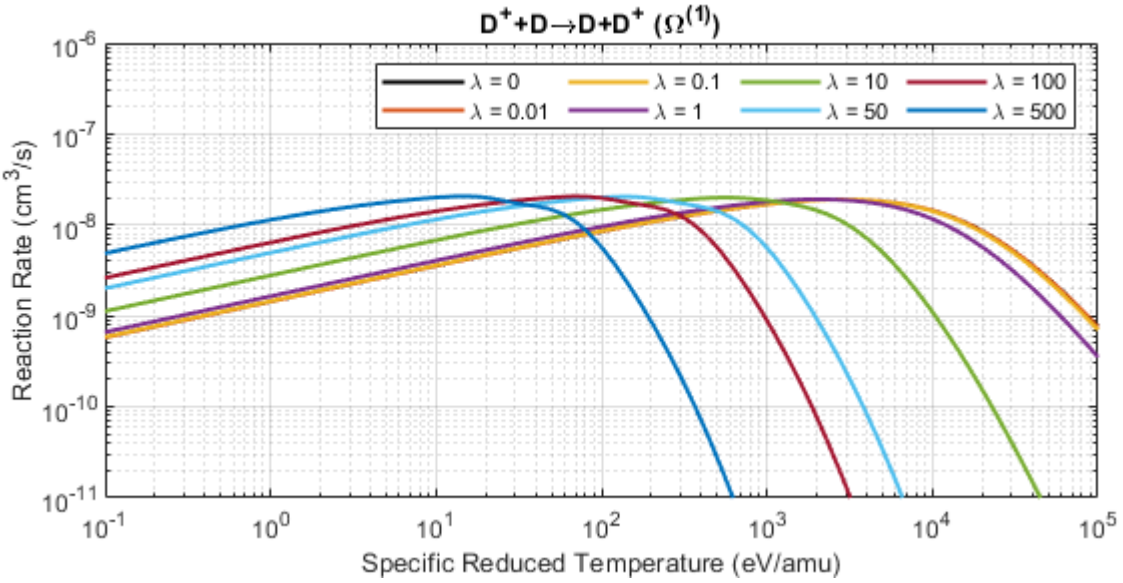

Figure 6.15: First generalized collision integral $\overline{\Omega}^{(1)}$ for resonant charge exchange of D^+ (HP 1).

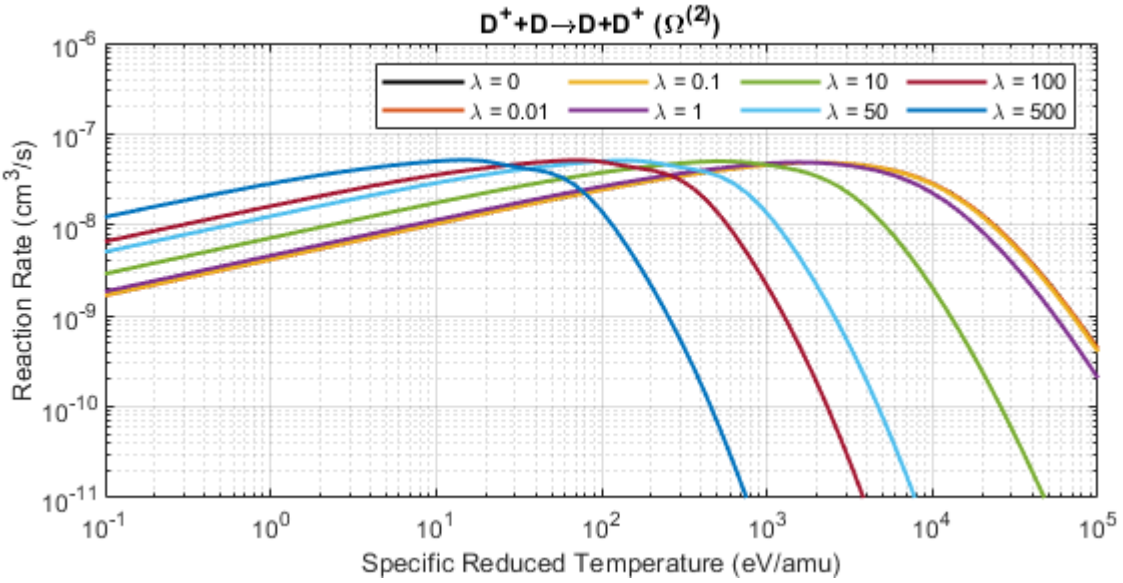

Figure 6.16: Second generalized collision integral $\overline{\Omega}^{(2)}$ for resonant charge exchange of D^+ (HP 1).

reaction, the collision operators for D, D_2, D^+ and D_2^+ can be represented as

$$
\begin{aligned}
C_{D^+} &= -C_{D^+}^{D^+D_2} \\
C_{D_2^+} &= \frac{m_{D^+}C_{D_2^+}^{D^+D_2} + m_{D_2}C_{D_2^+}^{D_2D^+}}{m_{D^+} + m_{D_2}} \\
C_D &= \frac{m_{D^+}C_D^{D^+D_2} + m_{D_2}C_D^{D_2D^+}}{m_{D^+} + m_{D_2}} \\
C_{D_2} &= -C_{D_2}^{D_2D^+}
\end{aligned}
$$

After some simplification, the collision term required for the fluid equations from this reaction are the following:

Continuity:

$$\frac{\delta n_{D^+}}{\delta t} = -\frac{\delta n_{D_2^+}}{\delta t} = -\frac{\delta n_D}{\delta t} = \frac{\delta n_{D_2}}{\delta t} = -8(1 - f_{di} - f_{ti}) f_{dn} n n_n \overline{\Omega}_{HP2}^{(0)} \tag{6.137}$$

Momentum:

$$\frac{\delta \mathbf{M}}{\delta t} = -\frac{\delta \mathbf{M}_n}{\delta t} \approx \frac{8}{3}(1 - f_{di} - f_{ti}) f_{dn} n n_n \overline{\Omega}^{(0)}_{HP2} m (4\mathbf{u}_n - \mathbf{u}) - \frac{32}{9}(1 - f_{di} - f_{ti}) f_{dn} n n_n \left(\overline{\Omega}^{(1)}_{HP2} - \frac{3}{2}\overline{\Omega}^{(0)}_{HP2} \right) \frac{T_i + 2T_n}{2T_i + T_n} m \mathbf{u}_{in} \quad (6.138)$$

Energy:

$$\frac{\delta E}{\delta t} = (1 - f_{di} - f_{ti}) f_{dn} n n_n \Bigg\{ 12 \frac{k T_i T_n}{2T_i + T_n} \overline{\Omega}^{(0)}_{HP2} - 4\overline{\Omega}^{(0)}_{HP2} \phi_{HP2} + \frac{16}{3} m u_{in}^2 \left[\frac{2}{3}\overline{\Omega}^{(1)}_{HP2} + \frac{T_i^2}{(2T_i + T_n)^2} \left(3\overline{\Omega}^{(0)}_{HP2} - 2\overline{\Omega}^{(1)}_{HP2} \right) \right] + \frac{16}{3} \frac{T_i + T_n}{2T_i + T_n} k (T_n - T_i) \left[\left(1 - \frac{2}{3}\lambda_{D_2 D^+} \right) \overline{\Omega}^{(1)}_{HP2} + \frac{4}{15}\overline{\Omega}^{(2)}_{HP2} \lambda_{D_2 D^+} \right] \Bigg\} \quad (6.139a)$$

$$\frac{\delta E_n}{\delta t} = -(1 - f_{di} - f_{ti}) f_{dn} n n_n \Bigg\{ 12 \frac{k T_i T_n}{2T_i + T_n} \overline{\Omega}^{(0)}_{HP2} + 4\overline{\Omega}^{(0)}_{HP2} \phi_{HP2} - \frac{4}{3} m u_{in}^2 \left[\frac{2}{3}\overline{\Omega}^{(1)}_{HP2} - \frac{T_n^2}{(2T_i + T_n)^2} \left(3\overline{\Omega}^{(0)}_{HP2} - 2\overline{\Omega}^{(1)}_{HP2} \right) \right] + \frac{16}{3} \frac{T_i + T_n}{2T_i + T_n} k (T_n - T_i) \left[\left(1 - \frac{2}{3}\lambda_{D_2 D^+} \right) \overline{\Omega}^{(1)}_{HP2} + \frac{4}{15}\overline{\Omega}^{(2)}_{HP2} \lambda_{D_2 D^+} \right] \Bigg\} \quad (6.139b)$$

For the generalized collision integral required for this reaction, the analytical fit for the cross section from Tabata and Shirai [81] for hydrogen is used. No low energy extrapolation is required for this reaction due to presence of the threshold energy at 2.5 eV. The high energy extrapolation is made by fitting a linear line at the tail of the cross-section tail in the log-space. The resulting generalized collision integral after numerical integration of the cross-section data is shown in Fig. 6.17–6.19 for the zeroth, first, and second collision integral.

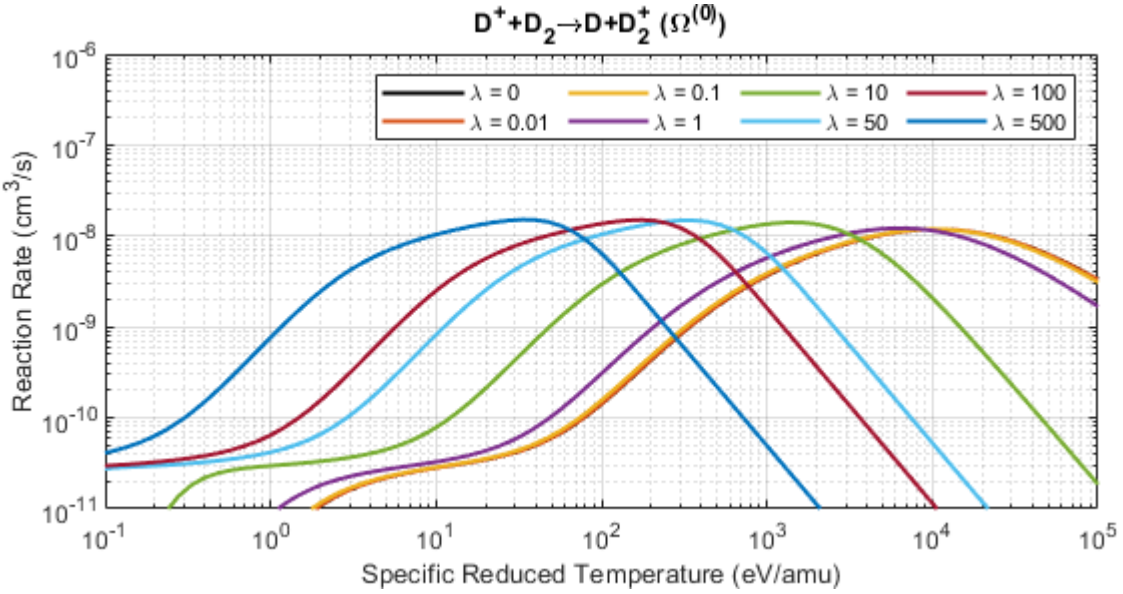

Figure 6.17: Zeroth generalized collision integral $\overline{\Omega}^{(0)}$ for non-resonant charge exchange of D^+ (HP 2).

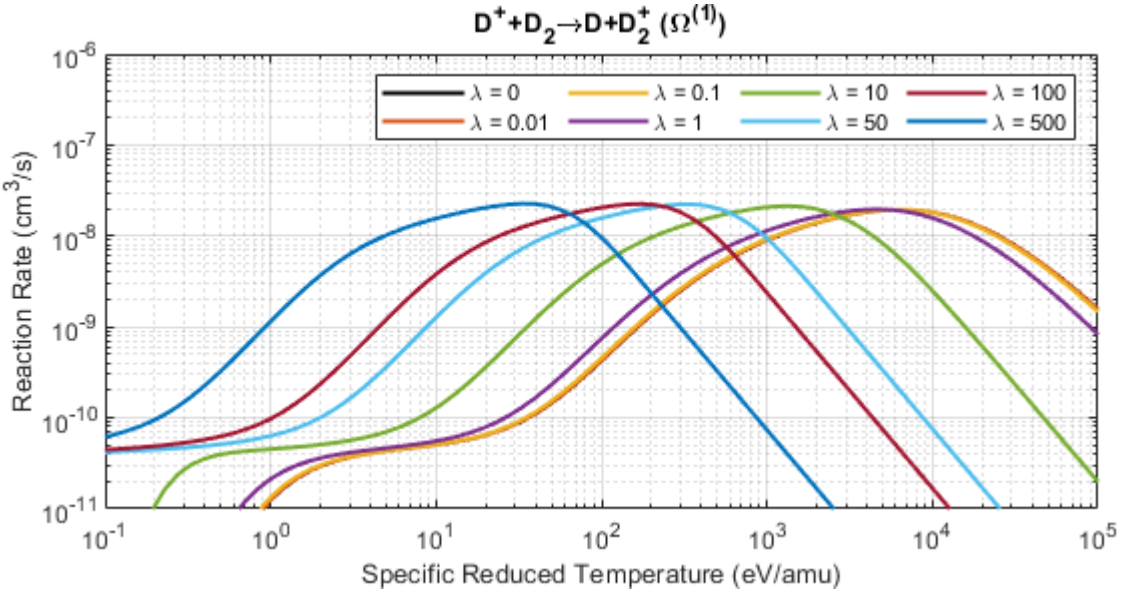

Figure 6.18: First generalized collision integral $\overline{\Omega}^{(1)}$ for non-resonant charge exchange of D^+ (HP 2).

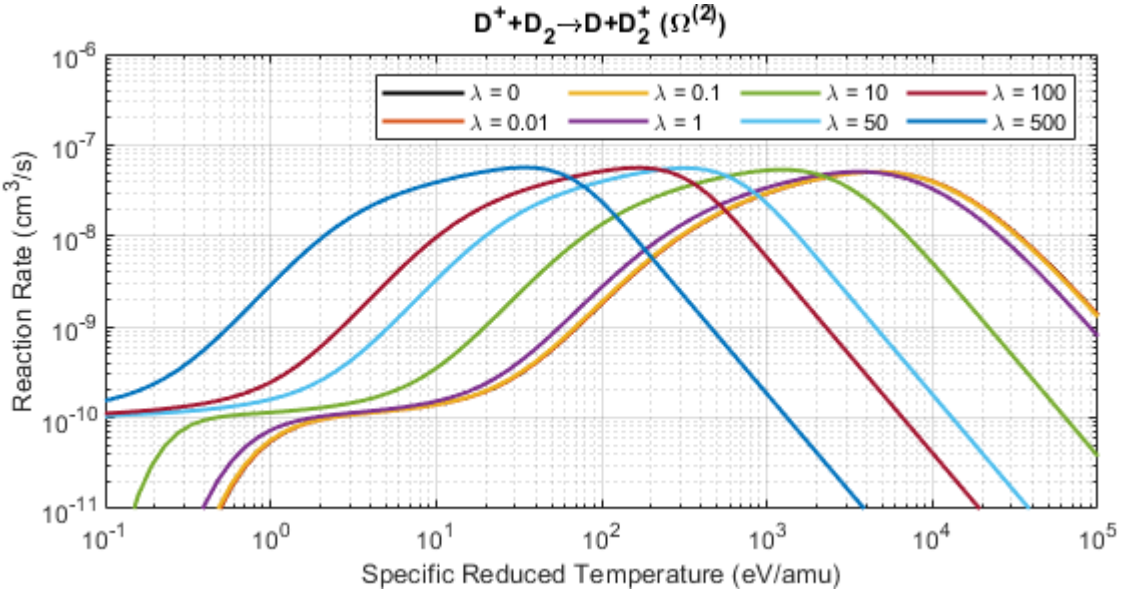

Figure 6.19: Second generalized collision integral $\overline{\Omega}^{(2)}$ for non-resonant charge exchange of D^+ (HP 2).

6.6.3 (HP 3) Heavy Particle Charge Exchange: $D_2^+ + D \rightarrow D_2 + D^+$

The quasi-resonant charge exchange between diatomic deuterium ions and atomic deuterium neutrals is given as

$$D_2^+ + D \rightarrow D_2 + D^+ - \phi_{HP3} \tag{6.140}$$

where $\phi_{HP3} = -2.5$ eV is the exothermic energy release from the reaction. For this reaction, the collision operators for D, D_2, D^+ and D_2^+ can be represented as

$$\begin{aligned}
C_{D^+} &= \frac{m_{D_2^+} C_{D^+}^{D_2^+ D} + m_D C_{D^+}^{D D_2^+}}{m_{D_2^+} + m_D} \\
C_{D_2^+} &= -C_{D_2^+}^{D_2^+ D} \\
C_D &= -C_D^{D D_2^+} \\
C_{D_2} &= \frac{m_{D_2^+} C_{D_2}^{D_2^+ D} + m_D C_{D_2}^{D D_2^+}}{m_{D_2^+} + m_D}
\end{aligned}$$

After some simplification, the collision term required for the fluid equations from this reaction are the following:

Continuity:

$$\frac{\delta n_{D^+}}{\delta t} = -\frac{\delta n_{D_2^+}}{\delta t} = -\frac{\delta n_D}{\delta t} = \frac{\delta n_{D_2}}{\delta t} = 8 f_{di}(1-f_{dn}) n n_n \overline{\Omega}^{(0)}_{HP3} \tag{6.142}$$

Momentum:

$$\frac{\delta \mathbf{M}}{\delta t} = -\frac{\delta \mathbf{M}_n}{\delta t} \approx -\frac{8}{3} f_{di}(1-f_{dn}) n n_n m \Bigg[\overline{\Omega}^{(0)}_{HP3}(4\mathbf{u} - \mathbf{u}_n) + \frac{4}{3}\left(\overline{\Omega}^{(1)}_{HP3} - \frac{3}{2}\overline{\Omega}^{(0)}_{HP3}\right)\frac{2T_i + T_n}{T_i + 2T_n}\mathbf{u}_{in}\Bigg] \tag{6.143}$$

Energy:

$$\begin{aligned}\frac{\delta E}{\delta t} = &-f_{di}(1-f_{dn}) n n_n \Bigg\{ 12\frac{kT_iT_n}{T_i+2T_n}\overline{\Omega}^{(0)}_{HP3} + 4\overline{\Omega}^{(0)}_{HP3}\phi_{HP3} \\ &- \frac{4}{3} m u_{in}^2 \left[\frac{2}{3}\overline{\Omega}^{(1)}_{HP3} - \frac{T_i^2}{(T_i+2T_n)^2}\left(3\overline{\Omega}^{(0)}_{HP3} - 2\overline{\Omega}^{(1)}_{HP3}\right)\right] \\ &- \frac{16}{3}\frac{T_i+T_n}{T_i+2T_n} k(T_n - T_i)\left[\left(1 - \frac{2}{3}\lambda_{D_2D^+}\right)\overline{\Omega}^{(1)}_{HP3} + \frac{4}{15}\overline{\Omega}^{(2)}_{HP3}\lambda_{D_2D^+}\right]\Bigg\}\end{aligned} \tag{6.144a}$$

$$\begin{aligned}\frac{\delta E_n}{\delta t} = &\; f_{di}(1-f_{dn}) n n_n \Bigg\{ 12\frac{kT_iT_n}{T_i+2T_n}\overline{\Omega}^{(0)}_{HP3} - 4\overline{\Omega}^{(0)}_{HP3}\phi_{HP3} \\ &+ \frac{16}{3} m u_{in}^2 \left[\frac{2}{3}\overline{\Omega}^{(1)}_{HP3} + \frac{T_n^2}{(T_i+2T_n)^2}\left(3\overline{\Omega}^{(0)}_{HP3} - 2\overline{\Omega}^{(1)}_{HP3}\right)\right] \\ &- \frac{16}{3}\frac{T_i+T_n}{T_i+2T_n} k(T_n - T_i)\left[\left(1 - \frac{2}{3}\lambda_{D_2D^+}\right)\overline{\Omega}^{(1)}_{HP3} + \frac{4}{15}\overline{\Omega}^{(2)}_{HP3}\lambda_{D_2D^+}\right]\Bigg\}\end{aligned} \tag{6.144b}$$

For the generalized collision integral required for this reaction, the analytical fit for the cross section from Ito et al. [80] for hydrogen is used. Because the fit function behaves normally in both the low energy region and high energy tail, the fit function is used to extrapolate in both low energy and high energy region for numerical integration. The resulting generalized collision integral after numerical integration of the cross-section data is shown in

Fig. 6.20–6.22 for the zeroth, first, and second collision integral.

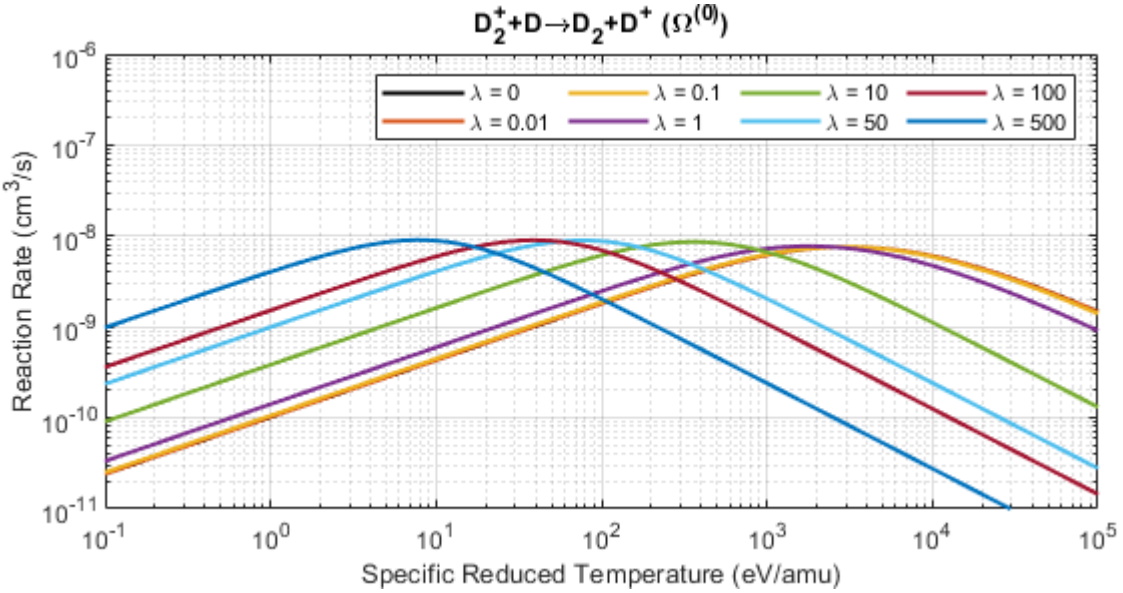

Figure 6.20: Zeroth generalized collision integral $\overline{\Omega}^{(0)}$ for quasi-resonant charge exchange of D_2^+ (HP 3).

6.6.4 (HP 4) Heavy Particle Charge Exchange: $D_2^+ + D_2 \rightarrow D_2 + D_2^+$

The resonant charge exchange between diatomic deuterium ions and diatomic deuterium neutrals is given as

$$D_2^+ + D_2 \rightarrow D_2 + D_2^+ \tag{6.145}$$

For this reaction, the collision operators for D_2, and D_2^+ can be represented as

$$C_{D_2^+} = \frac{m_{D_2^+} C_{D_2^+}^{D_2^+ D_2} + m_{D_2} C_{D_2^+}^{D_2 D_2^+}}{m_{D_2^+} + m_{D_2}} - C_{D_2^+}^{D_2^+ D_2}$$

$$C_{D_2} = \frac{m_{D_2^+} C_{D_2}^{D_2^+ D_2} + m_{D_2} C_{D_2}^{D_2 D_2^+}}{m_{D_2^+} + m_{D_2}} - C_{D_2}^{D_2 D_2^+}$$

After some simplification, the collision term required for the fluid equations from this

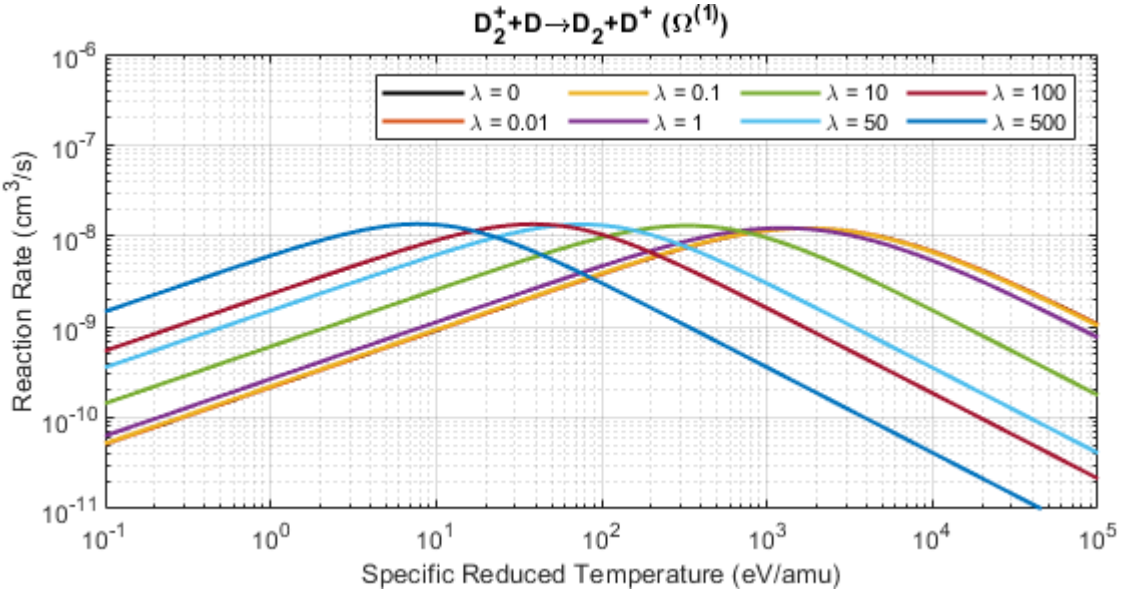

Figure 6.21: First generalized collision integral $\overline{\Omega}^{(1)}$ for quasi-resonant charge exchange of D_2^+ (HP 3).

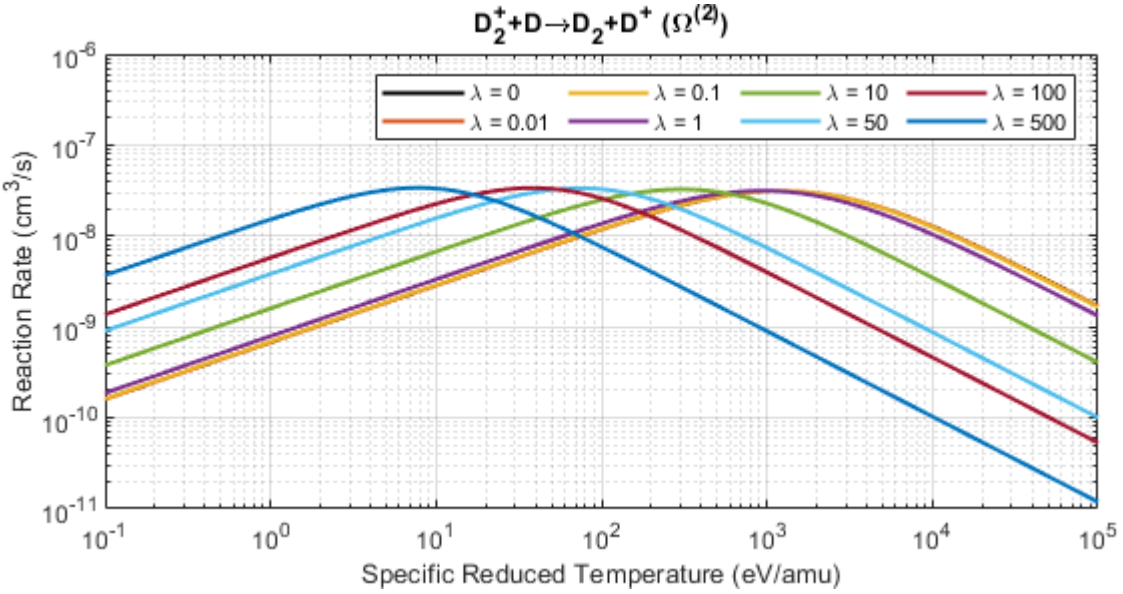

Figure 6.22: Second generalized collision integral $\overline{\Omega}^{(2)}$ for quasi-resonant charge exchange of D_2^+ (HP 3).

reaction are the following:

Continuity:

$$\frac{\delta n_{D_2^+}}{\delta t} = \frac{\delta n_{D_2}}{\delta t} = 0 \tag{6.147}$$

Momentum:

$$\frac{\delta \mathbf{M}}{\delta t} = -\frac{\delta \mathbf{M}_n}{\delta t} \approx -\frac{16}{3} f_{di} f_{dn} n n_n \overline{\Omega}^{(1)}_{HP4} m \mathbf{u}_{in} \tag{6.148}$$

Energy:

$$\begin{aligned}\frac{\delta E}{\delta t} = \frac{4}{3} f_{di} f_{dn} n n_n \Bigg\{ & 3k(T_n - T_i) \left[\left(1 - \frac{2}{3} \lambda_{D_2 D_2^+} \right) \overline{\Omega}^{(1)}_{HP1} + \frac{4}{15} \lambda_{D_2 D_2^+} \overline{\Omega}^{(2)}_{HP1} \right] \\ & + 2 m u_{in}^2 \overline{\Omega}^{(1)}_{HP1} \Bigg\}\end{aligned} \tag{6.149a}$$

$$\begin{aligned}\frac{\delta E}{\delta t} = -\frac{4}{3} f_{di} f_{dn} n n_n \Bigg\{ & 3k(T_n - T_i) \left[\left(1 - \frac{2}{3} \lambda_{D_2 D_2^+} \right) \overline{\Omega}^{(1)}_{HP1} + \frac{4}{15} \lambda_{D_2 D_2^+} \overline{\Omega}^{(2)}_{HP1} \right] \\ & - 2 m u_{in}^2 \overline{\Omega}^{(1)}_{HP1} \Bigg\}\end{aligned} \tag{6.149b}$$

For the generalized collision integral required for this reaction, the analytical fit for the cross section from Tabata and Shirai [81] for hydrogen is used. Because the fit function behaves normally in the low energy region, the fit function is used to extrapolate in the low energy region for numerical integration. For the high energy tail, while the fit function behaves normally, the resulting cross section begins to diverge from the theoretically expected cross section for resonant charge exchange. As such, the tail is approximated by cutting off the fit function and transitioning to a linear fit in the log-space. The resulting generalized collision integral after numerical integration of the cross-section data is shown in Fig. 6.23–6.25 for the zeroth, first, and second collision integral.

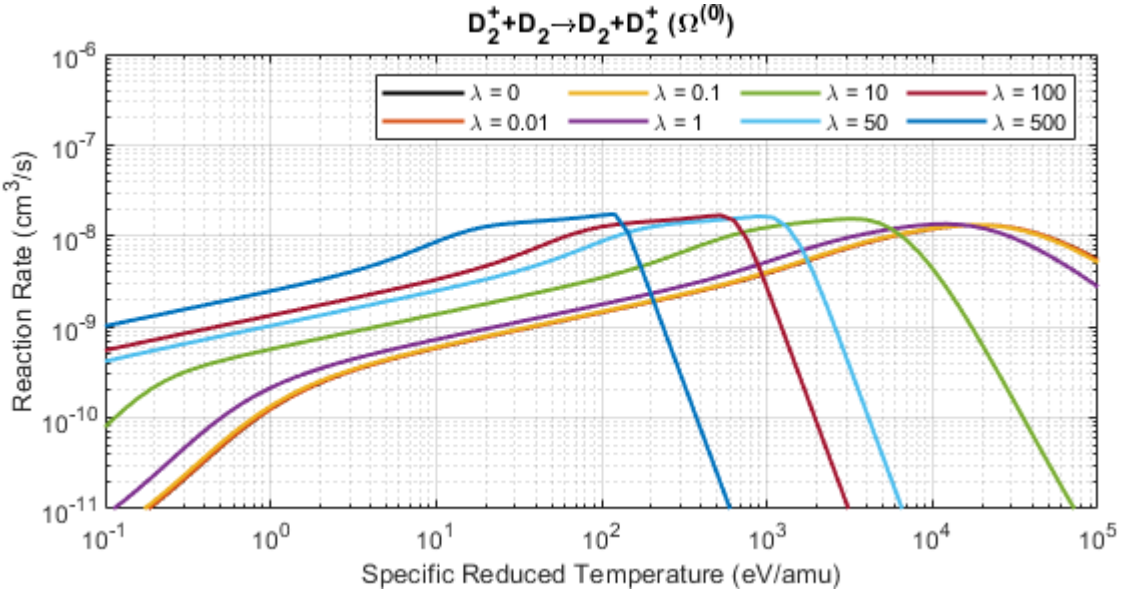

Figure 6.23: Zeroth generalized collision integral $\overline{\Omega}^{(0)}$ for resonant charge exchange of D_2^+ (HP 4).

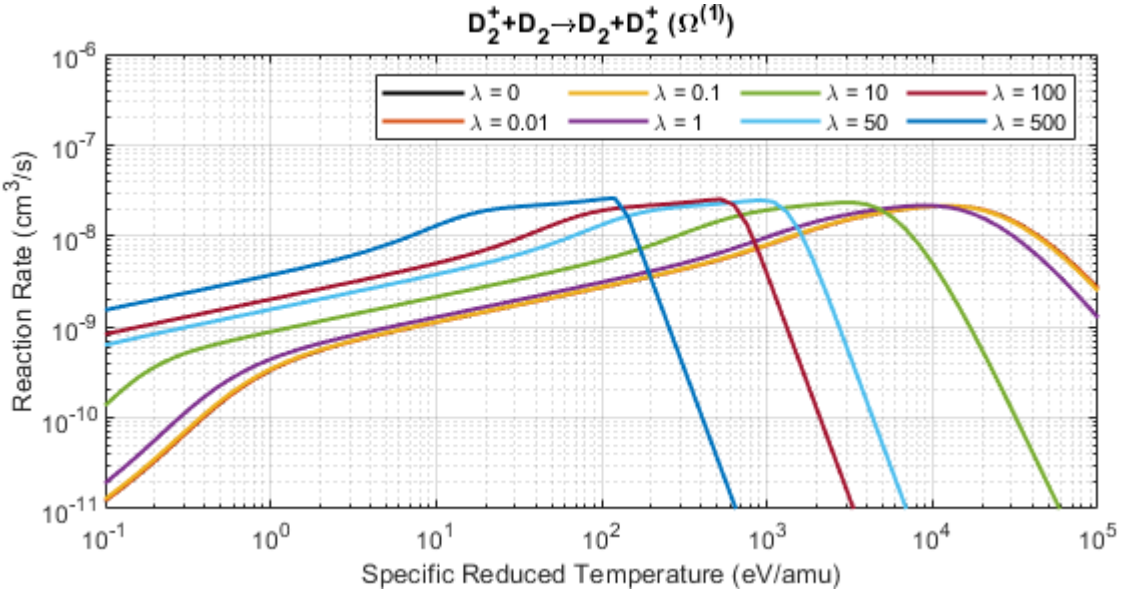

Figure 6.24: First generalized collision integral $\overline{\Omega}^{(1)}$ for resonant charge exchange of D_2^+ (HP 4).

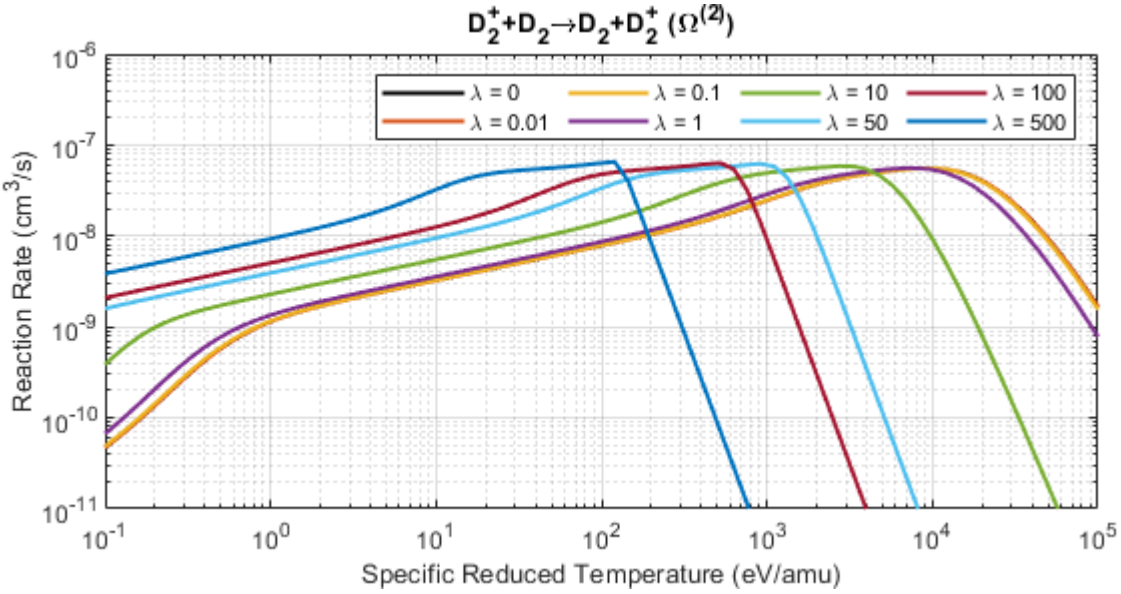

Figure 6.25: Second generalized collision integral $\overline{\Omega}^{(2)}$ for resonant charge exchange of D_2^+ (HP 4).

6.6.5 (HP 5) Triatomic Deuterium Production: $D_2^+ + D_2 \rightarrow D_3^+ + D$

The triatomic deuterium ion production due to interaction between diatomic deuterium ions and diatomic deuterium neutrals is given as

$$D_2^+ + D_2 \rightarrow D_3^+ + D - \phi_{HP5} \tag{6.150}$$

where $\phi_{HP5} = 1.17$ eV is the exothermic energy release from the reaction. For this reaction, the collision operators for D, D_2, D_2^+, and D_3^+ can be represented as

$$\begin{aligned} C_{D_2^+} &= -C_{D_2^+}^{D_2^+ D_2} \\ C_{D_3^+} &= \frac{m_{D_2^+} C_{D_3^+}^{D_2^+ D_2} + m_{D_2} C_{D_3^+}^{D_2 D_2^+}}{m_{D_2^+} + m_{D_2}} \\ C_D &= \frac{m_{D_2^+} C_D^{D_2^+ D_2} + m_{D_2} C_D^{D_2 D_2^+}}{m_{D_2^+} + m_{D_2}} \end{aligned}$$

$$C_{D_2} = -C_{D_2}^{D_2 D_2^+}$$

After some simplification, the collision term required for the fluid equations from this reaction are the following:

Continuity:

$$\frac{\delta n_{D_2^+}}{\delta t} = -\frac{\delta n_{D_3^+}}{\delta t} = -\frac{\delta n_D}{\delta t} = \frac{\delta n_{D_2}}{\delta t} = -8 f_{di} f_{dn} n n_n \overline{\Omega}_{HP5}^{(0)} \tag{6.152}$$

Momentum:

$$\frac{\delta \mathbf{M}}{\delta t} = -\frac{\delta \mathbf{M}_n}{\delta t} \approx f_{di} f_{dn} n n_n m \Bigg[4\overline{\Omega}_{HP5}^{(0)} (3\mathbf{u}_n - \mathbf{u}) - \frac{8}{3}\left(\overline{\Omega}_{HP5}^{(1)} - \frac{3}{2}\overline{\Omega}_{HP5}^{(0)}\right) \frac{T_i + 3T_n}{T_i + T_n} \mathbf{u}_{in} \Bigg] \tag{6.153}$$

Energy:

$$\begin{aligned} \frac{\delta E}{\delta t} = f_{di} f_{dn} n n_n \Bigg\{ & 6\frac{k T_i T_n}{T_i + T_n} \overline{\Omega}_{HP5}^{(0)} - 4\overline{\Omega}_{HP5}^{(0)} \phi_{HP5} \\ & + \frac{4}{3} m u_{in}^2 \left[3\overline{\Omega}_{HP5}^{(1)} + \frac{T_i^2}{(T_i + T_n)^2} \left(3\overline{\Omega}_{HP5}^{(0)} - 2\overline{\Omega}_{HP5}^{(1)} \right) \right] \\ & + 2\frac{k}{T_i + T_n} (3T_n^2 - T_i^2) \left[\left(1 - \frac{2}{3}\lambda_{D_2 D_2^+} \right) \overline{\Omega}_{HP5}^{(1)} + \frac{4}{15} \overline{\Omega}_{HP5}^{(2)} \lambda_{D_2 D_2^+} \right] \Bigg\} \end{aligned} \tag{6.154a}$$

$$\begin{aligned} \frac{\delta E_n}{\delta t} = -f_{di} f_{dn} n n_n \Bigg\{ & 6\frac{k T_i T_n}{T_i + T_n} \overline{\Omega}_{HP5}^{(0)} + 4\overline{\Omega}_{HP5}^{(0)} \phi_{HP5} \\ & - \frac{4}{3} m u_{in}^2 \left[\overline{\Omega}_{HP5}^{(1)} - \frac{T_n^2}{(T_i + T_n)^2} \left(3\overline{\Omega}_{HP5}^{(0)} - 2\overline{\Omega}_{HP5}^{(1)} \right) \right] \\ & + 2\frac{k}{T_i + T_n} (3T_n^2 - T_i^2) \left[\left(1 - \frac{2}{3}\lambda_{D_2 D_2^+} \right) \overline{\Omega}_{HP5}^{(1)} + \frac{4}{15} \overline{\Omega}_{HP5}^{(2)} \lambda_{D_2 D_2^+} \right] \Bigg\} \end{aligned} \tag{6.154b}$$

For the generalized collision integral required for this reaction, the analytical fit for the cross section from Tabata and Shirai [81] for hydrogen is used. Because the fit function behaves normally in both the low energy region and high energy tail, the fit function is used

to extrapolate in both low energy and high energy region for numerical integration. The resulting generalized collision integral after numerical integration of the cross-section data is shown in Fig. 6.26–6.28 for the zeroth, first, and second collision integral.

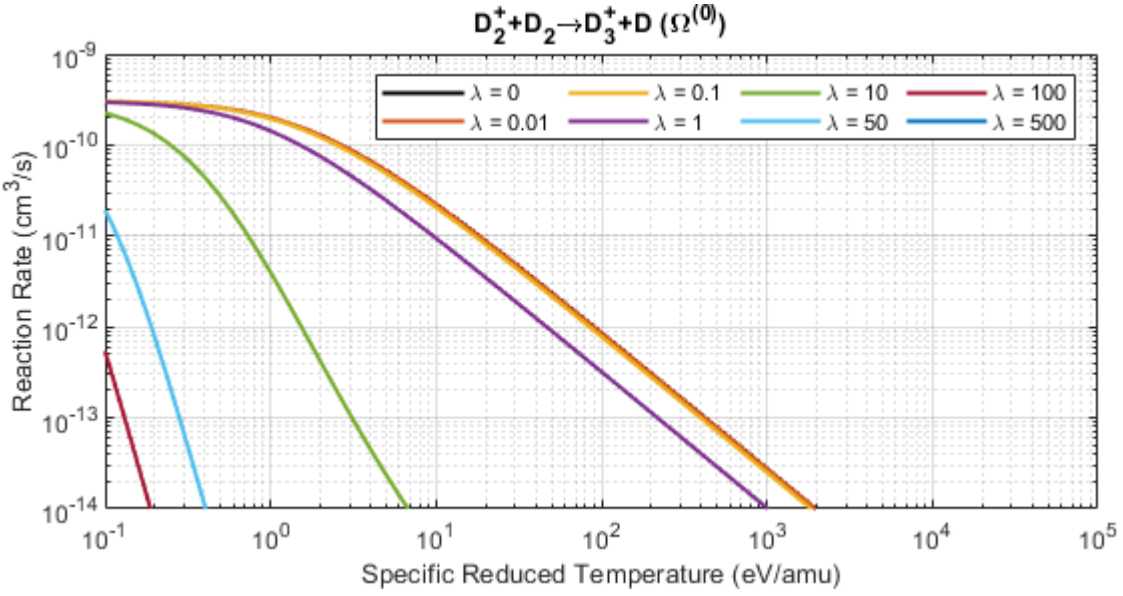

Figure 6.26: Zeroth generalized collision integral $\overline{\Omega}^{(0)}$ for D_3^+ production (HP 5).

6.7 Implementation in Cygnus

No major modifications to the time step algorithm implemented in Cygnus are necessary to implement the molecular model. This is due to the fact that the velocity and temperature advance are not modified significantly in this model other than the source terms. The only change in the velocity and energy advance is the use of the modified density ($\tilde{n}$ and $\tilde{n}_n$) in the definition of momentum and kinetic energy; this is a trivial change that requires negligible modifications.

The split-step density advance algorithm in Cygnus allows inclusion of additional species trivially. This is due to the fact that the ideal advance of the density given in Eq. 1.6 can be performed to each species independent of each other. Thus, instead of advancing the species

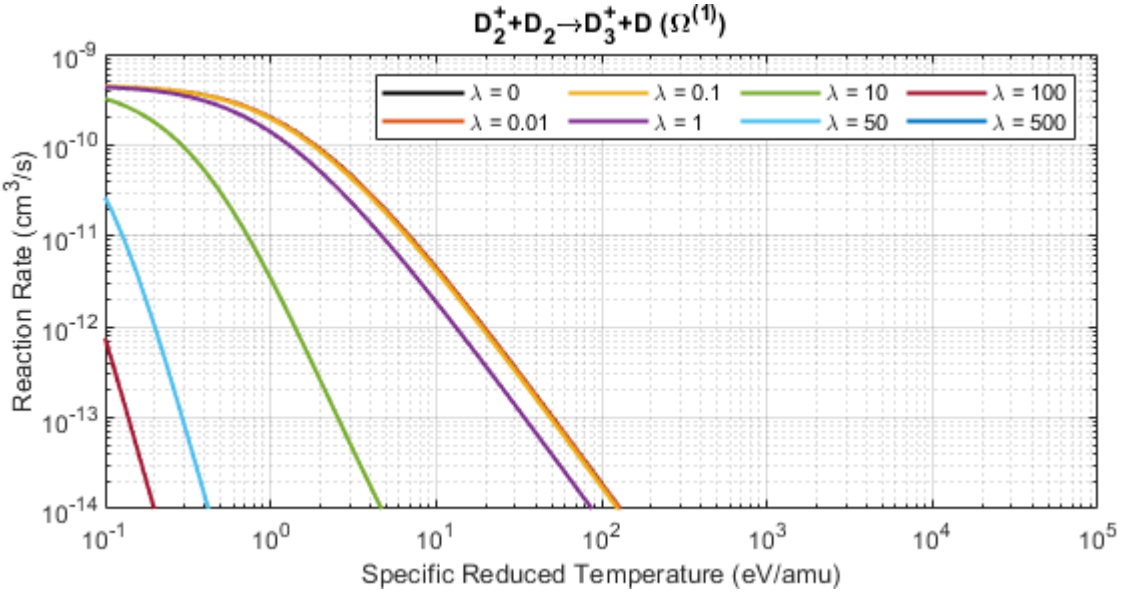

Figure 6.27: First generalized collision integral $\overline{\Omega}^{(1)}$ for D_3^+ production (HP 5).

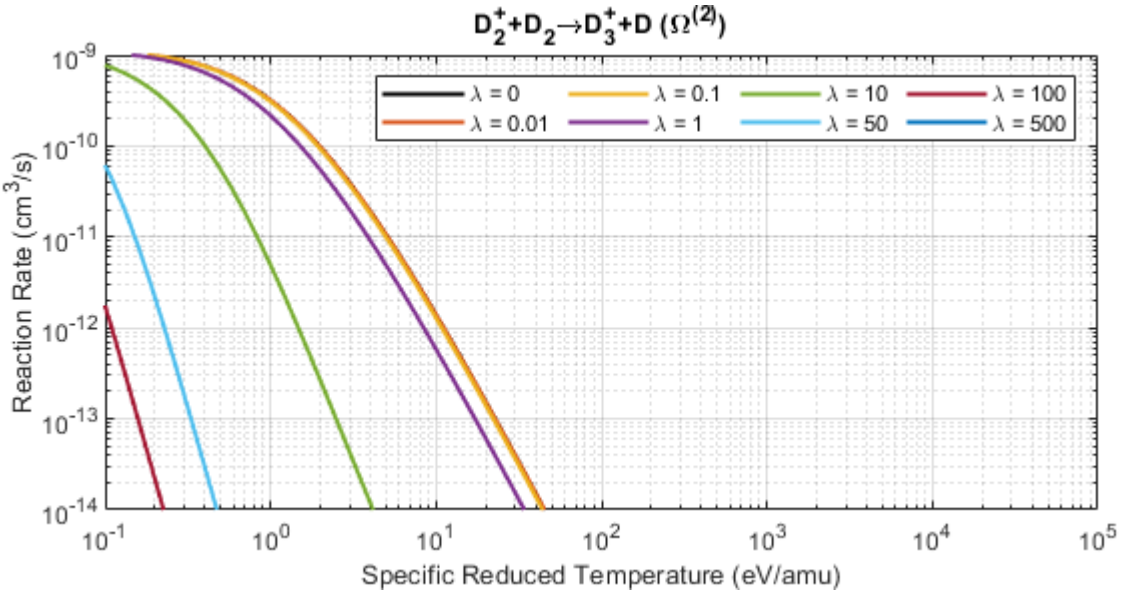

Figure 6.28: Second generalized collision integral $\overline{\Omega}^{(2)}$ for D_3^+ production (HP 5).

partition equations (Eq. 6.3–6.5) directly, the species number densities are advanced directly for D_2^+, D_3^+, and D_2 in the ideal advance, and the updated f_{di}, f_{ti}, and f_{dn} are computed

from the resulting densities.

The implicit reaction advance is where the most change is made to support the molecular model. Again, since there are no advective contributions, the species number density at each computation node can be updated independent of each other. At each node, the time discretized equation that is solved is of the following form:

$$n_\alpha^{n+3/2} - \Delta t \left(\frac{\delta n_\alpha}{\delta t} \right)^{n+3/2} - n_\alpha^{**} = 0 \tag{6.155}$$

where the $**$ state corresponds to the densities after the ideal density advance. The reaction source terms are all function of the density products $n_\alpha n_\beta$ at the updated time step. To solve the implicit non-linear Eq. 6.155, the iterative Newton's method is applied.

The magnetic field advance is unmodified by the changes made with the molecular model. Again, for the collisional electron momentum transfer term, similar assumptions made in Section 2.2.2 is used. In particular, only the terms corresponding to the current density $\mathbf{J}$ is kept, giving an isotropic formulation of the plasma resistivity. One modification that is made here is the inclusion of the reaction frequencies in the resistivity formulation.

Due to the complexity in defining effective threshold potentials (and similarly effective ionization potentials) to account for all possible molecular excitation reactions, the energy loss associated with the molecular and atomic excitations are neglected in the current implementation. Thus, the ideal values of the associated threshold potential energy are used for all reactions.

Chapter 7

SIMULATION OF VENTI-FORMATION EXPERIMENT USING DIATOMIC DEUTERIUM MODEL

In this chapter, the simulations for the Venti Formation shots 938, 974, and 3275 discussed in Chapter 4 are repeated using the molecular model discussed in the previous chapter.

7.1 Shot 938: Ringing Theta-Pinch Ionization

The descriptions of shot 938 conditions are given in Section 4.2.3, so they are not repeated here. In order to test the change to the preionization and FRC formation behavior due to the inclusion of the molecular species, the previous simulation in Section 4.2.3 is repeated with the initial neutral atomic species replaced with the molecular species. It is assumed that initially, all ions are atomic deuterium ions and all neutrals are diatomic deuterium neutrals. The mass densities of the ion and neutral species are configured to be the same as the previous calculation in Section 4.2.3. Thus, the initial neutral number density is cut in half to account for the diatomic molecules.

The resulting snapshots of the excluded flux radii at various times in the formation process calculated using the molecular model are shown in Fig. 7.1 together with the experimental and the simulation generated results from Section 4.2.3. The resulting agreement is mixed. A larger FRC is produced using the molecular model, but the FRC still drifts axially so the late time agreement with the experiment is still quite poor. It is hard to conclude whether the addition of the molecular physics improved the agreement of the simulation results to the experiment.

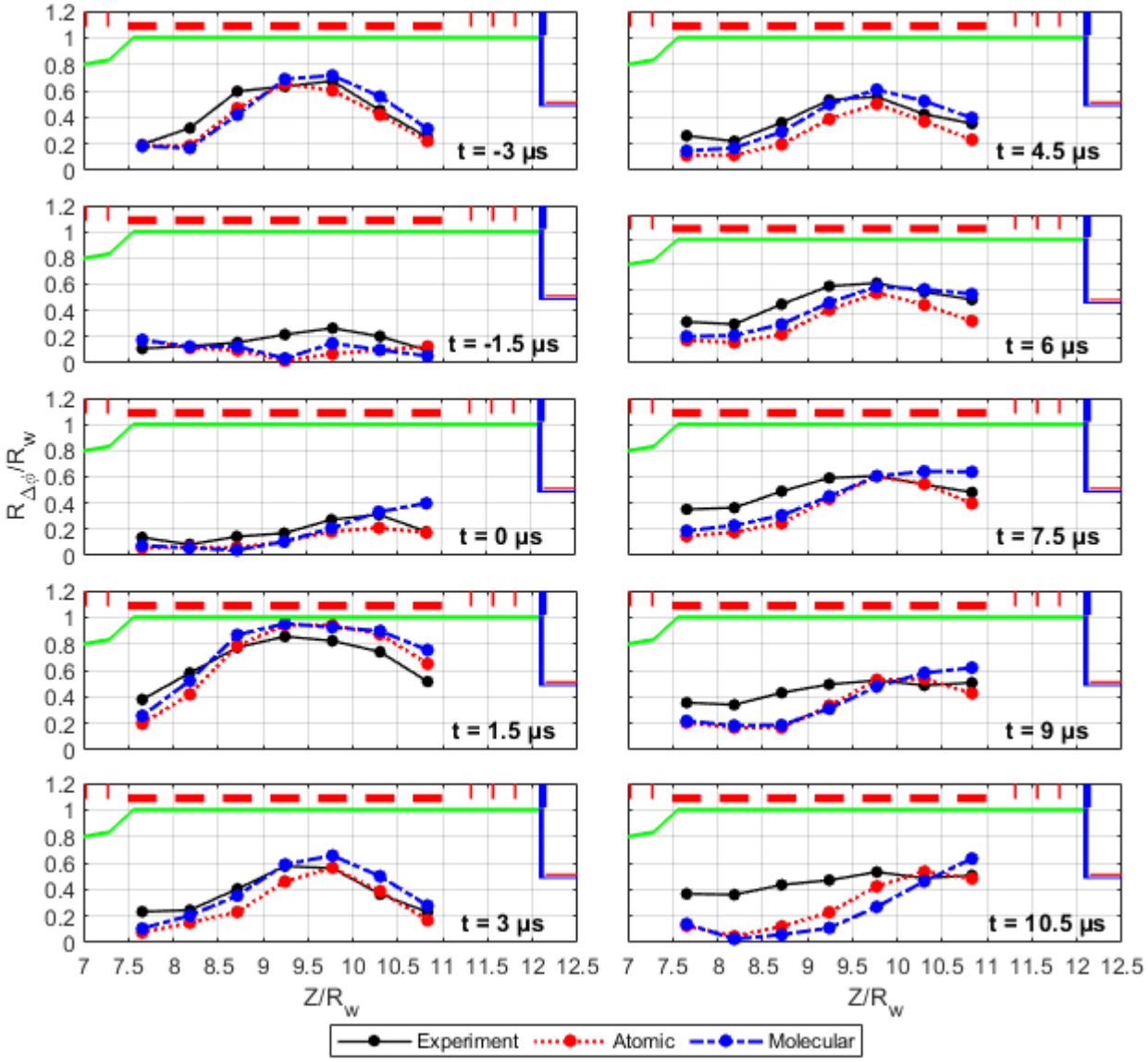

Figure 7.1: The experimental and the simulation generated excluded flux radii for Venti Formation shot 938 simulation. The coils geometry is also shown in the same figure.

The particle inventory in the reversed field region computed using both the atomic and the molecular model is shown in Fig. 7.2. In order to simplify the comparison with the atomic model, instead of the actual number of the neutral and the ion particles in the FRC, the atomic equivalent particle inventory is shown by normalizing the volume integration of

the mass density in the reversed field region with the atomic deuterium mass. It can be seen that with the molecular model, there is more ionization during the ringing theta-pinch. Furthermore, number of the trapped particles in the FRC is larger.

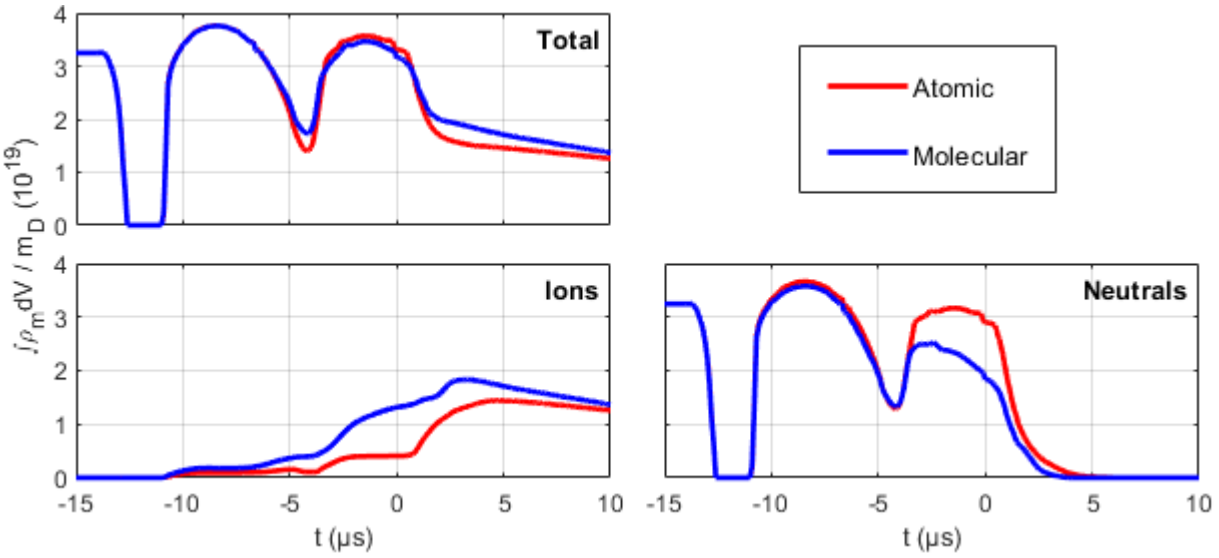

Figure 7.2: The total mass in the reversed field region normalized by the atomic deuterium mass during the ringing theta-pinch ionization and FRC formation for Venti Formation shot 938 simulation using the atomic and molecular model.

The increase in the ionization during the ringing theta-pinch can be attributed to the fact that there are no electron impact excitation loss in the current implementation of the molecular model. Nevertheless, unlike the case when the atomic model is run with the effective ionization potential of 13.6 eV, the ionization does not begin to increase until about -6 μs. Thus, the additional reactions that are required to ionize diatomic deuterium neutrals are sufficient to hinder the early ionization reactions. The start of the ionization process in the molecular model matches better with the results from the visual light diagnostic shown in Fig. 4.5.

The mass fraction of the tracked species in the reversed field region is shown in Fig. 7.3. As it can be seen, early in the ringing theta-pinch ionization, the dissociation of the diatomic deuterium is the dominant reaction. Because the threshold energy of the dissociation

reaction is lower than that of the atomic deuterium ionization, early in time, the electron temperature is capped near the dissociation threshold energy, reducing the efficiency of the atomic deuterium ionization. Thus, the second zero-crossing of the ringing field is required to increase the electron temperature to allow ionization to take off in the formation chamber.

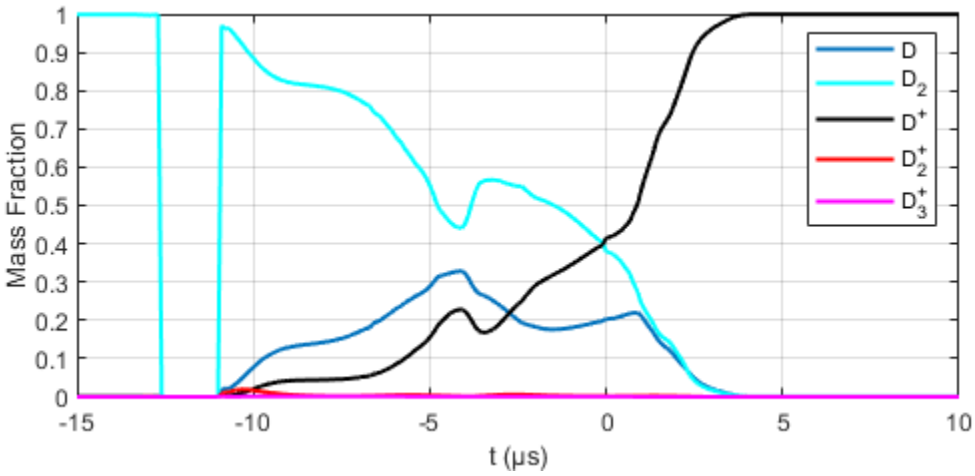

Figure 7.3: The mass fraction of tracked species in the reversed field region for Venti Formation shot 938 simulation using the molecular model.

For the entire simulation, the contribution from the molecular ion species are negligible inside the reversed field regions. The diatomic deuterium ions are no more than 2% of the total mass in the reversed field region, and the triatomic deuterium ions are no more than 0.2% of the total mass in the reversed field region. Thus, the preferential reaction path for the diatomic deuterium neutrals is to either dissociate or dissociatively ionize into atomic species. This suggests that the error in neglecting the molecular ion species are small for a typical FRC formation simulation using ringing theta-pinch ionization.

The simulation generated trapped flux and volume averaged FRC temperatures are shown in Fig. 4.15. It can be seen that the trapped flux is largely the same for both the atomic and molecular model. The molecular model starts with a higher electron temperature after the ringing theta-pinch ionization. In general, the molecular model has a higher temperature due to the lower electron energy loss and a more violent formation process with a higher

implosion kinetic energy.

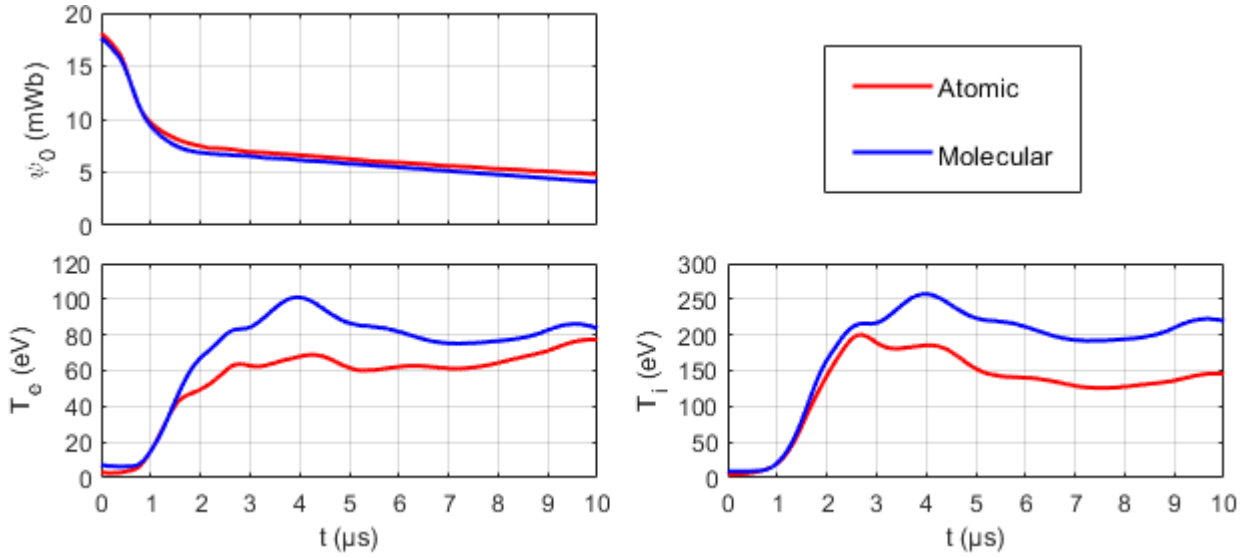

Figure 7.4: The time evolution of the FRC (top left) trapped flux, (bottom left) volume averaged electron temperature, and (bottom right) volume averaged ion temperature for Venti Formation shot 938 simulation using the atomic and molecular model.

7.2 Shot 974: Multistage Ringing Barrier Ionization

The descriptions of shot 974 are given in Section 4.3, so no additional details are given here. In order to test the change to the preionization and FRC formation behavior due to the inclusion of the molecular species, the previous simulation in Section 4.3 is repeated with the initial neutral atomic species replaced with the molecular species. Similar to the calculation for shot 938, all ions are initially atomic while the neutrals are diatomic. The mass densities of the ion and neutral species are configured to be the same as the previous calculation in Section 4.3, thus the initial neutral number density is cut in half to account for the diatomic molecules.

The resulting snapshots of the excluded flux radii at various times in the formation process calculated using the molecular model are shown in Fig. 7.5. The experimental data and the results from the atomic models are also shown in the same figure. In general, the

results from the molecular model are close to the results from the atomic model using the effective ionization potential of 13.6 eV, especially in the late time behavior. For the ringing theta-pinch phase, the solution from the molecular model is between the 13.6 eV and the dynamic case, and the agreement with the experimental result is improved. In general, the use of the molecular model improved the agreement with the experimental excluded flux radii.

The resulting NDL signal from the molecular model is shown in Fig. 7.6, together with the experimental and the atomic model results. Again, the late time behavior of the molecular model agrees with the 13.6 eV case from the atomic model and the experiment. During the ringing theta-pinch, similar to the 13.6 eV case using the atomic model, from -5 to 0 μs, the NDL from the molecular model agrees reasonably with the experimental measurement. The computed value is smaller than the 13.6 eV case, but the result is still within the noise in the experimentally measured signal. The computed value from -11 to -5 μs from the molecular model is much lower than the 13.6 eV case, and it is much more reasonable based on the noisy experimental measurement. Thus, the molecular model also improved density agreement with the experiment.

The particle inventory in the reversed field region computed using both the atomic and the molecular model is shown in Fig. 7.7. In order to simplify the comparison with the atomic model, instead of the actual number of the neutral and the ion particles in the FRC, the atomic equivalent particle inventory is shown by normalizing the total mass in the reversed field region with the atomic deuterium mass. From the atomic model, both the result using dynamic and constant 13.6 eV effective ionization potential are shown.

With the molecular model, it can be seen that the ionization is improved in the ringing theta-pinch region compared with the atomic model with the dynamic effective ionization, but is less rapid as the 13.6 eV case. Due to the additional dissociation process that occurs before the neutrals can be ionized, it slows down the initial ionization process. It can be seen on Fig. 7.7 that the neutral inventory remains relatively flat from -11 to -8 μs before it rapidly begins decaying. With the molecular model, the neutrals are not fully ionized

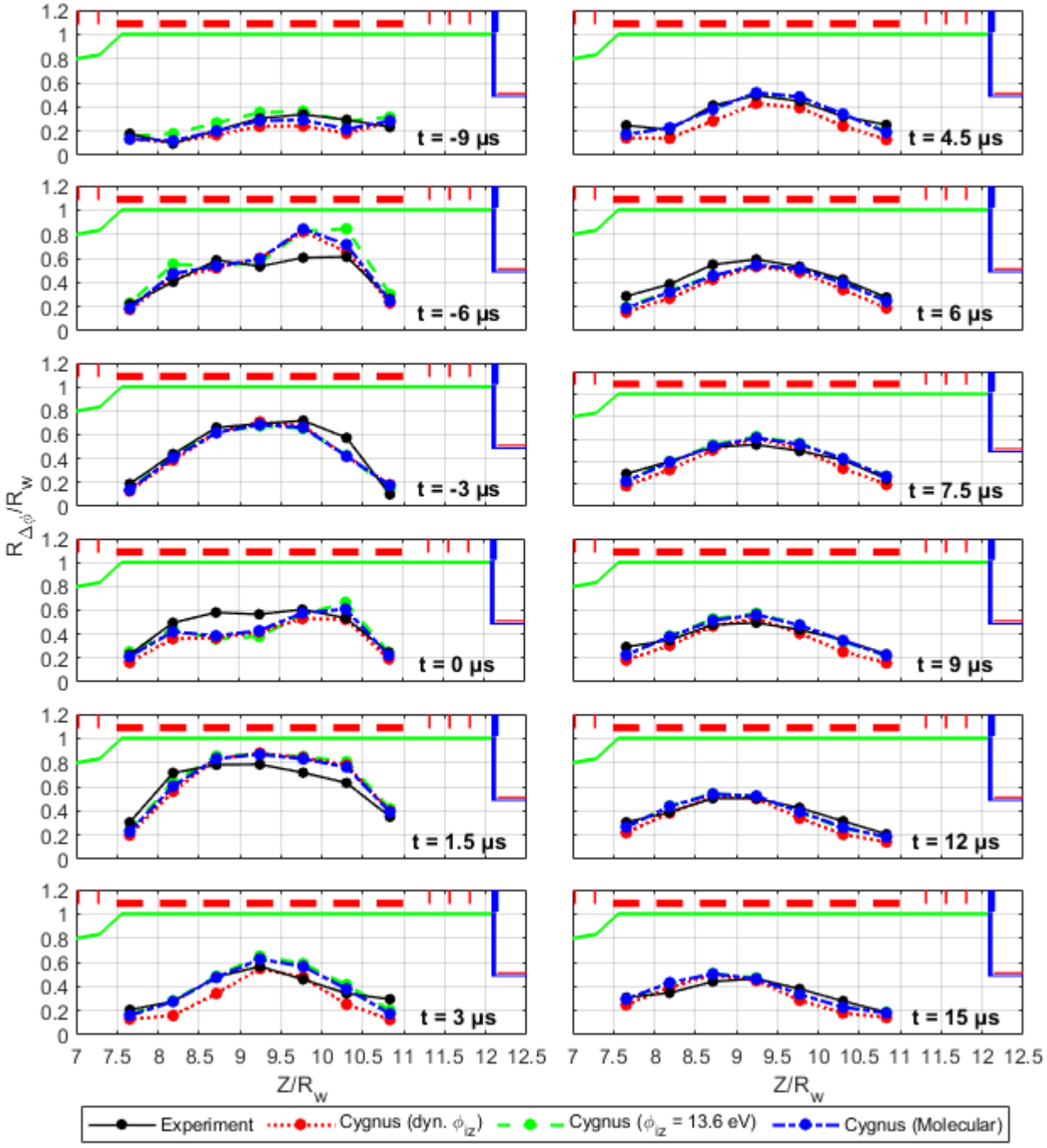

Figure 7.5: The experimental and the simulation generated excluded flux radii for Venti Formation shot 974 simulation. The coils geometry is also shown in the same figure.

by the ringing theta-pinch, and the initial ionization fraction before the main coil firing is

87%. Note that after the dissociation, since the molecular model does not have any electron impact excitation losses, it behaves similar to the 13.6 eV case. Again, the resulting particle inventory in the FRC is similar for all simulated cases.

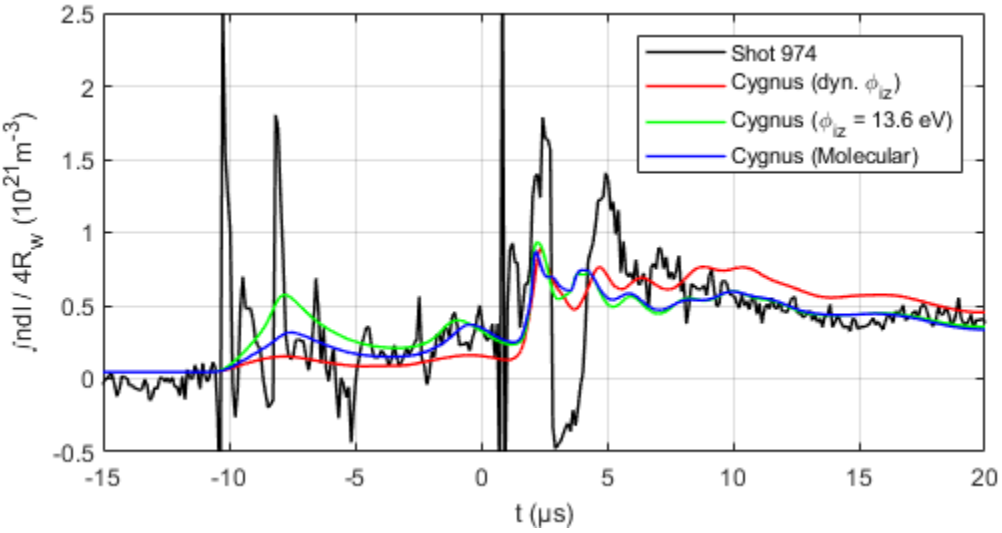

Figure 7.6: The experimental [65] and the simulation generated NDL signal for Venti Formation shot 974. The NDL signal is normalized by the path length through the chamber.

The mass fraction in the reversed field region of the tracked species in the molecular model is shown in Fig. 7.8. As expected, early in the ringing theta-pinch (before -7 μs), the dissociation is the most dominant process as the fraction of the diatomic deuterium is rapidly decreasing while the mass fraction of the atomic neutrals increases. Since the system starts with a significant population of the atomic deuterium ions due to the ringing barrier ionization, there are ionization occurring during the dissociation process. In fact, the rate of mass fraction increase for both atomic ions and neutrals are similar, suggesting that for each diatomic neutral, a pair of ion and neutral is produced. This can be caused by either the dissociative ionization processes, or through the two-step process involving deuterium dissociation followed by atomic deuterium ionization.

After -7 μs, the mass fraction of both the diatomic and atomic deuterium neutrals are decaying, suggesting that the ionization is the most dominant reaction at this time. After

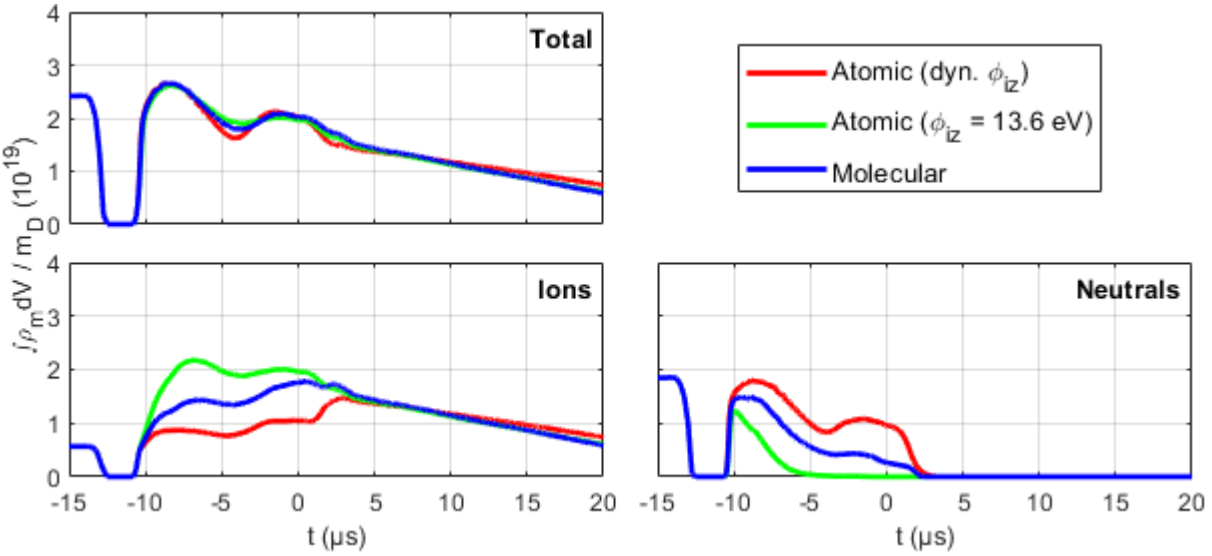

Figure 7.7: The averaged mass density in the reversed field region normalized by the atomic deuterium mass during the ringing theta-pinch ionization and FRC formation for Venti Formation shot 974 simulation using the atomic and molecular model.

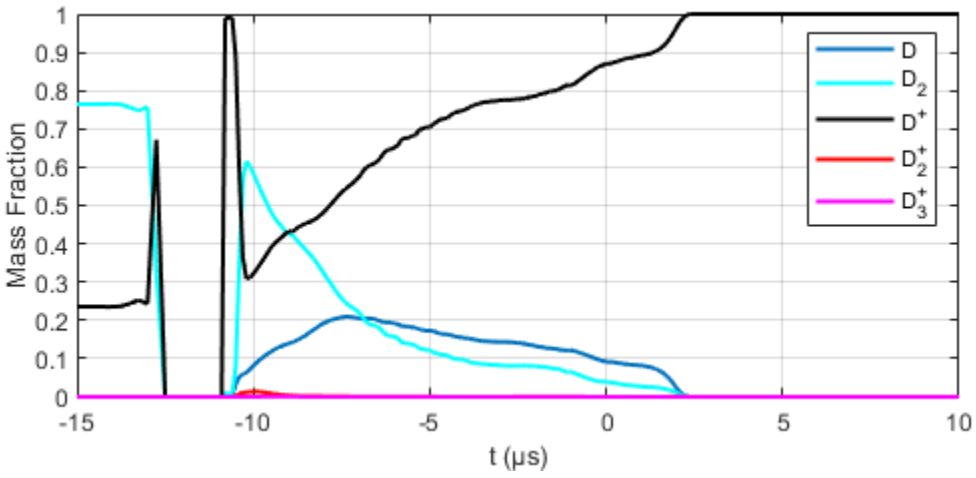

Figure 7.8: The mass fraction of tracked species in the reversed field region for Venti Formation shot 974 simulation using the molecular model.

about -5 μs, mass fraction of both neutral species decays at about same constant rate. During the radial implosion, the remaining atomic neutrals are rapidly ionized to form a fully ionized

FRC. For the entire simulation, the contributions from the molecular ion species are negligible inside the reversed field regions. The diatomic deuterium ions are no more than 1.4% of the total mass in the reversed field region, and the triatomic deuterium ions are no more than 0.042% of the total mass in the reversed field region. The contributions from the molecular ions are smaller for this simulation case than for shot 938 from the previous section.

The simulation generated trapped flux and volume averaged FRC temperatures are shown in Fig. 7.9. Again, the trapped flux is similar for all cases. It can be seen that the temperature results from the molecular model is largely the same as the 13.6 eV case using the atomic model. This is due to the fact that after the ringing theta-pinch ionization, since the diatomic neutral fraction is not large, the dominant reaction is the atomic deuterium ionization. Since no electron impact excitation processes are included in the molecular model, the resulting atomic deuterium ionization physics is equivalent to that when the effective ionization potential is set to 13.6 eV.

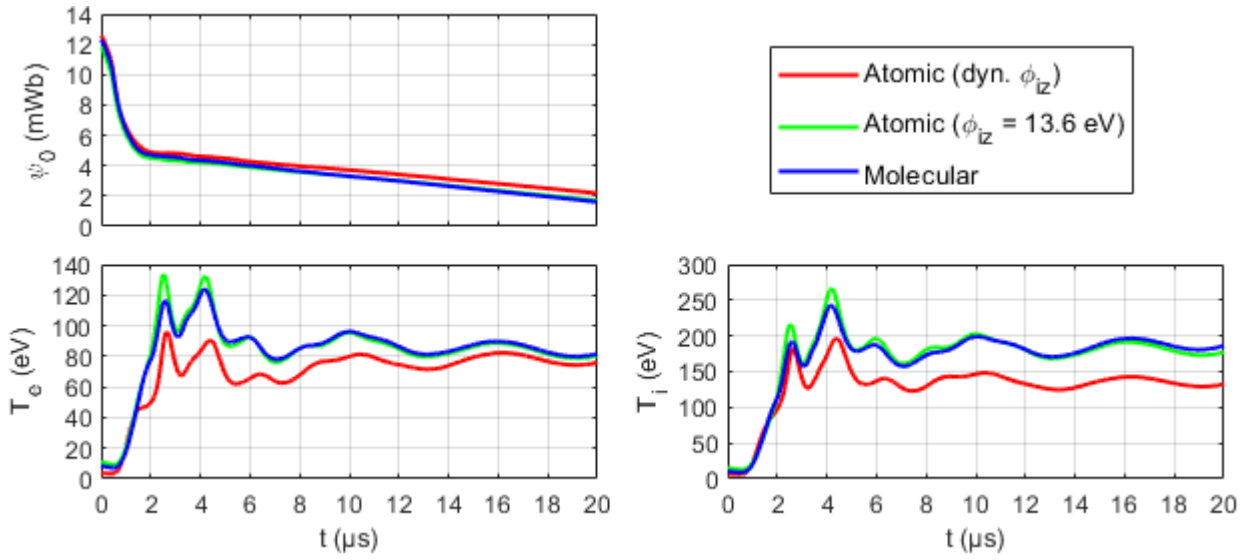

Figure 7.9: The time evolution of the FRC (top left) trapped flux, (bottom left) volume averaged electron temperature, and (bottom right) volume averaged ion temperature for Venti Formation shot 974 simulation using the atomic and molecular model.

7.3 Shot 3275: Unassisted Ringing Barrier Ionization

The description of shot 3275 are given in Section 4.4, so no additional details are given here. In order to test the change to the FRC formation and translation behavior due to the inclusion of the molecular species, the previous simulation in Section 4.4 is repeated with the initial neutral atomic species replaced with the molecular species. Similar to the calculation for shot 938, all ions are initially atomic while the neutrals are diatomic. The mass densities of the ion and neutral species are configured to be the same as the previous calculations in Section 4.4, thus the initial neutral number density is cut in half for the diatomic molecules.

The resulting snapshots of the excluded flux radii at various times in the formation process calculated using the molecular model are shown in Fig. 7.10. The experimental data and the results from the atomic models are also shown in the same figure. For this case, it is seen that there are no significant change to the agreement in the excluded flux signal by using the molecular model. In fact, for the excluded flux signal, the agreement is worse, and the 13.6 eV case using the atomic model matches better.

The resulting NDL signal from the molecular model is shown in Fig. 7.11, together with the experimental and atomic model results. The molecular model improves agreement prior to the main bank firing compared with the 13.6 eV case. The initial NDL signal for the molecular signal is similar to the dynamic effective ionization potential case. The late time behavior, on the other hand, follows similar to the 13.6 eV case. Again, similar to the atomic model, the late time agreement with the experiment is quite poor. Because the simulation generated FRC is smaller, the resulting late time NDL signal is small due to the interferometer chord missing the core of the generated FRC.

The particle inventory in the reversed field region computed using both the atomic and the molecular model is shown in Fig. 7.12. In order to simplify the comparison with the atomic model, the atomic deuterium mass normalized total mass is used. As it can be seen, prior to the main bank firing, the total ions in the reversed field region computed from the molecular model is similar to the atomic case with the dynamic effective ionization potential. Thus,

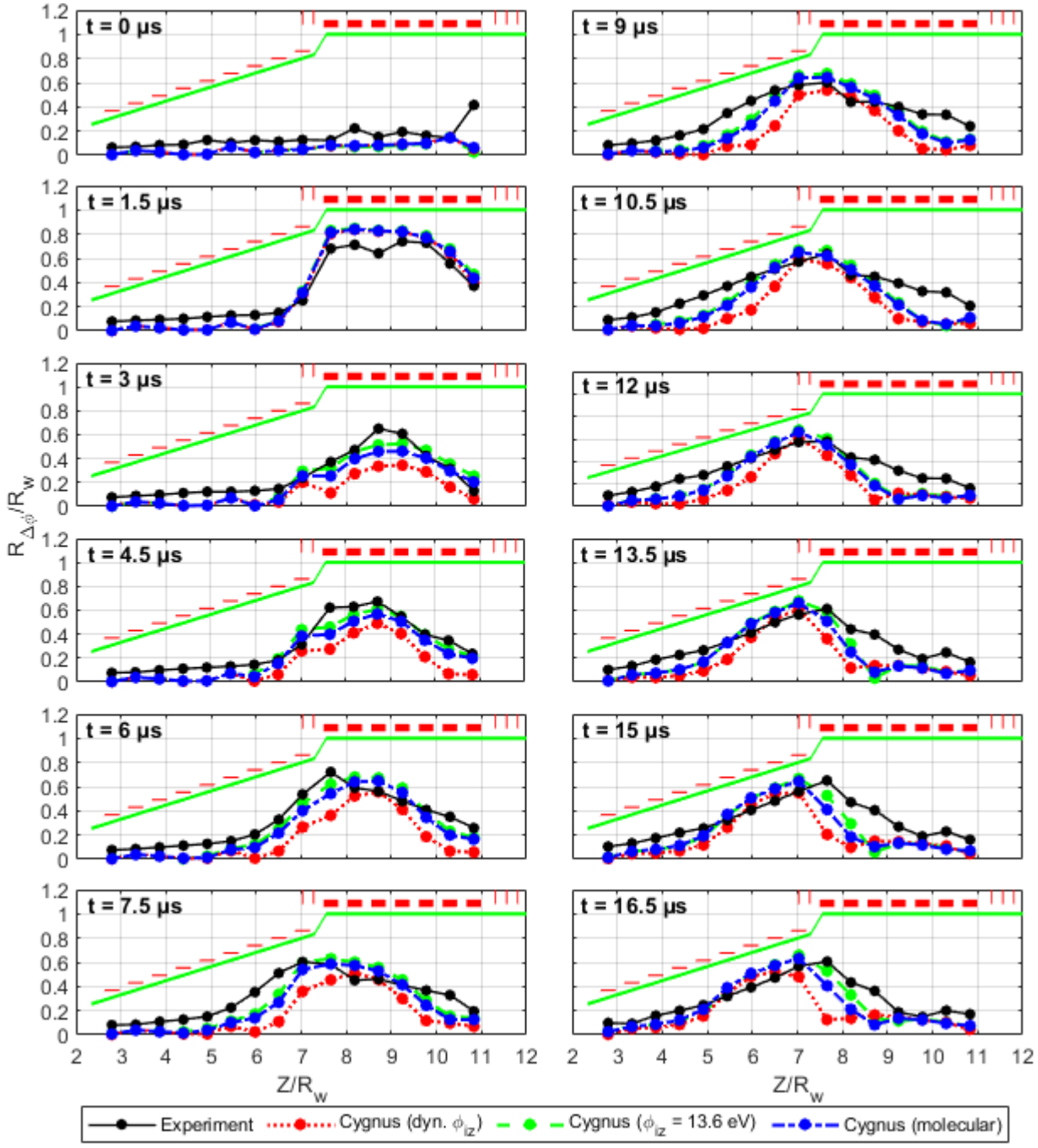

Figure 7.10: The experimental and the simulation generated excluded flux radii for Venti Formation shot 3275 simulation. The coils geometry is also shown in the same figure.

due to the additional energy required to dissociate the diatomic deuterium, the ionization

due to bias field injection is limited.

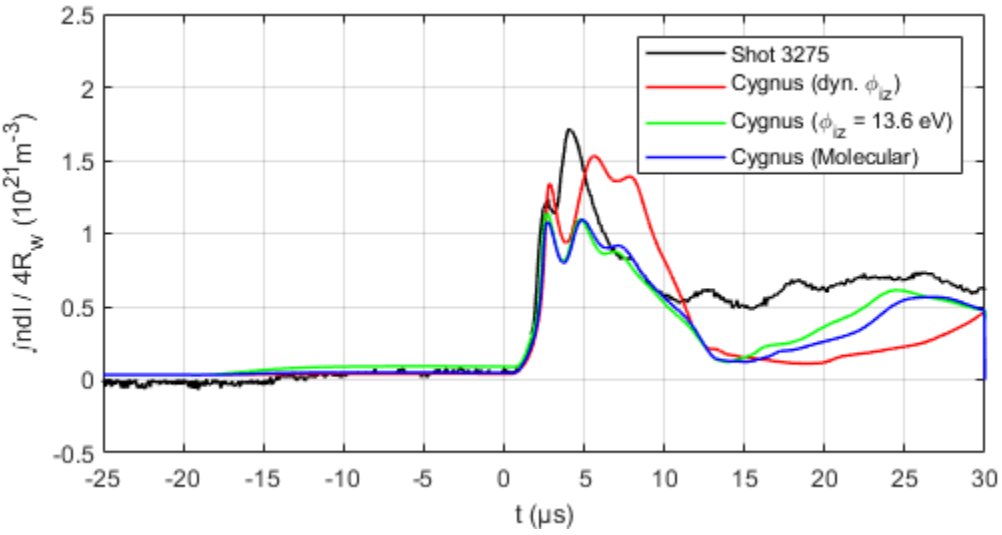

Figure 7.11: The experimental [65] and the simulation generated NDL signal for Venti Formation shot 3275. The NDL signal is normalized by the path length through the chamber.

After the main bank firing, the ionization in the molecular model is more rapid compared with the dynamic effective ionization potential case, as there are no losses associated with the electron impact excitation process. It is interesting to note, however, that there is still significant population of diatomic deuterium in the reversed field region at the time of main bank firing. This can be seen in Fig. 7.13, where the mass fraction of the tracked species in the molecular model are shown as a function of time. It can be seen that during the radial implosion, rapid ionization occurs, as both neutral species are rapidly converted to atomic ions. While there is additional energy loss from the dissociation, it can be seen that this energy loss is still smaller than what is computed by the dynamic effective ionization potential. Thus, the resulting particle inventory for the molecular model is similar to the 13.6 eV case.

Note that while there are some formation of the molecular ions during the radial implosion process, it can be seen that the contribution from the molecular ion species are largely negligible. The diatomic deuterium ions are no more than 1.8% of the total mass in the

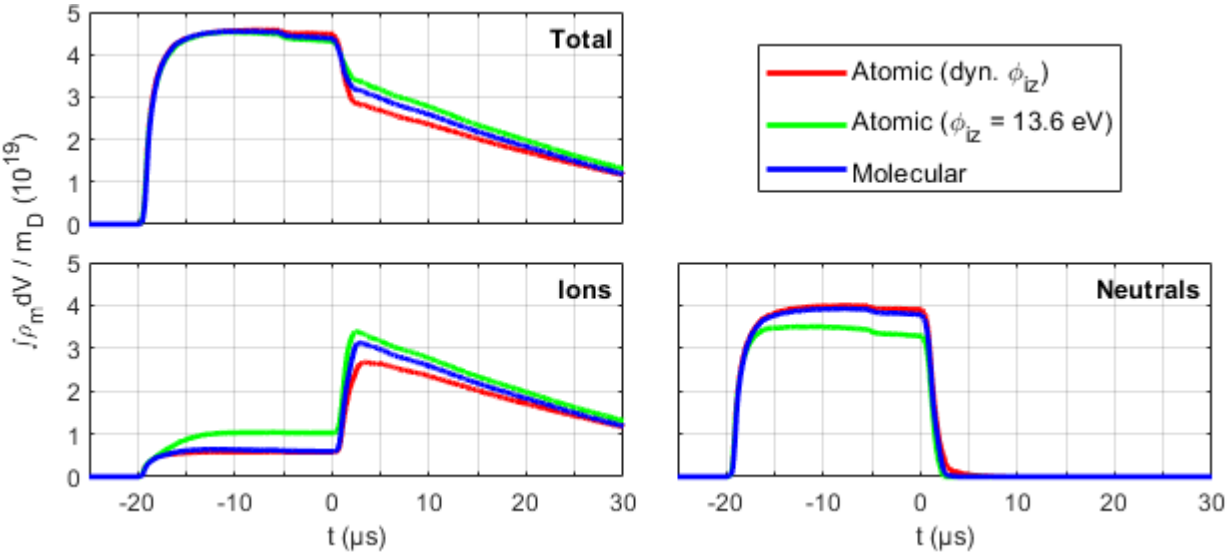

Figure 7.12: The averaged mass density in the reversed field region normalized by the atomic deuterium mass during the ringing theta-pinch ionization and FRC formation for Venti Formation shot 3275 simulation using the atomic and molecular model.

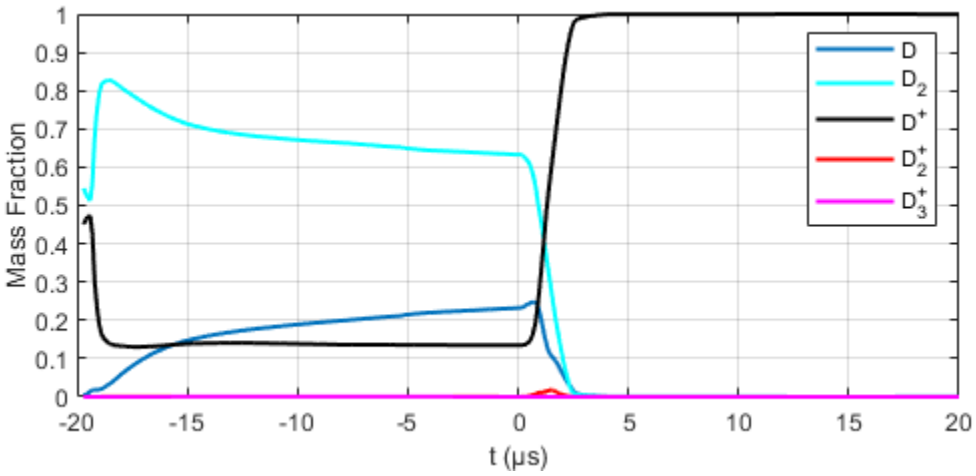

Figure 7.13: The mass fraction of tracked species in the reversed field region for Venti Formation shot 3275 simulation using the molecular model.

reversed field region, and the triatomic deuterium ions are no more than 0.05% of the total mass in the reversed field region. Thus, the preferred reaction path for the diatomic deu-

terium neutrals is dissociation and ionization, and the error in neglecting the molecular ion species are most likely small for a typical FRC formation simulations.

The simulation generated trapped flux and volume averaged FRC temperatures are shown in Fig. 7.14. The trapped flux for the molecular case lies in between the two atomic model cases. Similarly, the electron temperature for the molecular case lies in between the two atomic model cases, due to the additional energy loss associated with the diatomic deuterium dissociation. The ion temperature for the molecular case is largely the same as the 13.6 eV atomic case, since it is largely unaffected by the electron energy loss. The translational velocity of the FRC is slightly slower than the 13.6 eV case, but for the most part, it is equivalent.

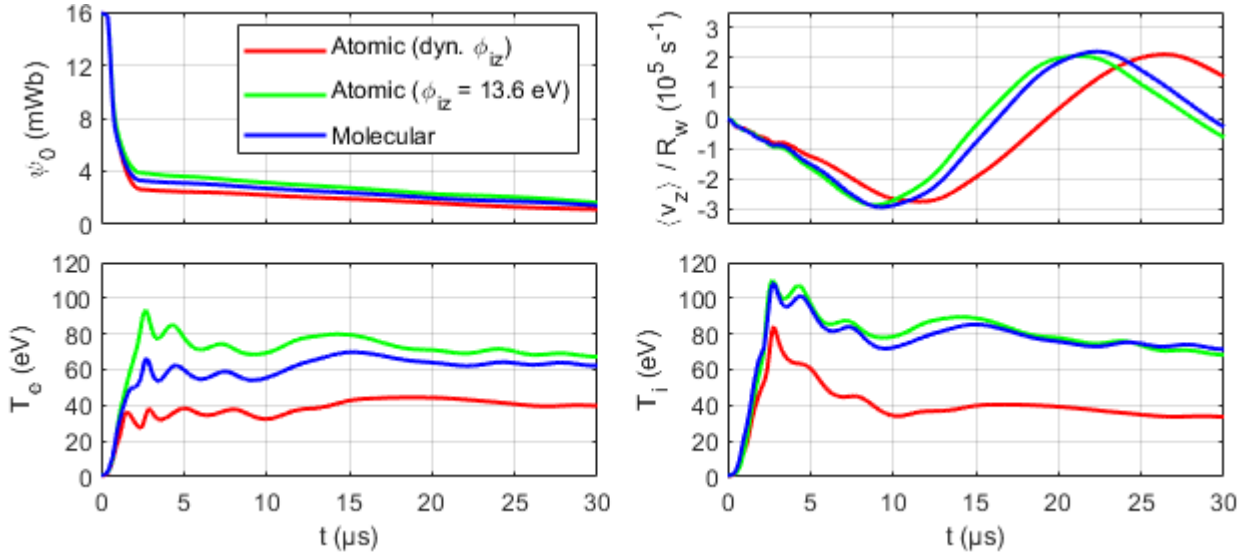

Figure 7.14: The time evolution of the FRC (top left) trapped flux, (bottom left) volume averaged electron temperature, and (bottom right) volume averaged ion temperature for Venti Formation shot 3275 simulation using the atomic and molecular model.

7.4 Discussion of Molecular Effects in FRC Formation

Based on the simulation results using the molecular model, improvements were seen in the agreement between the experimental and the simulation results. While the molecular model

did not resolve all of the disagreements seen with the original atomic model, it is useful in shedding some light on the ionization process occurring in the reversed field region of the formation chamber. It is seen that initially, dissociation reaction dominates during the preionization process. The ionization of the atomic deuterium does not take off until sufficient inventory of the atomic deuterium neutrals are produced from the diatomic deuterium neutrals. As such, the resonant charge exchange does not dominate until later in the preionization process.

For all cases tested, the fraction of the molecular ion species in the system are small, and they can be neglected from the model with little harm. The formation of the diatomic ions were no more than few percent for all cases and that of the triatomic ions were smaller than a percent. Thus, the molecular model can be simplified further by removing these two species and the associated reaction from the model. In most cases, tracking excited neutral states are most likely more important than the production of the molecular ions, as the ionization process is modified through the multi-step ionization process. In addition, the energy loss associated with the neutral excitations are important for electron temperature evolution. Future improvements to the model should make the addition of the excited neutral effects the number one priority.

One of the limitations of the present molecular model is the neglecting of the species specific temperatures and velocities. Since the effect from the molecular ions were negligible, only that of the diatomic neutrals are required to improve this model for FRC applications. Nevertheless, since anomalous transports are required to make the simulations match the experimental conditions, the error introduced from assuming single temperature and velocity is expected to be small compared with the uncertainty introduced from the anomalous transport. Rather, phenomena that directly affects the electron temperature, such as radiation, are more important, as it can change the preferred reaction path in the preionization and formation processes.

Chapter 8

CONCLUSION

The plasma-neutral interaction modeling capability was added to the Cygnus code and it was used to study effects of neutrals in FRC preionization and formation processes. The implementation details of the Meier and Shumlak's plasma-neutral model were discussed in Chapter 2. The algorithm that retains the original structure of the Cygnus code with the additional neutral and anisotropic viscosity transport models was presented. The original features of the Cygnus code, such as support for arbitrary axisymmetric geometry, both static and dynamic external circuits, capturing both boundary eddy and far field effects, and others were not compromised as a part of the upgrade process. Thus, the same FRC simulation capability as the original Hall MHD version of the code is retained but with additional neutral simulation options that allows study of neutral effects in FRC formation processes.

The influence of the plasma-neutral model on FRC formation and translation processes was studied in a controlled manner in Chapter 3. Simple but experimentally reasonable simulation conditions were used to simulate programmed and dynamic formations of FRCs. Various parametric sweeps of the initial ionization levels, initial ionization structures, and transport settings were performed to understand the behavior of the simulation results due to neutral physics. Data similar to experimental measurements were generated to study the response of the experimental output caused by the parametric sweeps.

When the initial ionization level in the preionized gas was reduced, a smaller FRC with lower trapped flux and particles was produced. The resulting FRC ion temperature was largely unaffected by the initial ionization. On the other hand, the electron temperature was lower due to increased ionization events. When the initial ionization level was insufficient,

the electron Joule heating during the radial implosion was not sufficient to maintain a rapid ionization during the radial implosion. When this occurred, the produced FRC was significantly smaller with poorer trapped flux and particles compared with the fully ionized case. In the cases tested, this effect was seen for the 10% ionization case. As such, the 10% case did not follow the general trend of other cases tested.

When the initial ionization was concentrated in the outer layer of the gas column, trapped flux and particles were increased compared to the equivalent uniform ionization cases. This was caused by the improved radial bucking of the magnetic field. Due to the skin depth effect, the rapidly increasing axial field during the radial implosion cannot penetrate far into a highly conductive plasma layer that has a thickness greater than the local skin depth. For the 10% ionization case, no improvements were seen because of its small plasma layer thickness. For all cases tested, the FRC length was shorter compared to the equivalent uniform ionization case. This was caused by the increased axial diffusion of the magnetic field into the gas column due to the concentration of the initial ionization in the outer radius shell.

When the initial ionization was radially imploded before firing the main formation bank, the FRC trapped flux was severely reduced. This was caused by the loss of all bias fields outside of the imploded plasma column during the field reversal process. Because the plasma column is conductive, the magnetic field outside of the plasma column cannot diffuse into the column during the implosion process. As such only the bias field trapped by the reduced radius plasma column is retained during the formation. On the other hand, particle inventory did not change significantly for this case. As such, more elongated FRC with lower trapped flux and higher trapped particles was produced. Due to the reduced implosion radius, both ion and electron temperatures were reduced.

For all cases tested, the excluded flux and NDL signals were inadequate to definitively conclude the initial ionization state of the injected gas. The excluded flux signals were insensitive to the small change in the FRC geometry caused by the initial ionization state. Furthermore, it was easy to misinterpret the change in the excluded flux signal as being

caused by additional anomalous resistivity effects; it was difficult to isolate neutral effects from other anomalous effects commonly expected in the FRC formation process. The NDL signals were better at indicating the initial ionization level in the chamber; however, unless the radial profile of the initial gas state was accurately known, it was easy to misinterpret the NDL results. Multi-chord measurements of the line integrated density is required to remove ambiguities caused by the radial density dependence. Additional electron temperature measurements in the experiment can significantly improve the understanding of the ionization process in FRC formations, as the final FRC electron temperature is strongly influenced by the number of ionization events that occurred during the FRC formation.

Since the effective ionization potential is the amount of energy lost by electrons for each ionization event, when the effective ionization potential was increased, the resulting electron temperature decreased. Due to the lower electron temperature, the ionization rates were reduced during the radial implosion for the case with higher effective ionization potentials; this resulted in a lower trapped flux for those cases. However, the FRC particle inventory in the quiescent state was largely the same for all cases tested. Thus, the amount of the final ions trapped in the FRC is only a weak function of the effective ionization potential. The results from the case using the electron temperature dependent dynamic effective ionization potential lined up with the 100 eV and 150 eV static effective ionization potential cases. This suggests that there are significant ionization events occurring in the 2 to 3 eV electron temperature regime.

When anomalous resistivities (Chodura and Bohm) were added to the simulation, trapped flux and particles were reduced. Only minor changes to the electron and ion temperatures were observed for increased anomalous resistivities. Compared with the Chodura resistivity, Bohm resistivity produced shorter and more elliptic FRCs. For Chodura resistivity, flux and particle losses were tightly coupled, and FRC volume averaged density remained mostly constant for a wide range of Chodura C-factors. On the other hand, FRC volume averaged density decreased when the magnitude of Bohm resistivity was increased. For both anomalous resistivities, when the resistivity was increased, both excluded flux and NDL signals

were reduced because a smaller FRC with lower particle inventory was produced.

Both isotropic and anisotropic viscosities gave ability to dampen the post-implosion oscillatory dynamics of the FRC in the simulation. Besides the ion temperature, the remaining FRC parameters were not influenced on average. In general, while the anisotropic viscosity offers finer control of the post-implosion FRC dynamics, for matching experimental results, the isotropic viscosity is more useful, because its effect on the FRC dynamics is better understood. The anisotropic Braginskii viscosity resulted in too much post-implosion radial and axial dynamics, suggesting presence of a larger anomalous viscosity for FRCs.

When a dynamically formed FRC was translated through a flux conserver filled with a neutral background, the particle sustainment in the translating FRC was improved. This improvement was caused by the enhanced plasma population in the FRC scrape-off layer due to the upstream neutral ionization layer in front of the translating FRC. The enhanced scrape-off layer plasma population reduced the cross-field diffusion of the plasma from the FRC, resulting in a lower particle loss rate. Due to the presence of the upstream ionization layer, background neutrals could not penetrate into the FRC core and then ionize. As such, the background neutrals did not have a strong effect on the FRC electron temperature.

In Chapter 4, the plasma-neutral model was used to simulate three experimental shots from the Venti Formation experiment that used different preionization methods: ringing theta-pinch (shot 938), multistage ringing barrier (shot 974), and unassisted ringing barrier ionization (shot 3275). For all simulated cases, the initial axial density profile was configured based on the prior neutral pressure measurements using fast ion gauge and static pressure probe. The transport coefficients for the simulation were configured to match the experimental results.

For all three simulations, significant amounts of transport coefficients tunings were required before reasonable agreements with the experiment were obtained. Furthermore, the electron temperature dependent effective ionization potential based on Lieberman and Lichtenberg produced FRCs that were smaller and lower density than what the experimental excluded flux and NDL suggested. Improved post-implosion agreements with the experiment

were seen when the theoretical minimum ionization potential for deuterium (13.6 eV) was used. However, when the theoretical minimum value of the ionization potential was used, the ionization during the preionization phase was excessive; the simulation results did not agree with the experimental NDL and visual light measurements during the preionization.

The difficulty in obtaining agreements with the experimental results suggests that the derivation of the neutral-plasma model based on a locally Maxwellian distribution function is inadequate for modeling FRCs. Thus, anomalous corrections to the plasma and neutral transports were required to match the experiment. This is not a surprising conclusion, as typical MHD simulation of an FRC requires tuning of anomalous transports before a reasonable match with the experiment can be obtained.

Once reasonable values of transport coefficients were determined, for shot 938, the simulation generated excluded radii that matched well with the experiment until 6 µs. The late time divergence of the results was blamed on the neutrally stable magnetic configuration used in the experiment. Since there were no mirror fields centering the FRC, a slight error in matching experimental circuit and field conditions resulted in a translating FRC out of the formation chamber in the simulation. Based on simulation results prior to the divergence, the trapped flux was estimated to be 5–6 mWb. The electron and ion temperatures were estimated to be 60–90 eV and 150–200 eV, respectively. The particle inventory from the simulation varied widely depending on the input, so no reasonable estimate could be made; the experiment lacked NDL measurements to help improve the simulation output.

For shot 974, good agreements with the experimental excluded flux measurements were obtained for the entire simulation. The simulation generated NDL signal matched the experimental one within the noise of the experimental signal except for early times in the simulation during the preionization phase. The simulation generated too much ionization during the first cycle of the ringing theta-pinch. However, this did not strongly influence the final particle inventory. Based on the simulation results, the trapped flux was estimated to be 4–4.5 mWb. The particle inventory was estimated to be 1.4×10^{19} atomic deuterium ions. The electron and ion temperatures were estimated to be 60–90 eV and 150–180 eV,

respectively.

The shot 3275 was the most difficult experiment to match with the simulation. There were reasonable agreements in the FRC locations estimated from the excluded flux radius signals; however, the shape of the FRC did not agree well, as the simulation calculated FRC was shorter. The agreement in the NDL was worse, most likely caused by the disagreement in the FRC shape. A reasonable agreement is obtained up to the first radial implosion, but the rate of ionization during the radial implosion is slower in the simulation compared with the experiment. This suggests enhanced ionization during the radial implosion, most likely caused by the multi-step ionization process.

For both shot 974 and shot 3275, the ringing barrier ionization could not be modeled with fidelity, since it has strong azimuthal dependence. To simulate the ionization produced by the ringing barrier, the simulation was initialized with a plasma layer with a thickness of 12% chamber wall radius to mimic the ionization produced by the ringing barrier. In order to account for the enhanced field diffusion due to the azimuthal dependence of the barrier field, the anomalous Bohm resistivity was used. In order to improve the modeling of the barrier field ionization process, a three-dimensional model is required.

In Chapter 5, possible sources of the simulation disagreement with the experiment were explored. In particular, four important effects that are missing in the plasma-neutral model were considered: 1) three-dimensional effects, 2) multi-step ionization processes, 3) molecular species effects, and 4) kinetic effects. The three-dimensional effects are concerned with the inability to model azimuthal dependencies in the axisymmetric model. The multi-step ionization processes concerns the presence of excited neutral species that can be ionized with a lower threshold potential. The molecular species effects are due to the use of deuterium that are diatomic gas in its stable neutral state. The kinetic effects are due to the local distribution function being non-Maxwellian during the FRC formation process. These are all physics missing in the plasma-neutral model that were identified to be potentially important during the simulation of the Venti Formation shots.

In order to test the importance of the molecular effects in the FRC formation process,

an extension to the two-fluid plasma-neutral model of Meier and Shumlak was derived in Chapter 6 to include diatomic deuterium neutrals. A simple two-fluid model that includes effects from D, D_2, D^+, D_2^+, D_3^+, and e is derived. The details of the necessary reaction collision terms were also given. The extended molecular model retains the simplicity of the Meier and Shumlak's model by tracking only a single temperature and velocity for ions and neutrals, respectively; all ions have equal fluid velocity and temperature, and all neutrals have equal fluid velocity and temperature. Only the partitions of the individual species are tracked. Thus, the molecular model is still computationally tractable, and only a minor modification to the code is necessary to implement this extension.

The simulations of the Venti Formation shots were repeated using the extended molecular model in Chapter 7 to determine effects of the molecular species in the FRC formation process. While the molecular model did not resolve all of the disagreements seen with the original atomic model, new understanding of diatomic neutral effects in the FRC formation process was obtained. For all simulated shots, the population of the diatomic deuterium neutrals was not negligible after the pre-ionization process. At the start of the field reversal, the mass fraction of the diatomic deuterium neutrals in the reversed field region was 37.9% for shot 938, 3.9% for shot 974, and 63.3% for shot 3275. In comparison, the mass fraction of the atomic deuterium neutrals in the reversed field region was 20.3% for shot 938, 9.1% for shot 974, and 23.2% for shot 3275. Thus, with the exception of shot 974, molecular neutrals must be accounted during the radial implosion process, as the mass fraction of the diatomic neutrals is larger than that of the atomic neutrals.

Based on the neutral population prior to the field reversal, one can see that the multistage ringing barrier ionization method used for shot 974 is most effective at dissociating and ionizing neutrals. The mass fraction of the atomic deuterium ions before the field reversal is 87.0%. The ringing theta-pinch method used for shot 938 is the second-best method for dissociating and ionizing neutrals. The mass fraction of the atomic deuterium ions before the field reversal is 41.5%. The unassisted ringing barrier ionization method was worst at dissociating and ionizing neutrals. The mass fraction of the atomic deuterium ions before

the field reversal is 13.5%.

For all cases simulated, the fraction of the molecular ion species in the system was small. The mass fraction of the diatomic ions was no more than few percent at all times for all simulations. The mass fraction of the triatomic ions was no more than a fraction of a percent at all times for all simulations. Thus, the influence from the molecular ions is largely negligible in the FRC formation process. Thus, the molecular model can be simplified further by removing the molecular ion species from the model.

The agreement of the excluded flux signals with the experiment for the molecular model was largely the same as the atomic plasma-neutral model. No drastic change in the excluded flux radii were seen. For the NDL signal, better agreement with the experimental results were obtained in the early time preionization phase. Due to the additional dissociation process for the diatomic neutrals, the start of the ionization process is delayed in time, and the NDL signal is reduced to the level suggested by the experimental measurements. After the field reversal, the agreement of the NDL signal is largely the same as the atomic plasma-neutral model. The improvement in the agreement of the early NDL signal suggests that the inclusion of the molecular species is a step in the right direction. However, the lack of significant improvement in the agreement of the excluded flux radii suggests that there are additional physics missing in the model.

In the future, the multi-step ionization physics should be added to the molecular model by either adding excited state neutral species or implementing the Sgro's model. The addition of the multi-step ionization physics should improve the agreement in the NDL signal during and after the radial implosion by increasing the ionization rate at these times. This is expected to improve the simulation of the ringing theta-pinch and unassisted ringing barrier ionization method, where there were significant neutral population at the start of the field reversal that needs to be rapidly ionized during the radial implosion.

As discussed previously, the kinetic and three-dimensional effects are the biggest missing physics in the present model. In order to simulate the FRC formation process reasonably using a fundamental physics model, a fully kinetic model is most likely necessary; the hybrid

models commonly used for FRC stability studies are insufficient, as the details of the local electron distribution function are important to obtain correct reaction rates for reactions with a threshold potential. Since such advanced model is expected to be computationally intractable for most experimental conditions, instead, better understandings of the anomalous transport effects should be studied experimentally in the future to increase fidelity in the anomalous transport model used in the simulation. The improved anomalous transport model is expected to reduce the time spent optimizing the transport parameters to match the experimental conditions and improve scalability of the fluid model for future experiments.

BIBLIOGRAPHY

[1] Slough, J., Kirtley, D., and Weber, T., "Pulsed Plasmoid Propulsion: the ELF Thruster," *31st International Electric Propulsion Conference*, No. IEPC-2009-265, Ann Arbor, Michigan, 2009.

[2] Kirtley, D., Pancotti, A., Slough, J., and Pihl, C., "Steady Operation of an FRC Thruster on Martian Atmosphere and Liquid Water Propellants," *48th AIAA/ASME/SAE/ASEE Joint Propulsion Conference & Exhibit*, No. AIAA-2012-4071, Atlanta, Georgia, 2012.

[3] "Next Space Technologies for Exploration Partnerships (NextSTEP) Projects," https://www.nasa.gov/feature/next-space-technologies-for-exploration-partnerships-nextstep-projects, Accessed: 2020-01-14.

[4] Brown, D. L., Beal, B. E., and Haas, J. M., "Air Force Research Laboratory High Power Electric Propulsion Technology Development," *2010 IEEE Aerospace Conference*, Big Sky, Montana, 2010.

[5] Siemon, R. E., Lindemuth, I. R., and Schoenberg, K. F., "Why Magnetized Target Fusion Offers a Low-Cost Development Path for Fusion Energy," *Comments on Plasma Physics and Controlled Fusion*, Vol. 18, No. 6, 1999, pp. 363–386.

[6] TAE Technologies, https://tae.com, Accessed: 2020-01-14.

[7] Tuszewski, M., Smirnov, A., Thompson, M. C., Akhmetov, T., Ivanov, A., Voskoboynikov, R., Barnes, D., Binderbauer, M. W., Brown, R., Bui, D. Q., Clary, R., Conroy, K. D., Deng, B. H., Dettrick, S. A., Douglass, J. D., Garate, E., Glass, F. J., Gota, H., Guo, H., Gupta, D., Gupta, S., Kinley, J. S., Knapp, K., Korepanov, S., Longman, A., Hollins, M., Li, X. L., Luo, Y., Mendoza, R., Mok, Y., Necas, A., Primavera, S., Ruskov, E., Schmitz, L., Schroeder, J. H., Sevier, L., Sibley, A., Song, Y., Sun, X., Trask, E., Drie, A. D. V., Walters, J. K., Wyman, M. D., and TAE Team, "A new high performance field reversed configuration operating regime in the C-2 device," *Physics of Plasmas*, Vol. 19, No. 056108, 2012, pp. 1–8.

[8] Binderbauer, M. W., Tajima, T., Steinhauer, L. C., Garate, E., Tuszewski, M., Schmitz, L., Guo, H. Y., Smirnov, A., Gota, H., Barnes, D., Deng, B. H., Thompson, M. C., Trask, E., Yang, X., Putvinski, S., Rostoker, N., Andow, R., Aefsky, S., Bolte, N., Bui, D. Q., Ceccherini, F., Clary, R., Cheung, A. H., Conroy, K. D., Dettrick, S. A., Douglass, J. D.,

Feng, P., Galeotti, L., Giammanco, F., Granstedt, E., Gupta, D., Gupta, S., Ivanov, A. A., Kinley, J. S., Knapp, K., Korepanov, S., Hollins, M., Magee, R., Mendoza, R., Mok, Y., Necas, A., Primavera, S., Onofri, M., Osin, D., Rath, N., Roche, T., Romero, J., Schroeder, J. H., Sevier, L., Sibley, A., Song, Y., Drie, A. D. V., Walters, J. K., Waggoner, W., Yushmanov, P., Zhai, K., and TAE Team, "A High Performance Field-Reversed Configuration," *Physics of Plasmas*, Vol. 22, No. 056110, 2015, pp. 1–16.

[9] Helion Energy, https://www.helionenergy.com, Accessed: 2020-01-14.

[10] "Staged Magnetic Compression of FRC Targets to Fusion Conditions," https://arpa-e.energy.gov/?q=slick-sheet-project/compression-frc-targets-fusion, Accessed: 2020-01-14.

[11] Meier, E. T. and Shumlak, U., "A general nonlinear fluid model for reacting plasma-neutral mixtures," *Physics of Plasmas*, Vol. 19, No. 7, 2012.

[12] Steinhauer, L. C., "Review of Field-Reversed Configurations," *The Physics of Fluids*, Vol. 18, No. 070501, 2011, pp. 1–38.

[13] Tuszewski, M., "Field Reversed Configurations," *Nuclear Fusion*, Vol. 28, No. 11, 1988, pp. 2033–2092.

[14] Es'kov, A. G., Kurtmullaev, R. K., Kreshchuck, A. P., Laukhim, Y. N., Malyutin, A. I., Markin, A. I., Martyushov, Y. S., Mironov, B. N., Orlov, M. M., Proshletsov, A. P., Semenov, V. M., and Sosunov, Y. B., "Principles of Plasma Heating and Confinement in a Compact Toroidal Configuration," *Plasma Physics and Controlled Nuclear Fusion Research*, Vol. 2, International Atomic Energy Agency, Vienna, 1978, pp. 187–204.

[15] Armstrong, W. T., Harding, D. G., Crawford, E. A., and Hoffman, A. L., "Flux-Trapping During the Formation of Field-Reversed Configurations," *The Physics of Fluids*, Vol. 25, 1982, pp. 2121–2127.

[16] Slough, J. and Milroy, R., "High Flux FRC Facility for Stability and Confinement Studies," *Journal of Fusion Energy*, Vol. 29, No. 6, 2010, pp. 567–570.

[17] Slough, J., Votroubek, G., and Pihl, C., "Creation of a High-Temperature Plasma Through Merging and Compression of Supersonic Field Reversed Configuration Plasmoids," *Nuclear Fusion*, Vol. 51, No. 053008, 2011, pp. 1–10.

[18] Slough, J., "Staged Magnetic Compression of FRC Targets to Fusion Conditions," *ALPHA 2016 Annual Review Meeting*, August 2016.

[19] Armstrong, W. T., Cochrane, J. C., Commisso, R. J., Lipson, J., and Tuszewski, M., "θ-pinch ionization for field-reversed configuration formation," *Applied Physics Letters*, Vol. 38, No. 9, 1981, pp. 680–682.

[20] Commisso, R. J., Armstrong, W. T., Cochrane, J. C., Ekdahl, C. A., Lipson, J., Linford, R. K., Sherwood, E. G., Siemon, R. E., and Tuszewski, M., "The Initial Ionization Stage of FRC Formation," *Proceedings of the Third Symposium on the Physics and Technology of Compact Toroids in the Magnetic Fusion Energy Program*, Los Alamos Scientific Laboratory, Los Alamos, New Mexico, 1980, pp. 184–187.

[21] Rej, D. J., Hugrass, W. N., Barnes, G. A., and Siemon, R. E., "FRC Formation Experiments with Tearing Reconnection on the FRX-C/LSM Device," Tech. Rep. LA-10818-MS, Los Alamos National Laboratory, Los Alamos, New Mexico, September 1986.

[22] Armstrong, W. T., Cochrane, J. C., Lipson, J., Linford, R. K., McKenna, K. F., Sgro, A. G., Sherwood, E. G., Siemon, R. E., and Tuszewski, M., "FRC Studies on FRC-B," *Proceedings of the Third Symposium on the Physics and Technology of Compact Toroids in the Magnetic Fusion Energy Program*, Los Alamos Scientific Laboratory, Los Alamos, New Mexico, 1980, pp. 180–183.

[23] Wang, G., Wang, S., Cui, H., and Liao, J., "Experiments of a field-reversed configuration," *Chinese Physics*, Vol. 4, No. 4, 1984, pp. 874–878.

[24] Slough, J. T. and Hoffman, A. L., "Observation of Tilt Stability of Field Reversed Configurations at Large S," *Nuclear Fusion*, Vol. 28, No. 6, 1988, pp. 1121–1125.

[25] Tuszewski, M., "Excluded Flux Analysis of a Field Reversed Plasma," Tech. Rep. LA-8512-MS, Los Alamos Scientific Laboratory, University of California, September 1980.

[26] Milroy, R. D., Personal communiation.

[27] "ALPA-E | ALPHA," https://arpa-e.energy.gov/?q=arpa-e-programs/alpha, Accessed: 2020-01-14.

[28] Barnes, D. C., Personal communiation.

[29] Armstrong, W. T., Linford, R. K., Lipson, J., Platts, D. A., and Sherwood, E. G., "Field-reversed experiments (FRX) on compact toroids," *The Physics of FLuids*, Vol. 24, No. 11, 1981, pp. 2068–2089.

[30] Meeks, W. C. and Rovey, J. L., "On the delayed gas breakdown in a ringing theta-pinch with bias magnetic field," *Physics of Plasmas*, Vol. 19, No. 052505, 2012, pp. 1–19.

[31] Milroy, R. D., Slough, J. T., and Hoffman, A. L., "Plasma Wall Sheath Contributions to Flux Retention During the Formation of Field-Reversed Configurations," *The Physics of Fluids*, Vol. 27, 1984, pp. 1545–1551.

[32] Sgro, A. G., "Calculations of the effects of incomplete preionization in high voltage theta pinches," *The Physics of Fluids*, Vol. 21, No. 8, 1978, pp. 1410–1416.

[33] Matsuzawa, Y., Asai, T., Takahashi, T., and Takahashi, T., "Effects of Background Neutral Particles on a Field-Reversed Configuration Plasma in the Translation process," *Physics of Plasmas*, Vol. 15, No. 082504, 2008, pp. 1–8.

[34] Matsuzawa, Y., Yamamoto, N., Takao, K., Tamura, H., Hiyoshi, M., Sasaki, T., Asai, T., Takahashi, T., Nogi, Y., and Takahashi, T., "Particle and Energy Recovery Process of a High-Beta Compact Toroid Translated Along an Asymmetric Mirror Field," *Fusion Science and Technology*, Vol. 55, No. 2T, 2009, pp. 76–81.

[35] Asai, T., Matsuzawa, Y., Okano, T., Kiguchi, T., Sakuraba, K., Takahashi, T., Takahashi, T., Hirano, Y., Mizuguchi, N., and Tomita, Y., "Heating and Particle Build-Up of Field-Reversed Configuration due to Neutral Particle Injection in a Translation Process," *Fusion Science and Technology*, Vol. 51, No. 2T, 2007, pp. 379–381.

[36] Takahashi, T., Kato, T., Kondoh, Y., and Iwasawa, N., "Power Deposition by Neutral Beam Injected Fast Ions in Field-Reversed Configurations," *Physics of Plasmas*, Vol. 11, 2004, pp. 3801–3807.

[37] Koike, S., Watanabe, T., and Mitsui, T., "Heating Effects of Background Neutral Particles on a Translated Field-Reversed Configuration," *Transations of Fusion Science and Technology*, Vol. 63, No. 1T, 2013, pp. 377–379.

[38] Brackbill, J., Cambier, J., Gimelshein, N. E., and Gimelshein, S. F., "Numerical Analysis of Neutral Entrinment Effect on Field-Reversed Configuration Thruster Efficiency," *Journal of Propulsion and Power*, Vol. 30, No. 6, 2014, pp. 1450–1458.

[39] Koo, J., Sousa, E. M., and Martin, R., "High Fidelity Modeling of FIeld-Reversed Configuration (FRC) Thrusters," Tech. Rep. AFRL-RQ-ED-TR-2017-0002, Air Force Research Laboratory (AFMC), April 2017.

[40] Kirtley, D., Slough, J., Pihl, C., Meier, E., and Milroy, R., "Pulsed Plasmoid Propulsion: Air-Breathing Electromagnetic Propulsion," *32nd International Electric Propulsion Conference*, No. IEPC-2011-015, Wiesbaden, Germany, 2011.

[41] Guo, H. Y., Binderbauer, M. W., Barnes, D., Putvinski, S., Rostoker, N., Sevier, L., Tuszewski, M., Anderson, M. G., Andow, R., Bonelli, L., Brandi, F., Brown, R., Bui, D. Q., Bystritskii, V., Ceccherini, F., Clary, R., Cheung, A. H., Conroy, K. D., Deng, B. H., Dettrick, S. A., Douglass, J. D., Feng, P., Galeotti, L., Garate, E., Giammanco, F., Glass, F. J., Gornostaeva, O., Gota, H., Gupta, D., Gupta, S., Kinley, J. S., Knapp, K., Korepanov, S., Hollins, M., Isakov, I., Jose, V. A., Li, X. L., Luo, Y., Marsili, P., Mendoza, R., Meekins, M., Mok, Y., Necas, A., Paganini, E., Pegoraro, F., Pousa-Hijos, R., Primavera, S., Ruskov, E., Qerushi, A., Schmitz, L., Schroeder, J. H., Sibley, A., Smirnov, A., Song, Y., Steinhauer, L. C., Sun, X., Thompson, M. C., Drie, A. D. V., Walters, J. K., Wyman, M. D., and TAE Team, "Formation of a long-lived hot field reversed configuration by dynamically merging two colliding high-β compact toroids," *Physics of Plasmas*, Vol. 18, No. 056110, 2011, pp. 1–10.

[42] Jardin, S. C., "Review of Implicit Methods for the Magnetohydrodynamic Description of Magnetically Confined Plasmas," *Journal of Computational Physics*, Vol. 231, 2012, pp. 822–838.

[43] Gaskell, P. H. and Lau, A. K. C., "Curvature-Compensated Convective Transport: SMART, a New Boundedness Preserving Transport Algorithm," *International Journal for Numerical Methods in Fluids*, Vol. 8, 1988, pp. 617–641.

[44] Harned, D. S. and Schnack, D. D., "Semi-implicit Method for Long Time Scale Magnetohydrodynamic Computations in Three Dimensions," *Journal of Computational Physics*, Vol. 65, 1986, pp. 57–70.

[45] Schnack, D. D., Barnes, D. C., Mikic, Z., Harned, D. S., and Caramana, E. J., "Semi-implicit Magnetohydrodynamic Calculations," *Journal of Computational Physics*, Vol. 70, 1987, pp. 330–354.

[46] Harned, D. S. and Mikic, Z., "Accurate Semi-implicit Tratment of the Hall Effect in Magnetohydrodynamic Computations," *Journal of Computational Physics*, Vol. 83, 1989, pp. 1–15.

[47] Sovinec, C. R., King, J. R., and the NIMROD Team, "Analysis of a Mixed Semi-implicit/Implicit Algorithm for Low-frequency Plasma Modeling," *Journal of Computational Physics*, Vol. 229, 2010, pp. 5803–5819.

[48] Braginskii, S. I., "Transport Processes in a Plasma," *Reviews of Plasma Physics*, edited by M. A. Leontovich, Vol. 1, Consultants Bureau, New York, 1965, pp. 205–311.

[49] Grad, H., "Asymptotic Theory of the Boltzmann Equation," *The Physics of Fluids*, Vol. 6, No. 2, 1963, pp. 147–181.

[50] Schunk, R. and Nagy, A., *Ionospheres: Physics, Plasma Physics, and Chemistry*, Cambridge University Press, New York, 2009.

[51] Burgers, J. M., *Flow Equations for Composite Gases*, Vol. 11 of *Applied Mathematics and Mechanics,*, Academic Press, New York, 1969.

[52] Chapman, S. and Cowling, T. G., *The Mathematical Theory of Non-Uniform Gases, 3rd Ed.*, Cambridge University Press, Cambridge, 1970.

[53] Milroy, R. D. and Brackbill, J. U., "Numerical Studies of a Field-Reversed Theta-Pinch Plasma," *The Physics of Fluids*, Vol. 25, No. 5, 1982, pp. 775–783.

[54] Sgro, A. G., "Simulations of the ZT-S reversed field pinch," *The Physics of Fluids*, Vol. 23, No. 5, 1980, pp. 1055–1061.

[55] Bydder, E. L., "On the Evaluation of Elastic and Inelastic Collision Frequencies for Hydrogenic-like Plasmas," Tech. Rep. EP-RR 17, Department of Engineering Physics Research School of Physical Sciences, The Australian National University, September 1967.

[56] Knoepfel, H., *Pulsed High Magnetic FIelds*, North Holland Publishing Company, Amsterdam, 1970.

[57] Zhdanov, V. M., *Transport Processes in Multicomponent Plasma*, Taylor & Francis, New York, 2002.

[58] Lieberman, M. A. and Lichtenberg, A. J., *Principles of Plasma Discharges and Material Processing, 2nd Ed.*, John Wiley & Sons, Inc., Hoboken, 2005.

[59] Gudmundsson, J. T., "Notes on the Electron Excitation Rate Coefficients for Argon and Oxygen Discharge," Tech. Rep. RH-21-2002, University of Iceland, Reykjavik, October 2002.

[60] Janev, R. K., Langer, W. D., Evans, Jr., K., and E. Post, Jr., D., *Elementary Processes in Hydrogen-Helium Plasmas*, Vol. 4 of *Springer Series on Atoms+Plasmas,*, Springer Berlin Heidelberg, Berlin, 1987.

[61] Park, C., "Electron Impact Excitation Rate Coefficients for Hydrogen, Helium and Alkali Atoms," *Journal of Quantitative Spectroscopy and Radiative Transfer*, Vol. 11, No. 1, 1971, pp. 7–36.

[62] Jackson, J. D., *Classical Electrodynamics*, John Wioley & Sons, Inc., New York, third edition ed., 1999.

[63] Gunter, S., Yu, Q., Kruger, J., and Lackner, K., "Modelling of heat transport in megnetised plasmas using non-aligned coordinates," *Journal of Computational Physics*, Vol. 209, 2005, pp. 354–370.

[64] Yu, Y., "The virtual power principle in fluid mechanics," *Journal of Fluid Mechanics*, Vol. 774, 2014, pp. 310–328.

[65] Data provided by Helion Energy with approval for public release.

[66] Goldston, R. J. and Rutherford, P. H., *Introduction to Plasma Physics*, Taylor & Francis, New York, 1995.

[67] Duchs, D. and Griem, H. R., "Computer Study of the Dynamic Phase of a Small θ-Pinch," *The Physics of Fluids*, Vol. 9, No. 6, 1966, pp. 1099–1109.

[68] Rapp, D. and Francis, W. E., "Charge Exchange between Gaseous Ions and Atoms," *The Journal of Chemical Physics*, Vol. 37, No. 11, 1962, pp. 2631–2645.

[69] Zhdanov, V. M. and Stepanenko, A. A., "Kinetic Theory of Transport Processes in Partially Ionized Reactive Plasma, I: General Transport Equations," *Physica A*, Vol. 446, 2016, pp. 35–53.

[70] Wang-Chang, C. S., Uhlenbeck, G. E., and de Boer, J., "The Heat Conductivity and Viscosity of Polyatomic Gases," *Studies in Statistical Mechanics*, edited by J. de Boer and G. E. Uhlenbeck, Vol. 2, North Holland Publishing Company, Amsterdam, 1964, pp. 241–268.

[71] Giovangigli, V. and Graille, B., "Kinetic Theory of Partially Ionized Reactive Gas Mixtures," *Physica A*, Vol. 327, 2003, pp. 313–348.

[72] Tawara, H., Itikawa, Y., Nishimura, H., and Yoshino, M., "Cross Sections and Related Data for Electron Collisions with Hydrogen Molecules and Molecular Ions," *Journal of Physical and Chemical Reference Data*, Vol. 19, No. 3, 1990, pp. 617–636.

[73] Janev, R. K. and Smith, J. J., "Cross Sections for Collision Processes of Hydrogen Atoms with Electrons, Protons, and Multiply Charged Ions," *Atomic and Plasma-Material Interaction Data for Fusion*, Vol. 4, International Atomic Energy Agency, Vienna, 1993.

[74] Yoon, J., Song, M., Han, J., Hwang, S., Chang, W., Lee, B., and Itikawa, Y., "Cross Sections for Electron Collisions with Hydrogen Molecules," *Journal of Physical and Chemical Reference Data*, Vol. 37, No. 2, 2008, pp. 913–931.

[75] Peart, B. and Dolder, K. T., "Production of De-Excited H_3^+ Ions and Measurements of the Energies of Two Electronically-Excited States," *Journal of Physics B: Atomic and Molecular Physics*, Vol. 7, No. 12, 1974, pp. 1567–1573.

[76] Peart, B. and Dolder, K. T., "Measurements of Cross Sections for the Production of Protons by Collision between Electrons and Vibrationally De-Excited H_3^+ Ions," *Journal of Physics B: Atomic and Molecular Physics*, Vol. 8, No. 12, 1975, pp. L143–L145.

[77] Sobelman, I. I., *Atomic Spectra and Radiative Transitions*, Vol. 12 of *Springer Series on Atoms+Plasmas,*, Springer Berlin Heidelberg, Berlin, Heidelberg, second edition. ed., 1992.

[78] Sobelman, I. I., *Excitation of Atoms and Broadening of Spectral Lines*, Vol. 15 of *Springer Series on Atoms+Plasmas,*, Springer Berlin Heidelberg, Berlin, Heidelberg, second edition. ed., 1995.

[79] Itikawa, Y., "Momentum-Transfer Cross Sections for Electron Collisions with Atoms and Molecules," *Atomic Data and Nuclear Data Tables*, Vol. 14, No. 1, 1972, pp. 1–10.

[80] Ito, R., Tabata, T., Shirai, T., and Phaneuf, R. A., "Analytic Cross Sections for Collisions of H, H_2, He and Li Atoms and Ions with Atoms and Molecules," Tech. Rep. JAERI-M 93-117, Japan Atomic Energy Research Institute, Tokaimura, Japan, June 1993.

[81] Tabata, T. and Shirai, T., "Analytic Cross Sections for Collisions of H^+, H_2^+, H_3^+, H, H_2, and H^- with Hydrogen Molecules," *Atomic Data and Nuclear Data Tables*, Vol. 76, No. 1, 2000, pp. 1–25.

VITA

Akihisa Shimazu earned a Bachelor of Science in Aeronautical & Astronautical Engineering and Bachlor of Science in Physics with Magna Cum Laude from University of Washington in 2014. In 2016, he recieved Master of Science in Aeronautics & Astronautics from University of Washington for his work in modeling inductively driven liner implosions for FRC targets. In 2020, he recieved his Ph.D. from William E. Boeing Department of Aeronautics & Astronautics at University of Washington for his work in modeling neutral effects in FRCs.